CRACK PATH DETERMINATION FOR NON-PROPORTIONAL MIXED-MODE FATIGUE

A Thesis
Presented to
The Academic Faculty

by

Shelby Highsmith, Jr.

In Partial Fulfillment
of the Requirements for the Degree
Doctor of Philosophy in the
George W. Woodruff School of Mechanical Engineering

Georgia Institute of Technology
May 2009

CRACK PATH DETERMINATION FOR NON-PROPORTIONAL MIXED-MODE FATIGUE

Approved by:

Professor W. Steven Johnson,
Committee Chair
School of Materials Science &
Engineering
George W. Woodruff School of
Mechanical Engineering
Georgia Institute of Technology

Professor Thomas H. Sanders, Jr.
School of Materials Science &
Engineering
Georgia Institute of Technology

Professor Richard W. Neu
George W. Woodruff School of
Mechanical Engineering
School of Materials Science &
Engineering
Georgia Institute of Technology

Professor Naresh N. Thadhani
School of Materials Science &
Engineering
George W. Woodruff School of
Mechanical Engineering
Georgia Institute of Technology

Professor Jianmin Qu
George W. Woodruff School of
Mechanical Engineering
Georgia Institute of Technology

Date Approved: 1 April 2009

To my father, Shelby, with whom I like to debate who is whose hero, and to my mother, Mary Jane, whose patience with, dedication to, and love for family is unsurpassed.

ACKNOWLEDGEMENTS

I owe more thanks than can reasonably be put in this preamble to my advisor, Dr. Steve Johnson, for his patience and understanding throughout my long and rambling tenure at Georgia Tech. I had no way of anticipating – and thus I imagine he was blindsided by – the detours away from fracture mechanics and into international affairs programs, political campaigns, and freelance journalism, but he has always demonstrated he had my (and all of his students') best interests at heart and has done everything he could to support them. I want to thank my committee members, Dr. Richard Neu, Dr. Jianmin Qu, Dr. Thomas Sanders, and Dr. Naresh Thadhani – as well as earlier members Dr. John Holmes and Dr. Rami Haj-Ali – for reviewing my work and helping to clarify the technical language where I wandered off the beaten path. Dr. Stephen Antolovich also provided valuable metallurgical insight and was a welcome "honorary" committee member. I am also grateful to several faculty members in International Affairs, particularly Dr. John Endicott, Dr. Bill Hoehn, and Dr. Seymour Goodman of the Sam Nunn Security Studies Program, for providing balance to my studies at Georgia Tech and nudging me toward my next career move.

Thanks go to Dr. Richard Pettit of Pratt & Whitney for initiating this research project and Dr. Gregory Swanson and Dr. Tarek Sayyah at NASA Marshall Space-flight Center for contributing their data to the task. All of their insights during many valuable conference calls along the way provided the foundation for everything in this document. Michael Middlemas in Materials Science & Engineering has our gratitude for manning the SEM and getting the great pictures. The Atlanta ARCS Foundation provided valuable financial support the last three years through the generosity of Mr.

and Mrs. Harmon B. Miller, III. Thanks to Team Johnson members in MPRL, past and present, for being good sports and labmates; take care of my stereoscope! And as always, Rick Brown and Robert Cooper of the Mechanical Properties Research lab deserve thanks for fielding endless technical questions about machines that seemed to have it in for me.

When you've been around this long, you rely on too many people to thank individually, but I am deeply grateful to all of the friends I have made in Atlanta who have provided support in the hard times and diversion in the good. My recent fellow travelers down the long, rocky road of soul-searching academic self-deprivation, Dr. Kristin Wuichet and the Rev. Justice Schunior, were particularly helpful many a late night for commiserating and contemplating the simple question: *why?*

Finally, thank you from the bottom of my heart, Mom and Dad, for never giving up hope. And for keeping the fridge stocked.

TABLE OF CONTENTS

LIST OF TABLES

LIST OF FIGURES

SUMMARY

Turbine engine components such as fan and compressor blades experience complex combinations of steady and vibratory loads that lead to in-service cracking in directions that cannot be predicted by current fracture criteria. Accurate crack path predictions are required in order to characterize the risk and extent of damage resulting from liberation of a fractured ligament from rotating components. Under proportional in-phase mixed Mode I / Mode II loading conditions, crack growth direction has been observed in some materials to shift from tensile-dominated Mode I to shear-dominated Mode II or mixed-mode crack growth at higher proportions of initial Mode II loading, but non- proportional loads are not well-characterized. An extensive database of crack growth direction under non-proportional 2-D mixed-mode loading conditions is required to expand crack path prediction models, which are likely to vary between alloys. An approach based on linear elastic fracture mechanics (LEFM) is desired in order to implement the model in crack growth software such as the boundary element-based fracture analysis package FRANC3D.

A novel specimen configuration has been designed and analyzed for generation of wide ranges of mixed-mode loading conditions in a single test. This specimen and a more conventional thin-walled tubular specimen have been used to test polycrystalline nickel-base superalloy Inconel 718 under proportional in-phase and 3 kinds of non-proportional fatigue loading. Stress intensity factors for the various configurations have been analyzed with FRANC3D.

Modal transition from Mode I (tensile) to Mode II (shear) crack branching has been observed in several load cases. Qualitative microscopy of fracture surfaces was used to characterize the crack growth behavior. An LEFM approach based on an effective stress intensity factor range, which incorporates the maximum value and range

of each appropriate stress intensity (Mode I or Mode II), has been used to successfully predict the crack deflection angles, and in most cases to quantify modal transition, within each load case considered. Variability between load cases and specimen configurations points to the limitations of LEFM, or at least the stress singularity-based approximation of crack tip stress fields, in providing a general predictor of crack path behavior across all types of non-proportional mixed mode loading.

CHAPTER 1

INTRODUCTION

1.1 Research Background

Advances in mechanical modeling of damage and in the sensitivity of in-service inspection of critical components have driven a shift from the traditional safe-life philosophy of fatigue life limits toward a damage tolerance approach. Instead of retiring components at a specified cycle limit based on smooth or notched bar low cycle fatigue data, a component capable of inspection is retired for cause upon detection of unacceptable damage, such as a fatigue crack. The associated inspection intervals are set by fracture mechanics analyses of crack growth from critical locations, so that no damage or flaw could grow from an undetectable level to a critical crack size between inspections. Accurate modeling of the hypothetical crack growth requires advance knowledge of critical fatigue initiation locations, the projected crack path, and the subsequent stress environment along the predicted crack path.

In addition to providing the appropriate stress solution for crack growth rate prediction, understanding of the crack path is also required to predict the ultimate effects of a fatigue failure. For example, in the case of a fatigue crack initiating along the span of a rotor blade in a turbine propulsion engine, the likely crack path will determine the mass of the segment of the blade that may ultimately be liberated if fracture occurs, and thus the kinetic energy released by the fragment, due to the extremely high rotational speeds of the engine. This can have a significant impact on the weight of the engine design, since the casing around the critical rotating components must take into consideration the ability to prevent ejection of any debris from the engine into other parts of the aircraft or may determine that containment is not possible.

In this example, the primary load experienced by the rotor blade is the radial

stress caused by the centripetal acceleration due to rotation, and intuition would suggest a crack path straight across the blade in a direction perpendicular to the load (normal crack growth). However, these components experience complex and dynamic stress distributions under the influence of transient aerodynamic pressure distributions that result in vibratory modes, leading to the superposition of bending and twisting stresses upon the primary radial tensile load. When a crack encounters stress fields that differ from a nominally crack-normal tensile state, the crack tip can experience any combination of three loading modes: Mode I, normal/tensile; Mode II, in-plane shear; and Mode III, out-of-plane shear. The crack tip stress fields under these loading modes are characterized by their respective stress intensity factors (SIFs), K_{I}, K_{II}, and K_{III}. Extensive prior data on quasi-static Mode I-II combinations have shown that cracks change direction under such circumstances toward a nominally Mode I-dominated direction, leading to development of the Maximum Tensile Stress Criterion (MTSC) [1] and similar theories for two-dimensional loading. These commonly used crack deflection theories generally predict crack propagation in a direction that maximizes K_{I} such that the tensile mode of cracking is the dominant mechanism.

However, cracks can propagate by gross shear mechanism in addition to the common tensile rupture or tearing mechanism. More recent experimental data and theoretical modeling have shown that in some cases a crack subjected to mixed K_{I}-K_{II} loading can turn to propagate in a different direction, along the plane of maximum shear stress, than that predicted by the conventional MTSC crack growth model in which the crack propagates along the direction normal to the maximum tensile stress. This alternate crack path is predicted by the Maximum Shear Stress Criterion (MSSC) [2, 3]. As mode mixity increases in the direction of Mode II, the crack path deflection can change drastically when a critical transition point is reached and the dominant fracture mechanism changes from tensile to shear.

These observations on the transition from MTSC- to MSSC-predicted crack extension come largely from the context of monotonic fracture. Similar transition phenomena have been observed in proportional mixed-mode fatigue loading of cracks, frequently by subjecting a specimen with an inclined crack to uniaxial fatigue loading, and have been reasonably predicted by the standard monotonic criteria. As loadings become more complex, the ability to characterize crack growth behavior in this standard framework becomes more challenging due to the time-varying value of mode mixity.

1.2 Research Objectives

Much of the work in crack path criteria has been performed for two-dimensional cases (Modes I and II crack loading) and largely under quasi-static conditions. In fatigue loading, existing mixed-mode fracture criteria can be applied to the fatigue crack growth case if the loading is in phase and Modes I and II remain proportional. However, mixed-mode fatigue loading in practice can take the form of many non-proportional waveforms, the simplest of which in the laboratory setting can include constant Mode I with cyclic Mode II; cyclic Mode I with constant Mode II; and cyclic Mode I with cyclic Mode II offset by any phase angle, such as 90° or 180°. The crack path criteria for quasi-static and proportional fatigue loading take as an input parameter some form of the ratio $K_{\mathrm{II}}/K_{\mathrm{I}}$ as the mode mixity. Thus they are not readily applicable to the non-proportional cases because the value of $K_{\mathrm{II}}/K_{\mathrm{I}}$ varies through time as the waveforms of each mode do not coincide. The research question at hand is then which values of each SIF – the range or maximum of K_{I} and K_{II} – should be used as inputs, and how should they be combined?

This project was initiated to provide data and a methodology for crack path prediction under non-proportional loading that could be implemented in a linear elastic fracture mechanics (LEFM)-based framework for efficient crack growth prediction.

In the absence of sufficient material for detailed study of material properties and micromechanisms of damage, the current approach focuses on the LEFM characterization of crack growth direction and transition, under the implicit assumption of isotropic, homogeneous material behavior. A novel test specimen configuration was proposed to generate broad ranges of mode mixity in a single test in order to generate sufficient data for model fitting and to look effectively for conditions of modal transition without requiring multiple specimen tests. This specimen was analyzed using the boundary element modeling-based fracture analysis package FRANC3D, distributed by the Cornell Fracture Group, and a closed-form SIF solution was developed. Specimens of this configuration were used to test the nickel-base superalloy Inconel 718 at Georgia Tech. These data have been combined with data from testing of thin-walled tubular specimens of Inconel 718 at NASA Marshall Spaceflight Center. Proportional in-phase fatigue testing was performed as a baseline and three non-proportional cases mentioned above – constant tension/cyclic torsion, constant torsion/cyclic tension, and 180° out-of-phase tension/torsion – were also tested at various ratios of $K_{\mathrm{IImax}}/K_{\mathrm{Imax}}$. As a baseline question it needed to be determined whether modal transition from tensile to shear cracking was a likely phenomenon in this alloy. Then the crack growth angles developed were used to seek a crack driving force parameter that could be used to predict the angle of crack branching by maximizing the crack driving parameter.

1.3 Outline

This thesis continues by presenting a survey of the literature on mixed-mode fracture and fatigue crack growth behavior in Chapter 2. Experimental observations and the challenges of predicting crack path behavior are examined beginning with the simple monotonic fracture case and progressing through proportional fatigue crack growth into more complex non-proportional cases. Chapter 3 describes the specimens

employed in the experimental work and lays out the test matrix covered and the rationale behind its construction. Chapter 4 goes into the details of the specimen designs in terms of fracture mechanics by presenting the FRANC3D models used to analyze the crack growth conditions tested, and an interesting by-product of manufacturing defects in specimens is described. (A catalog of all of the NASA specimen pre-cracks and the FRANC3D crack meshes used to generate the 3 SIF values is included in Appendix A.) The general procedure for generating a closed-form SIF solution for the new specimen design is described as well in Chapter 4, although the full details of that analysis are left to Appendix B.

The experimental data from first the NASA specimens and then the new specimens tested at Georgia Tech are presented in Chapter 5, including a portion of the scanning electron microscope (SEM) fractography. The full set of SEM images is collected in Appendix C. Trends in each data set and variations between them are described in terms of the LEFM quantities best suited for predicting the crack path. Finally, Chapter 6 presents the conclusions that can be drawn from the trends and shortcomings discussed in Chapter 5 and offers areas for further work to improve understanding of crack path behavior in non-proportional loading.

CHAPTER 2

LITERATURE REVIEW

The two primary aspects of crack propagation of interest in the present work are the direction of propagation and the transition between modes of propagation (i.e., tensile or shear crack growth). In accordance with the assumptions of the current work, focus in the literature review is restricted to polycrystalline alloys for which assumptions of isotropic, homogenous fracture properties can be made more reasonably than for the single crystal alloys used in several Stage I mixed-mode crack growth studies. This chapter will present an overview of the relevant past work leading to this study, from monotonic two-mode fracture through in-phase two-mode fatigue crack growth and finally to non-proportional fatigue crack growth. The review is organized by those three load cases, and within each group presented largely chronologically. Where symbols and abbreviations for the same quantities or concepts vary between earlier publications, their terminology may be altered herein to conform with a single standard. For additional references not cited herein, the reader is referred to a thorough literature survey of mixed mode fatigue crack growth compiled by Qian and Fatemi in 1996 [4].

2.1 Mixed-Mode (I-II) Fracture

2.1.1 Symmetric Fracture Models

One of the earliest and most widely used models for mixed-mode fracture was published by Erdogan and Sih in 1963 [1]. Known interchangeably as the Maximum Hoop Stress (MHS) or Maximum Tangential Stress (MTS) Criterion, it predicts that a crack loaded in a K_{I}-K_{II} mixed-mode condition will propagate in the direction perpendicular to the maximum tangential stress $\sigma_{\theta\theta}$ ahead of the crack tip (as a function of angle θ, see Fig. 2.1) when $\sigma_{\theta\theta}$ reaches a critical value at some characteristic

distance from the crack tip. Under linear elastic conditions, the stresses near the crack

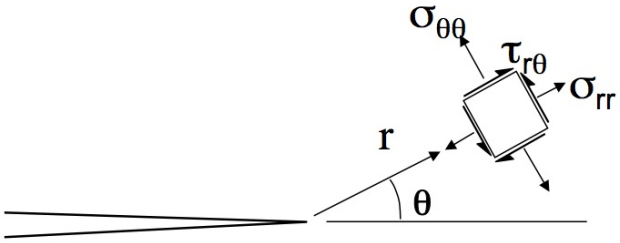

Figure 2.1: Crack tip stress components in cylindrical coordinates.

tip can be described by

$$\sigma_{rr} = \frac{1}{\sqrt{2\pi r}} \cos\frac{\theta}{2}\left[K_{\mathrm{I}}\left(1+\sin^2\frac{\theta}{2}\right) + K_{\mathrm{II}}\left(\frac{3}{2}\sin\theta - 2\tan\frac{\theta}{2}\right)\right] \tag{2.1}$$

$$\sigma_{\theta\theta} = \frac{1}{\sqrt{2\pi r}} \cos\frac{\theta}{2}\left(K_{\mathrm{I}}\cos^2\frac{\theta}{2} - \frac{3}{2}K_{\mathrm{II}}\sin\theta\right) \tag{2.2}$$

$$\tau_{r\theta} = \frac{1}{2\sqrt{2\pi r}} \cos\frac{\theta}{2}\left[K_{\mathrm{I}}\sin\theta + K_{\mathrm{II}}\left(3\cos\theta - 1\right)\right] \tag{2.3}$$

The angle of maximum tangential stress, θ^*, can found by solving

$$\frac{\partial\sigma_{\theta\theta}}{\partial\theta} = 0 \qquad \text{and} \qquad \frac{\partial^2\sigma_{\theta\theta}}{\partial\theta^2} < 0 \tag{2.4}$$

which has been shown analytically [5] to be

$$\theta^* = 2\tan^{-1}\left(\frac{D \pm \sqrt{D^2+8}}{4}\right) \tag{2.5}$$

where $D = K_{\mathrm{I}}/K_{\mathrm{II}}$, and the $\pm$ should take the opposite sign of D. Alternatively, as the plane of maximum $\sigma_{\theta\theta}$ is that on which the shear stress $\tau_{r\theta}$ is zero, the angle θ^* can be found by solving

$$K_{\mathrm{I}}\sin\theta^* + K_{\mathrm{II}}(3\cos\theta^* - 1) = 0 \tag{2.6}$$

from Eq. 2.3, discarding the trivial solution of $\cos\frac{\theta}{2} = 0$ (which corresponds to the crack surfaces behind the crack tip).

Sih [6] later proposed the strain energy density or S-criterion in 1974. This predicts crack extension along the direction of minimum strain energy density factor S given by

$$S = \frac{1}{16\pi\mu}\left[a_{11}K_{\mathrm{I}}^2 + 2a_{12}K_{\mathrm{I}}K_{\mathrm{II}} + a_{22}K_{\mathrm{II}}^2\right] \tag{2.7}$$

where

$$\begin{aligned} a_{11} &= (3 - 4\nu - \cos\theta)(1 + \cos\theta) \\ a_{12} &= 2\sin\theta(\cos\theta - 1 + 2\nu) \\ a_{22} &= 4(1 - \nu)(1 - \cos\theta) + (1 + \cos\theta)(3\cos\theta - 1) \end{aligned}$$

and μ is the shear modulus and ν is Poisson's ratio. Crack extension occurs when $S_{\min}$ reaches a critical value. (In 1980, Sih and Barthelmy [7] and Badaliance [8] used strain energy density as a driving force parameter for fatigue, replacing the commonly used $f(\Delta K)$ in Paris-like equations with $f(\Delta S)$. Both showed that this approach inherently accounted for mean loads in fatigue cycles, with Badaliance focusing on spectrum loading in Mode I crack growth. Such a consideration would also be required for some non-proportional fatigue waveforms considered in this research.) As the location of $S_{\min}$ is associated with dilatational strain energy (and $S_{\max}$ with distortional strain energy), the S-criterion should not be expected to predict shear-controlled failure.

Also using an energy approach, Hussain *et al.* [9] in 1974 developed a model for crack extension under mixed-mode loading occurring in the direction of maximum energy release rate (MERR), or $\mathcal{G}$, which was discussed originally by Erdogan and Sih but not mathematically feasible at the time. The energy release rate $\mathcal{G}$ for a kinked crack can be calculated as a function of angle from the crack tip θ using the standard Irwin formulation

$$\mathcal{G} = \frac{1}{E'}\left((K_{\mathrm{I}}{}^{(2)})^2 + (K_{\mathrm{II}}{}^{(2)})^2\right) \tag{2.8}$$

using newly derived "angular" stress intensity factors ${K_{\rm I}}^{(2)}$ and ${K_{\rm II}}^{(2)}$ to account for the kink angle,

$$ {K_{\rm I}}^{(2)}(\theta) = \left(\frac{4}{3+\cos^2\theta}\right)\left(\frac{\pi-\theta}{\pi+\theta}\right)^{\theta/2\pi}\left(K_{\rm I}\cos\theta+\frac{3}{2}K_{\rm II}\sin\theta\right) \tag{2.9} $$

$$ {K_{\rm II}}^{(2)}(\theta) = \left(\frac{4}{3+\cos^2\theta}\right)\left(\frac{\pi-\theta}{\pi+\theta}\right)^{\theta/2\pi}\left(K_{\rm II}\cos\theta-\frac{1}{2}K_{\rm I}\sin\theta\right) \tag{2.10} $$

where $E' = E/(1-\nu^2)$ (plane strain) or $E' = E$ (plane stress). (Later Chang *et al.* [10] in 2006 showed that a simpler approximation of $\mathcal{G}$ reduced identically to the MTS criterion, and even for the full formulation the difference between the MTS and MERR criteria are minor, becoming negligible approaching pure Mode I conditions.)

At the same time (1974), Shih [11] extended the MTS criterion to elastic-plastic fracture analysis following the analyses of a crack in strain-hardening material by Hutchinson [12] and Rice and Rosengren [13] (HRR). The predictions of Shih for the location of maximum tensile stress $\sigma_{\theta\theta}$ are identically those of Erdogan and Sih for $n = 1$ in the Ramberg-Osgood strain hardening constitutive equation implicit in the HRR analysis. For $n = \infty$ the difference in θ^* between Shih's model and the elastic MTS can be as high as approximately 10° (for pure $K_{\rm II}$ and near $K_{\rm I} = 2K_{\rm II}$) but the general trend is the same. Indeed all of the above models predict very similar crack deflection behavior for mixed mode I-II conditions, as shown in Fig. 2.2. The predicted crack deflection angle θ is plotted against the mode mixity angle ϕ given by

$$ \phi = \tan^{-1}\left(\frac{K_{\rm II}}{K_{\rm I}}\right) \tag{2.11} $$

such that $\phi = 0^\circ$ for pure Mode I and 90° for pure Mode II.[1]

It should be noted that this discussion has considered only the singular K-dominated stress field near the crack tip and does not account for second-order effects in the form

[1]The use of a pseudo-angle ϕ is primarily to avoid having an infinite value of mode mixity in the pure Mode II condition, which complicates development of analytical models. Other authors use the elastic mode mixity factor $M^e = 2/\pi\tan^{-1}(K_{\rm II}/K_{\rm I})$ so that $M^e = 0$ for Mode I and 1 for Mode II.

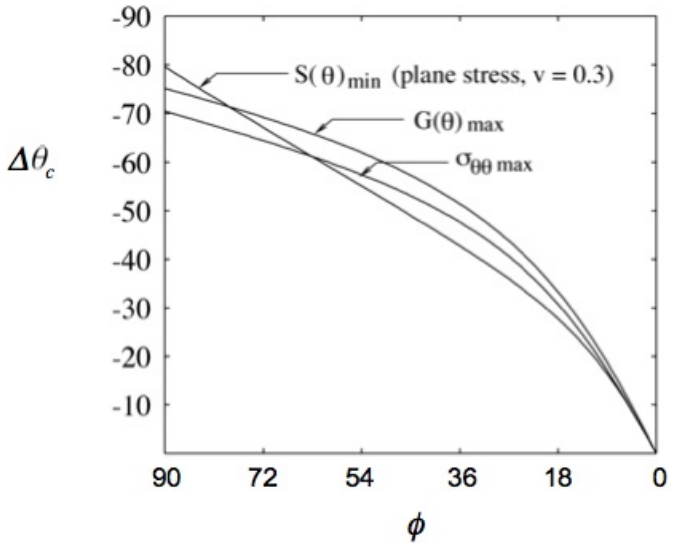

Figure 2.2: Comparison of crack deflection angle $\Delta\theta$ predictions versus mode mixity angle ϕ by different fracture criteria (from Pettit [14]).

of load biaxiality or the non-singular T-stress component of the crack tip stress field. The additional stress components neglected in Eqs. 2.1-2.3 in terms of T-stress are

$$\sigma_{rr}(T,\theta) = \frac{T}{2}(1+\cos 2\theta) \tag{2.12}$$

$$\sigma_{\theta\theta}(T,\theta) = \frac{T}{2}(1-\cos 2\theta) \tag{2.13}$$

$$\tau_{r\theta}(T,\theta) = -\frac{T}{2}\sin 2\theta \tag{2.14}$$

Liebowitz *et al.* [15] in 1978 discussed the inadequacy of the approximations of Eqs. 2.1-2.3 without the non-singular terms, citing the influence of biaxial stresses on local maximum shear stress, the shear stress distribution, and the angle of initial crack extension.

Neglecting the non-singular terms must be noted because in a review of first-order crack deflection theories to date in 2000, Pettit [14] showed them all to predict essentially a $K_{\mathrm{II}} = 0$ crack path. He also pointed out evidence of a process zone size effect on the influence of T-stress on crack path stability, showing a much greater influence for stable tearing fracture (under much higher loads) than for fatigue crack

growth. For purposes of this research into the behavior of fatigue cracks at relatively low loads, it is assumed that the damage process zone ahead of the crack tip is suitably small as to be dominated by the singular stress terms and thus only first-order theories of crack extension are being considered.

The similarity in predictions as shown in Fig. 2.2 is understandable when one considers that, as also discussed by Cotterell and Rice in 1980 [16], they are all formulated to predict the crack deflection angle of a crack that encounters a mixed-mode (or asymmetric) stress field. If stable crack growth will only remain co-planar under steady K_{I} loading and then will turn by some $\Delta\theta$ upon addition of any K_{II}, then it is reasonably expected that the new equilibrium sought by the growing crack will ultimately be one of $K_{\mathrm{II}} = 0$ to achieve a state of symmetry. Adherence to these essentially tensile stress-dominated criteria (particularly MTSC) has been well verified by Maccagno and Knott, especially with brittle materials such as PMMA (published in 1989) [17] as well as steels at cryogenic temperatures well below the ductility transition, failing by transgranular cleavage (published in 1991) [18]. This would be the case macroscopically even if the crack propagates in a zig-zag fashion along local shear bands, as the local deflections would be corrected back toward the crack plane. However, observations of a different fracture mechanism dominated by shear stress, which allows stable crack propagation under load asymmetry requires consideration of an alternative fracture criterion, discussed below.

2.1.2 Fracture Mode Transition

When the mechanism of crack extension is dominated by tensile stress, such as transgranular cleavage, the fracture models discussed above are almost equally successful at predicting crack deflection under mixed-mode loading. Maccagno and Knott repeated their experiments on HY130 steel, previously studied at cryogenic temperature [18], at room temperature in order to test the fracture criterion when the damage

mechanism involved decohesion along planes of maximum shear [2]. Their Mode I test results repeated previous observations of an overall co-planar crack extension even though the shear mechanism of fracture resulted in a zig-zag appearance locally[2]. However instead of a generally increasing fracture angle magnitude $|\theta|$ with an increase in mode mixity ϕ, as predicted by the MTSC, an initial increase in $|\theta|$ was followed by a decrease back to co-planar crack growth for $\phi = 45^\circ$ ($K_{\mathrm{II}} = K_{\mathrm{I}}$). Above $\phi = 45^\circ$ ($K_{\mathrm{II}} > K_{\mathrm{I}}$), even the zig-zag appearance was no longer evident as fracture was entirely co-planar with the initial slit and the fracture process was dominated by shear at the macroscopic level.

Hallback and Nilsson [3] in 1994 observed a similar Mode I to Mode II fracture transition in 7075-T6 aluminum. Using two different sizes (in the planform) of an Arcan-like specimen of the same thickness, they reported a tensile- to shear-dominated fracture mechanism transition between $\phi = 36.8^\circ$ and 48.2° for the smaller specimen and between $\phi = 40.4^\circ$ and 58° for the larger specimen when both were machined with the crack perpendicular to the rolling direction. (The large differences in ϕ surrounding the point of transition prevents any definitive observation of a size effect on fracture mode for this case.) Upon transition, the crack deflection angle jumped from a negative value of θ close to the MTS criterion to a positive θ close to the MSS criterion. They developed a fracture initiation model based on achievement of a critical plastic strain (resulting in expired work-hardening capacity) along localized shear bands ahead of the crack tip.

Amstutz *et al.* [19] in 1997 also described fracture mode transition in 2024-T3 aluminum in addition to assessing rolling orientation effects. In their work, extension from the pre-crack kinked in a tensile direction reasonably predicted by $J_{\mathrm{II}} = 0$ for

[2]Maccagno and Knott listed the fracture angle $|\theta| = 45^\circ$ for the Mode I test based on the first microscopic increment of crack extension although the macroscopic crack path was essentially $\theta = 0^\circ$. The subsequent increase and decrease in $|\theta|$ for $0^\circ < \phi < 45^\circ$ refers to the macroscopic fracture angle.

mode mixity values $\phi < 61°$, with plastic zones similar to rotated Mode I plastic zones and crack extension coinciding with the direction of minimal plasticity. Above $\phi = 48°$, the surface strain field shifted to a large shear-dominated Dugdale-type plastic zone along the pre-crack line; for $\phi \geq 68°$ they observed shear crack behavior (with both tensile and shear fractures observed at $\phi = 68°$ in both T-L and L-T orientations). They also observed traces of shear fractures at the surfaces of specimens with any non-zero K_{II}, although they coalesced with the dominant tunneling tensile fracture below the transition mixity, highlighting the competition between the two mechanisms.

Dalle Donne and Doker [20] also tested 2024-T3 as well as StE 550 steel using a biaxially-loaded cruciform specimen, as reported in 1997. They noticed a similar evolution in crack tip strain pattern for high-K_{II} loading in 2024-T3. Although their test conditions only provided broad ranges for possible fracture mode transition of $20° \leq \phi \leq 30°$ for the steel and $47° \leq \phi \leq 73°$ for the aluminum, this still highlights a significant difference between the materials.

Ghosal and Narasimhan [21] in 1994, citing other published observations of a fracture mode transition, performed finite element analyses of ductile crack initiation from a notch under mixed-mode (I-II) loading. They utilized a continuum damage model of fracture in addition to traditional finite deformation plasticity to explore the assumption of two competing mechanisms at the notch tip: micro-void nucleation and coalescence, associated with the dilatational component of the stress tensor, and localized shear band formation, associated with the deviatoric stress. Their model showed that while the zone of microvoid damage moved downward (toward negative, MTS-following values of θ) on the blunted side of a notch under increasing values of K_{II}, a narrow band of plastic strain concentration emanated from the sharpening upper portion of the notch (along positive, MSS-following values of θ), although they

did not include crack initiation in the shear band with this model. Upon incorporating previous experimental data showing two failure modes of mixed-mode fracture, however, their model showed an overlap of the competing mechanisms that would result in a failure mode transition from tensile (void coalescence) to shear (plastic strain banding) at higher levels of $K_{\mathrm{II}}/K_{\mathrm{I}}$.

All of this work established the need to consider an alternative fracture criterion – the maximum shear stress criterion (MSSC) suggested by Maccagno and Knott [2] – for materials that fail in a shear-dominated manner, particularly at high levels of $K_{\mathrm{II}}/K_{\mathrm{I}}$ where the fracture path is one of shear in the macroscopic sense. Chao and Liu [22] examined both mechanisms in 1997 to describe the transition between competing modes and criteria. Proposing a competition between the achievement of a critical shear stress or a critical normal stress at some characteristic distance ahead of the crack tip and performing elastic-plastic finite element analyses of a range of mixed mode loading, they developed a composite failure mode envelope shown in Fig. 2.3, which indicates the transition between the MTS (which they denote MHSC for "hoop stress") and MSS criteria at different mode mixities.[3] At lower values of $K_{\mathrm{II}}/K_{\mathrm{I}}$ (indicated by path A in Fig. 2.3(a)), the MTS criterion controls failure (and its direction θ^*) as $\sigma_{\theta\theta} > \sigma_c$ occurs before $\tau_{r\theta} > \tau_c$. Along loading path B above some material-dependent $K_{\mathrm{II}}/K_{\mathrm{I}}$ of transition, determined by the critical stresses as shown in Fig. 2.3(b), the MSS criterion predicts failure and its direction along the plane of maximum $\tau_{r\theta}$ when it exceeds τ_c. The angle θ^{**} of this maximum shear plane, which is found by solving

$$\frac{\partial \tau_{r\theta}}{\partial \theta} = 0 \qquad \text{and} \qquad \frac{\partial^2 \sigma_{\theta\theta}}{\partial \theta^2} < 0 \tag{2.15}$$

is determined numerically [22] to be given by

$$\theta^{**} = 9.347 \cdot 10^{-7}\beta_{eq}^4 - 3.222 \cdot 10^{-5}\beta_{eq}^3 + 9.086 \cdot \beta_{eq}^2 + 2.868 \cdot 10^{-1}\beta_{eq} - 4.884 \cdot 10^{-2} \tag{2.16}$$

[3] Liu *et al.* [23] later successfully extended this model to tensile-to-shear transition in mixed mode I-III loading in circumferentially cracked bars loaded in tension and torsion.

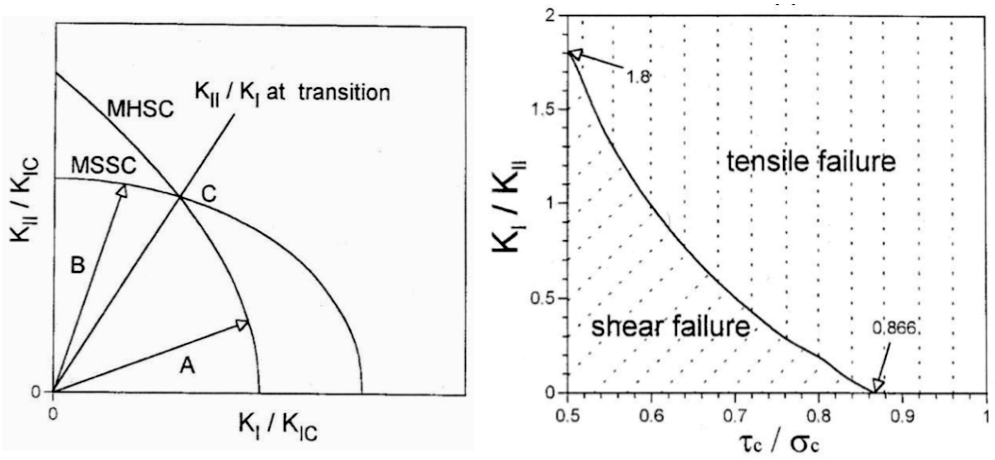

(a) (b)

Figure 2.3: Schematics showing (a) the competition of MTSC/MHSC and MSSC as a function of mode mixity; (b) critical mixity $K_{\mathrm{I}}/K_{\mathrm{II}}$ of transition as a function of material ductility τ_c/σ_c. (From [22])

where $\beta_{eq} = \tan^{-1}(K_{\mathrm{I}}/K_{\mathrm{II}}) = \pi/2 - \phi$.

Without delaying on contemplation of specific micromechanisms responsible for the observation of distinct fracture modes, Kfouri and Brown [24] in 1995 simply developed an empirical elliptical failure envelope for the MERR criterion. They argued that the Griffith fracture toughness $\mathcal{G}_c$ was not independent of the stress mode at the tip of a kinked crack, but rather was a function of the local kink tip mode mixity $q = k_2/k_1$, where k_1 and k_2 are the kink tip Mode I and II SIFs, as well as a material strength ratio $r = K_{\mathrm{II}r}/K_{\mathrm{I}r}$, where $K_{\mathrm{I}r}$ and $K_{\mathrm{II}r}$ are the instantaneous fracture resistances. They explored the effect of r on crack kink angles θ based on $\mathcal{G} > \mathcal{G}_c$ at the kink tip when

$$\mathcal{G}_c = (K_{\mathrm{I}r}^2/E')r^2(1+q^2)/(q^2+r^2) \tag{2.17}$$

This is similar to the earlier elliptical fracture criterion of Shah [25] at Boeing in 1975,

$$\left(\frac{K_{\mathrm{I}}}{K_{\mathrm{IC}}}\right)^2 + \left(\frac{K_{\mathrm{II}}}{K_{\mathrm{IIC}}}\right)^2 = 1 \tag{2.18}$$

but differs through its focus on the kink tip mode mixity of a deflected crack rather than the criticality of the baseline flat crack under mixed mode loading. By varying the material strength ratio r, Kfouri and Brown showed that for values $r \geq 0.82$, the crack deflection angle decreases monotonically with $K_{\mathrm{II}}/K_{\mathrm{I}}$ up to $K_{\mathrm{II}}/K_{\mathrm{I}} = \infty$, essentially following the MTS criterion. For $r \leq 0.81$, there exists a mode mixity $K_{\mathrm{II}}/K_{\mathrm{I}}$ at which the kink angle suddenly decreases in magnitude away from the MTS criterion back toward coplanar growth, and this transitional mode mixity decreases with r – that is, following the same general trend shown in Fig. 2.3(b). This shift in deflection angle is shown in Fig. 2.4(a) for several values of r. Although r is defined

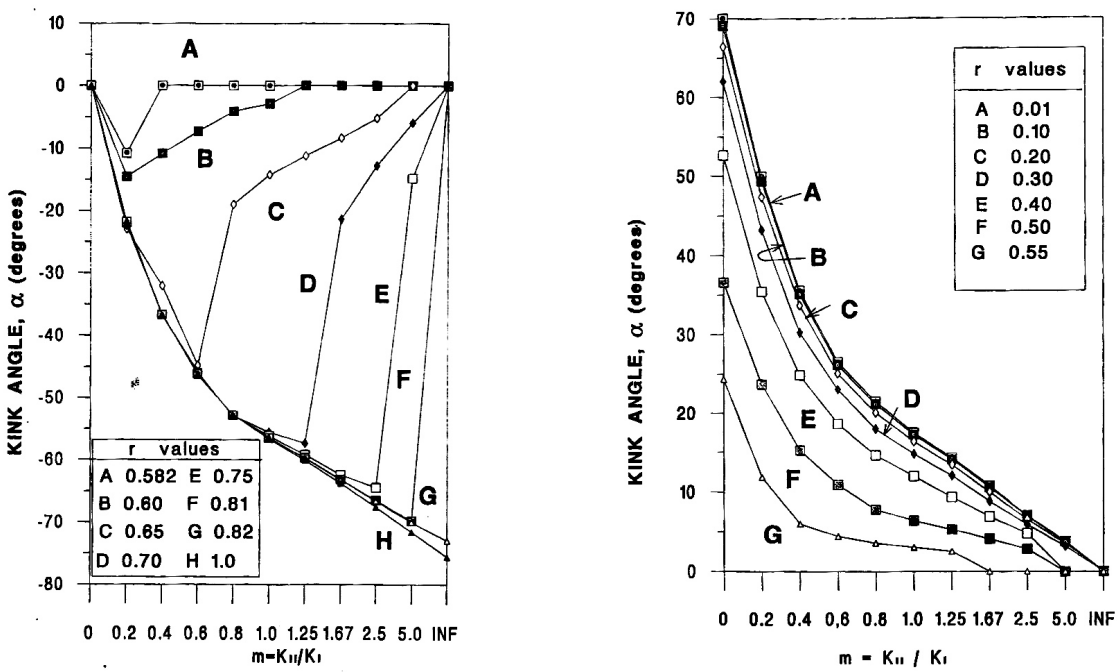

(a) (b)

Figure 2.4: Modeling of Kfouri and Brown showing (a) reduction in $K_{\mathrm{II}}/K_{\mathrm{I}}$ at which crack deflection transitions toward co-planar for decreasing r and (b) positive values of crack deflection angle under shear-dominated conditions for $r < 0.582$. (From [24].)

as the ratio of of "instantaneous" fracture resistances as the tip of a crack kink, in general it corresponds directly to $\tau_c/\sigma_c = K_{\mathrm{IIC}}/K_{\mathrm{IC}}$, and the values above which shear deflection does not occur (0.82 for Kfouri and Brown, 0.866 for Chao and Liu) are

comparable.

Kfouri and Brown also found that for $r < 0.582$ the critical condition $\mathcal{G} > \mathcal{G}_c$ was not achieved along the $\theta = 0$ plane for pure Mode I loading, but rather spread symmetrically out to higher values of $\pm\theta$ as r decreased. The positive values of these critical angles are shown on the $K_{\mathrm{II}}/K_{\mathrm{I}} = 0$ axis of Fig. 2.4(b) for several $r < 0.582$. This is qualitatively similar to the observation of shear-dominated zig-zag (but macroscopically Mode I) crack extension by Maccagno and Knott, although the values of θ fall somewhat short of the $\pm 45^\circ$ observed in HY130 steel even for the lowest realistic value of r. (Kfouri and Brown modeled as low as $r = 0.01$ even though a lower bound of 0.5 would be suggested by the τ_c/σ_c of the Tresca failure criterion.) Upon addition of any K_{II} loading, the positive angle solution for $\mathcal{G} > \mathcal{G}_c$ becomes dominant and moves toward co-planar for increasing K_{II}. The transition between Mode I and Mode II dominated fracture is smoother than that predicted by Chao and Liu for all values of r and does not match some experimental observations for the $r < 0.582$ cases.

In summary, for materials failing by ductile mechanisms there have been many observations of departure from the MTS criterion (and from the other theories predicting similar crack extension directions) and the possibility of co-planar Mode II fracture or even deflection in positive non-zero angles along planes of maximum shear. While the precise angle of shear crack extension and the value of mode mixity causing modal transition may vary somewhat with material properties and specimen effects on the non-singular stress field, a general trend of two competing failure modes can be asserted. These failure modes have so far been described for monotonic, proportional loading; their extension to cyclic fatigue loading must be considered next.

2.2 Fatigue Loading

The consideration of shear crack growth was arguably advanced in studies of fatigue before those of monotonic fracture due to the nature of early crack initiation under cyclic loading, or Stage I crack growth. In 1975, Otsuka *et al.* [26] studied the conditions for K_{II}-controlled crack initiation and began to extend the traditional notion of shear crack growth beyond the crystallographic Stage I growth seen at the microstructurally small scale. For this research, the realm of interest is Stage II long-crack behavior, and examination of fatigue crack growth literature will focus therein.

2.2.1 Fatigue Crack Path in Proportional Loading

When mixed-mode fatigue loads are applied proportionally – such as an inclined crack in a plate subject to cyclic uniaxial tension – it would seem straightforward to extend many of the monotonic fracture models to fatigue crack growth extension using the maxima of K_{I} and K_{II}. While there may still be variations in the crack growth rate for different mean stress values, since K_{I} and K_{II} are applied in proportion the maximum stress-based models would still predict the same angular location θ for $\sigma_{\theta\theta,\max}$ and $\tau_{r\theta,\max}$. Similarly the transition between $\sigma_{\theta\theta} > \sigma_c$ and $\tau_{r\theta} > \tau_c$ would be dictated by $\Delta K_{\mathrm{II}}/\Delta K_{\mathrm{I}}$ in the same way as $K_{\mathrm{II}}/K_{\mathrm{I}}$ due to proportionality. There have, however, been other approaches to modeling mixed-mode fatigue crack growth that merit consideration before moving on to the non-proportional case.

In 1974 Tanaka [27] cited already conflicting behavior in the earliest reported studies of mixed Mode I-II fatigue crack growth: that of Iida and Kobayashi [28] in 1969 showing a pre-crack under mixed-mode loading turning toward a path of $\Delta K_{\mathrm{II}} = 0$ in 7075-T6 aluminum; and Roberts and Kibler [29] in 1971 identifying cases where $\Delta K_{\mathrm{II}} = 0$ was not applicable. Both studies however showed a marked increase in propagation rate with the addition of ΔK_{II}. Pursuing the enhancing effect

of ΔK_{II}, Tanaka sought crack growth threshold data in commercially pure aluminum sheets with inclined cracks subject to uniaxial loading. Assuming an elliptical form for an equation combining the two modes similar to Sih's S-criterion (Eq. 2.7), Tanaka determined a crack growth threshold envelope of

$$0.0262\Delta K_{\mathrm{I}}^2 + 0.0081\Delta K_{\mathrm{I}} K_{\mathrm{II}} + 0.0381\Delta K_{\mathrm{II}}^2 = 1 \tag{2.19}$$

for ϕ values from 0° to 60°. It was also observed that crack growth deflected normal to the applied tensile stress near threshold, but for $\phi = 45°$-60° there was near co-planar growth when the applied stress was approximately 1.6 times the threshold value. The crack growth rate data were fit to a Paris-type equation when an effective SIF range was defined as

$$\Delta K_{\mathrm{eff}} = \left(\Delta K_{\mathrm{I}}^4 + 8\Delta K_{\mathrm{II}}^4\right)^{1/4} \tag{2.20}$$

which relied on the assumptions that (1) yield stress under Mode II (shear) deformation is half that under Mode I (tensile) deformation at the crack tip and (2) the plastic deformations due to Mode I and II loading respectively are not interactive. Alternate physical assumptions of crack growth produce similar definitions of

$$\Delta K_{\mathrm{eff}} = \left(\Delta K_{\mathrm{I}}^2 + 2\Delta K_{\mathrm{II}}^2\right)^{1/2} \tag{2.21}$$

$$\text{or} \qquad \Delta K_{\mathrm{eff}} = \left(\Delta K_{\mathrm{I}}^4 + 4\Delta K_{\mathrm{II}}^4\right)^{1/4} \tag{2.22}$$

but both models (including that leading to Eq. 2.20) are based on the plastic deformations directly ahead (i.e., assuming co-planar damage) of the crack tip.

In 1980 Badaliance [8] and Sih and Barthelmy [7] applied the strain energy density factor S to mixed-mode fatigue crack growth. Badaliance focused on spectrum fatigue loading and asserted that the use of ΔS in place of ΔK in a Paris-type equation should naturally account for mean stress effects (in addition to mixed-mode loading) for spectrum loads due to its quadratic form. However for several materials this approach still required that an entirely empirical scale factor $\alpha = (1 + R)/[1 + R(\sigma_u/\sigma_y)^2]$ be

applied to ΔS to collapse all R-ratios for the Mode I data considered. (Lam [30] later modified the theory to account for crack closure in order to account for the remaining variation with R-ratio, but claimed their modified ΔS_p – incorporating plastic hysteresis – would not affect prediction of crack growth direction compared to ΔS.) Sih and Barthelmy considered crack life calculations for several mixed-mode loading cases including numerical modeling of two experimental cases ($\beta = 30°$ and $43°$) of inclined crack under remote tension in Ti-6Al-4V, achieving success only with the latter. All of the cases considered were for in-phase fatigue, so while Sih and Barthelmy did at least explicitly consider non-co-planar crack propagation, determination of the deflection angle θ_o for non-proportional cycles (for which the orientation of $S_{\min}$ may change among the different load maxima) remained an open question.

A number of studies into shear fatigue crack growth focused on near-threshold Stage I FCG, as small crack initiation and growth behavior at the crystalline scale is dominated by shear deformation along slip systems before turning normal to the maximum tensile stress.[4] Gao *et al.* [32] studied mixed-mode crack growth thresholds in SS316 and found that cracks initiated in mixed-mode from an EDM slit propagated in a co-planar shear mode for a short distance before deflecting in general compliance with the MTS criterion. The tensile branch cracks propagated under

$$\Delta K_{\theta max} = (\Delta K_{\mathrm{I}} \cos^2 \frac{\theta^*}{2} - \frac{3}{2} \Delta K_{\mathrm{II}} \sin \theta^*) \cos \frac{\theta^*}{2} \tag{2.23}$$

where θ^* satisfies the MTS condition of Eq. 2.6. Specimens that were pre-cracked in Mode I load-shedding showed a small amount of co-planar mixed-mode growth before arresting, and would only propagate as tensile branch cracks outside of a higher load

[4]Indeed, cyclic shear deformation is the predominant damage mechanism for Stage II fatigue crack growth, so it might be considered the exception rather than the rule for fatigue cracks to obey the maximum tensile stress macroscopically. Nevertheless, many of the early attempts to study shear crack growth discussed in a 1985 literature review by Liu [31] showed ΔK_{II}-loaded cracks to turn normal to the axis of maximum tensile stress.

envelope. This was attributed to Mode II-induced crack closure of highly crystallographic near-threshold fracture surfaces, an effect that contradicted the intrinsic crack accelerating effect Mode II loading had on crack tip plasticity.

Later Gao *et al.* [33] tested several R-ratios in SS316 and showed the envelope for Mode I branch crack formation to approach the threshold curve for co-planar mixed-mode growth as the effect of closure decreased, i.e., mixed-mode growth would only occur for near-threshold conditions before Mode I crack growth dominated. Based on results from the steel and three additional alloys they offered a crack growth model based on the maximum crack tip reversed plastic deformation,

$$\frac{da}{dN} = k\frac{r_p(\theta_p)}{\gamma_{\mathrm{f}}} \tag{2.24}$$

where r_p is the extent of the crack tip reversed plastic zone at the angle θ_p which maximizes r_p, k is a material constant and γ_{f} is the true fracture ductility. The stress state at the crack tip affects the fracture ductility according to

$$\gamma_{\mathrm{f}} = \gamma_{\mathrm{ft}} + (\gamma_{\mathrm{fu}} - \gamma_{\mathrm{ft}})\frac{\sigma_{\theta\theta}(\theta_p)}{|\tau_{r\theta}(\theta_p)|} \tag{2.25}$$

where γ_{ft} and γ_{fu} are the true fracture ductilities measured in tension and torsion, respectively.

Using a tubular specimen under in-phase tension-torsion similar to the one employed in this research, Yokobori *et al.* [34] also observed crack propagation to turn normal to maximum tension. They correlated the crack growth direction with the plane of the global maximum principal stress in the gage section, which was a shallower deflection than the θ^* of maximum $\sigma_{\theta\theta}$ in the crack-tip stress field. However in many cases the crack path exceeded the angle of global maximum principal stress while still falling short of the crack tip stress field θ^* angle.

Still other studies reinforced the observation that fatigue cracks tend to propagate in a direction to maximize ΔK_{I} and minimize ΔK_{II}. Even in a specimen designed by Magill and Zwerneman [35] specifically to promote crack growth oblique to the applied

load, post-test finite element modeling showed the resulting curved crack paths in A572 steel plate experienced predominantly Mode I loading. Tong *et al.* [36] found the adherence of branch crack angle to the MTS criterion (based on $\Delta K_{\mathrm{II}}/\Delta K_{\mathrm{I}}$) to be insensitive to load ratio from $R = 0.1$ to 0.7, within experimental scatter, in edge-cracked BS4360 50D steel under asymmetrical 4-point bending (A4PB). Campbell and Ritchie [37, 38] found the MTS, MERR and S-criteria all to fall within experimental scatter of Ti-6Al-4V using the A4PB specimen for $R = 0.1$ to 0.8.

Otsuka *et al.* [26, 39] observed shear crack deflection in aluminum alloy 2017-T3 using a center-cracked plate and special loading apparatus that allowed $\Delta K_{\mathrm{II}}/\Delta K_{\mathrm{I}}$ ratios up to infinity ($\phi = 90°$). Shear fatigue crack growth occurred for $\Delta K_{\mathrm{II}} > 3$ MPa$\sqrt{\mathrm{m}}$ and $\Delta K_{\mathrm{II}}/\Delta K_{\mathrm{I}} > 1.6$, and two types of cracks were observed: some continued to grow co-planar with the initial fatigue crack in a ΔK_{II}-dominated mixed-mode condition for the highest ΔK_{II} conditions, and some curved toward the direction of $\Delta K_{\mathrm{I}} = 0$. Below the shear crack growth threshold of 3 MPa$\sqrt{\mathrm{m}}$ and above the crack initiation threshold $\Delta\sigma_{\theta\theta}\sqrt{2\pi r} = 1.6$ MPa$\sqrt{\mathrm{m}}$ (corresponding to approximately ΔK_{II}= 1.4 MPa$\sqrt{\mathrm{m}}$) cracks loaded even in pure ΔK_{II} deflected to tensile cracks. Aluminum alloy 7075-T6 tested in the same configuration displayed qualitatively similar behavior, initiating in shear for $\Delta K_{\mathrm{II}} > 8$ MPa$\sqrt{\mathrm{m}}$ and $\Delta K_{\mathrm{II}}/\Delta K_{\mathrm{I}} > 1.6$, but shear crack propagation only continued well beyond initiation for the pure ΔK_{II} case in their test matrix; near-ΔK_{II} tests grew a short distance co-planar to the pre-crack before deflecting into tensile cracks. Crack deflection angles generally followed the MTS criterion for tensile branches (though it over-predicted the angle of deflection for lower $\Delta K_{\mathrm{II}}/\Delta K_{\mathrm{I}}$ values) and the MSS criterion for shear crack growth.

In a 1992 review of several mixed-mode crack growth studies, Bold *et al.* [40] point out that Otsuka's definitions of tensile and shear SIFs ahead of a mixed-mode loaded crack tip,

$$K_\sigma = \sqrt{2\pi r}\ \sigma_{\theta\theta} = \cos\frac{\theta}{2}\left[K_{\mathrm{I}}\cos^2\frac{\theta}{2} - \frac{3}{2}K_{\mathrm{II}}\sin\theta\right] \tag{2.26}$$

$$K_\tau = \sqrt{2\pi r}\ \tau_{r\theta} = \frac{1}{2}\cos\frac{\theta}{2}\left[K_{\mathrm{I}}\sin\theta + K_{\mathrm{II}}(3\cos\theta - 1)\right] \tag{2.27}$$

yields almost identical predictions as those obtained by Melin [41] using an alternate formulation for SIFs at an infinitesimal kink.[5] Using the ranges of these SIFs is essentially applying the monotonic MTS and MSS criteria to fatigue crack growth. They did, however, point out shortcomings of these basic criteria, primarily in their under-prediction of the threshold values for Mode I branch crack growth for high proportions of $\Delta K_{\mathrm{II}}/\Delta K_{\mathrm{I}}$, particularly at low R-ratios This suggests a sliding-induced crack closure effect; Campbell and Ritchie [37, 38] explicitly studied this effect in Ti-6Al-4V and found that machining out most of the pre-crack wake greatly reduced the influence of mode mixity on threshold.

There was no clear explanation for separate observations [33, 39] of a short amount of co-planar shear or mixed-mode growth prior to Mode I crack branching, although residual stress from load-shedding pre-cracking is suggested. (Campbell and Ritchie did not observe this transient co-planar growth despite its occurrence in the same material and specimen type as Gao *et al.*, but the former tested at 1000 Hz and the latter at 15-80 Hz. The two sets of crack growth envelopes are compared in Fig. 2.5.) The inherent susceptibility of different alloys to shear mode crack growth, as well as the magnitude of loading (higher loads and larger plastic zone sizes being favorable to shear cracking), were also discussed as significant factors. This highlights a kind of paradox around shear crack growth, which has been noted to be more likely at very low, near-threshold loads (in Stage I crack growth) and also at higher loads in Stage II crack growth, but apparently quite unlikely at low Stage II loads. At the near-threshold values, however, crack growth resistance is generally lower in Mode II than Mode I ($\Delta K_{\mathrm{IIth}} < \Delta K_{\mathrm{Ith}}$). Sustained Stage I (crystallographic) mixed-mode

[5]The first-order approximation of kink tip SIFs k_1 and k_2 described by Cotterell and Rice [16] are merely a different formulation of Otsuka's definitions based on original crack tip stresses and give a very good approximation of a more rigorous definition of SIF at a kinked crack.

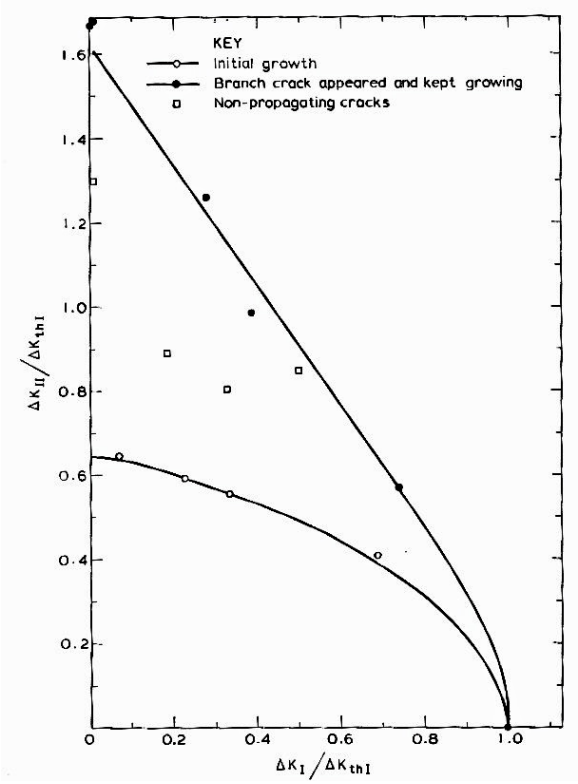

(a) Gao *et al.* $R = 0.2$

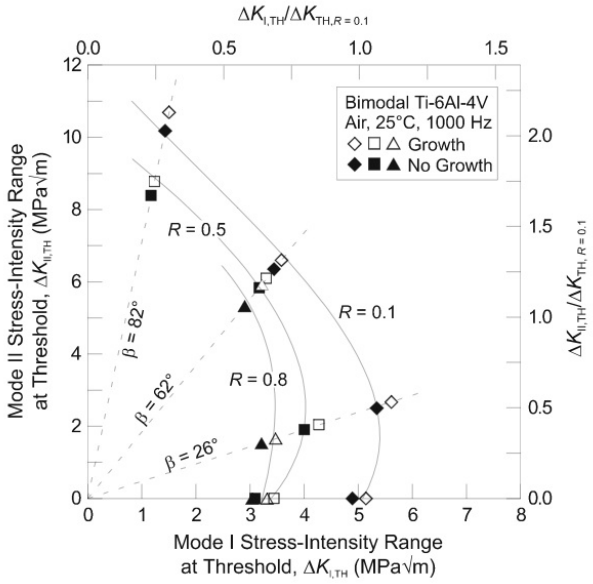

(b) Campbell and Ritchie

Figure 2.5: Comparison of mixed-mode crack growth threshold envelopes in Ti-6Al-4V of (a) Gao *et al.* [33], who observed co-planar cracking, and (b) Campbell and Ritchie [37], who did not.

crack growth has been studied more closely and effectively in single-crystal alloys (e.g., references [42, 43, 44, 45, 46]), but the present work focuses on Stage II FCG in polycrystalline materials in which isotropic behavior may be reasonably assumed.

In summary, the selection of in-phase mixed-mode fatigue crack growth studies discussed above, many of the simple inclined-crack case, have established that the same tensile-to-shear transition observed in fracture can occur in fatigue. With some exceptions, the same basic MTS and MSS criteria can generally be used to explain the transition behavior. However, input parameters for these criteria are not straightforward for non-proportional or out-of-phase loading cases, which will be examined next.

2.2.2 Non-Proportional Mixed-Mode Fatigue Crack Growth

The extension of monotonic fracture path criteria to proportional fatigue loading was a relative simple matter, but analysis of non-proportional load cases presents a greater challenge, at the very least because of the lack of a single parameter with which to characterize the load path. Hourlier *et al.* [47] in 1985 explicitly considered the differences between proportional and non-proportional fatigue loading in crack growth direction and the challenge the latter case posed for clear criterion formulation. Starting with two criteria predisposed to predict tensile crack deflection – $k_{1,\max}$ and $\Delta k_{1,\max}$, where k_1 is the Mode I SIF for the branched crack – they point out that the common shortcoming of both is lack of consideration of mean stress or R-ratio effects on crack growth rate. As an improvement they propose a $(da/dN)_{\max}$ criterion, in which crack deflection is predicted to occur in the direction yielding maximum FCGR based on the range and maximum of the kink Mode I SIF (i.e., $k_{1,\max}$ and Δk_1) and baseline FCGR data from simple Mode I testing. All three criteria were applied to non-proportional biaxial Mode I-II testing of 35NCD16 steel and AU4G aluminum, where the steel displayed only mild R-ratio dependence in Mode I FCGR data and the

aluminum a much more significant dependence. The $\Delta k_{1,\max}$ criterion best predicted crack angles in the steel, with $(da/dN)_{\max}$ performing poorly at low R-ratios. The $(da/dN)_{\max}$ criterion was superior to the other two throughout test conditions of the aluminum, suggesting the new criterion is best suited for materials displaying a significant mean stress effect on crack growth rate. It also did fairly well predicting deflection angles of earlier tests by Hourlier and Pineau [48] of cyclic K_{I}/steady K_{II} in thin-walled tubular specimens of aluminum and steel alloys; in contrast, $k_{1\max}$ showed almost no correlation with the data and $\Delta k_{1,\max}$ invariably predicts co-planar growth for this load case. In these tests Hourlier and Pineau also described a correlation between da/dN and deflection angle θ for a given ratio of $K_{\mathrm{II}}/K_{\mathrm{I,max}}$, in which the deflection increased for higher FCGR tests, which is implied in the formulation of their criterion.

However the more common analyses of non-proportional loading (and of shear crack growth in general) were inspired by rolling contact stresses that lead to fatigue largely in rail and bearing applications. A number of these studies in the 1970s and 1980s are reviewed in summary papers by Liu [31] and Bold [40]. However, in the special case of rolling contact fatigue (RCF), the loading history considered is often a cyclic Mode II stress with a superimposed compressive Mode I stress; this condition greatly complicates analysis of the crack driving forces due to the exacerbation of crack wake contact (for specific study of crack wake lockup in Mode II fatigue see, e.g., Smith and Smith [49]).

Bold *et al.* [50] and later Bogdanski *et al.* [51] modeled the RCF crack growth case based on an earlier supposition that embedded fluid within a shallow sub-surface crack enabled shear crack propagation. Experimental results in rail steel using A4PB specimens under proportional mixed-mode loading gave similar results to Gao *et al.* and Otsuka *et al.* cited above [33, 39] regarding brief co-planar crack growth before arrest or tensile branching. Superposing static Mode I on cyclic Mode II loading

in a biaxially-loaded plate with an inclined crack did not alter these results. They were ultimately able to produce sustained co-planar crack growth using a sequential Mode I-Mode II load cycle in which a fully reversed (R = -1) Mode II sub-cycle follows a tensile ($R = 0$) Mode I sub-cycle, an idealization of the numerically-predicted load history of a fluid-filled crack under RCF. In this case, co-planar crack growth is coincident with both the maximum ΔK_{I} of the tensile sub-cycle and the maximum ΔK_{II} of the shear sub-cycle. The ability for Mode II crack growth to continue was attributed to a residual opening displacement at the crack tip left by the Mode I load [52]. Crack propagation reverted to tensile branching, however, if ΔK_{I} fell below approximately half of ΔK_{II}, attributed similarly to insufficient residual opening displacement. The residual plastic opening displacement was later confirmed by Doquet and Pommier [53] in elastic-plastic finite element modeling of similar load cycles in rail steel. Doquet and Pommier did not observe similar tensile branching, however, until ΔK_{I} fell below 0.25 ΔK_{II}, which they attributed to different T-stress between Bold's equibiaxial-loaded specimen and their notched tubular specimen.

Continuing this work, Wong *et al.* [54] varied the amount of overlap between the Mode I and Mode II sub-cycles from $\Psi = 0^\circ$ to 90° in phase. They found an empirical relationship between tensile crack branching and phase overlap, such that the threshold ΔK_{I} below which branching occurred increased parabolically with Ψ, but they could not offer a justifiable physical basis yet for the transition behavior. Later Desimone and Beretta [55] challenged that envelope of shear crack growth, since their results for 180° of overlap between ΔK_{I} and ΔK_{II} displayed a short period of Mode II propagation before branching whereas Wong's parabolic ΔK_{I} threshold for branching would render it effectively impossible.

One hypothesis offered by Bold and implemented by Wong [54] was a $(da/dN)_{\max}$ criterion similar to that of Hourlier but in this case based on different FCGR equations for each mode (co-planar Mode II-dominated mixed-mode growth and Mode

I-dominated branching). Empirical relations for each mode were given as

$$\left(\frac{da}{dN}\right)_{\text{Mode II}} = C_2 \left\{ \Delta K_{\text{II,eff}} \left[1 + \left(\frac{\Delta K_{\text{I,eff}}}{\Delta K_{\text{II,eff}}} \right)^{m_{21}} \right] \right\}^{m_{22}} \tag{2.28}$$

$$\left(\frac{da}{dN}\right)_{\text{branch}} = C_1 \left(\Delta K_{\text{I,eff}}\right)^{m_1} \tag{2.29}$$

where the "eff" subscript refers to effective SIF ranges corrected for crack face contact on an experimental and material-specific basis. The influence of the opening load on Mode II propagation is explicit in Eq. 2.28. And while it was not specified that $\Delta K_{\text{I,eff}}$ in Eq. 2.29 is the local Mode I kink SIF $\Delta k_{1,\text{eff}}$, this is suggested by the specification that the Mode I and II sub-cycles contribute to $(da/dN)_{\text{branch}}$ separately and cumulatively, since the Mode II contribution to crack growth would be greatest in its rotated contribution to k_1.

It may be noted that the above treatment by Wong *et al.* of individual crack increment per sub-cycle could also be applied to sinusoidal mixed-mode loading with a phase difference of 180°, as in the current work. However in a later analysis of the data, Wong *et al.* [56] attempted to separate linearly the contributions of each sub-cycle in order to isolate Mode II FCGR and, unsuccessful, concluded there was an interaction effect between the sequential loads that must be considered. Doquet and Pommier observed similar sub-cycle synergy in their tests on rail steel, both in the crack growth rate and in the evolution of the plastic opening displacement, which grew four times more quickly in sequential loading than for pure Mode I crack growth. In fact even if it was assumed the co-planar crack growth was driven primarily by a Mode I mechanism, a crack growth law with the form of Eq. 2.28 but with ΔK_{I} and ΔK_{II} interchanged collapsed the data nearly as well as the Mode II assumption.

The full reversal of Mode II loading ($R_{\text{II}} = $ -1) utilized above is another characteristic common to RCF loading. Otsuka *et al.* [57] studied this case in aluminum alloys 7075-T6 and 2017-T4 and an annealed mild steel, with a positive (crack-opening) static Mode I load superimposed in most cases. Using a load-shedding technique, they

established threshold conditions for Mode II (co-planar) crack growth ($\Delta K_{\mathrm{IIth(ModeII)}}$) and Mode I branching ($\Delta K_{\mathrm{IIth(tensile)}}$) in the direction of maximum tensile stress. Their results also highlighted the material-dependent nature of crack deflection. In 7075-T6, $\Delta K_{\mathrm{IIth(ModeII)}}$ was higher than $\Delta K_{\mathrm{IIth(tensile)}}$, so that above the latter non-propagation threshold cracks deflected and grew in a tensile manner, and at higher ΔK_{II} values they grew in a co-planar shear manner. The situation was reversed in the steel, with deflected tensile crack growth occurring at higher ΔK_{II} and co-planar Mode II growth occurring below $\Delta K_{\mathrm{IIth(tensile)}}$ but above the non-propagation threshold $\Delta K_{\mathrm{IIth(ModeII)}}$. In 2017-T4, the two thresholds nearly coincided (with $\Delta K_{\mathrm{IIth(ModeII)}}$ slightly higher) and no tensile crack branching was observed.

It is not clear, however, how well the results of fully reversed ΔK_{II} loading would compare to the positive R-ratio cases in this study. The MSS criterion for fracture predicts non-zero crack deflections for high-K_{II} cases that result in continued asymmetric crack extension. Full reversal of ΔK_{II} in fatigue introduces a level of symmetry in the average sense over the full cycle. And conceptually it may also introduce "false" cases of shear crack propagation which are merely zig-zag accumulations of tensile crack increments that are macroscopically co-planar, a case suggested by Roberts and Kibler in 1971 to explain sustained co-planar growth under alternating K_{II}, as cited in Plank and Kuhn [58]. Such cases may be difficult to distinguish fractographically due to crack face abrasion, depending on any superposed opening load.

Plank and Kuhn did show sustained Mode II crack growth for a non-fully reversed ΔK_{II} loading by superposing static K_{I} loading in several aluminum alloys, but only for cyclic loading of $R < 0.6$. For load ratios as low as $R = 0.1$ where closure may be significant, the Mode II cyclic loading required for shear-mode growth could be driven down to a minimum threshold $\Delta K_{\mathrm{IIth,sm}}$ by increasing the static opening K_{I} load. Below $\Delta K_{\mathrm{IIth,sm}}$, tensile crack branching was observed. There was also an inverse correlation between grain size and $\Delta K_{\mathrm{IIth,sm}}$ comparable to the Hall-Petch

relation for yield strength. No shear crack growth was observed for ΔK_{I}/static K_{II} loading or non-proportional in-phase loading[6] in any of the aluminum alloys. They suggested a dual-threshold criterion to explain this: for shear crack growth to be possible, the Mode II loading on the pre-crack ΔK_{II} must exceed both the inherent material threshold $\Delta K_{\mathrm{IIth,sm}}$ and a quasi-SIF of an infinitesimal tensile kink, $\Delta k_1(\Delta\theta)$, which they defined as

$$\Delta k_1(\Delta\theta) = k_1(\theta^*_{F_{\max}}) - k_1(\theta^*_{F_{\max}}) \tag{2.30}$$

where k_1 is the usual kink tip SIF and $\theta^*_{F_{\max}}$ or $\theta^*_{F_{\min}}$ is the angle of maximum k_1 at the maximum and minimum load point in the cycle, respectively. It is difficult to justify the physical relevance of a SIF range at a hypothetical kink tip based on two different deflection angles, particularly when neither is necessarily the angle at which k_1 experiences a maximum range.[7] They argue that this artificial kink SIF range, unlike the maximum Δk_1 on a single θ^* plane which will always be larger than the initially applied ΔK_{II}, may for some non-proportional loadings be less than ΔK_{II} thus enabling co-planar shear crack growth. This does not consider that Mode II crack growth resistance may be considerably lower than that for Mode I, which is borne out by their own FCGR data as well as other published studies. They do however show that for tensile crack branches in the case of non-proportional (but in-phase) ΔK_{I}-ΔK_{II} loading, the deflection angle is reasonably predicted by the MTS criterion based solely on K_{Imax} and K_{IImax}.

Rather less problematic are three approaches to selecting an appropriate input for the MTS criterion under non-proportional loading modeled by Prasad *et al.* [59] for thermomechanical fatigue applications:

1. Evaluate MTSC deflection angle θ^* at the point in the cycle when $|K_{\mathrm{II}}|$ is

[6] A static K_{I} was superposed on proportional mixed-mode fatigue loading of a compact tension shear specimen, producing in-phase loads with different load ratios, R_{I} and R_{II}.

[7] In one of the non-proportional cases used, $\theta^*_{F_{\max}}$ and $\theta^*_{F_{\min}}$ are approximately -40° and -10°, whereas $k_{1\max}$ occurs at approximately -55° and is larger than $\Delta k_1(\Delta\theta)$.

maximum, as crack growth seeks to minimize K_{II}

2. Evaluate MTSC at the time of maximum $\sigma_{\theta\theta}$ in the entire cycle

3. Evaluate MTSC with the average values of K_{I} and K_{II} over the entire cycle, such that crack growth will minimize average K_{II}

However, these variants of the criterion were compared solely in a numerical study with no experimental verification, and the differences in crack path between them were slight. This methodology could be extended to include a comparison to MSSC at similar maxima.

Dahlin and Olsson [60] applied approach #2 above (and others) to the Plank and Kuhn data using elastic-plastic finite element analyses of the non-proportional load cases. They found that including the plastic residual stresses of cyclic loading in evaluation of the maximum $\sigma_{\theta\theta}$ for the entire cycle predicted crack deflection in 2017 aluminum much better than the elastic analysis, leading them to differentiate $\mathrm{MTS_p}$ and $\mathrm{MTS_e}$ criteria for "plastic" and "elastic." While $\mathrm{MTS_p}$ performed well for higher strength, lower ductility alloys, the more ductile alloys were better predicted by the maximum range of $\sigma_{\theta\theta}$ over the entire cycle, also factoring in residual stresses (which they labelled $\mathrm{MTSR_p}$). Still, Tanaka *et al.* [61] showed excellent agreement between the elastic maximum $\sigma_{\theta\theta}$ range ($\mathrm{MTSR_e}$ in Dahlin's terminology) for cyclic torsion in a notched tubular specimen of a medium carbon steel, both with and without static tensile loads superposed.

Instead of seeking maxima over an entire non-proportional cycle, Spievak *et al.* [62] developed an algorithm for use with the FRANC3D fracture modeling software to build an aggregate crack trajectory from incremental load steps in the cycle. The algorithm was based solely on tensile crack growth determined by MTSC. At each load step, an increment of crack growth is calculated using MTSC at an angle θ^* to the current crack tip based on the mode mixity of the time step. The length

of the increment da is a fraction the increment Δa for the whole cycle, calculated from the FCGR law of the material based on ΔK_{I} for the whole cycle, proportional to the relative increase in K_{I} for the time step as a fraction of ΔK_{I} for the cycle. These increments are then added vectorially from the initial crack tip of the cycle and the total crack extension for the cycle is the resultant vector. This method is computationally intensive but, as with the previous approach, could be applied using MSSC at each time step and the resulting crack trajectory be based on the greater of the two summations (MTSC versus MSSC), along the lines of Hourlier's $(da/dN)_{\max}$.

Yu and Abel [63] studied various mixed-mode tension-torsion loadings in notched tubular specimens of A106 steel. For the constant K_{II}/cyclic ΔK_{I} case, discussed above in work by Hourlier, they observed a slight deflection of θ = -6° to -14.5°. Hourlier attributed the crack path to the influence of mean stress on crack growth rate using the $(da/dN)_{\max}$ approach, but Yu and Abel cited an effect of roughness-induced crack closure based on strain gage readings near the crack tip [64]. They argued that crack surface asperity contact at low opening loads induced a small cyclic variation in the nominally constant K_{II}, reducing it slightly at the minimum K_{I}. This addition of a small in-phase ΔK_{II} cycle would, based solely on the angle of maximum kink tip Δk_1, result in the observed -6° to -14.5° deflection angles for a closure-induced variation of 10%-25% of the K_{IImax} levels cited.

An interesting result of their more complex load paths was the difference in crack deflection for the two variants of a two-step loading shown in Fig. 2.6. Nearly proportional in-phase loading to the same stresses resulted predictably in tensile deflection (θ = -32°) close to the MTSC prediction (θ = -40° based on SIF ranges, -35° based on maximum SIFs). Three tests of the load path in Fig. 2.6(a) produced shear deflections close to the MSSC prediction (θ = 28.5° based on SIF ranges, 33° based on maximum SIFs). A hybrid load path shown in Fig. 2.6(b), with a nearly proportional loading to maximum tension and half torsion followed by a torsional cycle of $R_{\mathrm{II}} = 0.5$

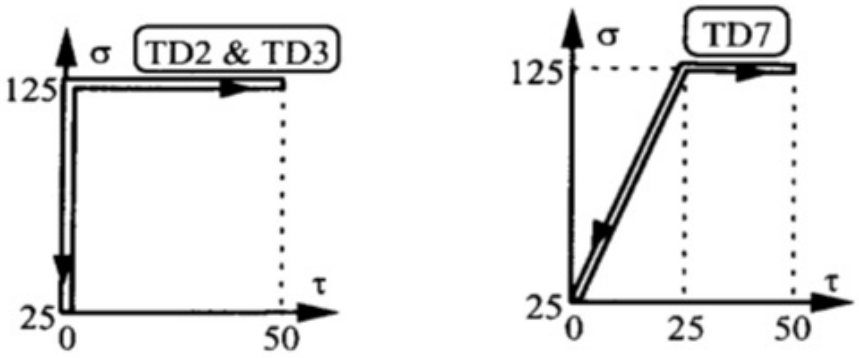

(a) Deflection $\theta = 30°$-$36°$ (b) Deflection $\theta = 15.5°$

Figure 2.6: Non-proportional load paths resulting in different shear-dominated crack deflections (from Yu and Abel [63]).

under constant tension, resulted in deflection toward the shear-dominated direction but not predicted by MSSC using any standard combination of SIFs. The authors did note that the fracture surfaces of both load cases in Fig. 2.6 were devoid of fatigue striations seen on MTSC-controlled branches and had an appearance similar to other definitive MSSC deflections.

2.3 Summary

An overview of the evolution of crack path prediction models has been presented, beginning with the simplest cases of monotonic fracture through much more complex mixed-mode fatigue loadings. Of primary concern in this research is the existence of two fatigue crack growth mechanisms for stable Mode I or Mode II propagation and the prediction of the dominant mode for a given loading. It has been shown that the possibility of stable Mode II crack growth depends on the material, with some alloys branching invariably toward a maximum tensile stress or K_{I}-driven orientation. Despite the frequent occurrence of shear crack growth, many analyses continue to consider only tensile crack branching in the prediction of crack path under complex loading. Most of the studies that consider the possibility of competing modes of crack growth follow two general schemes: stress or stress intensity-based criteria, in which

the dominant mode of crack growth depends on the relative magnitudes of near-tip stresses or infinitesimal kink tip stress intensities; and energy-based approaches. In complex loading, a primary challenge is the determination of an appropriate scalar quantity as an input to any given criterion when the magnitude or location/orientation of that quantity changes throughout the cycle. Several approaches to selecting this criterion at a particular point or points of a cycle have been presented, while others avoid this challenge through the use of total-cycle quantities like energy or extent of plastic deformation. The bulk of work in non-proportional loading has been performed on steels under a particular class of RCF load cycle common in rail applications, with a notable population of aluminum data as well. The literature is still populated with sometimes contradictory material-dependent results and there appears not to be a trend toward a consensus criterion.

CHAPTER 3

EXPERIMENTAL METHODS

3.1 Material

This work was performed on specimens of the precipitation hardened nickel-base superalloy Inconel 718. Inconel 718 is a high-temperature alloy used widely in the hot section of gas turbine engines for rotor disks and static structures, and it is also used for the Space Shuttle main engine turbopumps. The nominal chemical composition of the alloy is given in Table 3.1. Prior to final machining, all of the specimens were heat treated for precipitation hardening according to AMS 5662.

Table 3.1: Nominal chemical composition of Inconel 718 superalloy in weight percent.

Ni	**Cr**	**Nb**	**Mo**	**Ti**	**Al**	**Co**	**Fe**
50-55	17-21	4.75-5.5	2.8-3.3	0.65-1.15	0.2-0.8	0-1.0	Bal

Although fatigue crack growth rate is not explicitly addressed in the present study, some knowledge of FCGR properties of Inconel 718 is required to implement some crack path prediction approaches. Specifically, the $(da/dN)_{\max}$ approach of Hourlier *et al.* discussed in Section 2.2.2 requires a formula for calculating da/dN for a given material (as Hourlier's paper used numerical interpolation of data tables and not a particular FCGR equation). Soboyejo *et al.* [65] published a multiparameter model for FCGR in Inconel 718 based on their room temperature test data published by Mercer *et al.* [66] at four load ratios from $R = 0.1$ to 0.8. With a correlation coefficient of $r^2 = 0.97$ they model FCGR as

$$\frac{da}{dN} = 1 \times 10^{-10} \Delta K^{3.63} R^{0.52} \tag{3.1}$$

where da/dN is in mm/cyc and K is in $\mathrm{MPa}\sqrt{\mathrm{m}}$, in order to account for ΔK and K_{max} effects on crack growth.

3.2 Specimens

A novel specimen design, the inclined through-crack round (ITCR) specimen, was developed under this program for the purposes of generating a variety of 3-D mixed-mode loading conditions, with significantly higher proportions of K_{III} than previously published three-mode specimen configurations generated (see [67], e.g.). A more conventional notched thin-walled tubular specimen was used to generate non-proportional mixed-mode crack loadings that were dominated by K_{I} and K_{II}, similar to much of the literature. Detailed analyses of each specimen design to determine the SIF at the crack front(s) are presented in Chapter 4, but brief descriptions follow below. Due to mechanical failure of the two available axial-torsional servohydraulic load frames, only one configuration of the ITCR specimen, with no significant K_{III} loading, was able to be tested.

3.2.1 Thin-Walled Tubular FCG Specimen

For testing Mode I-II mixities with independent mode control, tubular specimens shown in Fig. 3.1 were fabricated by NASA Marshall for tension-torsion testing. The entire specimen had an inner diameter of 25.4 mm. The gage section had a wall thickness of 2.54 mm and a length between fillets of 31.75 mm. The grip sections had an outer diameter of 48.9 mm and a length of 69.85 mm. Transverse through-holes 19.1 mm in diameter were machined in the grip sections 38.1 mm on center from the ends of the specimen for a clevis pin to assist in load transmission from the grips. The initial flaw was a thin straight-through slot cut by electro-discharge machining (EDM) in the wall of the tube at the midpoint of the gage section, approximately 2 mm wide (circumferentially) and 0.4 mm high. Once a pre-crack was generated from the EDM slot, K_{I} and K_{II} were independently controlled by the applied tension and torsion, respectively.

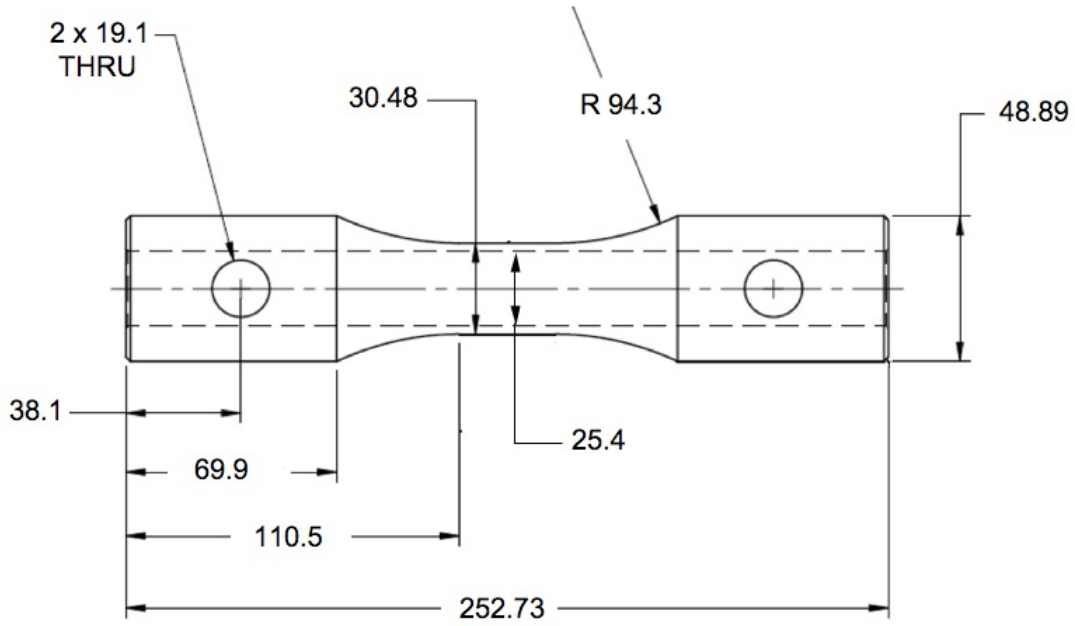

Figure 3.1: Drawing of thin-walled tubular specimen design (dimensions in mm).

3.2.2 Inclined through-crack round specimen

In order to test Modes I, II and III simultaneously, two novel specimen configurations were developed as part of this research. The first of these will be referred to as the inclined through-crack round (ITCR) specimen and is shown in Fig. 3.2. The ITCR is a solid round bar with a thin straight-through slot cut by EDM across the diameter of the gage section at its midpoint for an initial flaw. The plane of the initial slot may be normal to the load axis of the specimen or inclined at an angle, β, as shown in the drawing.

For non-zero values of β, the tensile load on the specimen decomposes into normal (Mode I) and out-of-plane shear (Mode III) stress components along the notch root of the slot, and the Mode III component increases with β. A torque applied to the specimen produces an in-plane shear (Mode II) stress distribution along the notch root which increases from zero at the specimen center to maxima at the surface

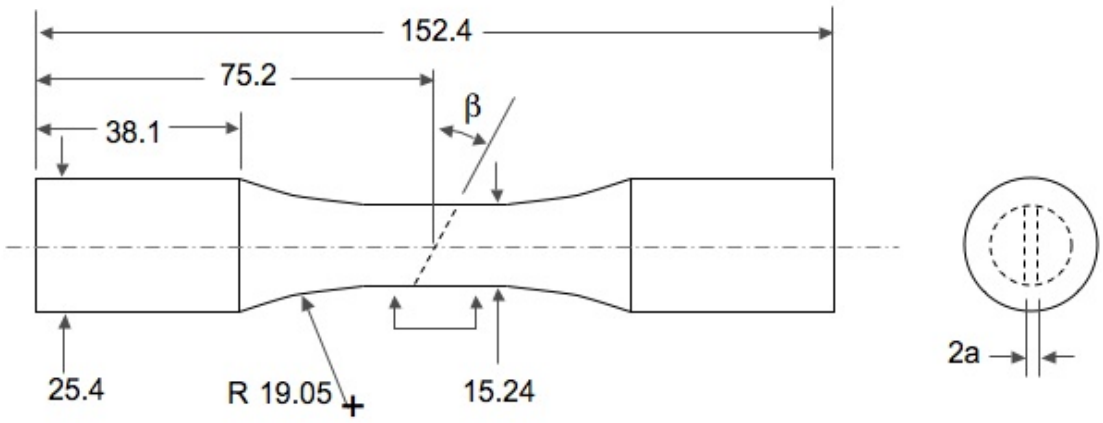

Figure 3.2: Drawing of inclined through-crack round (ITCR) specimen design (dimensions in mm).

intercepts. Therefore this specimen is useful in experiments that seek a transition in crack growth behavior as a function of K_{I}-K_{II} mixity because it generates range of mode mixities from the center to the surface due to the radial dependence of Mode II. Inclining the initial slot by an angle β then adds a Mode III component to crack loading in order to study its influence on any transitional Mode I-II mixity.

For this research program, specimens were fabricated with a gage section diameter of 15.24 mm and an initial slot width of approximately 1.6 mm. Two sets of four specimens each were fabricated, with slot angles of $\beta = 0^\circ$ and $\beta = 30^\circ$ to test duplicate K_{I}-K_{II} conditions with and without the addition of K_{III}. However, due to the testing equipment failures mentioned above, only the $\beta = 0^\circ$ specimens were able to be tested. As will be discussed in Section 4.2.1, inclination of the pre-crack by a non-zero angle β adds a Mode III out-of-plane shear loading to the crack tip, which may interact with the Mode II in-plane shear load to promote transition to shear crack propagation.

3.3 Fatigue Testing

3.3.1 Thin-Walled Tubular Specimens

3.3.1.1 Test Procedures

All of the thin-walled tubular FCG specimens were tested at NASA Marshall under the supervision of Dr. Tarek Sayyah and Dr. Gregory Swanson. The tests were performed on a computer-controlled axial-torsional servohydraulic load frame. The ends of the specimens were clamped by hydraulic collet grips. Prior to data acquisition, sharp fatigue cracks were generated from the initial EDM slots by applying 120,000 cycles of cyclic compression from -17.8 kN to -178 kN followed by 150,000 cycles of low-level cyclic tension from 2 kN to 20 kN. This generated a pre-crack that extended nominally 0.15 mm from the root of the EDM slot, for a total initial crack size $2a$ of nominally 2.3 mm.

After pre-cracking, cyclic tension-torsion loading was applied to the specimen as prescribed by the test matrix until the fatigue crack reached a total length of approximately 14 mm (in the circumferential projection, regardless of the actual propagation length of deflected cracks). No interim values of crack length versus cycle count were recorded.

3.3.1.2 Test Matrix

Prior to beginning collaboration with Georgia Tech, NASA Marshall had tested six specimens at various load ratios and waveforms, shown in Table 3.2, where P is the tensile load, T is torque and R is load ratio. This test matrix is also shown graphically in Fig. 3.3, where vertical lines represent constant torsion/cyclic tension tests; horizontal lines represent constant tension/cyclic torsion tests; and lines with positive slope represent in-phase tests.

For the remaining tests, a systematic test matrix was laid out that would test

Table 3.2: Fatigue loads applied in preliminary NASA testing of tubular specimens.

Spec. #	$P_{\max}$ (kN)	R_P	$T_{\max}$ (Nm)	R_T	Cycle type	$K_{\mathrm{I,max}}$ (MPa$\sqrt{\mathrm{m}}$)	$K_{\mathrm{II,max}}$ (MPa$\sqrt{\mathrm{m}}$)
N01	56.9	0.6	554	0.6	IP	21.0	11.3
N02	56.9	0.6	554	0.6	IP	21.3	11.8
N03	56.9	1	554	0.6	$\mathrm{P_{const}}$	19.4	12.6
N04	56.9	1	554	-1	$\mathrm{P_{const}}$	19.6	12.9
N05	56.9	0.6	554	1	$\mathrm{T_{const}}$	23.6	11.9
N06	56.9	1	554	0	$\mathrm{P_{const}}$	22.5	11.5

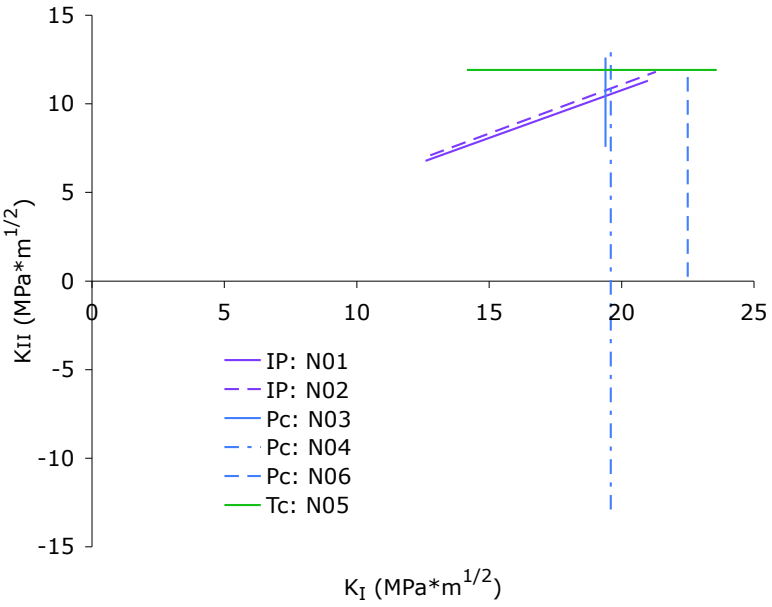

Figure 3.3: Graphic representation of preliminary NASA testing of tubular specimens in K_{I}-K_{II} space.

three different levels of mode mixity in terms of $K_{\mathrm{II,max}}/K_{\mathrm{I,max}}$, and each of these levels would be tested by a group of four specimens: one each of in-phase; 180° out-of-phase; constant tension/cyclic torsion; and constant torsion/cyclic tension. Within each group, the constant tension or torsion tests would be held at a same constant $K_{\mathrm{I,max}}$ or $K_{\mathrm{II,max}}$, respectively, as the in-phase test in that group while the cyclic torsion or tension achieved the same $K_{\mathrm{II,max}}$ or $K_{\mathrm{I,max}}$, respectively, as the in-phase test. The goal was to seek a consistent energy release rate $\mathcal{G}$ at maximum load so that crack growth rates might be fairly consistent. The out-of-phase test in each group would alternate between the $K_{\mathrm{I,max}}$ and $K_{\mathrm{II,max}}$ values; this would result in a lower $K_{\mathrm{eff,max}}$ for the cycle, but the cycle count is in a sense doubled due to the specimen undergoing a peak K_{I} and then a peak K_{II} for each full cycle. The proposed test matrix is shown graphically in terms of applied tension and torque in Fig. 3.4, with the load values and waveforms detailed in Table 3.3.

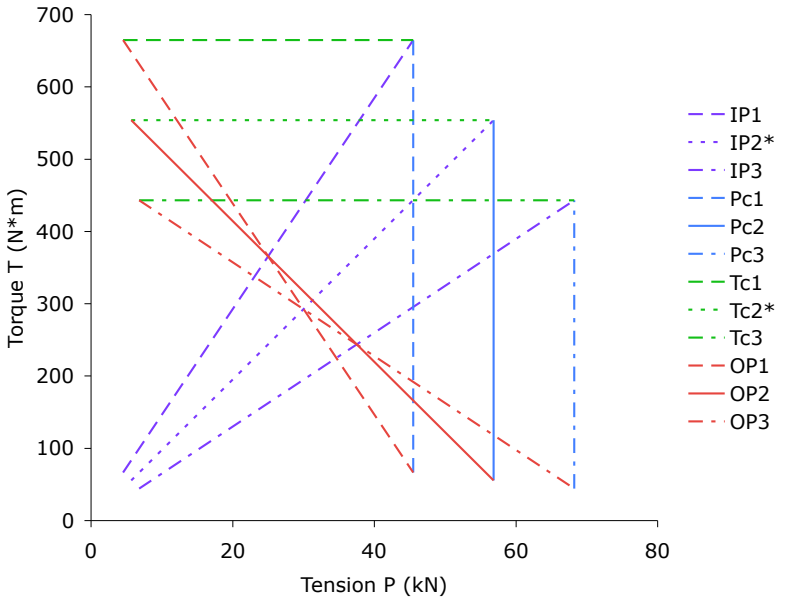

Figure 3.4: Graphic representation of proposed test matrix for second batch of tubular specimens in terms of applied tension and torque.

Table 3.3: Fatigue load matrix for NASA testing of second batch of tubular specimens.

Specimen	P_{max} (kN)	R_P	T_{max} (Nm)	R_T	Waveform
N07	45.5	0.1	665	1	T_C
N08*	45.5	0.1	665	0.1	IP
N09*	45.5	0.1	665	0.1	IP
N10	45.5	1	665	0.1	P_C
*N14***	*56.9***	*0.1***	*554 ***	*1***	*T_C***
N16	56.9	0.1	554	0.1	In-phase
*N15***	*56.9***	*1***	*554***	*1***	*P_C ***
N11	68.3	0.1	443	1	T_C
N12	68.3	0.1	443	0.1	In-phase
N13	68.3	1	443	0.1	P_C
N17	56.9	0.1	554	0.1	OP
N18	45.5	0.1	665	0.1	OP
N19	68.3	0.1	443	0.1	OP

P_C = Constant Tension; **IP** = In-Phase; **T_C** = Constant Torque; **OP** = 180° Out-of-Phase.

* Due to unexpected experimental observations, this condition was duplicated.

** Due to pre-cracking problems and limited specimens, these conditions were ultimately not tested.

Due to variations in pre-crack size and shape (discussed in Section 4.1.3), the actual matrix of K_{I}-K_{II} conditions tested did not adhere precisely to the desired overlapping arrangement of loads within groups as shown in Fig. 3.4. The resulting test matrix as tested – with the incomplete testing of specimens N14 and N15 removed – is shown graphically in K_{I}-K_{II} space in Fig. 3.5.

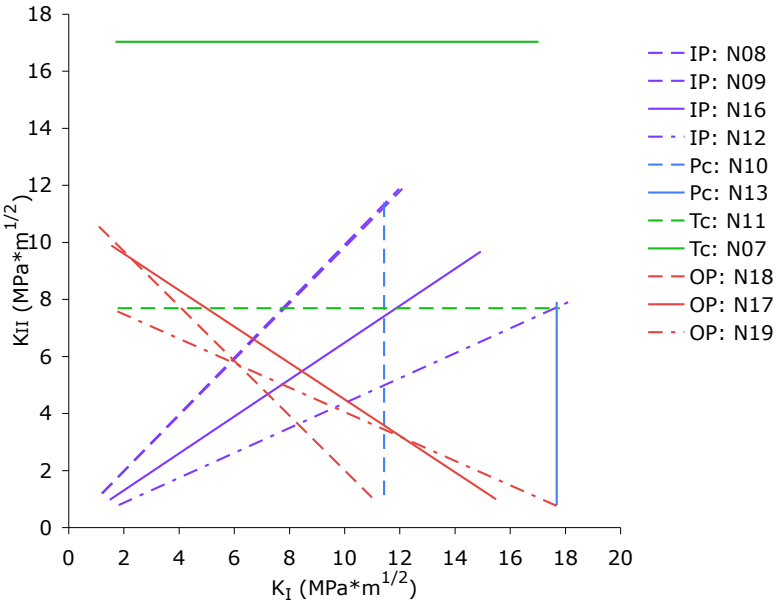

Figure 3.5: Graphic representation of final NASA testing of second batch of tubular specimens in K_{I}-K_{II} space.

3.3.2 0° ITCR Specimens

3.3.2.1 Test Procedures

Four 0°-flaw ITCR specimens were tested at Georgia Tech. The tests were performed on a computer-controlled axial-torsional servohydraulic load frame capable of 445 kN axial force (limited to 223 kN by grip capacity) and 5.65 kN-m torque. The ends of the specimens were clamped by hydraulic collet grips pressurized at nominally 34 MPa. Prior to data acquisition, sharp fatigue cracks were generated by applying

40,000 to 80,000 cycles of compression from -14.5 kN to -145 kN followed by 150,000 cycles of low-level tension from 1.6 kN to 16.4 kN. These pre-cracking loads were selected to replicate the applied stresses (-800 MPa maximum compression and 90 MPa maximum tension) of the NASA pre-cracking procedure. The number of compressive cycles was reduced from 120,000 to 40,000 to 80,000 based on visual observation of crack growth and arrest at the sides of the EDM slot. This was done in order to prevent generation of longitudinal cracks from the top and bottom of the EDM slot, where there was a tensile stress concentration at the centered plunge-EDM pilot hole in the middle of the wire-EDM slot. The maximum applied SIF at the end of pre-cracking was 5.3 MPa$\sqrt{\text{m}}$. This places the applied ΔK at 4.8 MPa$\sqrt{\text{m}}$, well below the reported threshold value of $\Delta K_{\text{th}} = 8.2$ MPa$\sqrt{\text{m}}$, suggesting that the final increment of pre-crack growth under this tensile loading only propagated through the residual stress field of the compressive pre-cracking stage and then arrested.

After pre-cracking, cyclic tension-torsion loading was applied to the specimen as prescribed by the test matrix. Periodic optical measurements of surface intercept crack length versus cycle count were taken with a traveling microscope on at least one side of the specimen at intervals of approximately 1,000 to 5,000 cycles. Fatigue testing was run until specimen failure for the 180° out-of-phase and the constant torque conditions. Testing was interrupted when the actuator displacement or rotation amplitude began to increase noticeably on the control system scope for the in-phase and constant tension conditions. The in-phase specimen was returned to minimum loads and fatigued to failure under cyclic tension. The constant tension specimen specimen was returned to the loads and then fatigued to failure under cyclic tension while torque was held constant.

3.3.2.2 Test Matrix

The test matrix for the ITCR specimens was selected to replicate the four loading conditions from the NASA testing of the tubular specimens and overlap load ranges of interest. Because the values of K_{II} and mode mixity increase radially in this specimen design and the experiments sought to reveal transitions in crack growth behavior, the loads for each condition were selected to replicate possible transition conditions from the tubular specimen testing at approximately one-half to two-thirds of the gage section radius, as shown schematically in Fig. 3.6.

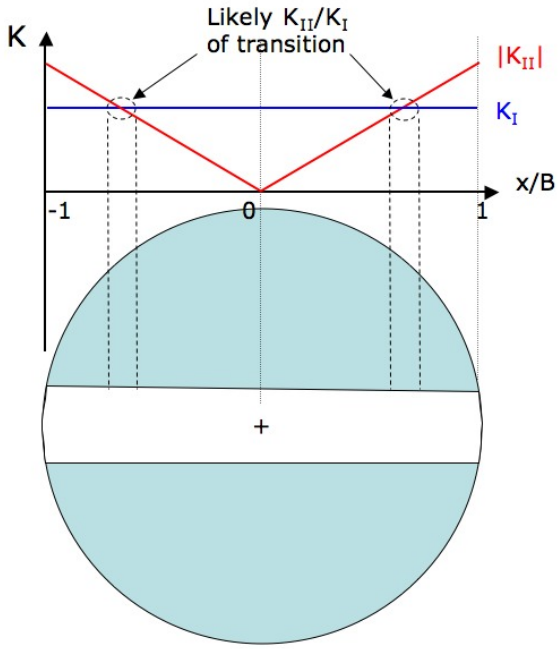

Figure 3.6: Schematic of ITCR gage cross-section indicating regions of interest guiding selection of test conditions.

The loads selected and the resulting SIFs of interest are given in Table 3.4, in which $K_{\mathrm{I,avg}}$ is the nominally constant maximum value across the crack front and $K_{\mathrm{II},x/b=0.5}$ is the maximum value at the mid-span ($x/b = 0.5$) of the crack front where it was attempted nominally to overlap previous NASA test conditions. The test conditions are presented graphically K_{I}-K_{II} space in Fig. 3.7. Each test condition is

represented by a polygon in K_{I}-K_{II} space due to the radial distribution of K_{II} along the crack front. The relevant test conditions from the tubular specimen testing are also plotted in Fig. 3.7 for comparison.

Table 3.4: Fatigue load matrix for 0° ITCR specimen testing.

Specimen	P_{max} (kN)	R_P	T_{max} (N-m)	R_T	Cycle type	$K_{\mathrm{I,avg}}$ (MPa$\sqrt{\mathrm{m}}$)	$K_{\mathrm{II},x/b=0.5}$ (MPa$\sqrt{\mathrm{m}}$)
ITCR0-1	33.9	0.1	310	0.1	IP	10.6	13.0
ITCR0-2	69.8	1	240	0.1	P_{const}	21.9	10.0
ITCR0-3	48.5	0.1	271	0.1	OP	15.2	11.3
ITCR0-4	43.6	0.1	310	1	T_{cont}	13.6	13.0

3.3.3 Crack Deflection Angle Measurement

Due to the radial distribution of SIFs generated in the ITCR specimen and the generally non-planar nature of the fracture surface, direct optical observation of the crack deflection angles was not possible. The fracture surfaces were documented after testing through the sectioning of plastic castings of the specimen halves. A negative silicone mold was created for one half of each specimen as shown in Fig. 3.8. Then a hard casting resin was used to create multiple copies of the fractured specimen for sectioning and documentation as shown in Fig. 3.9(a). The plastic castings were then carefully ground in small increments to create planar surfaces normal to the through-crack and parallel to the loading axis in order to take optical images normal to the crack growth direction at different radial positions within the specimen, as shown in Fig. 3.9(b). This enabled digital measurement of the local crack deflection angle at the end of the normal pre-crack. These angles were then correlated with the local SIF mixity created by the radial distribution of K_{II} to generate the results discussed in Section 5.2.

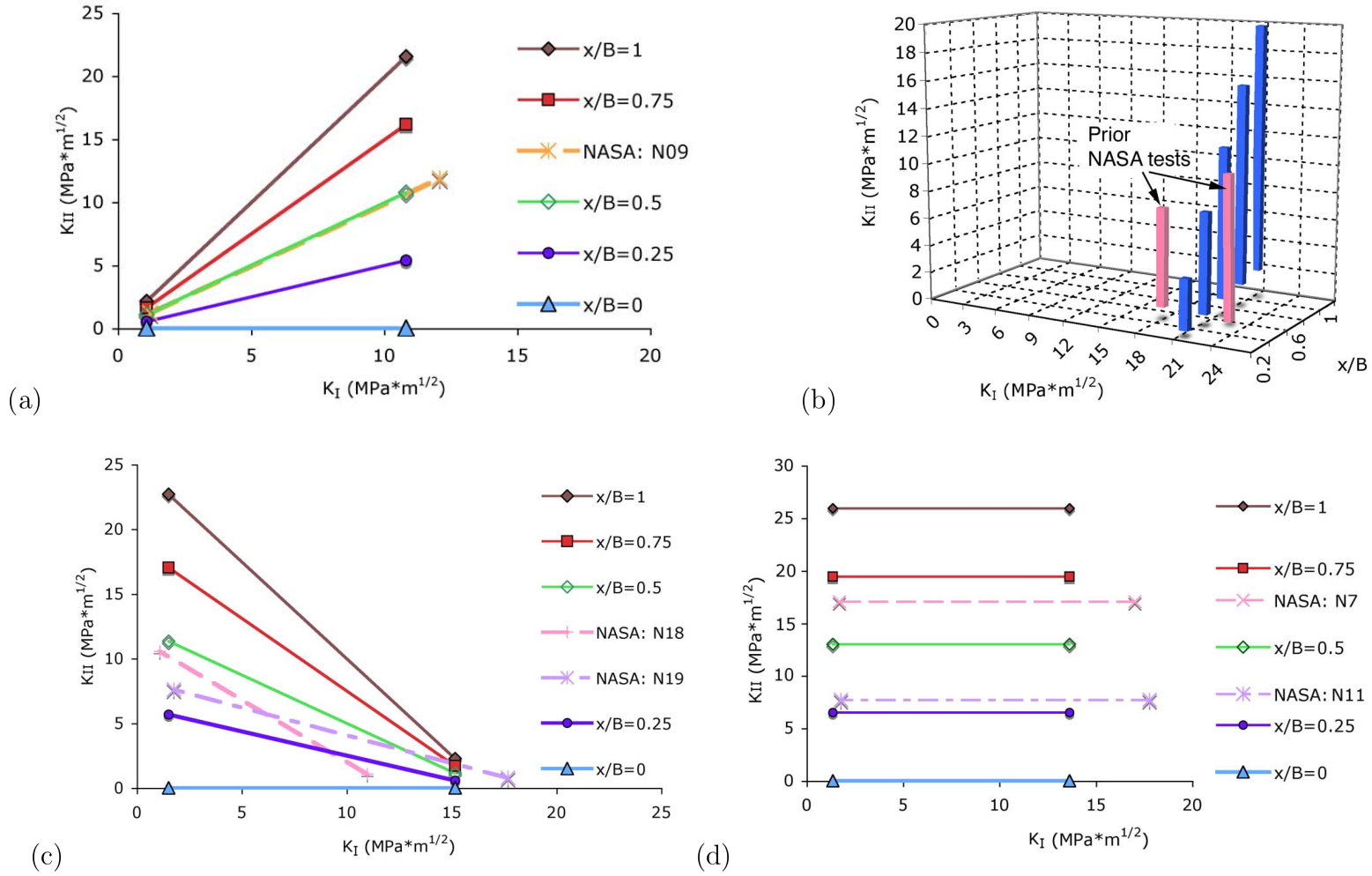

Figure 3.7: Graphic representation of 0° ITCR specimen test conditions in K_{I}-K_{II} space for (a) in-phase, (b) out-of-phase, (c) constant tension (K_{I})/cyclic torsion (K_{II}), and (d) constant torsion (K_{II})/cyclic tension (K_{I}), along with relevant tubular specimen test conditions for each case.

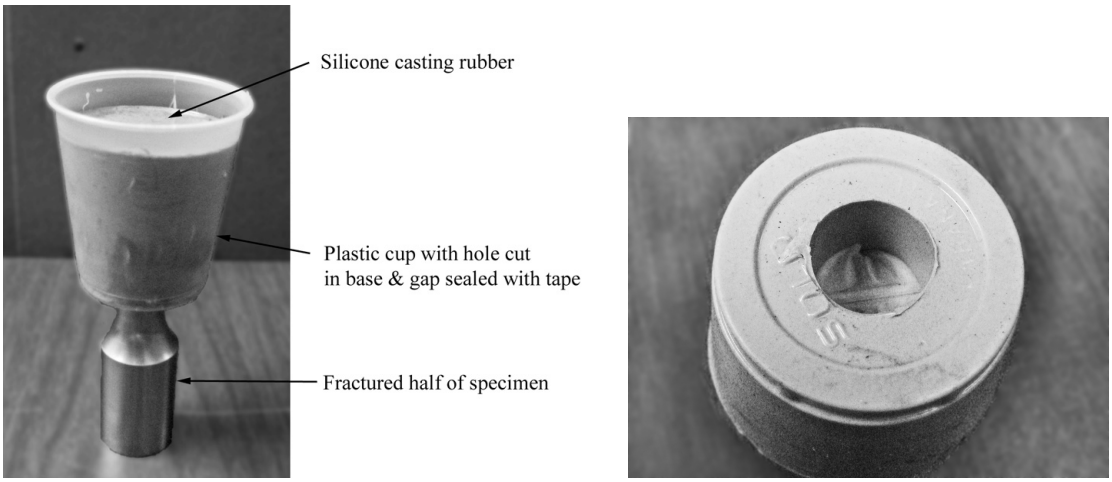

(a) (b)

Figure 3.8: Half of each fractured specimen was used to create a reusable mold by immersing the gage section in a silicone compound (a), which upon curing contained a negative impression of the fracture surface (b).

(a)

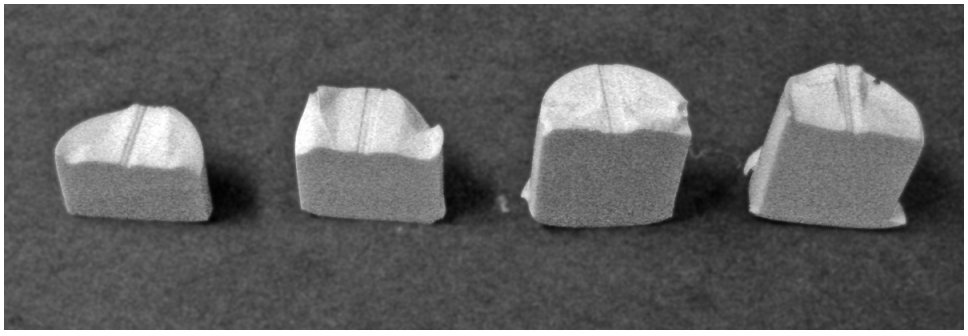

(b)

Figure 3.9: (a) Plastic castings replicating the fracture surfaces of ITCR specimens; (b) castings were ground down incrementally for measurement of local crack deflection.

CHAPTER 4

STRESS ANALYSIS OF SPECIMENS

The purpose of this work was to explore the ability to predict crack path deflection under non-traditional loadings using simple LEFM stress intensity factors – K_{I}, K_{II}, and K_{III} – as input variables. Therefore, all of the test conditions were analyzed with linear elastic boundary element models using the OSM (Object Solid Modeler), FRANC3D (FRacture ANalysis Code for 3D) [68] and BES (Boundary Element System) [69] software packages available from the Cornell Fracture Group. The gage sections of the specimen designs were modeled with sharp initial pre-cracks and subjected to tension and torsion in order to determine the SIFs after pre-cracking and prior to the generation of data at the specified test condition. For the new ITCR specimens, a number of initial crack sizes, a, were modeled in order to develop a general closed-form expression for the SIF as a function of normalized crack size a/R (where R is the radius of the gage section), tension P, and torque T.

4.1 Tubular FCG Specimen

4.1.1 Model Geometry and Boundary Conditions

All of the tubular specimens were modeled using common overall geometry and boundary conditions. The analysis approach of FRANC3D treats the underlying topology (created using the OSM program) separately from the geometry of the boundary element mesh, and boundary conditions are applied directly to the topological surface patches independent of discretization. For computational speed and simplicity, only a 50.8 mm high gage section was modeled, with the crack plane at the mid-height, as shown in Fig. 4.1.

The inner and outer surfaces of the gage section were created in OSM as the union of two separate cylinders by extruding the circular profiles first through 48.26 mm

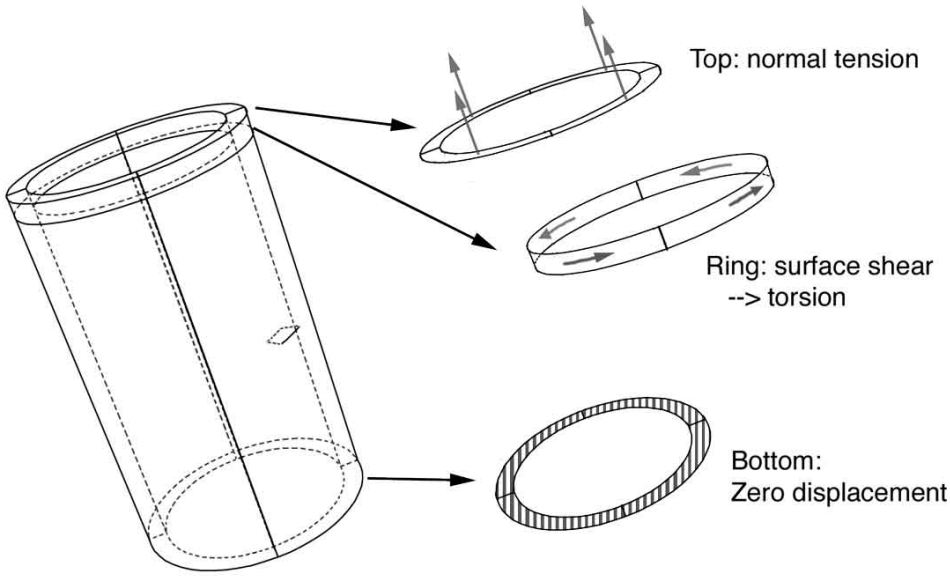

Figure 4.1: Discrete surface patches created in OSM and boundary conditions applied in FRANC3D for tubular specimen model.

along the z-axis, then through an additional 2.54 mm. This created circumferential edge features on the inner and outer cylinders between distinct topological surface patches at an axial location 2.54 mm from the top edge. The separate surface patches were necessary to facilitate application of the torsional tractions since a discrete, remote torque loading was required to simulate experimental conditions, and in FRANC3D boundary conditions are applied to entire topological entities (such as the surface patches) created in OSM. The precise location of the dividing edge for this "torsion ring" was arbitrary. Only the outer cylinder needed to be divided in order to apply the tractions, but generating the topology and consistent mesh generation were both facilitated by the creation of similar inner and outer topologies. Since the generating circles were composed of four arcs and vertices, the resultant surfaces were composed of four quadrant surface patches and four longitudinal edges for each cylinder section.

To generate a torque on the specimen, a shear traction of 152.4 MPa was applied in the surface-local angular direction to the outer 2.54 mm high annular patches, as

shown in Fig. 4.1, corresponding to a torque of 565 N-m:

$$\begin{aligned} T &= \pi \frac{D_o^2}{2} h t_{r\theta} \qquad (4.1) \\ &= \pi \frac{(30.48 \times 10^{-3} \text{ m})^2}{2} (2.54 \times 10^{-3} \text{ m})(152.4 \times 10^6 \text{ Pa}) \\ &= 565 \text{ N-m} \end{aligned}$$

where D_o is the cylinder outer diameter, h is the height of the subdivided annular surface patches, and $t_{r\theta}$ is the applied shear traction in the circumferential direction.

A normal traction of 798.06 MPa was applied to the four top surface patches in the positive global z-direction, corresponding to a tensile load of 44.5 kN:

$$\begin{aligned} P &= \frac{\pi}{4}(D_o^2 - D_i^2) t_{zz} \qquad (4.2) \\ &= \frac{\pi}{4}\left[(30.48 \times 10^{-3} \text{ m})^2 - (25.4 \times 10^{-3} \text{ m})^2\right](798.06 \times 10^6 \text{ Pa}) \\ &= 44.5 \times 10^3 \text{ N} \qquad (4.3) \end{aligned}$$

where D_i is the cylinder inner diameter and t_{zz} is the applied normal traction in the axial direction.

Finally, the bottom surface was constrained in a fully-fixed condition:

$$u_i = \omega_i = 0 \qquad (4.4)$$

where u_i and ω_i are the displacement along and rotation about the i^{th} axis, respectively. While this resulted in a local stress concentration at the end due to restriction of the Poisson contraction, these effects dissipated within several millimeters of the fixed end and did not disturb the stress distribution near the cracks. The same loads were applied to each model; a tension-only case was also analyzed to verify the separate contributions to each SIF from tension and torsion respectively. Final SIF values for each cracked specimen were calculated by scaling the resultant values from the modeled loads to the corresponding applied loads for each test.

The fatigue pre-crack was introduced into each model at mid-height of the gage section geometry in the FRANC3D program. Due to variations in EDM pre-flaw

and subsequent pre-crack shapes, SIFs for each of the tubular specimens tested were calculated individually using FRANC3D in order to capture variations in K_{I}, K_{II}, and K_{III} both between specimens as well as along individual crack fronts through the thickness, as discussed below. The fractographic pre-crack measurements and their corresponding BEM geometries are presented for each specimen in Appendix A.

4.1.2 Model Discretization

Local refinement of the boundary element mesh around a small portion of the gage section surrounding the pre-crack was employed for computational efficiency. One quadrant of the inner and outer cylindrical surfaces was subdivided by circumferential mesh edges 5.08 mm above and below the plane of the pre-crack as shown in Fig. 4.2. Large quadrilateral elements were used to mesh the specimen surfaces outside of the

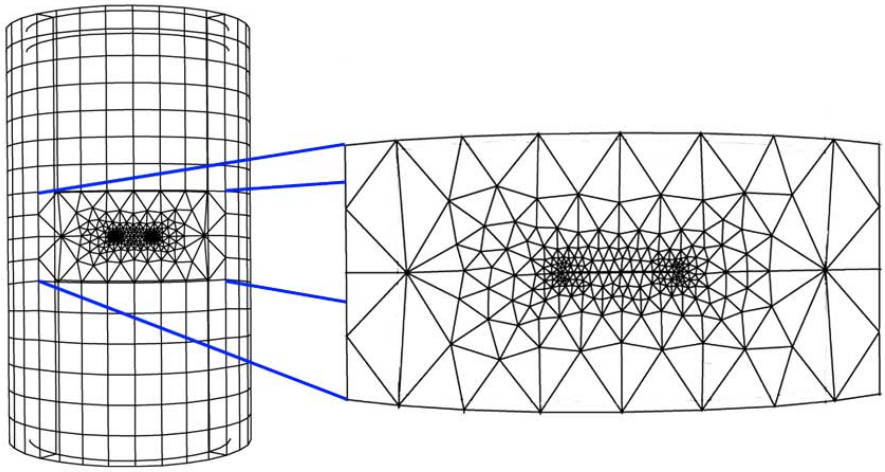

Figure 4.2: BEM mesh refinement employed around the crack surface intercepts for tubular FCG specimen.

subdivided region, while triangular elements were used to refine the mesh from the subdivision boundaries to the crack surface intercept edges. Outside the crack plane region, the mesh was comprised of quadrilateral elements nominally 3 mm wide and 4 mm high.

Several variants of mesh edge subdivision were initially modeled for one specimen, and the influence of the remote mesh refinement on SIF results was found to be minor compared to the mesh density on the crack surface itself. Fig. 4.3(a) shows a model mesh with 29 longitudinal and 32 circumferential subdivisions over the entire gage section, while Fig. 4.3(b) shows a mesh of twice the density with 43 longitudinal and 48 circumferential subdivisions. Analyses using these two remote meshes and

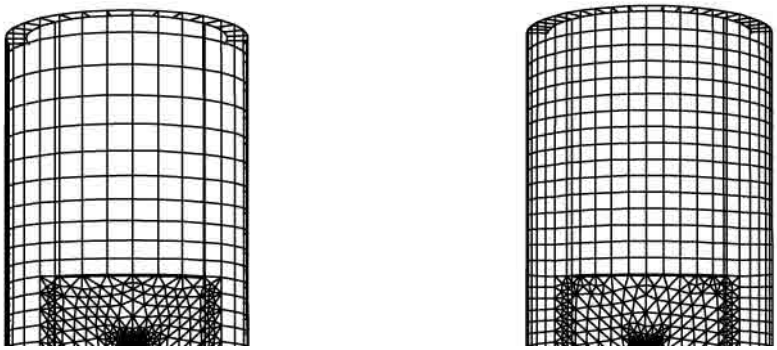

(a) (b)

Figure 4.3: (a) Coarse and (b) fine remote mesh densities employed in refinement studies for tubular FCG specimen.

varying crack meshes showed that doubling the remote mesh density only resulted in approximately 1-2% change in SIF (for both K_{I} and K_{II}); however, doubling and then quadrupling the crack mesh density produced better results with much less computation. Doubling the crack mesh density from Fig. 4.4(a) to Fig. 4.4(b) resulted in over 6% change in SIF (in the same increasing direction as doubling the remote density) with much less model processing time. Quadrupling the crack mesh density again to Fig. 4.4(c) resulted in only an additional 1% change in SIF but without a significant increase in processing time, so this finest iteration (with 16 elements through the wall thickness of 2.54 mm) was used for the remaining models. Therefore, the coarser remote mesh of Fig. 4.3(a) was employed for the remaining models while focusing refinement on the crack mesh density in order to balance accuracy and speed.

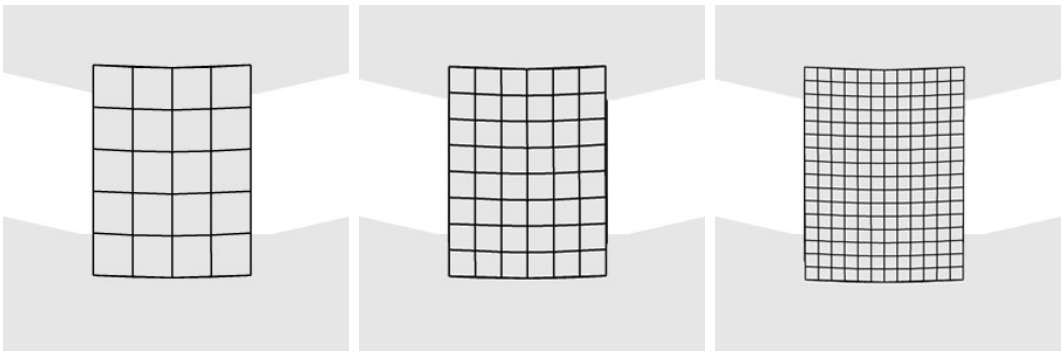

(a) 4x5 elements (b) 6x8 elements (c) 12x16 elements

Figure 4.4: (a) Initial coarse, (b) double refinement, and (c) quadruple refinement of crack surface mesh densities employed in refinement studies for tubular FCG specimen.

The refined crack mesh employed resulted in a nominal quadrilateral element size of 0.16 mm.

It should be noted that the models presented in Fig. 4.3 and used for the refinement study were based on a geometry created in OSM of a 76.2 mm long gage section, not the 50.8 mm model ultimately used. The refinement area around the crack surface intercepts was delineated at 7.62 mm above and below the crack plane instead of 7.62 mm. When the shorter geometry was adopted, remote mesh density was based on 13 longitudinal and 32 circumferential subdivisions. The resulting change in SIFs between the two geometries was less than 0.4%.

4.1.3 Influence of Pre-Crack Geometry

Fabrication of the specimens with an EDM-generated initial slot resulted in some variation in parallelism and straightness of the sides of the slot and subsequent variation of pre-crack shape. In order to capture any influence of pre-crack front skew (relative to the radial axis) and curvature, a unique crack shape geometry was created for the model of each tested specimen. Pre-crack shapes on tested specimens were digitally photographed under an optical microscope and measured using calibrated

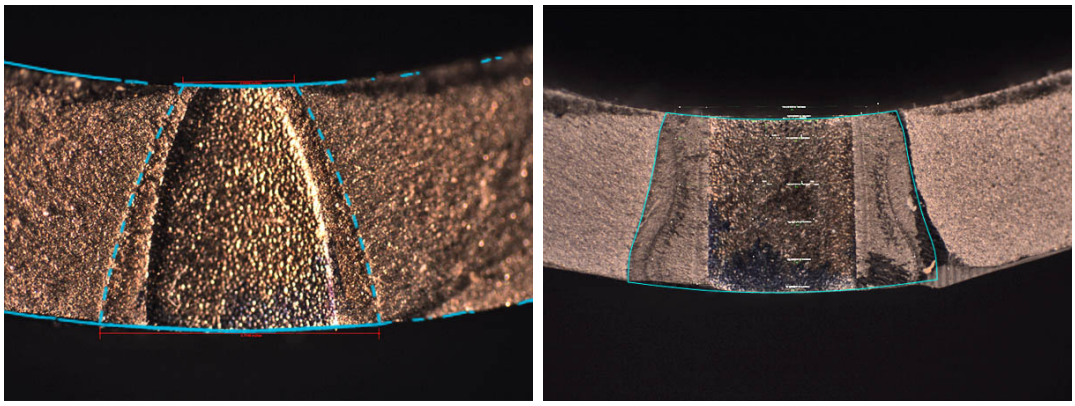

(a) (b)

Figure 4.5: Photographs of experimental pre-cracks and associated FRANC3D model surfaces (superimposed outline) for (a) 3-point cubic polynomial-fit curved crack front, Specimen N11, and (b) multi-point cubic B-spline crack front, Specimen N07.

pixel-to-length conversions in ImagePro and Photoshop software. Depending on the curvature of the crack front, sufficient measurements were taken to model the crack front either as a cubic polynomial based on inner, mid-thickness and outer crack front distances from the nominal crack front centerline, or as a cubic B-spline based on several manually-inputted crack front vertices. The crack surfaces were meshed with quadrilateral elements nominally 0.16 mm square along the crack front edge, although some elongation of crack surface elements was unavoidable in the central region (away from the crack front edges) of skewed and/or thumbnailed cracks (see Appendix A). An example of each type of crack front shape in FRANC3D along with the photographed fracture surface is shown in Fig. 4.5.

Specimen N17 was initially used as a case study to justify detailed modeling of all remaining fracture surfaces. There are two geometric characteristics that distinguish the crack front from an "ideal" straight-through radial crack front: *skew*, the angle between a straight-line approximation of the crack front and the radial axis of the specimen; and *camber*, the amount of curvature of the crack front, commonly called "thumbnail" crack fronts. (For a rigorous analysis, camber can be characterized by

two values: the maximum distance from the curved crack front to the straight line drawn between the two crack surface intercepts, and the relative radial location of the maximum distance.) In this study, the straight-line approximation of the crack front was determined by drawing a line parallel to the line between the two crack surface intercepts and through the curved crack front such that the area of the straight-line approximation crack shape would be the same (this was estimated visually). This approximation and the angle of skew are illustrated in Fig. 4.6.

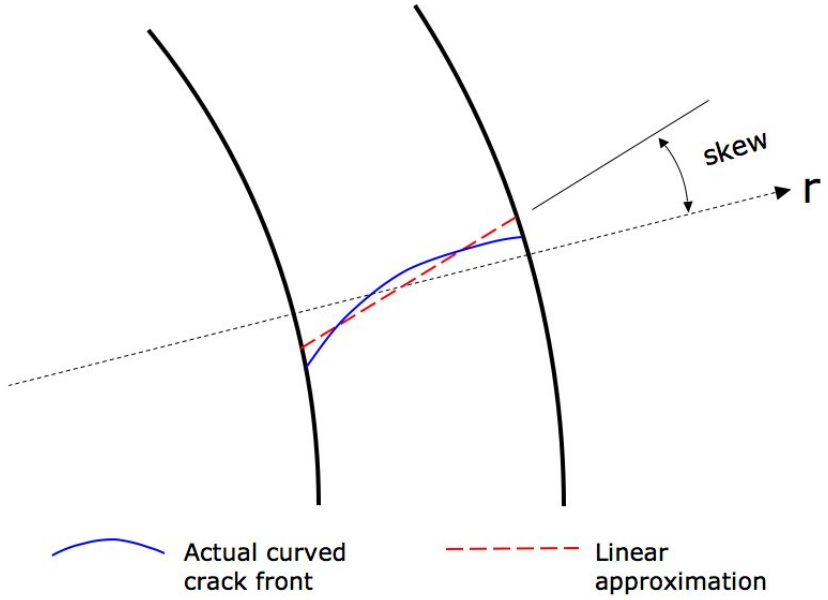

Figure 4.6: Illustration of defining skew angle from straight-line approximation of a curved/cambered crack front.

The skew of the straight-line approximation of the pre-crack in specimen N17 was 17°, as shown in Fig. 4.6. When torque is applied to this type of specimen, any skew between the actual crack front and the radial axis would result in a projection of the torsional shear stress along the out-of-plane shear (or Mode III) direction, whereas a perfectly straight crack front with zero skew would be subjected only to in-plane shear (Mode II). Therefore, to examine the relative impact of the actual skew in specimen N17 on the stress state, two other straight-line crack fronts were modeled, with no

skew angle (0°) and an intermediate value (8°). The 8°- and 0°-skew linear approximations were both drawn to intersect the 17° at the specimen wall mid-thickness to maintain a constant average crack width. Finally, camber was introduced to model the actual crack front shape accurately. For this crack shape, a simple approach in FRANC3D was employed using three equally-spaced measurements of crack front height from the pre-crack centerline. The BEM meshes ultimately generated for these four crack shape models are shown in Fig. 4.7.

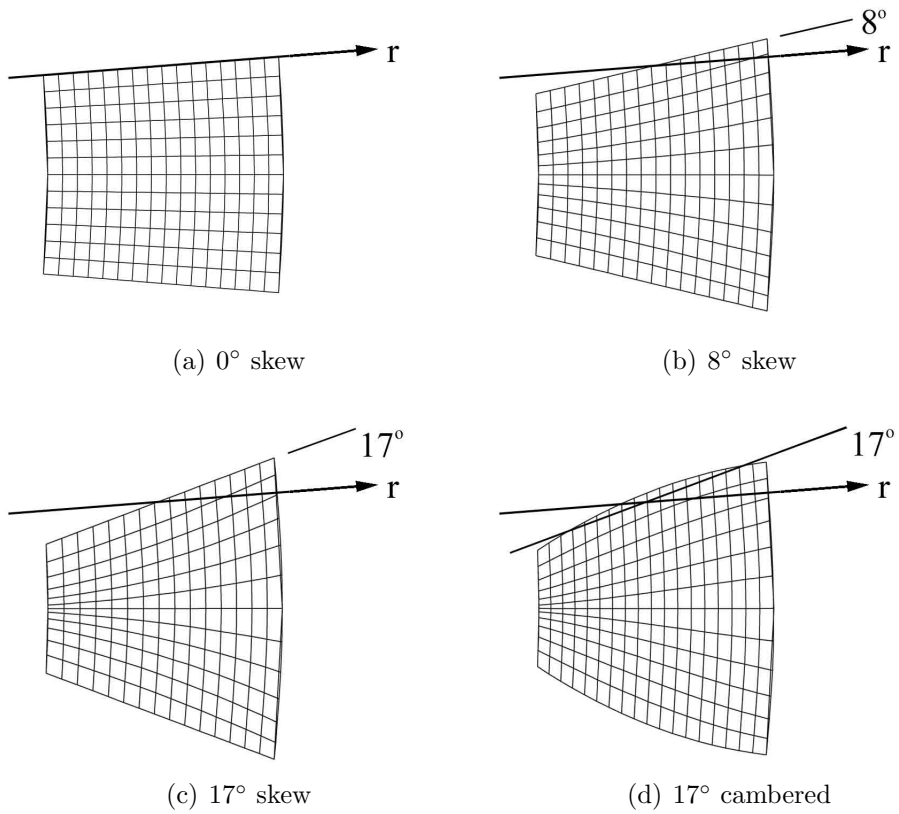

(a) 0° skew (b) 8° skew

(c) 17° skew (d) 17° cambered

Figure 4.7: Four different BEM approximations of the pre-crack in specimen N17, shown with meshes: (a) straight line, 0° skew; (b) straight line, 8° skew; (c) straight line, 17° skew; (d) curved cubic fit of three measured points from fractograph.

All four crack shapes were subjected to the same tension-torsion loading conditions described above in Section 4.1.1. The resulting SIF distributions along the crack fronts drawn in Fig. 4.6 are presented in Fig. 4.8, and the average value of each SIF is

presented in Table 4.1. The models showed that the impact of crack front geometry

Table 4.1: Average SIF values resulting from different approximations of the crack front for specimen N17 (MPa$\sqrt{\text{m}}$).

	K_{I}	K_{II}	K_{III}
Straight 0° skew	12.01	10.63	0.43
Straight 8° skew	12.00	10.53	1.93
Straight 17° skew	11.91	9.89	3.15
Curved (cubic) 17° skew	12.12	10.10	3.08

on average K_{I} was almost negligible as shown in Fig. 4.8(a), with no more than 2% variation in average value between the approximations, although the spread in K_{I} across the crack front increased more appreciably (from approximately 10% for the 0°-skew to 20% for the 17°-curved).

The shear modes, K_{II} and K_{III} shown in Fig. 4.8(b) and Fig. 4.8(c) respectively, are more affected by crack front shape. The spread in K_{II} across the crack front similarly increases from approximately 10% for the 0°-skew to 20% for the 17°-curved, but the average value drops more significantly (7%) from 0°-skew to 20% for the 17°-skew. The effect of crack front shape on K_{III} is most significant. While it is not very enlightening to discuss the relative spread in K_{III} across the crack front when the average value is so small, it should be noted that all three straight-line approximations cover a range of approximately 5 MPa$\sqrt{\text{m}}$ in a nearly linear distribution. The average value of K_{III} increases markedly with skew angle, and introduction of camber to the 17°-skew crack front restores a more uniform distribution to K_{III} while only changing the average value by a few percent.

For the purposes of studying non-proportional waveforms in nominally K_{I}-K_{II} mixed-mode loading, the contribution of K_{III} loading was not considered. The intent of the tubular specimen testing was to compare the standard crack path deflection predictions based on monotonic or in-phase K_{I}-K_{II} loading to the actual deflection

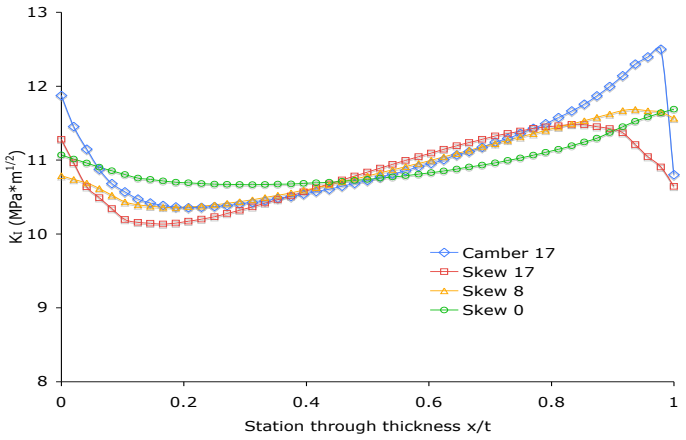

(a)

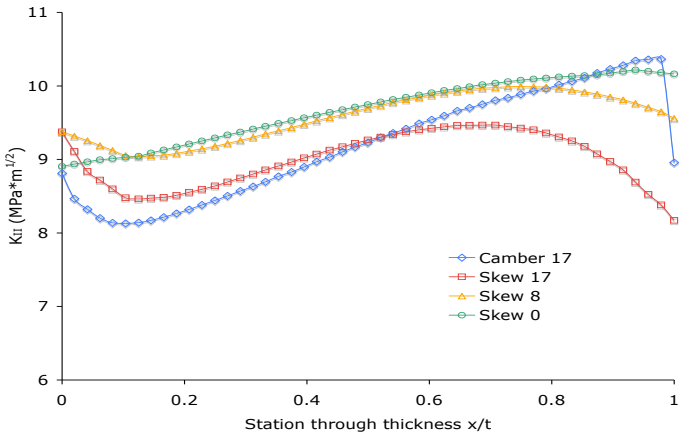

(b)

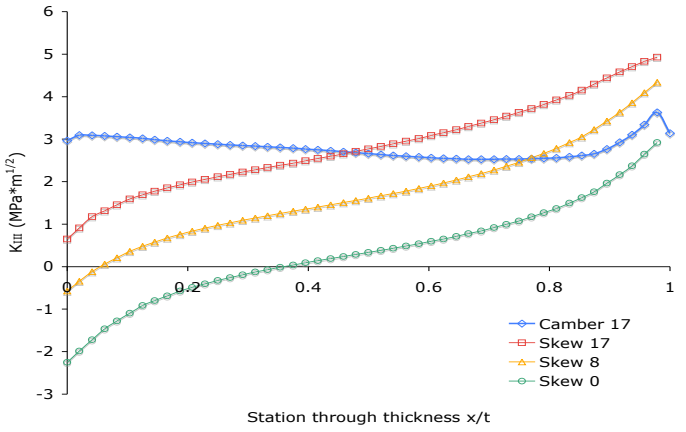

(c)

Figure 4.8: SIF distributions resulting from different approximations of the crack front for specimen N17 in (a) Mode I, (b) Mode II and (c) Mode III.

angles for non-proportional mixed-mode loads comprised primarily of K_{I} and K_{II}. The minor amounts of K_{III} were assumed not to influence significantly the interaction between K_{I} and K_{II}, but the additional contribution to crack tip shear stress from K_{III} should be considered in future model development.

4.1.4 Numerical Results

All of the individual pre-crack shapes modeled and the corresponding FRANC3D meshes are shown in Appendix A. The average value of both crack fronts on each specimen are presented in Table 4.2 for the as-modeled condition: a tensile load of 44.5 kN and a torque of 564.92 N-m for all specimens. (The average values of K_{I} and K_{II} as scaled to the tested load condition are given in Tables 3.2 and 3.3.) Table 4.2 also shows the average, maximum, minimum, and range of values for the SIFs and the mode mixity ratios which indicate the importance of accounting for any pre-crack geometry variation in analyzing specimens of this type.

4.2 Inclined Through-Crack Round Specimen

4.2.1 Model Geometry and Boundary Conditions

All of the ITCR specimens were initially modeled using common overall geometry and boundary conditions as shown in Fig. 4.9. For computational speed and simplicity, only a 76.2 mm high gage section was modeled, with the through-crack (generated later in FRANC3D) centered longitudinally in the cylinder. As with the tubular specimen (see Section 4.1.1), the cylindrical surface was created in OSM as the union of two separate cylinders by extruding the circular profile first through 73.66 mm along the z-axis, then through an additional 2.54 mm. This created circumferential edge features on the specimen surface between distinct topological surface patches at an axial location 2.54 mm from the top edge.

Also like the tubular specimen model, torque was simulated by applying a shear

Table 4.2: Average SIF values in MPa$\sqrt{\text{m}}$ and mode mixity ratios for tubular specimens in the as-modeled condition (P = 44.5 kN, T = 564.92 N-m).

Specimen	$K_{\text{I,avg}}$	$K_{\text{II,avg}}$	$K_{\text{III,avg}}$	$K_{\text{II}}/K_{\text{I}}$	$K_{\text{III}}/K_{\text{I}}$
N01	16.45	11.51	6.28	0.70	0.38
N02	16.70	11.95	6.38	0.72	0.38
N03	15.21	12.56	3.62	0.83	0.24
N04	15.27	13.07	2.82	0.86	0.18
N05	18.44	12.05	7.88	0.65	0.43
N06	17.53	11.68	7.14	0.67	0.41
N07	16.62	14.44	2.26	0.87	0.14
N08	11.75	10.10	2.02	0.86	0.17
N09	11.84	10.01	2.57	0.85	0.22
N10	11.22	9.67	2.05	0.86	0.18
N11	11.62	9.76	2.75	0.84	0.24
N12	11.79	10.04	2.41	0.85	0.20
N13	11.55	10.07	1.49	0.87	0.13
N16	11.68	9.90	2.67	0.85	0.23
N17	12.14	10.10	3.10	0.83	0.26
N18	10.69	9.00	2.58	0.84	0.24
N19	11.51	9.67	2.75	0.84	0.24
Average	13.65	10.92	3.57	0.81	0.25
Range	7.75	5.44	6.40	0.22	0.30
Max	18.44	14.44	7.88	0.87	0.43
Min	10.69	9.00	1.49	0.65	0.13

traction of 78 MPa in the surface-local angular direction to this "torsion ring" at the top of the specimen, as shown in Fig. 4.9, corresponding to a torque of 113 N-m. The tensile load of 44.5 kN was applied by a normal traction on the four top surface patches in the positive global z-direction of 156 MPa. Finally, the four bottom surface patches were subjected to the fully-fixed displacement condition of Eq. 4.4. As with the tubular specimen, the local stress concentration at the fixed end due to constraint of the Poisson contraction dissipated well before disturbing the crack region.

Fatigue pre-cracks of various sizes and orientations were introduced into each

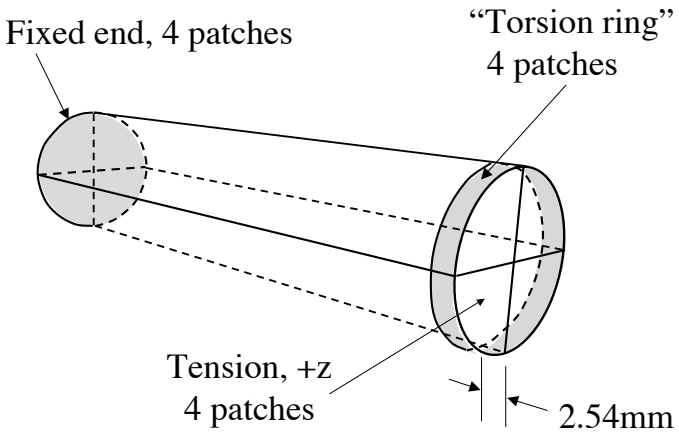

Figure 4.9: Discrete surface patches created in OSM and boundary conditions applied in FRANC3D for ITCR specimen model.

model at mid-height of the gage section in the FRANC3D program. Based on specimens fabricated, three crack angles, β, that were modeled are discussed here: $\beta = 0°$, 15°, and 30°. A fourth specimen configuration of $\beta = 45°$, was analyzed as well at a single crack size for use in curve-fitting the influence function for β so that the specimen configuration actually used would not be the endpoint of the analysis interval; details are in Appendix B. At each angle, three pre-crack sizes, $2a$, were modeled: $2a = 2.54$ mm, 3.05 mm, and 4.45 mm, resulting in non-dimensional crack sizes $a/r = 0.133$, 0.167, and 0.233. All crack configurations were subjected to the same boundary conditions for SIF calculation. Each was analyzed with tension-only and tension-torsion loading in order to separate the contribution to the SIFs from tension and torsion respectively and look for any interactions prior to reducing the data to a closed-form solution.

After the closed-form SIF solution was determined from the analysis of the nine models described above, two additional specimen configurations were modeled to check the accuracy of the solution at different length scales. A smaller specimen of

$D = 12.7$ mm and a larger specimen of $D = 25.4$ mm were analyzed. Both pre-cracks were inclined at an angle of $\beta = 30°$ and sized at $a/r = 0.133$, giving a crack size $2a = 1.694$ mm and 3.388 mm for the smaller and larger specimen, respectively.

4.2.2 Model Discretization

Local refinement of the boundary element mesh in the center of the specimen was employed for computational efficiency. The entire cylindrical surface was subdivided by two circumferential mesh edges spaced equally above and below the mid-plane of the specimen at a distance dependent on the crack angle β, as listed in Table 4.3. The full circumference of the central region boundaries was subdivided into 80 to 96 segments, and fine quadrilateral elements were used within the crack region. The number of gage section subdivisions for the 30° specimen was limited by computational capacity due to the increased number of crack surface elements for the largest crack surface; any greater refinement resulted in aborted analyses by FRANC3D. A scaling subdivision scheme was used on the region boundaries to ensure that the length of subdivision segments directly above and below the crack surface intercepts were comparable to the subdivision size of the crack itself in order to minimize element distortion near the crack. The outer regions of the specimen were meshed with triangular elements that decreased in size from the ends toward the center. An example of this mesh refinement scheme is shown for each crack angle in Fig. 4.10.

All crack surfaces for the nine specimen configurations ($\beta = 0°$, 15°, 30° and $2a =$ 2.54 mm, 3.05 mm, 4.45 mm) were meshed with nearly square quadrilateral elements 0.30-0.32 mm in size. This resulted in an 8 by 60 element mesh for the smallest crack surface ($\beta = 0°$, $2a = 2.54$ mm) and a 14 by 68 element mesh for the largest ($\beta =$ 30°, $2a = 4.45$ mm). An example crack mesh for the $\beta = 0°$, $2a = 3.05$ mm condition is shown in Fig. 4.11. As state above, the largest crack size model already needed to be reduced in refinement so as not to exceed the computational capacity available, so

Table 4.3: Parameters of local mesh refinement in central crack region for ITCR specimen models.

Crack angle β	**0°**	**15°**	**30°**
Crack intercept distance z from center plane	0 mm	±2.55 mm	±5.50 mm
Refined mesh region height z from center plane	±5.08 mm	±7.62 mm	±10.16 mm
Crack region mesh vertical subdivisions	16	24	28
Crack region mesh circumferential subdivisions	96	96	80

no further refinement was attempted in order to keep a consistent crack surface mesh among all specimen configurations.

However, as a check of mesh sensitivity, three additional, coarser mesh variations were analyzed at the $\beta = 30°$, $2a = 4.45$ mm condition. The first reduced the crack mesh from 14 by 68 elements to 12 by 58 elements (27% reduction) without changing the surrounding gage section. The second reduced the surrounding gage mesh from 28 axial by 80 circumferential elements to 24 axial by 72 circumferential (23% reduction) without changing the crack mesh. The third, shown in Fig. 4.12, employing a very coarse quadrilateral mesh from the ends to the gage section and automatic triangular element generation around the crack surface intercepts similar to the tubular specimen meshes described in Section 4.1.2. Over the regions of interest, the SIF distributions for all four mesh designs fell within a 2% scatter band of each other, confirming adequate refinement of even the coarsest mesh employed for the ITCR specimen.

The two additional $\beta = 30°$ models that were analyzed at different specimen diameters in order to check the accuracy of the closed-form solution were meshed similarly. The crack length $2a$ was subdivided into 8 segments for both new designs (simulating the smallest a/r condition), resulting in 8 by 46 and 8 by 92 element crack meshes, respectively, for the 12.7 mm and 25.4 mm diameter models. The remaining

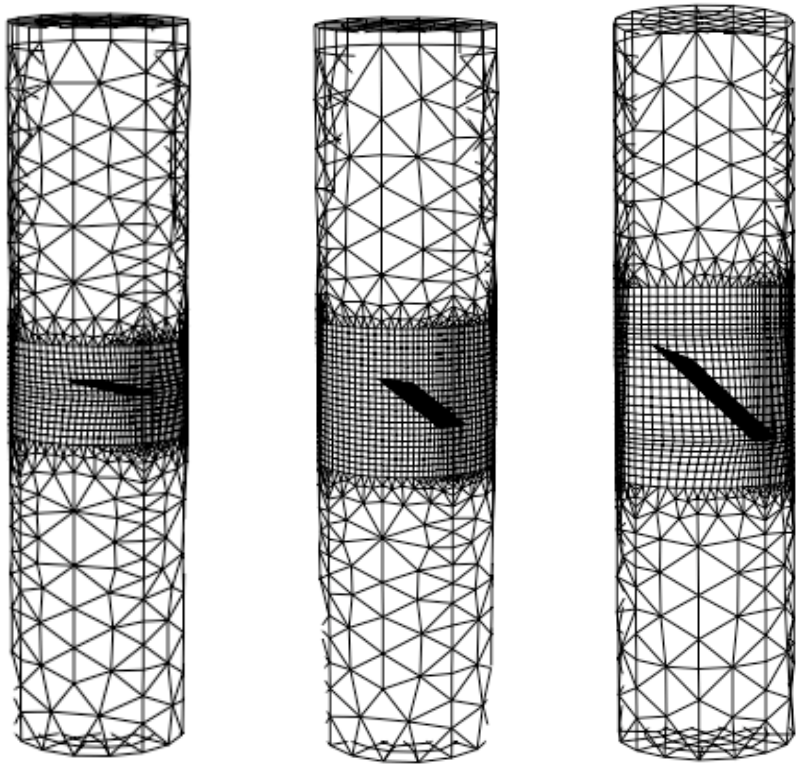

Figure 4.10: BEM mesh refinement employed in central crack region for ITCR specimen configurations, crack angle $\beta = 0°$, $15°$, $30°$ (from left to right).

mesh subdivision lengths were scaled accordingly.

4.2.3 Numerical Results and Closed-Form Solution

In discussing the SIF results for the ITCR specimen, a distinction must be made between the two different crack fronts and will be denoted by a prime notation, as in K_{I} and K'_{I}. This is necessitated by the different ways tension and torsion interfere on either crack front, producing constructive and destructive effects on K_{I} and K_{III}. Fig. 4.13 shows the different stress components of applied tension and torsion on the two crack fronts of a specimen with an inclined crack. As shown in Fig. 4.13(a), the projection of the global tensile load parallel to the crack plane creates out-of-plane

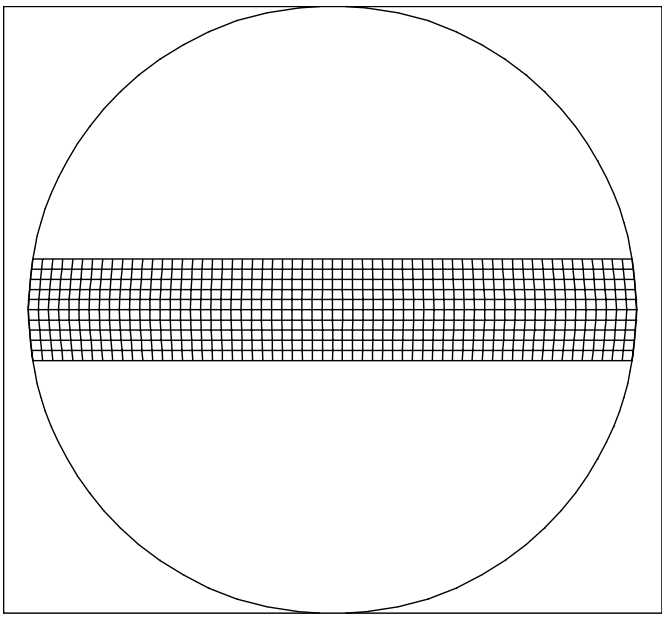

Figure 4.11: Crack surface mesh for $\beta = 0°$, $2a = 3.05$ mm ITCR specimen.

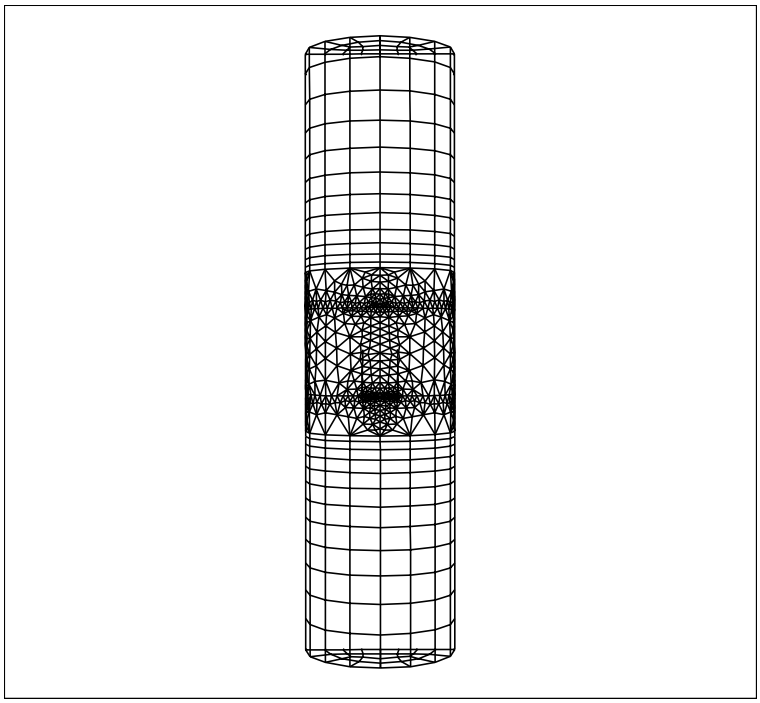

Figure 4.12: Alternative ITCR model mesh design employed in refinement sensitivity study.

shear stresses on both crack fronts equal in magnitude but in opposite orientations relative to the local coordinate system. This is the primary contribution to K_{III} on both crack fronts, resulting in a positive value of K_{III} on the far ($y > 0$) crack front and a negative K_{III} on the near ($y < 0$) crack front. In Fig. 4.13(b), the projection of the applied torque parallel to the crack plane creates out-of-plane shear stresses of equal magnitude and in the same local orientation on both crack fronts. This results in secondary contributions of negative K_{III} on both crack fronts, which increases the magnitude of K_{III} on the near side but decreases its magnitude on the far side.

Similarly, Fig. 4.13(b) shows that the projection of the applied torque normal to the crack plane results in crack opening tensile stresses on the near crack front and crack closing compressive stresses on the far front. While the tensile load is the major source of a positive K_{I}, the superposition of torsion contributes additively to K_{I} on the near side and destructively to K_{I} on the far side. In discussing the ITCR specimen, the SIFs for the far crack front, upon which tension and torsion interfere destructively for Mode I stresses (and constructively for Mode III stresses) will be designated by the prime-annotated variables K'_{I}, K'_{II} and K'_{III}. The SIFs for the front on which tension and torsion are additive for Mode I (and destructive for Mode III) are designated conventionally.

The full results of the BEM analyses are presented in Appendix B. As an example, Fig. 4.14 shows the SIF distribution across the crack fronts for the case $\beta = 30°$, $2a =$ 2.5 mm. The SIF values are plotted along the normalized coordinate x/b, where $b = \sqrt{r^2 - a^2}$ is the length of the crack front as projection on a plane normal to the specimen axis, and the primed SIF values (K'_{I} etc.) are shown by dashed lines. This plot clearly shows the different interactions between tension and torsion on either crack front: K_{I} is slightly higher than K'_{I} due to the constructive contribution from torsional stresses, while the magnitude of K_{III} is slightly lower than that of K'_{III} due to destructive interference of the tensile and torsional stresses on the inclined crack

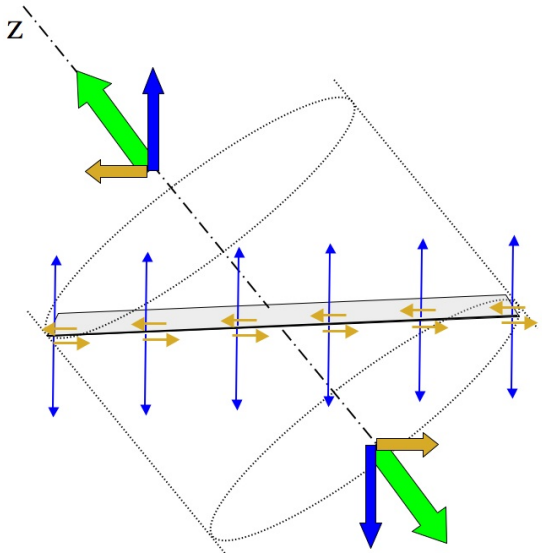

(a)

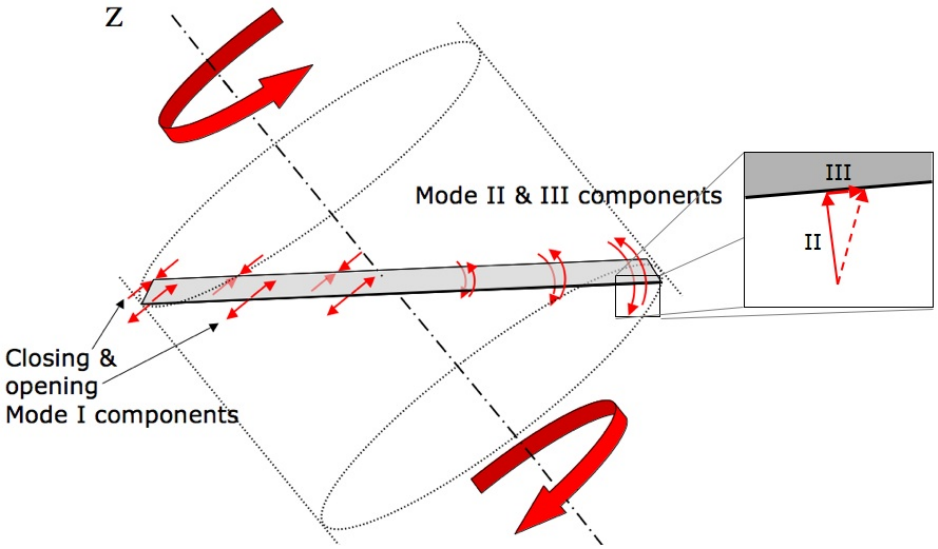

(b)

Figure 4.13: Illustration of crack front stress components produced in ITCR specimen by (a) tension, resulting in Mode I and III crack front stresses, and (b) torsion, resulting in opening and closing Mode I stresses on opposite crack fronts and Mode II and III stresses increasing with radius. Expanded view in (b) shows how local crack front orientation relative to the circumferential direction breaks down into Mode II and III loads.

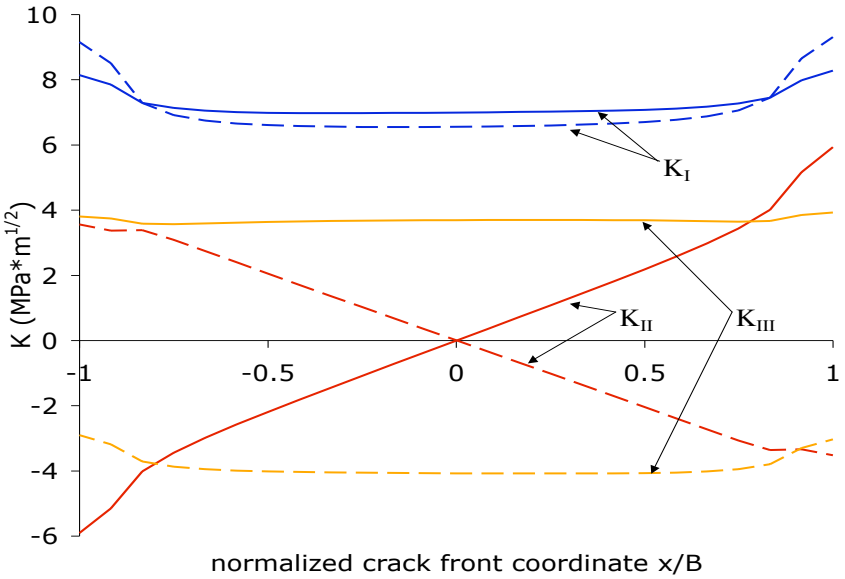

Figure 4.14: SIF results for ITCR specimen, β=30°, $2a$=2.5 mm, P=44.5 kN, T=113 N-m.

plane.

The absence of interaction between tension and torsion is illustrated in Fig. 4.15, which shows the SIF distribution for the case of $\beta = 0°$, $2a = 4.45$ mm. In this instance, $K_{\mathrm{I}} = K'_{\mathrm{I}}$ due to the lack of a torsional projection on crack-normal stresses, and $K_{\mathrm{III}} = K'_{\mathrm{III}}$ due to the lack of a tensile projection on crack plane shear stresses. The small contribution of torsional loading to in-plane shear stresses is evident in the non-zero value of both K_{III} and K'_{III}.

For the purposes of quickly determining test matrix conditions, the BEM results were reduced to closed-form solutions. The full derivation is presented in detail in Appendix B but will be described briefly here. For simplicity, the SIF distributions along the crack front for all three modes were treated as linear (i.e., neglecting the free surface effects in the BEM at either end and the very slight nonlinearity in Modes I and III). From x/b = -0.75 to 0.75, the values of all three SIFs are within a 5% band of linear, so the SIF values within that region were used to calculate an average

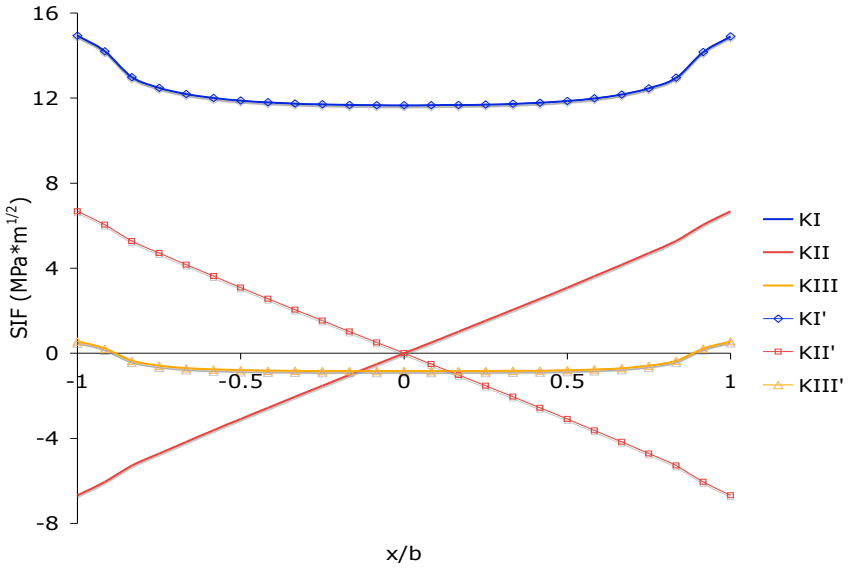

Figure 4.15: SIF results for ITCR specimen, β=0°, $2a$=4.45 mm, P=44.5 kN, T=113 N-m.

constant value for Modes I and III and a linear slope (of K_{II} versus x/b) for Mode II. The stress intensity equations determined by this approach are

$$\begin{aligned} \mathrm{K_I} =& \sigma_o\sqrt{\pi a}\ \cos^2\beta\left(0.8162+0.8286\frac{a}{r}\right) \\ &\pm\ \tau_o\sqrt{\pi a}\ \sin\beta\cos\beta\left(-0.018+0.759\ \frac{a}{r}\right) \end{aligned} \tag{4.5}$$

$$\mathrm{K_{II}} = \frac{x}{b}\left[\tau_o\sqrt{\pi a}\ \cos\beta\left(0.7114+2.3439\frac{a}{r}-4.6816\left(\frac{a}{r}\right)^2\right)\right] \tag{4.6}$$

$$\begin{aligned} \mathrm{K_{III}} =& \sigma_o\sqrt{\pi a}\ \sin\beta\cos\beta\left(0.8513+0.3933\frac{a}{r}\right) \\ &\pm\ \tau_o\sqrt{\pi a}\ \left(\sin^2\beta-\cos^2\beta\right)\left(-0.0199+0.6846\frac{a}{r}\right) \end{aligned} \tag{4.7}$$

where

$$\sigma_o = P/\pi r^2$$

$$\tau_o = 2T/\pi r^3.$$

Fig. 4.16 shows a comparison of the linearized predictions and the BEM data shown previously in Fig. 4.14. These SIF solutions were verified against two FRANC3D

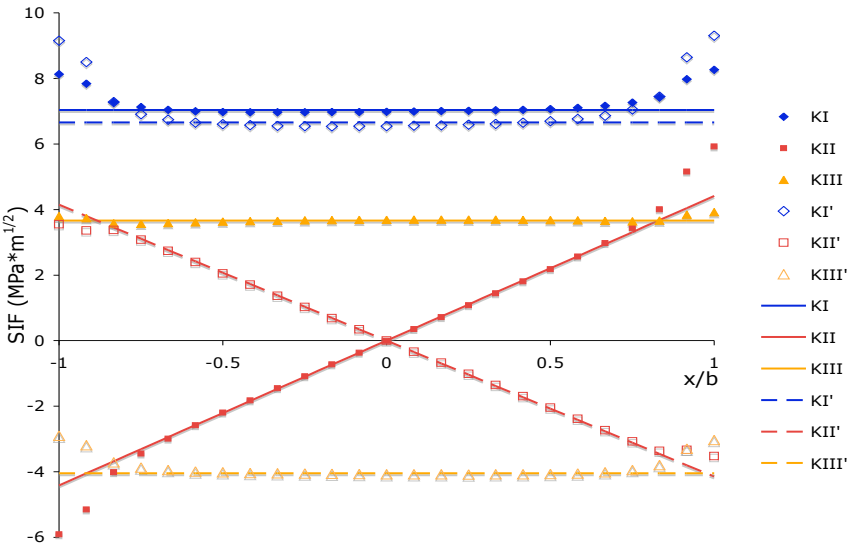

Figure 4.16: Comparison of linear fits of Eqs. 4.5-4.7 SIF results for ITCR specimen, β=30°, $2a$=2.5 mm, P=44.5 kN, T=113 N-m.

models of larger and smaller diameter specimens for the $\beta = 30°$ case as described in Sections 4.2.1 and 4.2.2. Error for both cases was less than 3% in the linear region ($|x/b| < 0.75$) for K_{I} and K_{III} and in the region $|x/b| < 0.62$ for K_{II}; the maximum error in K_{II} at $x/b = 0.75$ was 6%.

CHAPTER 5

EXPERIMENTAL RESULTS AND DISCUSSION

This chapter will present the results of mixed-mode crack growth testing primarily in terms of crack deflection angles for given combinations of constant SIFs and cyclic SIF ranges. Data from NASA testing of the thin-walled tubular specimens are presented first, along with scanning electron microscope (SEM) fractography of selected specimens, and trends within and between the sets of loading conditions are discussed. Then data from Georgia Tech testing of the new ITCR specimens are presented, including descriptions of the fracture surface geometries, and trends in that specimen data are discussed. Results from the two specimen types are then compared to assess common trends and differences in crack path behavior, and crack path data from the four types of loading are evaluated against various prior models.

5.1 Tubular Specimens

The first data generated were from NASA testing of thin-walled tubular specimens which nominally produced a single crack loading condition for each specimen (with minor variations in mode mixity), although results for each crack front were recorded individually resulting in at least two points per specimen. These results are presented below according to the type of mixed-mode loading. Selected specimens were examined by SEM in order to compare the fractographic features of apparently different crack growth mechanisms.

5.1.1 In-Phase Loading

Six NASA specimens were tested under in-phase fatigue loading as discussed in Section 3.3.1.2. These were used to establish baseline data on the fidelity to the monotonic MTS and MSS criteria and the existence of a modal transition in Inconel

718.

5.1.1.1 Crack Deflection Angles

The crack deflection angles are presented in Table 5.1 along with their corresponding mode mixity ϕ. Due to variations in crack front shape resulting in slight differences in ϕ between crack fronts and different deflection angles for left and right crack fronts, the data are presented for each crack front separately for the NASA specimens. Additionally, during testing some cracks were observed to branch from the crack front, so two deflection angles are given for certain crack fronts.

Table 5.1: Crack deflection angles and mode mixity values for left (L) and right (R) crack fronts under in-phase testing of NASA thin-walled tubular specimens.

Specimen	ϕ_L (deg)	θ_L (deg)	ϕ_R (deg)	θ_R (deg)
N01	28.2	-37	28.2	-37
N02	28.8	-37	28.8	-37
N08	44.7	-38, 7	44.7	10
N09	44.0	-58, 16	44.4	-55, 18
N12	23.5	-30	23.5	-26
N16	33.0	-38	33.0	-30

The trend in crack deflection can be seen in Fig. 5.1 which plots crack angle versus mode mixity ϕ, along with the predictions of the MTS and MSS criteria. Crack deflection for the in-phase loading follows the MTS criterion for lower levels of ϕ as expected. At a mode mixity ϕ of 44° the specimens begin to show crack deflections toward the MSS criterion, as seen in specimens N08 and N09. Only one crack front (N08R) deflected purely in the direction of the MSS criterion without bifurcation. Three other crack fronts (N08L, N09L and N09R) displayed MSS-controlled crack deflection but also had MTS-controlled branches from the pre-crack. From the N09L pre-crack, the bifurcation of crack growth took place discretely at mid-thickness rather than concurrently at overlapping sections of the crack front, as shown in Fig. 5.2.

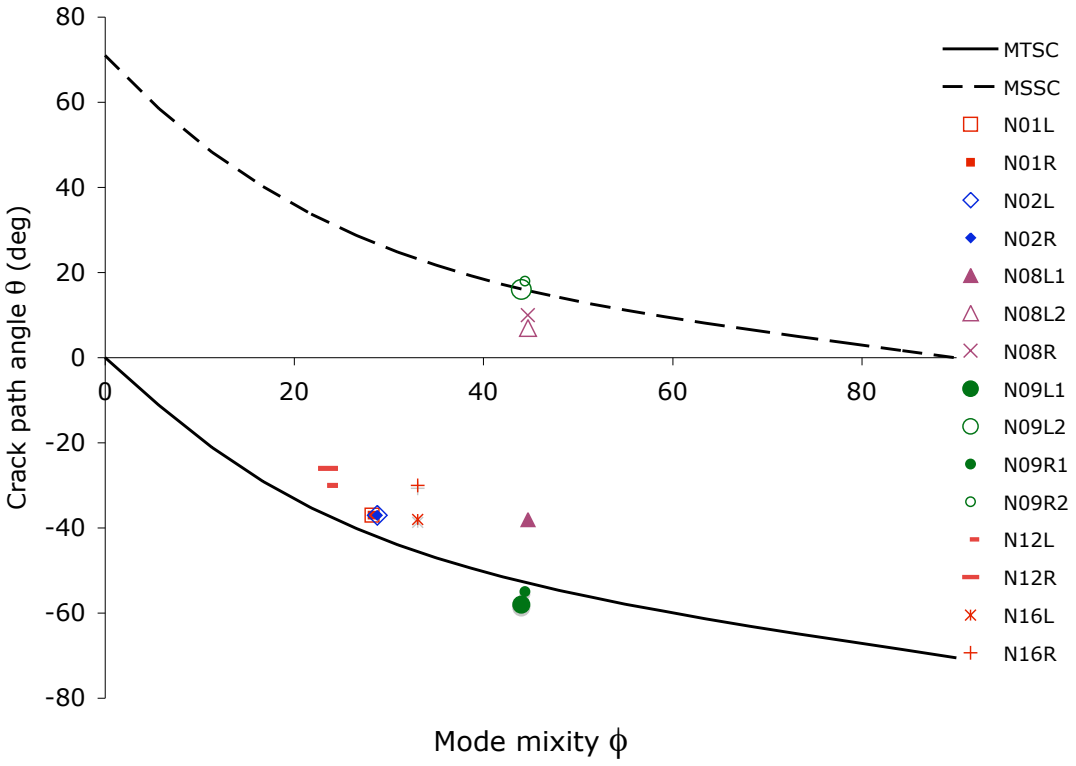

Figure 5.1: Crack deflection angles versus crack loading mode mixity ϕ for in-phase tests of NASA thin-walled tubular specimens. Legend describes specimen number and crack front as viewed in load frame, e.g. 01L = Specimen N01 left crack front.

Roughly the outer half of the crack front propagated according to the MSS criterion while the inner half deflected toward MTS; it is also apparent in Fig. 5.2 that the inner tensile crack eventually spread outward and cut through the outer shear crack surface. The opposing crack front N09R displayed similar partial bifurcation, with discrete sections at the central and outer portion of the pre-crack front propagating according to the MSS criterion while the bulk of the crack front deflected toward MTS.

The bifurcation behavior of crack front N09L can be explained by the effect of the notch and pre-crack shape on the distribution of SIFs and mode mixity across the crack front. The initial EDM notch in specimen N09 created a curved pre-crack due to a reduction in the EDM electrode penetration through the specimen wall thickness.

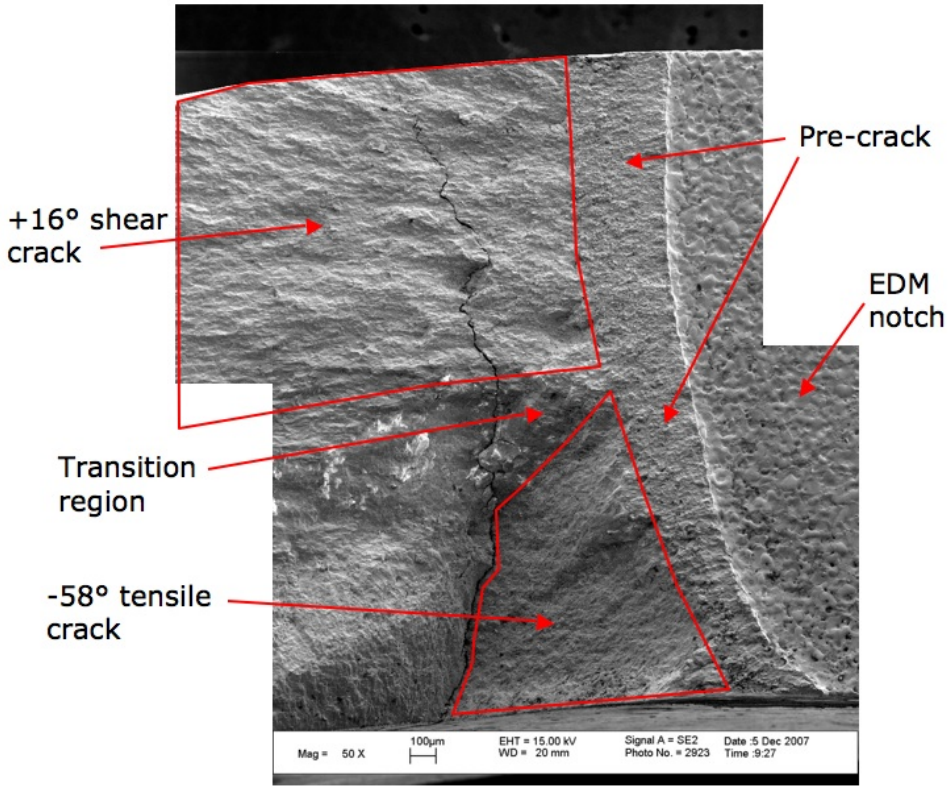

Figure 5.2: SEM image of N09L crack at low magnification showing two different crack branches along pre-crack front: MSS-controlled Mode II crack branch at +16° near outer diameter and MTS-controlled Mode I crack branch growing down (into image) at -58° near inner diameter.

The change in angle between the pre-crack front and the torsional stress from the outer to the inner surface resulted in a decrease of K_{II} and ϕ, apparently passing through the modal transition value in mid-thickness. Fig. 5.3 shows the distribution of K_{I}, K_{II} and ϕ from the outer surface (x/L = 0) to the inner surface (x/L = 1) for the maximum load condition as analyzed in FRANC3D. (The BEM mesh used to generate this distribution is shown in Appendix A.) While K_{I} and K_{II} distributions across the crack front are very similar, there is a fairly significant drop in ϕ from 45.4° to 42.2° that coincides well with the observed crack growth behavior.

The tensile branches from both N09 pre-cracks adhered closely to the MTS criterion at mode mixities of ϕ = 44.0°-44.4°, while the tensile branch from N08L was approximately 15° shallow of the MTS criterion at ϕ=44.7°. Testing at higher mode

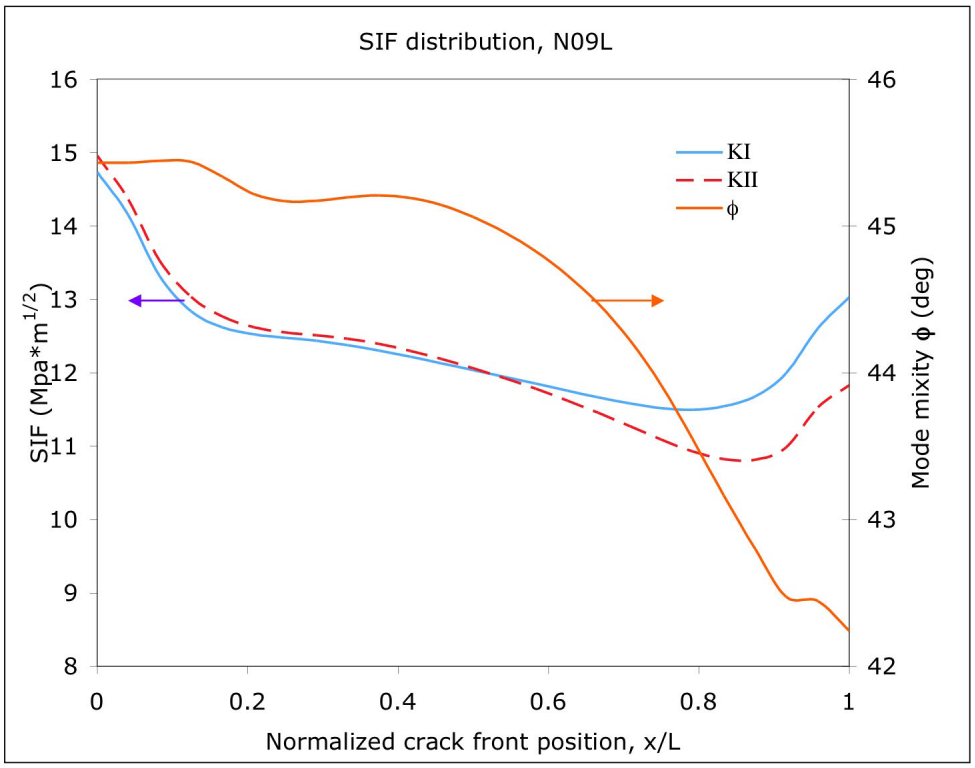

Figure 5.3: Stress intensity factor and mode mixity distribution along crack front N09L.

mixity values to confirm tracking to the MSS criterion was prevented by load frame limitations. However, the data available from specimens N08 and N09 strongly indicate that crack propagation mode transition from the MTS to the MSS criterion occurs very close to ϕ = 44°-45° under plane-stress conditions for the Inconel 718 tested.

5.1.1.2 SEM Fractography

Selected specimens were sectioned and examined by SEM to assess fracture surface morphology differences between crack deflection modes. Only a few of the images are presented here to support key observations; the full set of SEM images for all NASA load conditions is included in Appendix C. Fig. 5.4(a) shows the fracture surface for the N12R crack front, an MTS-controlled Mode I deflection of θ = -26° at ϕ = 23.5°,

centered approximately 0.5 mm from the pre-crack tip. Fig. 5.4(b) shows the MSS-controlled Mode II deflection ($\theta = 16°$ at $\phi = 44.0°$) of N09L centered approximately 0.25 mm from the pre-crack tip. The clear difference in fracture surface morphology between the two deflections reinforces the difference in dominant crack propagation mechanism between the two deflection criteria. The Mode I (tensile) crack deflection in Fig. 5.4(a) is similar in appearance to the "transgranular, faceted, crystallographic fracture mode" documented in Mode I Paris-regime FCGR of Inconel 718 at room temperature by Mercer *et al.* [66] in 1999. It is more sharply faceted in appearance than the somewhat flatter Mode II (shear) crack deflection in Fig. 5.4(b), which appears to be a slip-enhanced transgranular cleavage.

Because shear crack deflections under mixed-mode loading turn in an ostensibly crack-closing direction (i.e., such that the global Mode II load would result in a negative or compressive local Mode I displacement), flatter features can sometimes be attributed to crack face smearing due to contact. However, at higher magnification, the flat regions of the shear crack (N09L) displayed features including fatigue striations, as seen in Fig. 5.5, that indicate they were not the result of contact smearing. Fig. 5.5 also highlights a feature seen in many locations of Fig. 5.4(b) in which micro-cracks appear to be tunneling into the material at angles suggestive of MTS-controlled crack deflection. These micro-cracks coincide with the fatigue striations visible on the shear crack surface. Since the global condition of specimen N09 is very close to the transition value of mode mixity, it would appear that the crack path is almost equally disposed to deflect in the tensile direction at the micro-scale even as it propagates in the shear direction at the macro-scale.

The labeled feature in Fig. 5.5 was subject to EDS analysis to ensure that it was not the result of surface contamination (such as cutting fluids used in SEM sample sectioning), since it appeared to lay on top of the visible fatigue striations. However, as Fig. 5.6 shows, the composition of this feature is essentially that of the base alloy.

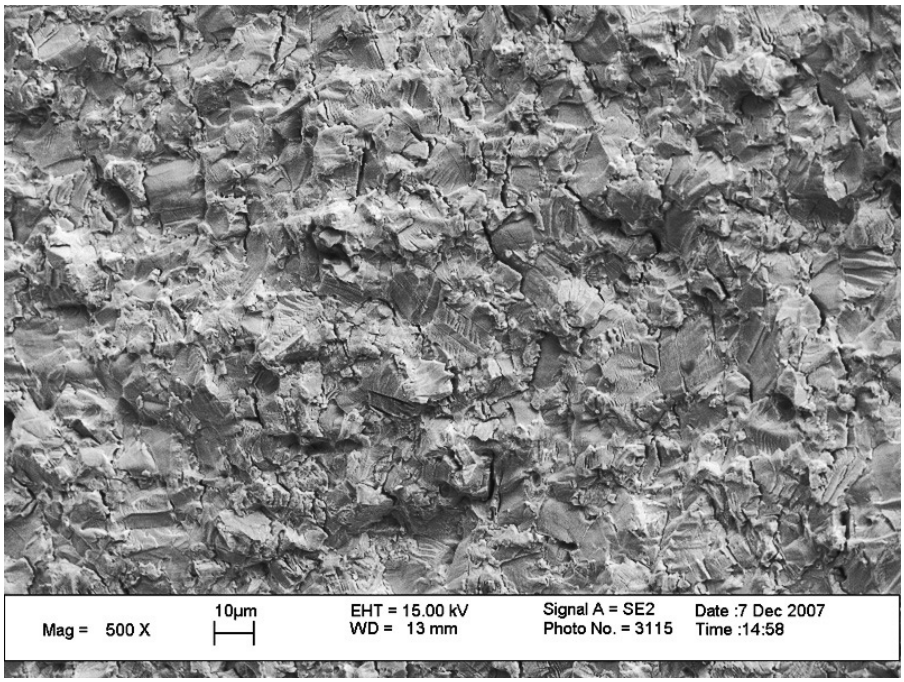

(a)

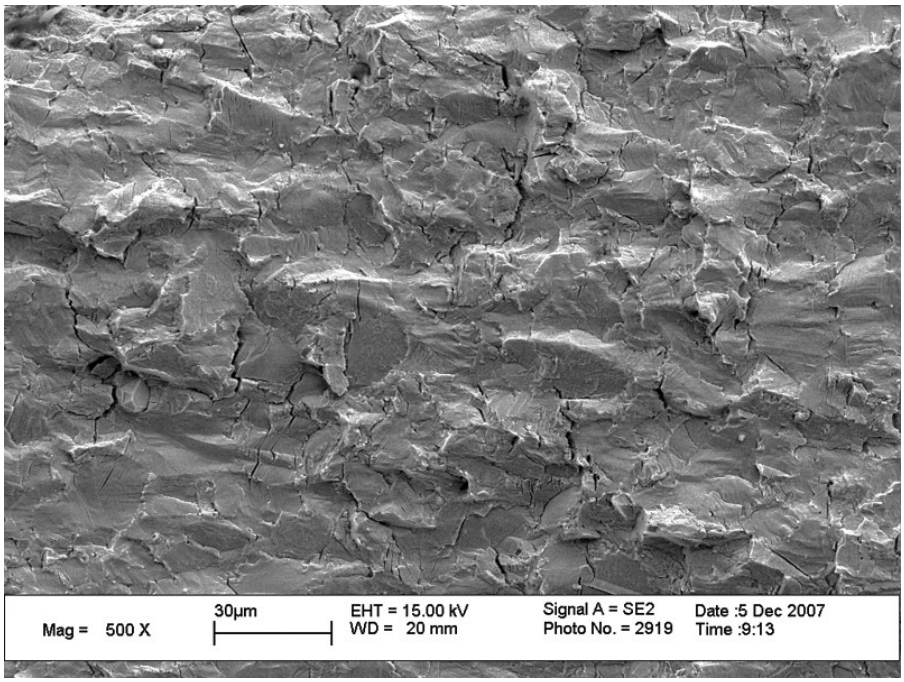

(b)

Figure 5.4: Scanning electron micrographs of two crack branches reveal different fracture surface morphologies: (a) MTS-controlled Mode I crack deflection of N12R (θ = -26° at ϕ = 23.5°) shows a more sharply faceted crystallographic transgranular cracking appearance, and (b) MSS-controlled Mode II crack deflection of N09L (θ = 16° at ϕ = 44.0°) shows a relatively flatter slip-enhanced transgranular cleavage appearance.

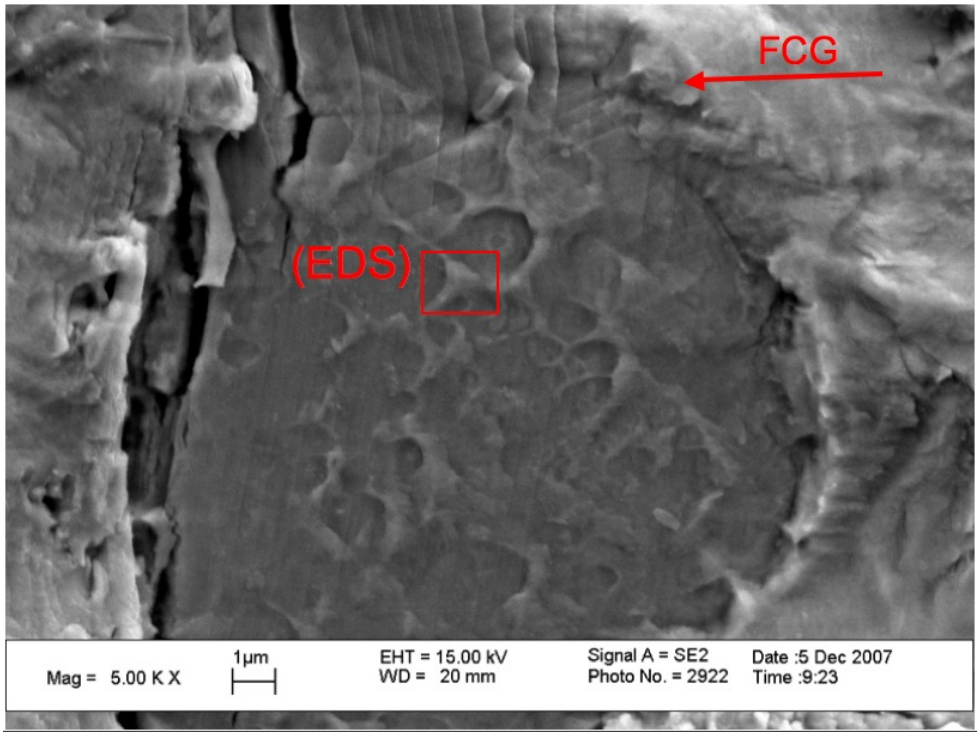

Figure 5.5: Scanning electron micrograph of MSS-controlled Mode II crack deflection of N09L showing fine microstructural features that counter-indicate crack face contact-induced smearing. The label "(EDS)" indicates the region subjected to subsequent EDS analysis for element identification and "FCG" indicates crack growth direction.

Although there was no evidence of gross crack face contact or smearing for shear-deflected cracks, the shear deflection on N09R ($\theta = 18°$) did display a number of apparent wear particles adhering to the fracture surface, as shown in Fig. 5.7. The center of one of the large particles labeled in Fig. 5.7(b) was examined by EDS, and the results shown in Fig. 5.8 confirm the anticipated result that these are oxide particles of the base alloy. Such wear-induced oxide particles are consistent with crack face rubbing, which would be expected for crack deflections in the crack-closing direction followed by shear crack branches, even though there was no gross wear deformation or smearing observed.

Since tensile crack deflections turn toward the crack-opening direction, there is

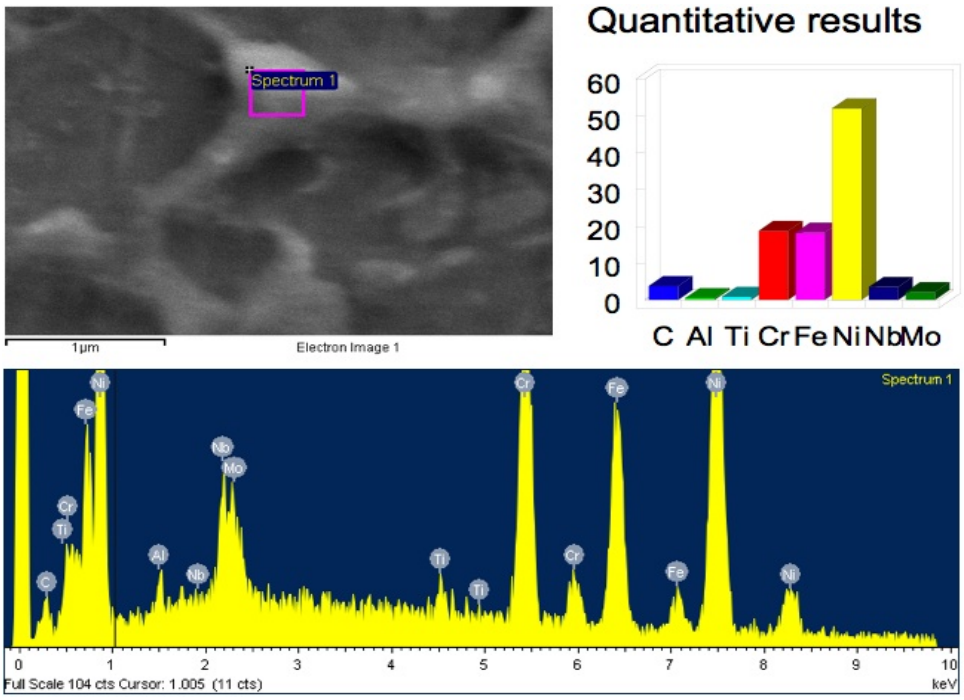

Figure 5.6: Results of EDS analysis of the fracture surface feature highlighted in Fig. 5.5.

less expectation of the formation of wear particles than for shear cracks. However, similar particles were observed to be distributed over the tensile deflections of N09, much more extensively on the left crack, as shown in Fig. 5.9, front but also in isolated clusters on the right. As with the particles found on the shear-oriented crack deflection, EDS analysis shown in Fig. 5.10 indicates these particles are oxides of the base material. Such a significant distribution of wear particles was not evident on the tensile cracking of specimen N12 that was studied under SEM.

5.1.1.3 Summary of In-Phase Results

Increasing the in-phase mode-mixity phase angle ϕ over six specimens resulted in increasingly negative crack deflections that closely followed the standard MTS criterion as expected. At approximately $\phi = 44°$ shear-controlled crack deflections were produced at angles which conformed with the MSS criterion. In one case there was partial crack branching in both directions divided by a transition at the specimen

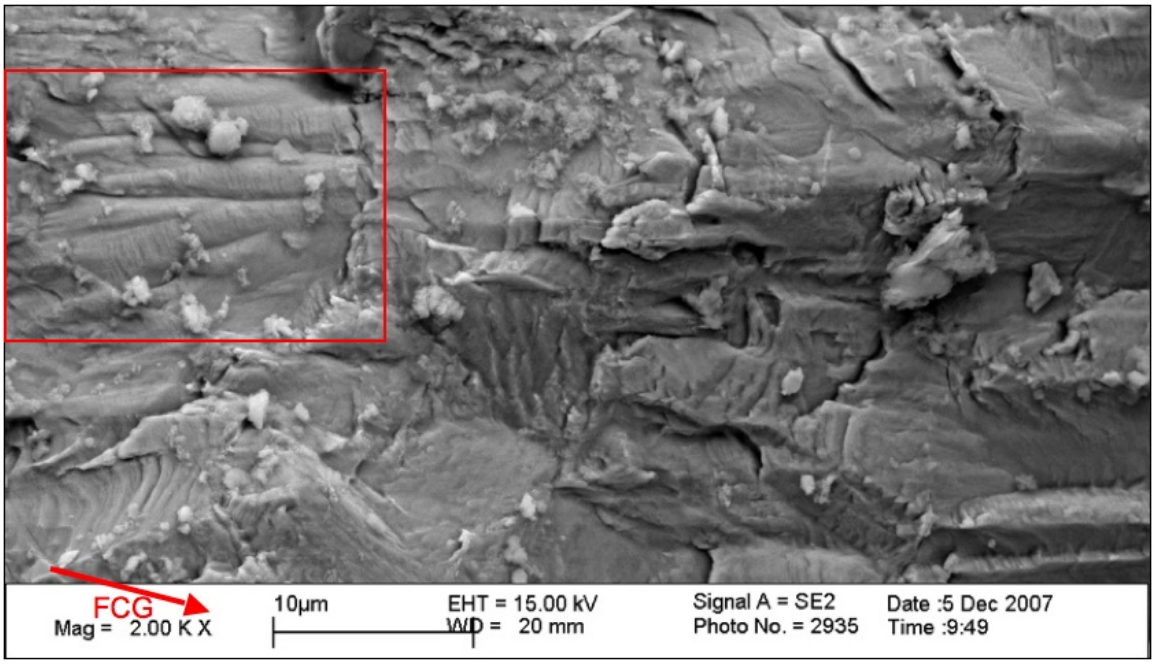

(a)

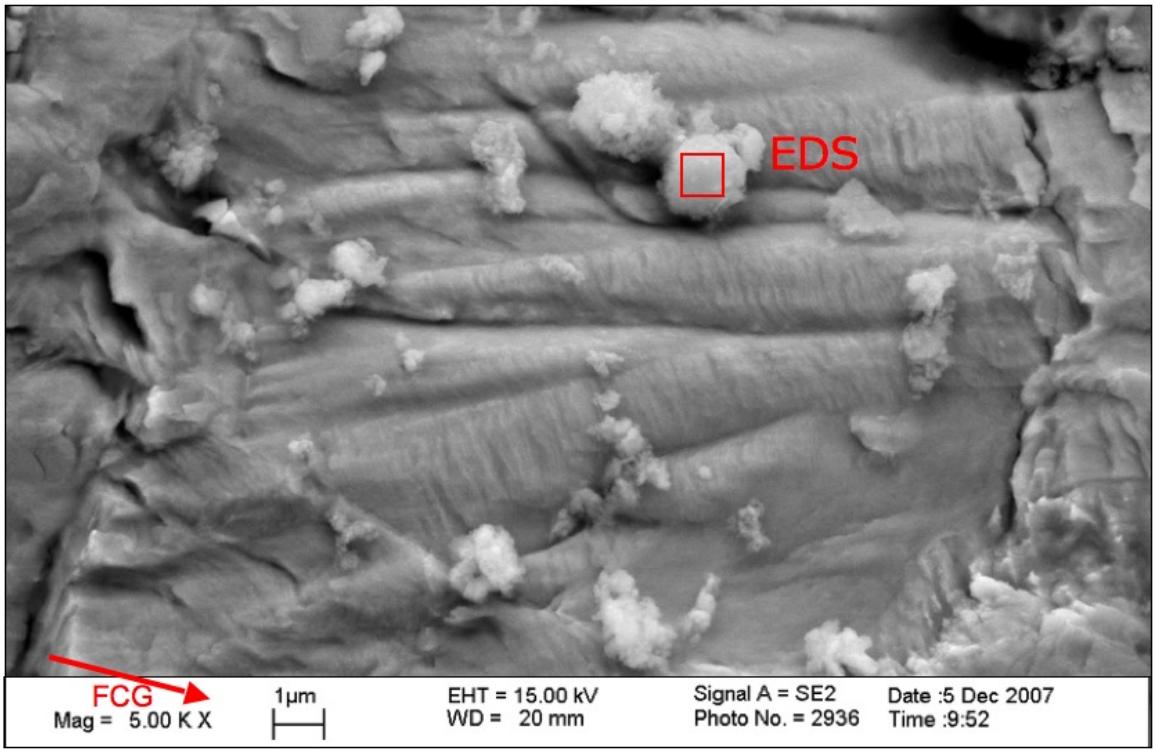

(b)

Figure 5.7: (a) Scanning electron micrograph of wear-induced oxide particles on shear deflection of N09R, and (b) close-up of highlighted region in (a) showing larger particle subject to EDS analysis, as labeled.

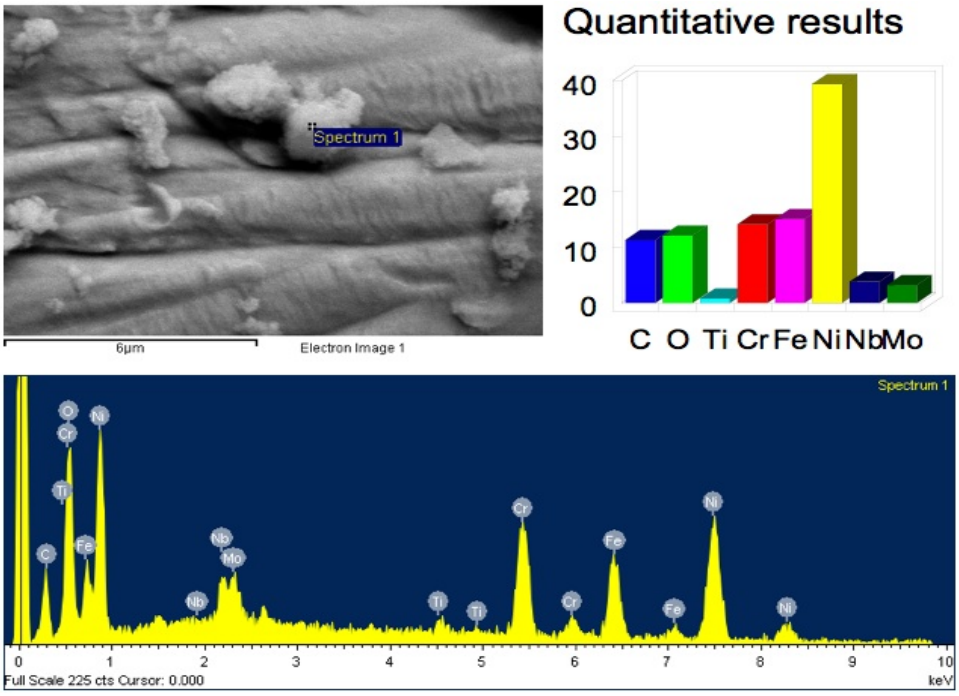

Figure 5.8: Results of EDS analysis of particle highlighted in Fig. 5.7(b).

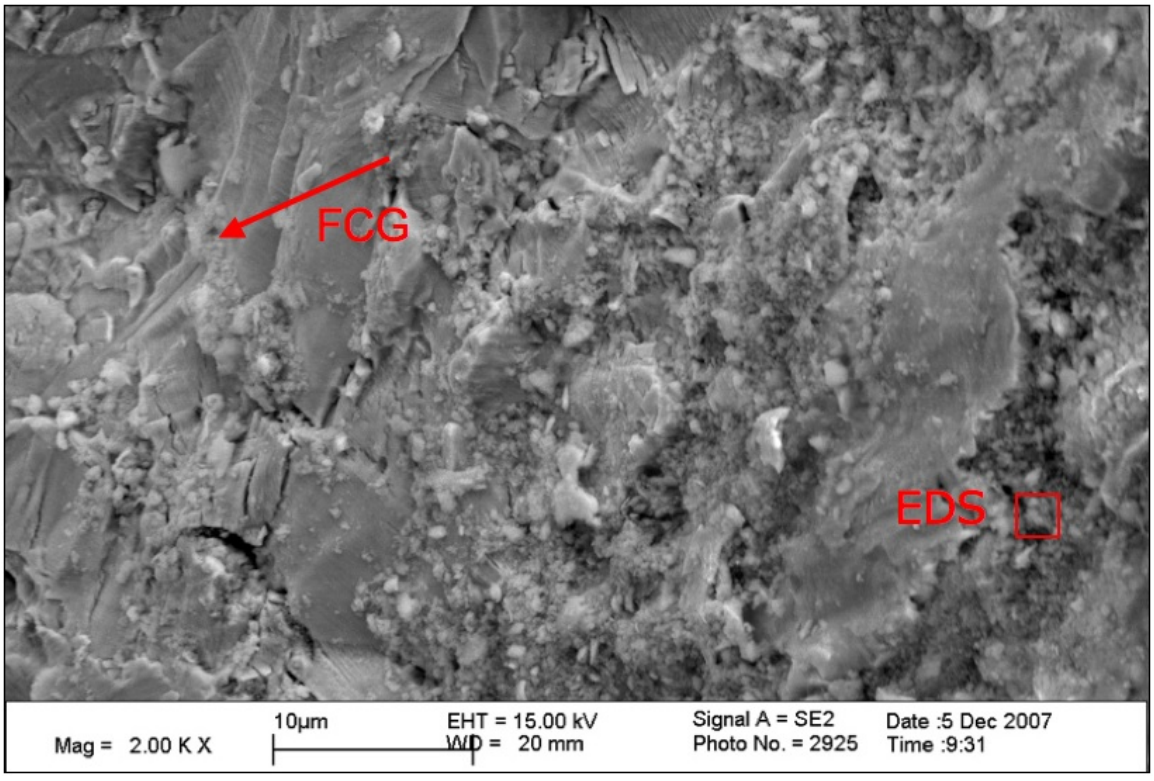

Figure 5.9: Scanning electron micrograph of wear-induced oxide particles on tensile deflection of N09L; label indicates location of EDS analysis of particles.

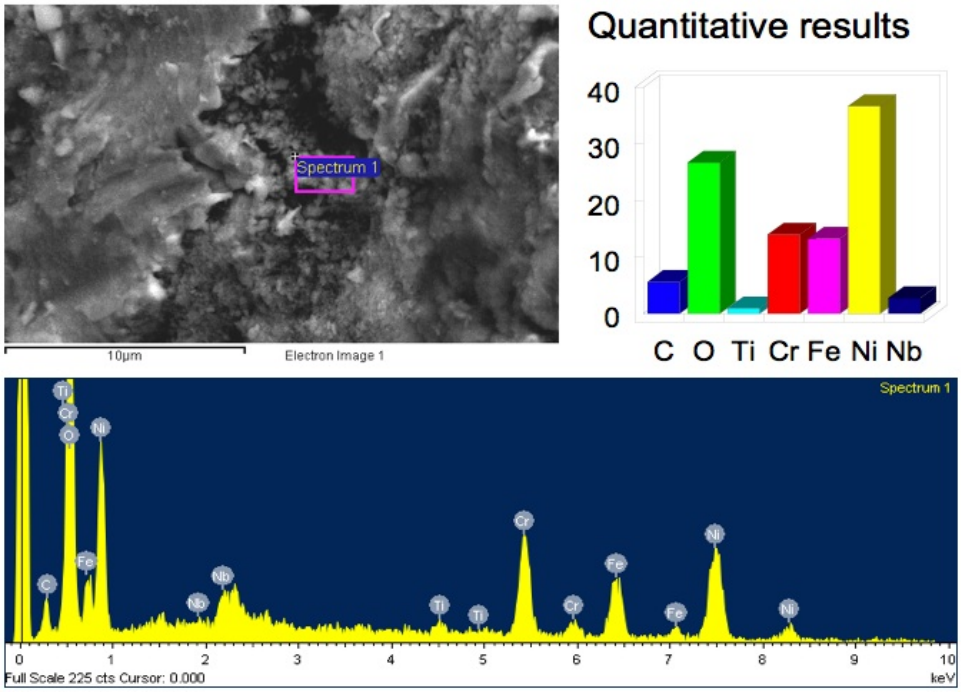

Figure 5.10: Results of EDS analysis of particles highlighted in Fig. 5.9.

wall mid-thickness. Detailed analysis of the SIF and mode mixity distribution along this curved pre-crack showed that the MSS-controlled deflection occurred from the section of pre-crack with the highest mode mixity $\phi = 45°$, and MTS-controlled deflection occurred over the remaining portion of the crack front over which ϕ dropped toward $\phi = 42°$. Examination of selected fracture surfaces under SEM showed distinct fracture surface morphologies between the two types of crack deflection, with tensile cracks displaying a more faceted and granular appearance than shear cracks, which displayed larger regions of relatively flat propagation covered occasionally by very fine microstructural features. Wear-induced oxide particles were present on both the shear and tensile crack deflections of specimen N09 which was tested at the transition value of ϕ, but there was no clear evidence of such particles on the tensile crack surface of specimen N12, tested at a much lower mixity of $\phi = 23.5°$.

5.1.2 Constant Tension/Cyclic Torsion

Five NASA specimens were tested under constant tension/cyclic torsion loading in order to promote shear stress-controlled crack growth. Crack growth behavior falls into two distinct groups of deflection angles, although the variables of non-proportional loading highlight the shortcomings of the single monotonic mixity parameter ϕ in clearly presenting such data. Examination of fracture surfaces under SEM reinforce the difference in crack growth mechanism between the two types of deflection as already observed.

5.1.2.1 Crack Deflection Angles

Constant tension/cyclic torsion crack deflection angles are presented in Table 5.2 with their corresponding mode mixity maxima and minima. As with the in-phase test data, each front is presented individually, and crack fronts that bifurcated to different angles (specimen N13) have two angles for each crack front. An initial

Table 5.2: Crack deflection angles and mode mixity values for left (L) and right (R) crack fronts under constant tension/cyclic torsion testing of NASA thin-walled tubular specimens.

Crack front	K_{I} (MPa$\sqrt{m}$)	K_{IImax} (MPa$\sqrt{m}$)	ΔK_{II} (MPa$\sqrt{m}$)	ϕ_{min}, ϕ_{max} (deg)	θ (deg)
N03L	19.5	12.7	5.1	21.3, 33.0	-54
N03R	19.4	11.7	4.7	19.9, 31.1	-55
N04L	19.5	12.8	25.6	-33.3, 33.3	-1
N04R	19.5	12.8	25.6	-33.3, 33.3	-1
N06L	22.5	11.5	11.3	0.6, 27.1	5
N06R	22.4	11.4	11.2	0.6, 27.1	4
N10L	11.5	11.5	10.4	5.7, 45.0	1
N10R	11.5	11.3	10.2	5.6, 44.5	1
N13L	17.7	7.8	7	2.5, 23.9	-52, 10
N13R	17.7	7.9	7.1	2.5, 23.9	-41, 1

graphic presentation of the data is shown in Fig. 5.11, using the same crack angle

versus mode mixity ϕ as the in-phase data.[8] The conventional MTS and MSS criteria

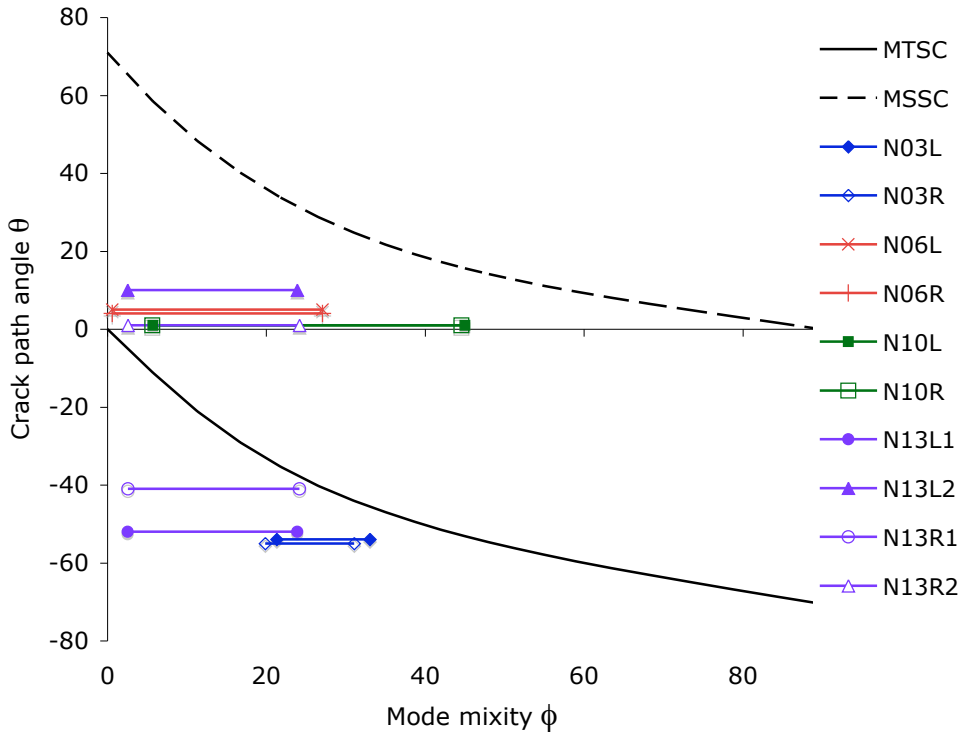

Figure 5.11: Crack deflection angles versus range of mode mixity ϕ for constant tension/cyclic torsion tests of NASA thin-walled tubular specimens. (Specimen N04 not plotted; see footnote 8.)

are also plotted based solely on the mode mixity ϕ, and for this type of loading the maximum load K_{II} (and possibly most damaging state) results in the higher value of ϕ (right side of each bar).

The inability to assess clearly the data from non-proportional loadings with the standard formulation of MTSC, MSSC and ϕ is apparent in Fig. 5.11. While it is at least clear that there are two distinct groups of crack direction – ostensibly in the tensile- and shear-dominated directions – the lack of clarity in the driving factor can be seen by the overlap of ranges of mode mixity. The tensile deflections of specimens

[8]Data points for specimen N04, which was tested at R_{II} = -1, are not shown in this graph. This is both for visual clarity and, as discussed in Section 2.2.2, the lack of insight likely to be gained by a fully-reversed torsional loading. As expected, crack growth occurred co-planar to the pre-crack.

N03 and N13 could arguably be said to follow the MTSC based on their maximum load conditions. However, this is much less plausible for the upper group of likely shear cracks. Additionally, the maximum ϕ values being notably higher than those of N06 and the tensile N13 branches would seem to thwart identifying a single transition value of ϕ.

If a kinked crack is driven primarily by either Δk_1 or Δk_2 at the tip of the kink (and thus turns toward tensile or shear deflection, respectively), the maximum of each SIF range alone cannot provide any insight. Using the first-order approximation of Cotterell and Rice [16] for kink tip SIFs[9],

$$k_1 = \sqrt{2\pi r}\ \sigma_{\theta\theta} = \cos\frac{\theta}{2}\left(K_{\mathrm{I}}\cos^2\frac{\theta}{2} - \frac{3}{2}K_{\mathrm{II}}\sin\theta\right) \tag{5.1}$$

$$k_2 = \sqrt{2\pi r}\ \tau_{\mathrm{r}\theta} = \frac{1}{2}\cos\frac{\theta}{2}\Big[K_{\mathrm{I}}\sin\theta + K_{\mathrm{II}}(3\cos\theta - 1)\Big] \tag{5.2}$$

it can easily be shown that Δk_1 and Δk_2 in this load case are functions of ΔK_{II} only, and thus are maximized for a single value of θ each. Under constant K_{I}/cyclic K_{II},, $\Delta k_{1\max}$ occurs at an angle $\theta^* = 70.5°$, and $\Delta k_{2\max}$ occurs at $\theta^{**} = 0°$.

Taking these two constant angles into account along with the loose correlation in Fig. 5.11 between the maximum load condition and the MTS and MSS criteria based on maximum loads, there appears to be a joint effect of Δk and $k_{\max}$. This is reinforced by examining the distributions of potential kink SIFs (essentially the distribution of tensile and shear stresses and ranges) ahead of each crack tip, as in Fig. 5.12. In these plots, $k_{1\mathrm{a}}$ or $k_{2\mathrm{a}}$ are the kink SIF at maximum torsion, and $k_{1\mathrm{b}}$ and $k_{2\mathrm{b}}$ are at minimum torsion. The observed crack angles generally fall between Δk and $k_{\max}$ for their respective modes, suggesting an effective crack driving force that accounts for both.

[9] A different trigonometric form of Eqs. 5.1-5.2 is often published, but this formulation is presented here to clarify the relationship to Eqs. 2.2 and 2.3. In other works, k_1 and k_2 are often denoted K_σ and K_τ, respectively, to emphasize their direct derivation from the singular stress field of the original unkinked crack, as in Eqs. 2.26-2.27.

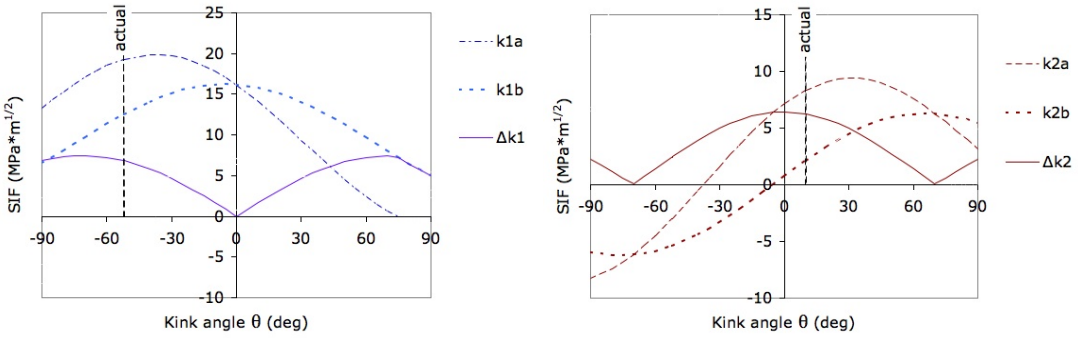

(a) N13L1 tensile branch

(b) N13L2 shear branch

Figure 5.12: Distributions of kink tip SIFs for (a) tensile crack deflection and (b) shear crack deflection, specimen N13.

Based on previous studies discussed in Chapter 2, a $(da/dN)_{\max}$ approach would appear to be most effective provided the crack growth law included a K_{max} or R-ratio effect. All of the ΔK_{eff} definitions by Tanaka in Eqs. 2.20 - 2.22 are based solely on SIF ranges and thus are not suitable, predicting crack co-planar crack growth for all of these tests. The crack growth law for Inconel 718 provided by Soboyejo in Eq. 3.1 was therefore used in an attempt to predict the tensile crack deflections for this load case. This approach, however, would not be applicable to the shear crack deflections as it is based on pure Mode I crack growth testing. Furthermore, it greatly over-predicted the magnitude of θ^* for all of the tensile crack deflections (θ^* = -69.8° for N03 and θ^* = -68.2° for N13), apparently placing too much emphasis on Δk_1 and not enough on $k_{1\max}$.

An alternate crack growth driving force along the lines of the ΔK_{eff} used in Walker's equation [70] was employed based on initial attempts to quantify the relative influences of K_{max} and ΔK. A first attempt at merging the two quantities was a simple geometric average, $\Delta K^{0.5} K_{\max}^{0.5}$, which did reasonably well for all of the observed deflections. This is essentially the same form of crack driving force employed in Walker's equation as discussed by Highsmith and Johnson [71], in which load ratios

can be collapsed into a single crack growth law of the form

$$\frac{da}{dN} = C_0 \overline{\Delta K}^m \tag{5.3}$$

$$\text{where} \qquad \overline{\Delta K} = \frac{\Delta K}{(1-R)^{1-w}} \tag{5.4}$$

and w is the Walker coefficient, a fitting parameter. Rewriting Eq. 5.4 in terms of K_{max}, it is simply

$$\overline{\Delta K} = \Delta K^w K_{\max}^{1-w} \tag{5.5}$$

and the first approximation of this form attempted simply used $w = 0.5$. In Highsmith and Johnson's [71] application of this model to a directionally solidified nickel-base superalloy, different methods for quantifying material scatter resulted in a small range of Walker coefficients with a nominal value of $w = 0.3$. While there is little basis for assuming similar material behavior in this equiaxed, forged superalloy, use of this same exponent in the current data and maximizing kink tip $\overline{\Delta k}$ improved the prediction of crack deflection angle for the tensile branches. However, the shear crack branches adhered more closely to Δk_2 than to $k_{2\max}$, so reducing w from 0.5 to 0.3 detrimentally emphasized the wrong parameter. Arbitrarily reversing the exponents of the two terms, such that $w = 0.7$, improved predictions of shear crack growth at the cost of the tensile branch predictions.

The fully reversed loading of N04 stood out as a special to this approach. Any exponent w less than 1 (introducing a $k_{2\max}$ effect) resulted in a slight local minimum of Eq. 5.5 at $\theta = 0°$, with the locations of the surrounding maxima spreading out to $\theta = 11°$ for $w = 0.5$ and $\theta = 23°$ for the pure $k_{2\max}$ dependence of $w = 0$. However, as discussed before, the reversal-induced symmetry of this case could result in co-planar crack growth, even if equally influence by SIF range and maximum, simply as an aggregate of alternating directions of maximum damage.

The relative performance of these different Walker-based effective SIF ranges at the kink tip is shown in Fig. 5.13, in which predicted values of θ are plotted against

the observed values and the dashed diagonal line represents perfect prediction. The

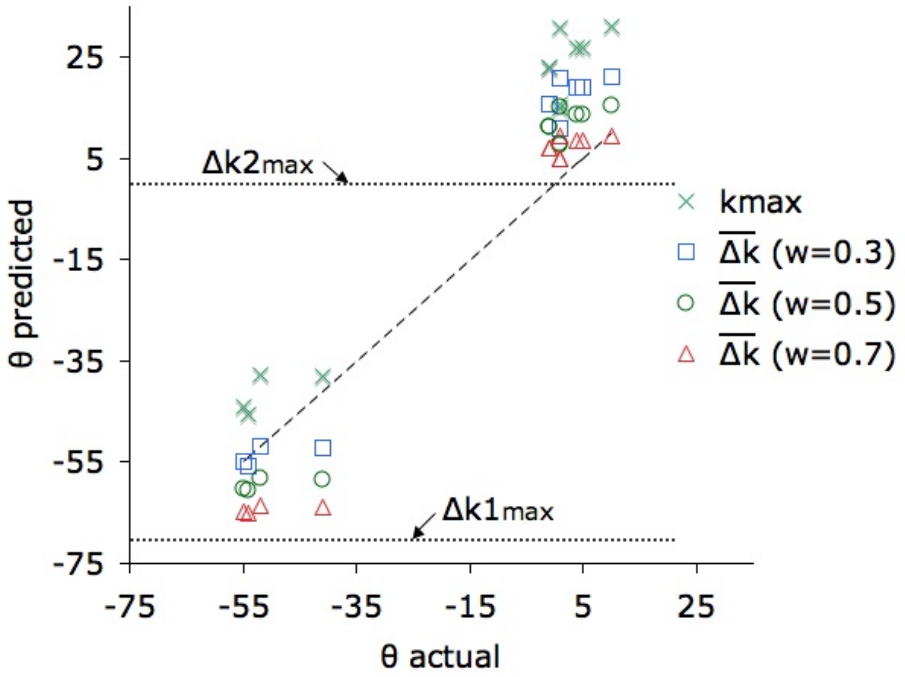

Figure 5.13: Relative performance of different forms of $\overline{\Delta k}$ in predicting crack deflection under constant tension/cyclic torsion loading for various Walker exponents w.

tensile and shear branch angles are predicted by $\overline{\Delta k}_1$ and $\overline{\Delta k}_2$, respectively. The horizontal lines for the constant angles predicted by Δk_1 and Δk_2 as well as the angles predicted solely by the appropriate $k_{\max}$ are plotted in order to provide a sense of the relative bounds of the two components of $\overline{\Delta k}$. At the lower end of the graph it can be seen how tensile crack branching is best predicted by $\overline{\Delta k}_1$ when $w = 0.3$, which was selected based on Mode I FCGR testing of a different superalloy. However at the upper end the use of $w = 0.7$ is clearly superior.

It might seem desirable at this point to choose a compromise value of $w = 0.5$ for the sake of consistency and modeling simplicity, rather than have the exponents in Eq. 5.5 arbitrarily swapped in order to fit two different sets of crack deflections. However, use of two discrete parameters for each mode is not without justification or precedent. This is similar in concept to the fracture transition approach employed by

Kfouri and Brown [24], in which the fracture toughness $\mathcal{G}$ described by Eq. 2.17 varies as a function of local mode mixity due to a lower material resistance to fracture under Mode II than Mode I loading. Kfouri and Brown's approach is not directly applicable here, however, as their crack path transition merely resulted in crack extension returning to co-planar and could not predict the positive shear deflections observed.

The current approach can be seen as the obverse to modeling a variable strength: instead the crack driving force is formulated differently for two types of crack growth process. The physical argument can also be made that tensile crack growth, which is generally promoted by hydrostatic stresses, would depend more strongly on $k_{1\max}$ and therefore be better predicted by a Walker exponent w less than 0.5 (resulting in a higher exponent for $k_{1\max}$), whereas the same cannot be said of $k_{2\max}$. Thus, while the particular values of $w = 0.3$ and 0.7 are quite arbitrary – necessitated by the lack of appropriate crack growth data and guided by related previous work – the general approach is not, justifiable from a physical as well as a modeling perspective. No attempt has been made to refine the exact values of w for each crack driving force based on the limited data as the number of, and scatter in, the data would not provide any more confidence that the presented values, which do quite well as shown.

A final validation of the dual exponent approach is its ability to delineate a fracture mode transition. The values of $\overline{\Delta k}_{2\max}$ versus $\overline{\Delta k}_{1\max}$ for each pre-crack front are presented in Fig. 5.14.[10] The diagonal lines represents a constant effective mode mixity below which tensile crack branching (solid data symbols) should be predicted and above which should be shear branching (hollow symbols). The solid line and square data symbols are for the dual exponent case $w_1 = 0.3$ and $w_2 = 0.7$; the dashed line and diamond symbols are for the single exponent $w = 0.5$. It is clearly possible to delineate a transition for the former case but not the latter. The line of

[10]The maximum possible values of each $\overline{\Delta k}$ from the pre-crack front, and not the actual $\overline{\Delta k}$ evaluated at the observed deflection angle, is employed in order to eliminate minor experimental error in measurement as well as slight deviations from the ideal path in the material.

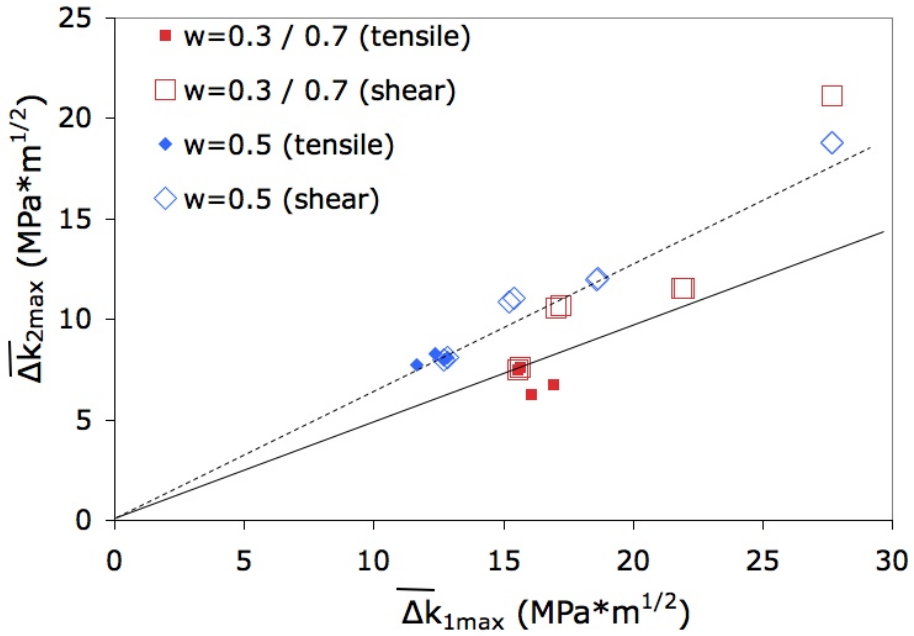

Figure 5.14: Transition from tensile to shear crack deflection under constant tension/cyclic torsion as a function of $\overline{\Delta k}_{2\max}$ versus $\overline{\Delta k}_{1\max}$ predicted by using separate values of w for different fracture modes.

transition passes through the overlapping points of tensile and shear crack branching of specimen N13, which experienced both types of crack growth through bifurcation, suggesting its load condition was nearly upon the point of transition. Using this approach, the values of $\overline{\Delta k}_1$ and $\overline{\Delta k}_2$ are calculated for a given loading condition, transition from tensile to shear is predicted at a material-specific value of $\overline{\Delta k}_2/\overline{\Delta k}_1$, and the direction of crack growth is predicted by the angle along which the relevant parameter is maximum.

5.1.2.2 SEM Fractography

Selected specimens were sectioned and examined by SEM in order to determine if the two distinct groupings of crack deflection angles displayed similar morphological differences as seen in the in-phase testing (and thus confirm the operation of different crack growth mechanisms). Fig. 5.15(a) shows the fracture surface for crack N13R, a tensile branch of θ = -41°, centered approximately 0.4 mm from the pre-crack

tip. Fig. 5.15(b) shows the shear deflection of crack front N10R, oriented at $\theta = 1°$, centered approximately 0.25 mm from the pre-crack tip. The two fracture surface morphologies in Fig. 5.15 show the same distinct features of the tensile and shear crack deflections of the in-phase testing shown in Fig. 5.4, confirming the two groupings of crack deflections as the product of different dominant fracture mechanisms. The tensile branch crack has the more sharply faceted crystallographic transgranular cracking appearance whereas the shear branch crack has the flatter slip-enhanced transgranular cleavage appearance. The transition from one mode to another is shown in Fig. 5.16, which shows the pre-crack and initial growth of the test condition crack. The Mode I pre-crack on the right side of the image displays the sharp angular facets of tensile crack growth which transitions to the smoother shear crack appearance on the left upon application of cyclic tension. At higher magnifications, the shear crack branches of specimens N10, shown in Fig. 5.17(a), and N13, shown in Fig. 5.17(b), displayed similar features to those seen on crack front N09L in Fig. 5.5. These and other features similarly indicated a lack of gross surface contact damage. The constant tension load maintaining a Mode I crack opening displacement also resulted in the notable absence of wear-induced oxide particles seen previously in Figs. 5.9 - 5.10.

5.1.2.3 Summary of Constant Tension/Cyclic Torsion Results

Testing several different combinations of constant tension (Mode I) and cyclic torsion (Mode II) resulted in two distinct clusters of crack deflection angles. The standard criteria of MTS or MSS evaluated based on the maximum loads or SIF ranges were not directly applicable to these results. Since crack deflection angles tended to fall between the angles of maximum kink tip SIF k_i and the maximum kink tip SIF range for the appropriate mode of loading, a crack driving force combining the influence of both was suggested. Defining a kink tip effective stress range $\overline{\Delta k}$ for each

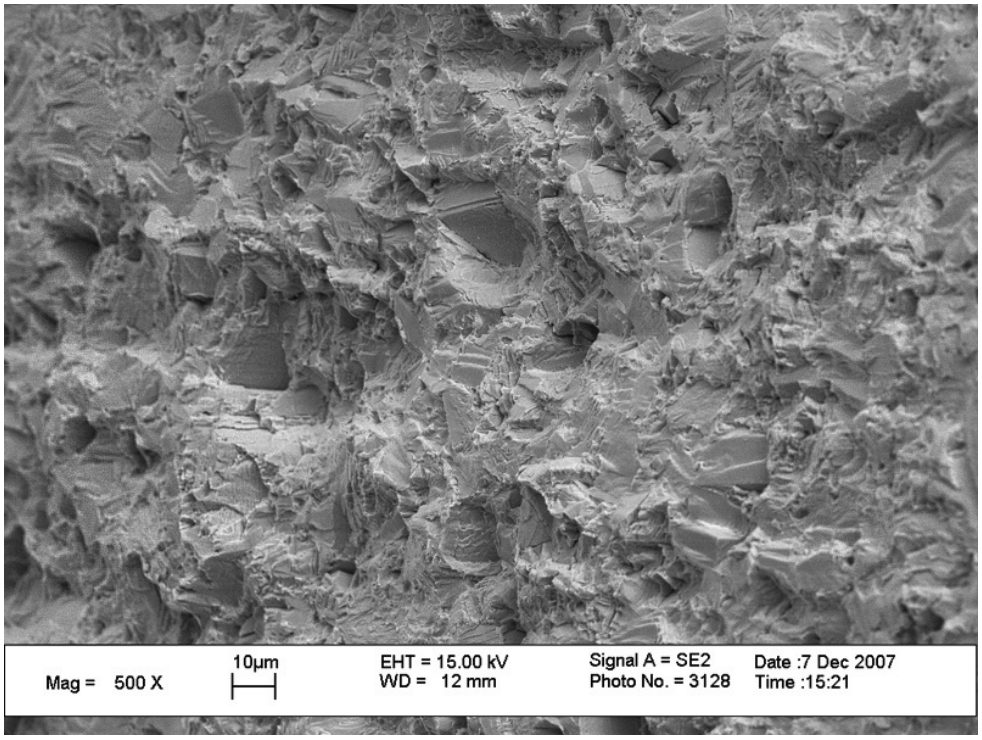

(a)

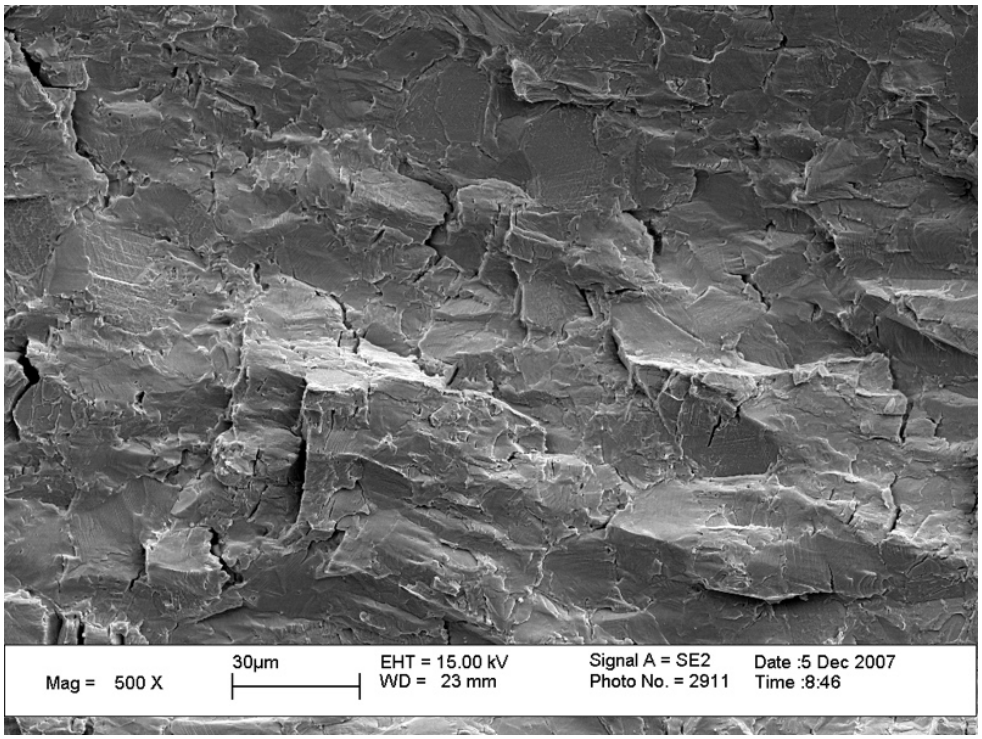

(b)

Figure 5.15: Scanning electron micrographs of (a) tensile Mode I crack branch of N13R (θ = -41°) and (b) shear Mode II crack branch of N10R (θ = 1°) revealing differences in fracture surface morphology as seen for in-phase testing.

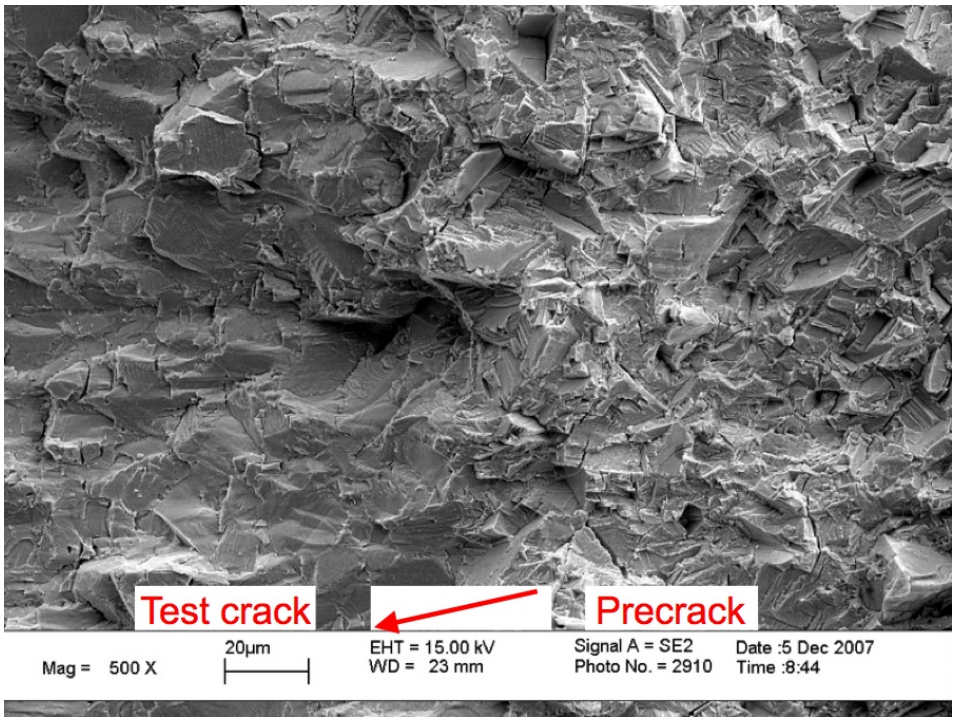

Figure 5.16: Scanning electron micrograph of pre-crack front of N10R, showing transition from tensile crack growth of Mode I pre-crack (right) to shear crack growth of Mode II branch (left) in constant tension/cyclic torsion condition.

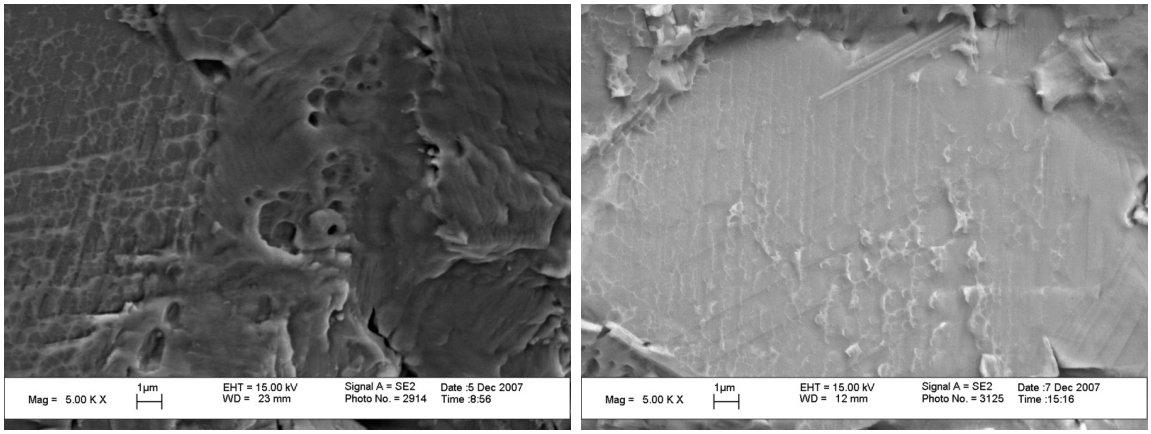

(a) (b)

Figure 5.17: Scanning electron micrographs of shear cracks from (a) N10R and (b) N13R, displaying the same appearance as the shear deflection of N09L in Fig. 5.5.

mode based on Walker's equation for crack growth at different load ratios provided a good predictor of crack path direction and modal transition when a different Walker exponent w is defined for each mode. The use of different exponents can be justified on the basis of the different mechanisms of crack growth between the two groups of deflections.

5.1.3 Constant Torsion/Cyclic Tension

Three NASA specimens were tested under constant torsion/cyclic tension loading in order to determine if any level of static K_{II} could promote shear deflection in a crack subjected to solely Mode I fatigue, and what effect the static shear stress had on the path of tensile crack growth. Only one group of crack deflection angles was observed in a slightly negative (tensile) direction, suggesting the influence of the constant K_{II}-induced $k_{1\mathrm{max}}$. SEM images of one fracture surface are similar to previously observed tensile crack deflections.

5.1.3.1 Crack Deflection Angles

Constant torsion/cyclic tension crack deflection angles are presented in Table 5.3 for each crack front with their corresponding mode mixity maxima and minima. No crack front bifurcations were observed in this set of testing. As for the constant tension/cyclic torsion data, an initial graphic presentation of the data in the conventional form for monotonic MTS and MSS evaluation is shown in Fig. 5.18. For this type of loading, the maximum load condition results in the lower value of ϕ (left side of each bar). Once again, this type of presentation provides scant insight to the controlling parameter, other than to suggest the dominant influence of tension.

Comparing pairs of specimens does however suggest the same Δk_1–$k_{1\mathrm{max}}$ interaction discussed in Section 5.1.2.1. For this type of loading, $\Delta k_{1\mathrm{max}}$ will always occur at $\theta = 0°$. Similarly the static K_{II} loading imposes a constant k_1 along θ = -70.5°

Table 5.3: Crack deflection angles and mode mixity values for left (L) and right (R) crack fronts under constant torsion/cyclic tension testing of NASA thin-walled tubular specimens.

Crack front	ΔK_{I} (MPa$\sqrt{m}$)	K_{Imax} (MPa$\sqrt{m}$)	K_{II} (MPa$\sqrt{m}$)	ϕ_{min}*, ϕ_{max} (deg)	θ (deg)
N05L	9.5	23.6	12.0	27.0, 40.4	-18
N05R	9.5	23.6	11.6	26.2, 39.4	-14
N07L	15.3	17.0	17.0	45.0, 84.3	-14
N07R	15.3	17.0	17.0	45.0, 84.3	-17
N11L	16.0	17.8	7.7	23.2, 76.9	-10
N11R	16.0	17.8	7.7	23.2, 76.9	-11

*Maximum load condition.

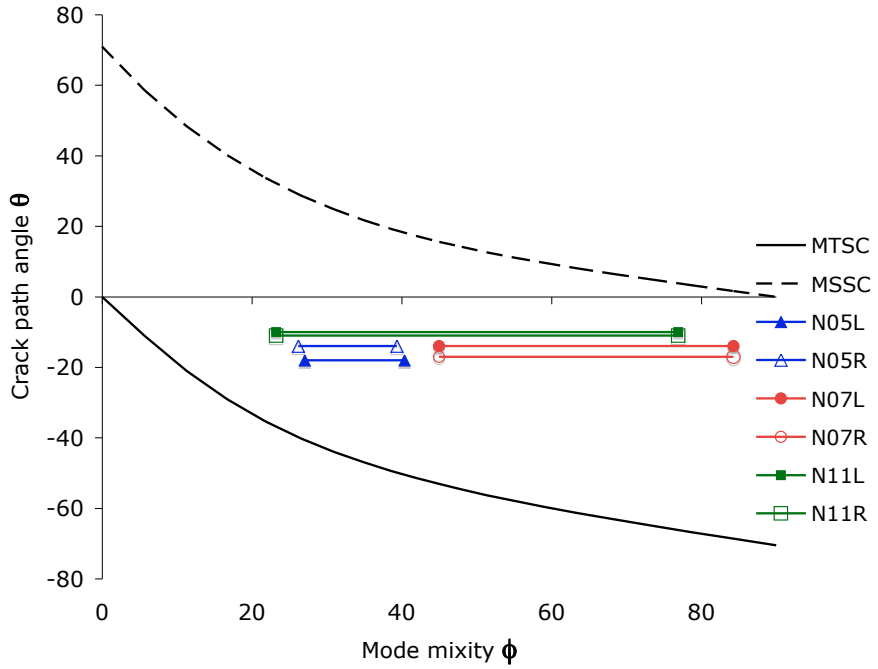

Figure 5.18: Crack deflection angles versus range of mode mixity ϕ for constant torsion/cyclic tension tests of NASA thin-walled tubular specimens.

(although the location of $k_{1\max}$ will vary under the combined influence of K_{I} and K_{II}). Specimens N05 and N11 have similar maximum loading conditions ($\phi = 26.2°$-$27°$ and $23.2°$ respectively) and both have non-zero branch angles, but N11 deflects closer to co-planar under the influence of a greater ΔK_{I} relative to K_{II}. And while N07 undergoes a much larger relative ΔK_{I} loading than N05, they follow similar deflection angles because of the higher K_{II} in N07 creating a stronger attraction to the constant k_1 at $\theta =$ -70.5°. An example of the kink tip SIF distributions is shown in Fig. 5.19.

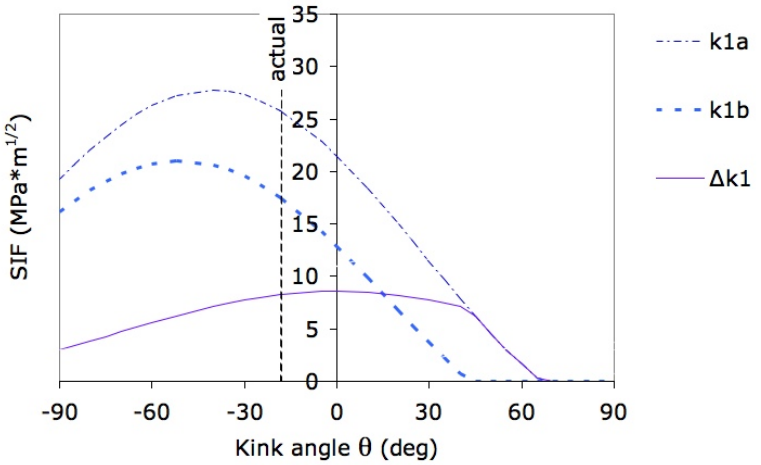

Figure 5.19: Distributions of kink tip SIFs for tensile crack deflection, specimen N05.

Applying the same $\overline{\Delta k}$ method described in Section 5.1.2.1 to these data, however, leads to conflicting results between the two load cases. Fig. 5.20 shows the predictive performance of $\overline{\Delta k_1}$ (as these are all tensile deflections) for the three values of Walker exponent employed previously ($w = 0.3$, 0.5 and 0.7). In this case, a Mode I branch Walker exponent $w_1 = 0.7$ is the best predictor among the three values, indicating a primary influence of Δk_1 on the branch crack, whereas for the constant tension/cyclic torsion case the best fit was $w_1 = 0.3$ and $w_2 = 0.7$. This was defended from a physical standpoint on the basis of the maximum stress promoting tensile crack growth in the previous case, but that physical influence appears diminished in this case. Since there were no crack deflections in the shear direction, the utility of this version of $\overline{\Delta k}$ in

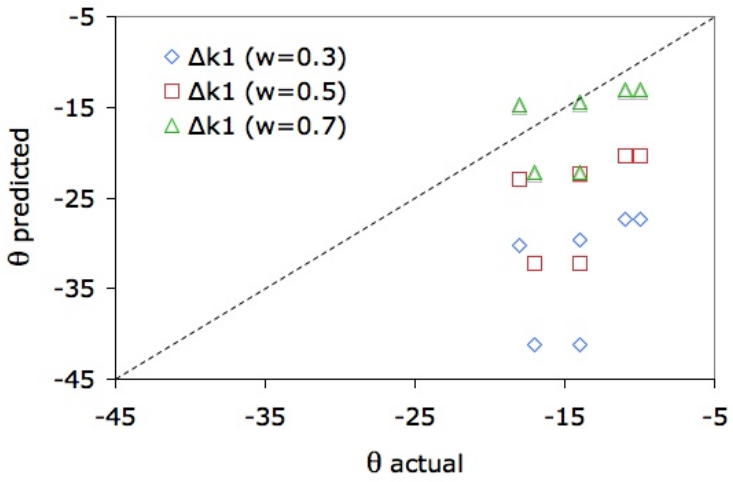

Figure 5.20: Relative performance of $\overline{\Delta k}$ in predicting crack deflection for various Walker exponents w.

predicting modal transition (as shown for the previous case in Fig. 5.14) cannot be used as a validation.

An initial assumption could be that this is experimental error brought about by unmeasured crack closure. Previous studies have shown the exacerbating effect of mixed-mode loading on closure, as the relative Mode II displacement of fracture surface asperities can enhance crack face contact. However this is unlikely as it would supposedly predict the opposite result: the resulting decrease in ΔK_{I} would in turn reduce the major Δk_1 loading along the pre-crack plane, and thus there would be an apparent increase in the influence of $k_{1\max}$.

If this load case is to require a different fitting exponent for improved fidelity, then a new justification is needed if crack path prediction for general non-proportional loading is to be anything other than arbitrary empirical fits for each kind of loading. As discussed previously, the approach of using different formulations of $\overline{\Delta k}$ for different modes of deflection was an alternative to the approach of Kfouri *et al.* which assumed the resistance to crack propagation to be a function of the stress state imposed on the crack. If we follow a similar line of thought for the current model, the data suggest that the relative influence of Δk and $k_{\max}$ on the deflection-driving $\overline{\Delta k}$ for each

mode is somehow a function of the global stress state. That is, for the case of global $K_{\mathrm{Is}}/\Delta K_{\mathrm{II}}$ loading, the influence of Δk is dominant for $\overline{\Delta k}_2$ (thus requiring $w_2 > 0.5$ so the exponent for Δk_2 is larger), and $k_{\max}$ is dominant for $\overline{\Delta k}_2$ (requiring $w_1 < 0.5$ so the exponent for $k_{1\max}$ is larger).

Accounting for the influence of the global stress state is not unprecedented. As discussed in Section 2.2.1, Yokobori *et al.* [34] observed on tests of this same specimen configuration that tensile cracks branched in the direction perpendicular to the global maximum principal stress in the gage section, which resulted in a shallower deflection angle than predicted by the MTS criterion based on singular crack tip stresses. If this is the necessary justification for the different formulations of effective crack driving force, it would indicate that relying solely on the singular crack-tip stress terms for crack path prediction is insufficient. The role of the non-singular stress terms, increasingly cited as influential for monotonic fracture under high loads for which the damage process zone may extend beyond the singularity-dominated crack tip zone, was dismissed as a factor in fatigue crack path determination due to the lower stresses and smaller process zone involved. This assumption would be unwarranted if the correlating parameter for crack path is in fact influenced by the global stress state.

To conclude this argument, we should examine the application of this approach to the proportional in-phase data, which were quickly explained by the standard monotonic MTSC/MSSC formulation based on maximum stresses. Regardless of the exponents selected, $\overline{\Delta k}_1$ and $\overline{\Delta k}_2$ predict the same angles as MTSC and MSSC for tensile and shear deflections in the case of proportional loading. It then falls to the ability to delineate modal transition to serve as evidence of appropriateness for this particular parameter. Fig. 5.21 shows the same kind of plot for in-phase loading as Fig. 5.14, in which open symbols are shear crack deflections and solid symbols are tensile. These are plotted as $\overline{\Delta k}_{2\max}$ versus $\overline{\Delta k}_{1\max}$ in order to see if there is a discrete

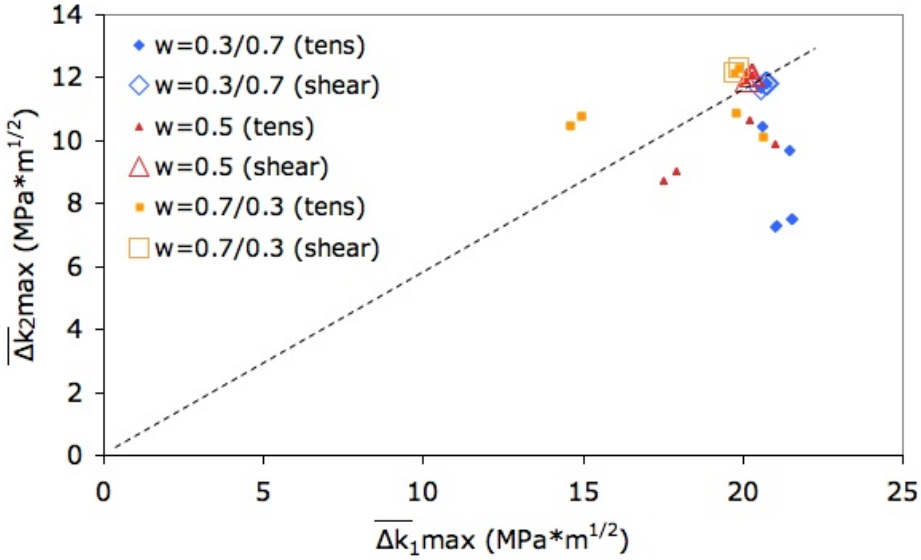

Figure 5.21: Transition from tensile to shear crack deflection under proportional loading as a function of $\overline{\Delta k}_{2\max}$ versus $\overline{\Delta k}_{1\max}$ predicted by using separate values of w for different fracture modes.

separation between the two kinds of crack branch. This separation is possible for two of the three cases discussed so far, shown by the dashed line between two possible transition points: $w_1 = 0.3$ and $w_2 = 0.7$; and $w_1 = w_2 = 0.5$. For the third case of $w_1 = 0.7$, $w_2 = 0.3$, there are tensile crack branches that fall both above and below the transition value of $\overline{\Delta k}_2/\overline{\Delta k}_1$, so it is not an appropriate predictor of crack behavior. If additional data were generated that supported the choice of $w = 0.5$ for proportional loading, this would be consistent with the hypothesis that the form of the crack branch driving for $\overline{\Delta k}$ is influenced by the global stress state.

5.1.3.2 SEM Fractography

As all of the crack deflections for this case fell into a small group of angles, only one specimen was observed under the assumption a single crack growth mechanism was operating. Specimen N07 was tested at the highest constant torque and the left crack deflected to θ = -14°. Fig. 5.22 shows the fracture surface of N07L, centered approximately 0.7 mm from the pre-crack tip. The fracture surface morphology has

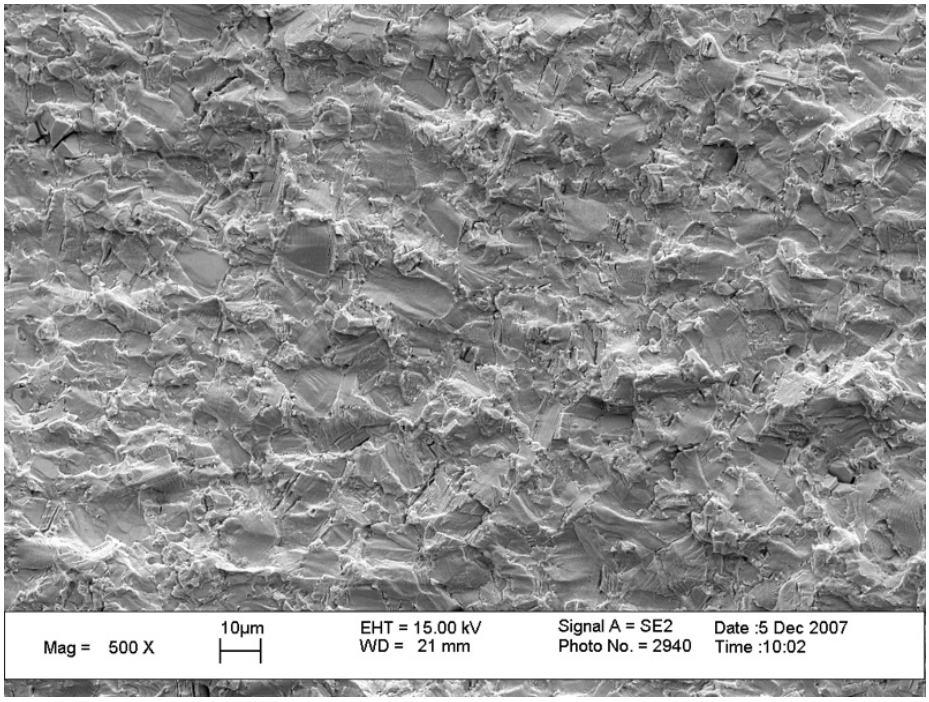

Figure 5.22: Scanning electron micrograph of N07L displaying similar faceted crystallographic transgranular cracking morphology as seen in MTS-controlled Mode I deflection of in-phase-tested N12R (Fig. 5.4(a)).

the same sharply faceted crystallographic transgranular cracking appearance of the in-phase MTS-controlled Mode I branch of N12R shown in Fig. 5.4(a). Similarities at higher magnifications can be seen among the three in Appendix C. If there is a damage mechanism basis for the modeling challenges discussed above (in terms of exponent selection), it is not readily apparent in the fractography.

5.1.3.3 Summary of Constant Torsion/Cyclic Tension Results

Three specimens tested at this condition resulted in a narrow range of crack deflection angles in a shallow tensile direction. SEM fractography reinforces a Mode I dominant crack growth mechanism for the observed deflections. Applying the same Walker effective SIF range model to the data again showed the interaction of Δk_1 and $k_{1\max}$ in predicting the crack deflection angle. However, the relative influences of the two parameters was the opposite of what was expected for tensile cracking from

a physical perspective; Δk_1 was the primary driver of crack angle, whereas $k_{1\max}$ had a primary influence for tensile crack branches in the previous non-proportional case. An alternative justification for the particular fitting of an effective SIF range suggests that the role of non-singular stresses may not be negligible for fatigue loading conditions.

5.1.4 180° Out-of-Phase Loading

Three NASA specimens were tested in 180° out-of-phase (OP) loading, alternating from almost pure K_{I} to almost pure K_{II} loads ($R = 0.1$ for each mode). The resulting crack paths covered a range of angles, from -74° for the highest K_{II} loading to 18° for the lowest K_{II}, rather counterintuitively. The highest K_{II} specimen (N18) experienced very different crack growth angles at either crack front, with the second deflection occurring along 6°. SEM images of two specimens showed the expected surface features for tensile cracking on the -74° branch, but the appearance of the 18° deflection was difficult to characterize, possibly due to contact damage.

5.1.4.1 Crack Deflection Angles

Deflection angles for 180° OP testing are presented in Table 5.4. In addition to

Table 5.4: Crack deflection angles and mode mixity values for left (L) and right (R) crack fronts under constant torsion/cyclic tension testing of NASA thin-walled tubular specimens.

Crack front	K_{Imax} (MPa$\sqrt{m}$)	K_{IImax} (MPa$\sqrt{m}$)	ϕ_{I}, ϕ_{II} (deg)	$\phi_{\mathrm{II/I}}$ (deg)	θ (deg)
N17L	15.5	9.9	3.7, 81.1	32.5	-31
N17R	15.5	9.9	3.7, 81.1	32.5	-45
N18L	10.9	10.6	5.5, 84.1	44.1	6
N18R	10.9	10.6	5.5, 84.1	44.1	-74
N19L	17.7	7.6	2.5, 76.9	23.2	11
N19R	17.6	7.6	2.5, 76.9	23.3	18

the mode mixity values for the maximum tension and torsion endpoints of loading (ϕ_{I} and ϕ_{II}), a "composite" value of mode mixity $\phi_{\mathrm{II/I}} = \tan^{-1}(K_{\mathrm{II,max}}/K_{\mathrm{I,max}})$ is also given to provide a sense of the relative magnitudes of the load maxima as compared to in-phase testing. These values are plotted as before in Fig. 5.23, which shows the ranges of ϕ for each specimen; the composite value $\phi_{\mathrm{II/I}}$ is marked by an interior point along each range.

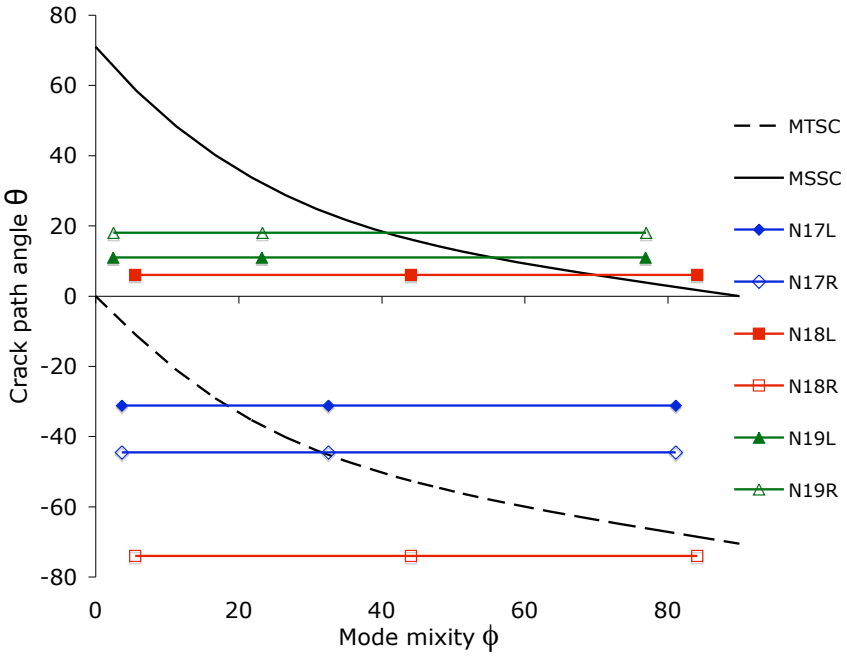

Figure 5.23: Crack deflection angle versus range of mode mixity ϕ for 180° out-of-phase tests of NASA thin-walled tubular specimens. The interior point on each range represents $\phi_{\mathrm{II/I}}$.

The crack front N18L experienced a change in deflection from 6° to approximately -55° after a millimeter or more of crack growth. This angle is not listed among the data as only the initial crack growth angle from the pre-crack is considered; however, this probably indicates that if there is a modal transition condition for this type of loading, specimen N18 was tested very close to it.

The limited data are initially difficult to explain in the traditional framework.

Comparing N17 and N18 on the basis of their composite mixity $\phi_{\mathrm{II/I}}$, it could be suggested that the increase in K_{II} resulted in an increased deflection magnitude for tensile branch cracks along the MTS trend and, for crack front N18L, a modal transition to shear cracking above a critical value of ϕ near 44°. The supposedly shear deflections toward positive θ angles at much lower values of ϕ for specimen N19, tested at the lowest $K_{\mathrm{II}}/K_{\mathrm{I}}$ ratio, would appear to contradict that trend.

However, this type of mixed-mode waveform seems to contradict expectations of increased likelihood of shear crack branching with increased global K_{II} loading. Examining the distribution of kink SIFs ahead of the crack tips for specimen N19, shown in Fig. 5.24, it appears that the positive-angle deflections of N19 are not shear cracks after all. Although the deflection angles for both crack fronts are near

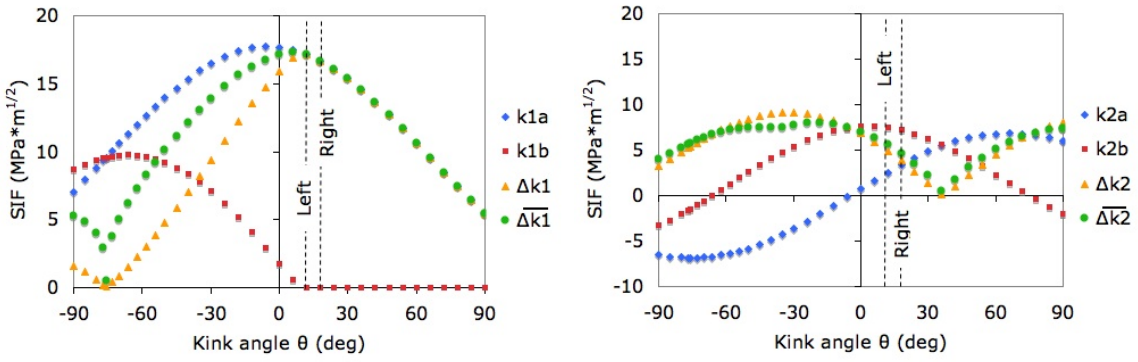

(a) (b)

Figure 5.24: Distributions of (a) Mode I and (b) Mode II crack kink SIFs for specimen N19.

the maximum k_2 at maximum torque, they more closely coincide with $\Delta k_{1\max}$ and $\overline{\Delta k}_{1\max}$.

The apparent transition of specimen N18 may also not be a transition from tensile to shear cracking, but rather divergent crack path selection along two different peaks of $\overline{\Delta k}_{1\max}$, as shown in Fig. 5.25. Fig. 5.25(b) shows that the steeply negative deflection of N18R does not fall near any peaks of Mode II parameters. But Fig. 5.25(a) shows that both of the crack deflections coincide well with $\overline{\Delta k}_{1\max}$, which experiences

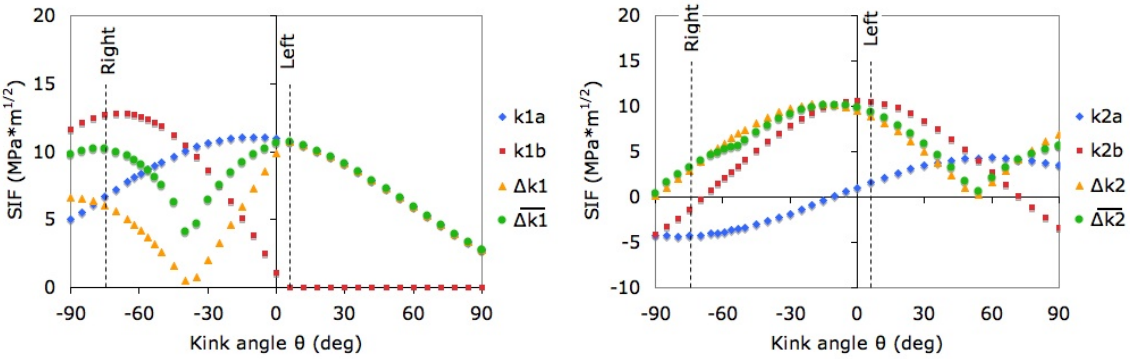

(a) (b)

Figure 5.25: Distributions of (a) Mode I and (b) Mode II crack kink SIFs for specimen N18.

two local maxima. For the selection of $w_1 = 0.3$ and $w_2 = 0.7$ – which is the set of exponents used for all kink SIF plots in this section – these peaks are nearly equal in magnitude, whereas for $w_1 = w_2 = 0.5$ the negative-angle peak is 17% lower than the positive-angle peak, and for $w_1 = 0.7$, $w_2 = 0.3$ the difference is 27%. Thus the exponent set that explains the divergent crack paths of N18 is in accordance with the constant tension/cyclic torsion case and one option for the in-phase case, but not the constant torsion/cyclic tension case.

Finally, specimen N17 presents its own interpretive challenges. This specimen was tested at K_{I} and K_{II} values between the other two, but may be the shear-driven condition of the three. In Fig. 5.26(a) it can be seen that the crack paths fall near the minima of Δk_1 and $\overline{\Delta k}_1$, and while they do not coincide very well with the maxima of Δk_2 and $\overline{\Delta k}_2$ in Fig. 5.26(b), they are at least within a region of high values of these ranges. This is despite the fact that $\overline{\Delta k}_{1\mathrm{max}}$ is roughly 50% higher than $\overline{\Delta k}_{2\mathrm{max}}$, while cracks in N18 followed the former SIF range even though the two were nearly equal in magnitude. If this load cycle consisted of sequential K_{I} and K_{II} loadings, it could be supposed that the crack was following a path between the alternating peaks of k_1 under tension and torsion. However, as Figs. 5.27(a) and (b) show, under 180° out-of-phase sinusoidal loadings, there is no significant drop in k_1 between the peaks

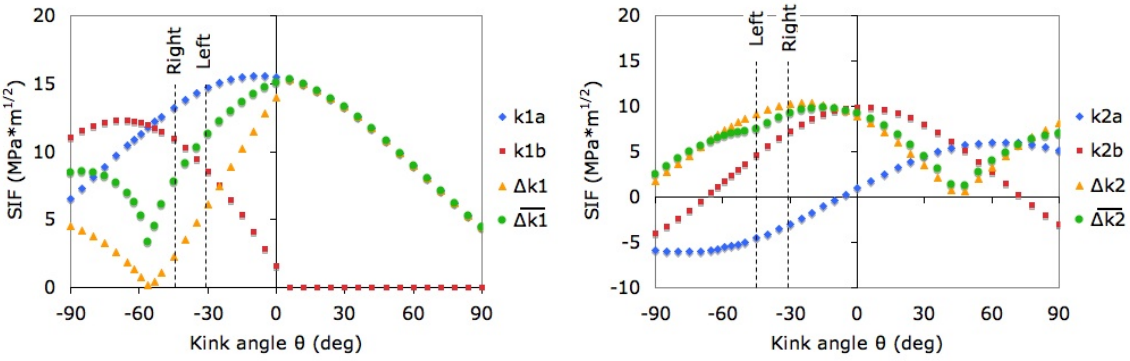

(a) (b)

Figure 5.26: Distributions of (a) Mode I and (b) Mode II crack kink SIFs for specimen N17.

of tension and torsion. In fact as Fig. 5.27(b) shows there is almost no variation in k_1

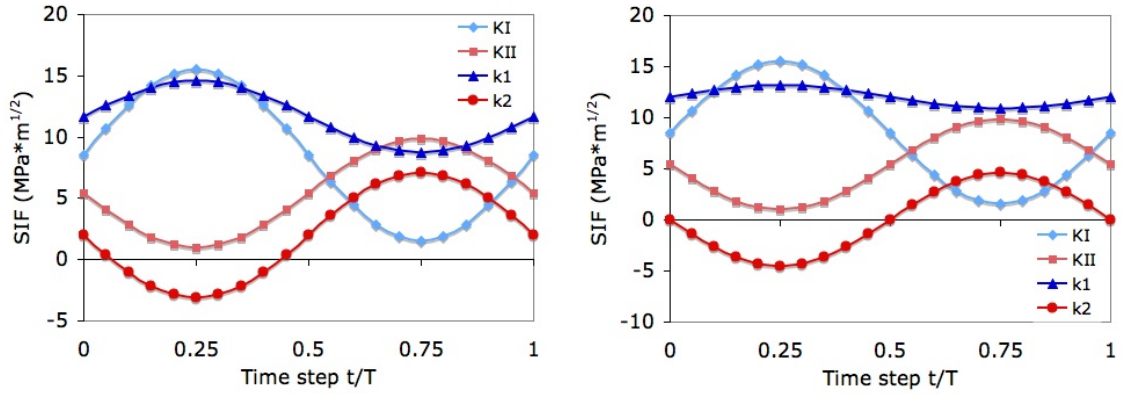

(a) N17L (b) N17R

Figure 5.27: Global loading K_{I} and K_{II} and kink SIF k_1 and k_2 along actual crack deflection angle of (a) N17L and (b) N17R as a function of time for 180° out-of-phase sinusoidal loading.

with time for N17R, leaving some function of k_2 as the only apparent crack driving force.

The best indicators of crack path direction are summarized in Fig. 5.28.

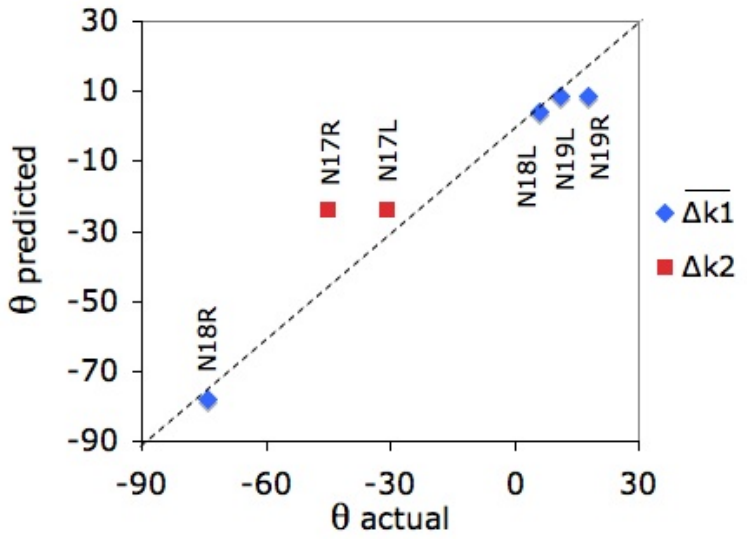

Figure 5.28: Predictions of best correlating parameters for 180° out-of-phase testing ($\overline{\Delta k}_1$ evaluated with $w = 0.3$).

5.1.4.2 SEM Fractography

Crack fronts N18R and N19R were examined by SEM as they were assumed to be the most likely crack deflections to be operating under different mechanisms. Crack front N18L was visibly too damaged by crack face contact to suggest any surface features related to crack mechanism could be distinguished; and specimen N17 was not examined as it was mistakenly assumed that it would be similar in nature to N18R (in terms of dominant crack growth mechanism or crack driving force) because they were both oriented at steep negative angles.

Fig. 5.29 shows the fracture surface of N18R centered approximately 0.3 mm from the pre-crack tip. It displays the same faceted crystallographic transgranular cracking of previously observed tensile crack branches shown in Figs. 5.4(a), 5.15(a), and 5.22, with a particularly sharp angular faceting most similar to N13R as seen in Fig. 5.15(a).

Fig. 5.30 shows the fracture surface of N19R at a lower and higher magnification centered approximately 0.4 mm from the pre-crack tip. While Fig. 5.30(a) is some-

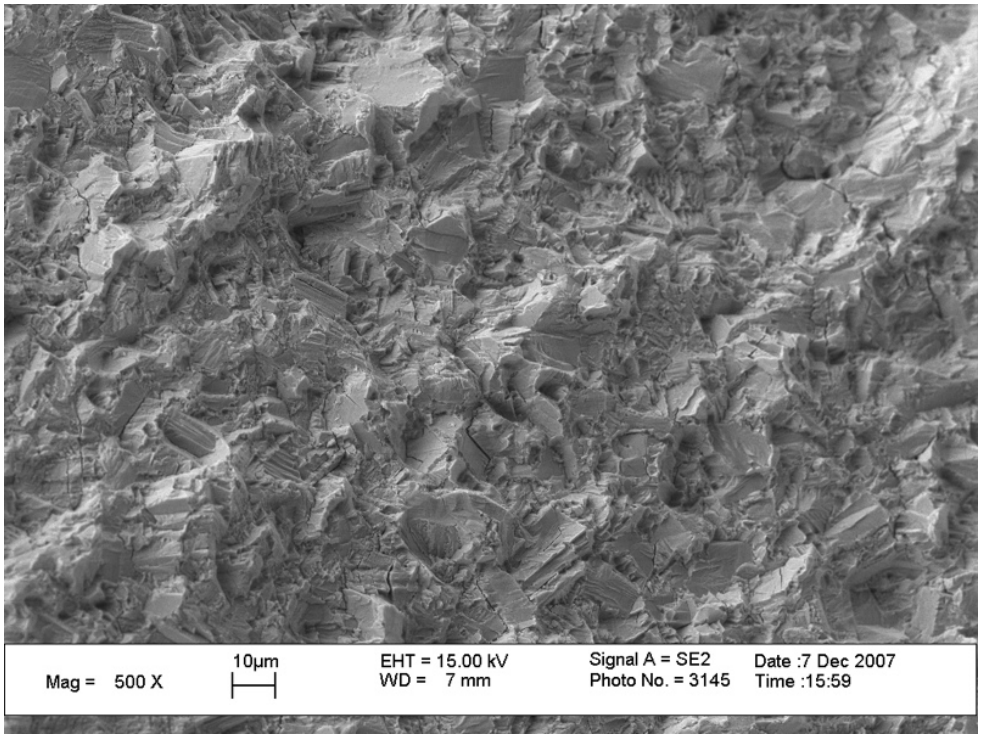

Figure 5.29: Scanning electron micrograph of N18R displaying sharply faceted crystallographic transgranular cracking morphology similar to previous Mode I-dominant crack branches.

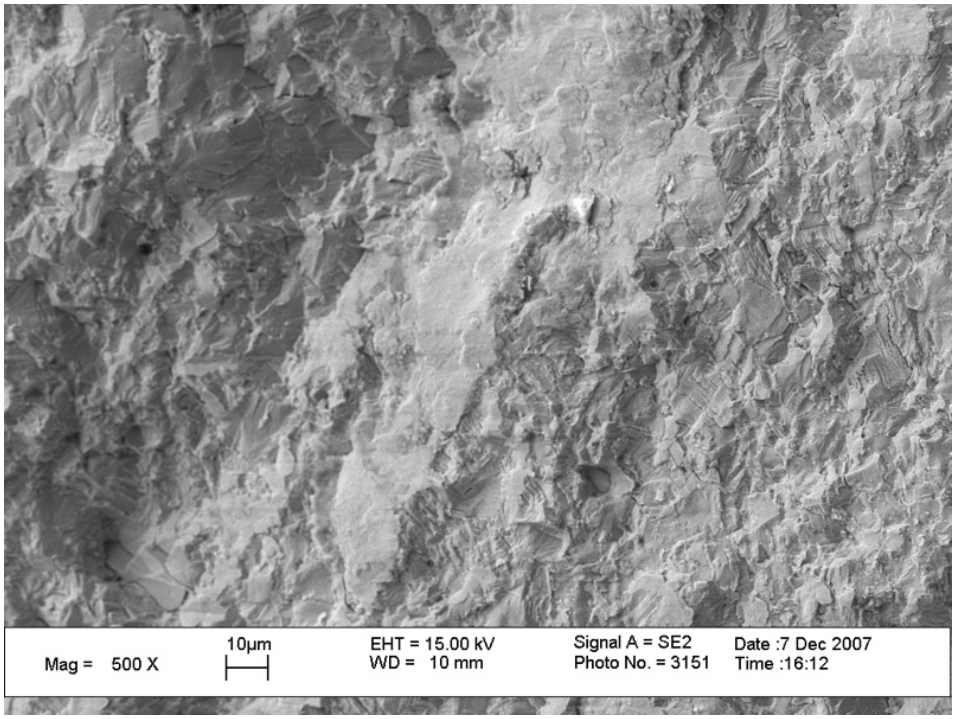

(a)

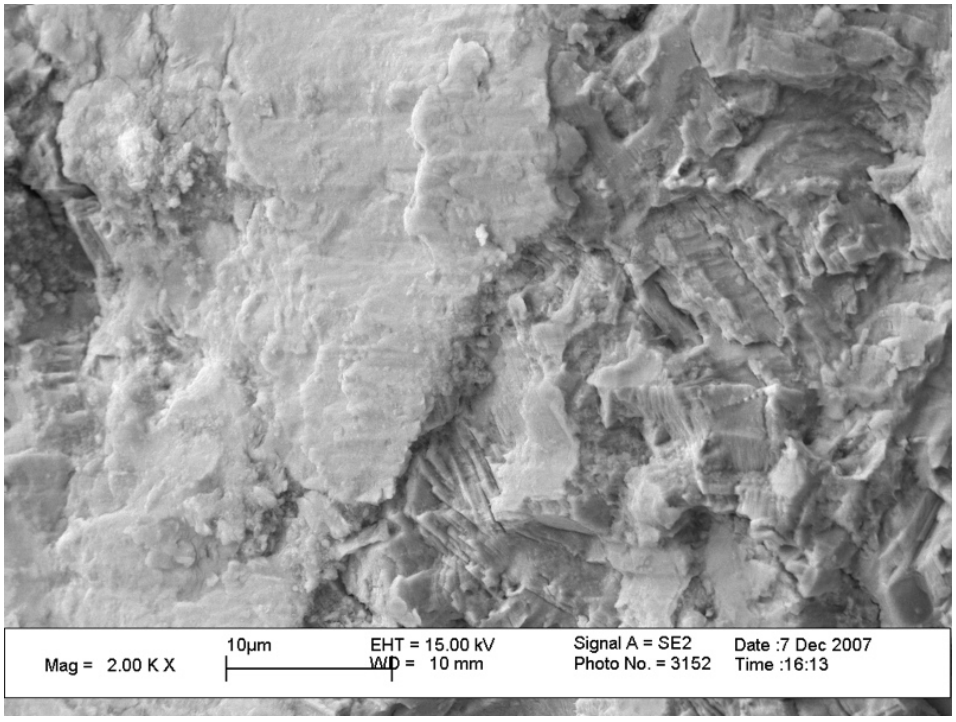

(b)

Figure 5.30: Scanning electron micrographs of N19R (a) at lower magnification, showing distributed evidence of contact damage, and (b) at higher magnification centered on same point, which shows features indicative of tensile cracking at right and likely contact damage at left.

what ambiguous in appearance with smooth regions similar to previous shear cracks as well as more faceted regions, higher magnifications such as Fig. 5.30(b) indicate that the smooth regions do appear to be the result of crack face contact damage which has smeared the fracture surface. The more sharply faceted appearance of the protected recessed regions that were not damaged support the Mode I-dominant driving force of this crack.

5.1.4.3 Summary of 180° Out-of-Phase Results

Testing of three tubular specimens under 180° out-of-phase sinusoidal loading produced initially counter-intuitive results. Specimen N19, with the lowest $K_{\mathrm{II}}/K_{\mathrm{I}}$ ratio, generated crack deflections at shallow positive angles which were initially supposed to be shear cracks but actually coincided with peak Δk_1 and $\overline{\Delta k}_1$ values. Specimen N18, with the highest $K_{\mathrm{II}}/K_{\mathrm{I}}$ ratio, generated two very different crack angles (6° and -74°) which initially suggested a modal transition but may actually follow two local maxima of Mode I SIF ranges, as even the 6° crack falls closer to the $\overline{\Delta k}_{1\max}$ peak at 4° than the Δk_2 peak at -10°. Destruction of the 6° crack face by contact wear prevented verification of the crack growth mode by SEM fractography, but examination of N18R and N19R support a Mode I crack growth mechanism even though N19R displayed significant wear damage. Finally, in specimen N19, which falls between the other two tests in both $K_{\mathrm{II}}/K_{\mathrm{I}}$ and crack branch angle, cracks grew in directions that fell close to Δk_2 and $\overline{\Delta k}_2$ maxima and very low values of Δk_1 and $\overline{\Delta k}_1$. Thus it seems shear crack branching took place in this middle condition specimen even though its $\Delta k_2/\Delta k_1$ ratio was much lower than the other two specimens, so a transition condition based on the traditional framework cannot be established at this time.

5.2 ITCR Specimens

The inclined through-crack round (ITCR) specimen design is intended to provide a wide range of mode mixity values in a single test, which can aid in identification of modal transition conditions. Only four 0°-slot specimens were able to be made for this project; they were tested under the same loading types as the NASA specimens but are presented here in the order in which they were tested, which is slightly different than the ordering of the NASA data above. None of the ITCR specimens have been subject to SEM fractography at this time.

5.2.1 In-Phase Loading

The first ITCR specimen test was used to establish baseline data for this new specimen design and to confirm some basic observations from the NASA testing of thin-walled specimens. The results generally followed the expected trend under the framework of the MTS/MSS criteria.

5.2.1.1 In-Situ Crack Growth Observations

During testing, optical measurements of the crack surface intercept on the left side of specimen ITCR #1 were made with a traveling stage microscope at several intervals while holding the load at 70% of maximum. These data may be used for future calibration or validation of crack growth models that incorporate some effective SIF as the crack driving force. The physical test setup precluded direct observation of the right side crack surface intercepts, a problem which was corrected in subsequent testing.

Table 5.5 presents the projected crack lengths for the left front and back surface intercepts measured from the center of the EDM slot. The projected crack lengths are measured in the plane normal to the specimen axis (coincident with the initial

slit/flaw) and along the axis normal to the through-slit, thus neglecting crack deflection from the normal plane and specimen surface curvature.

Table 5.5: In-situ visual measurements of projected crack surface intercept lengths (in mm from center of EDM slot; LF = left front, RB = right back, e.g.) for ITCR #1.

N	a_F	a_B
0 (pre-crack)	1.16	1.19
6,300	2.12	2.27
8,300	2.34	2.63
10,300	2.81	2.89
12,300	3.11	3.08
14,300	3.33	3.35
16,300	3.60	3.56
18,300	3.80	3.83

Post-fracture examination of the specimen indicates two distinct crack growth modes occurring from the pre-crack, as will be discussed below. Thus it should be noted here that the crack surface intercepts being measured in Table 5.5 are those of the shallow positive angle-deflected (shear-driven) cracks that were dominant near the surface. Examination of the above crack growth increments shows that there was no pronounced acceleration of crack growth rate with crack length, even though the total half-crack length roughly tripled during the test. Crack growth rate was nearly constant, varying between 0.9 and 2.4 $\times 10^{-4}$ mm/cyc (by the secant-slope method) for both crack intercepts, as shown in Fig. 5.31. This lack of acceleration is likely attributable to a reduction in local crack driving stress due to shielding from steeply negative-deflected tensile cracks to the interior which propagated outward and eventually intercepted the surface. During testing, apparent crack branching was observed on three of the four crack surface intercepts. However, post-test observation strongly suggests that rather than true crack branching, the observed crack branches were in fact the emergence of interior cracks spreading outward.

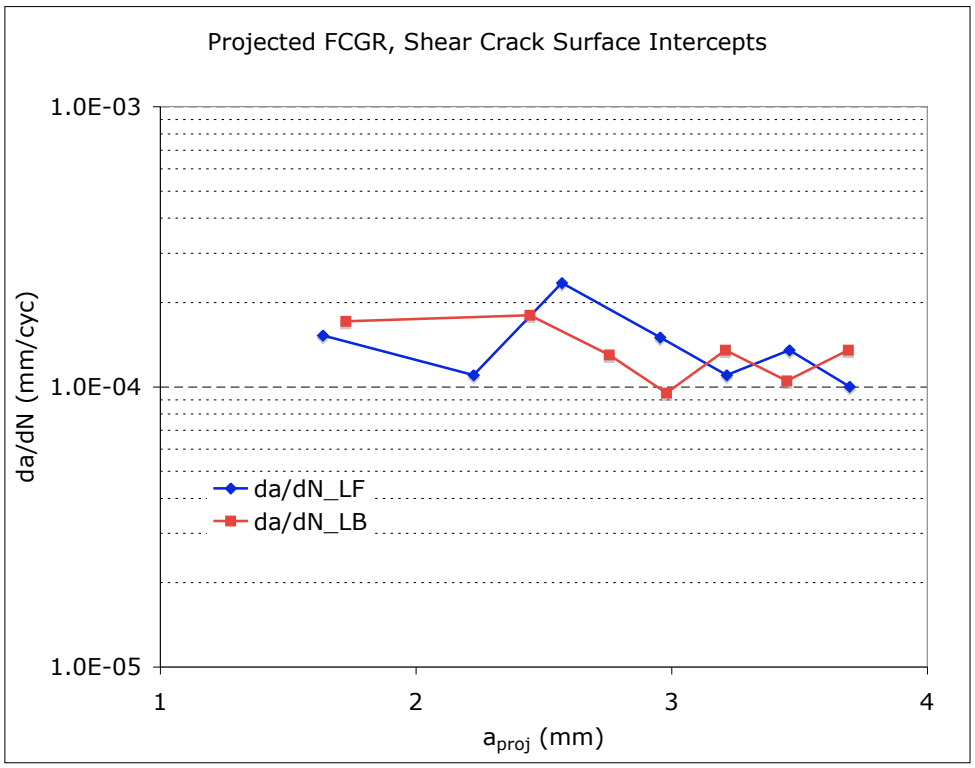

Figure 5.31: Crack growth rate (secant-slope of projected crack lengths) from in-situ observations of shear crack surface intercepts on front (LF) and back (LB) of left side of ITCR #1.

5.2.1.2 Post-Test Characterization

Examination of the fracture surfaces reveals crack growth mode transition behavior nominally in line with expectations based on the previous tubular specimen results. It appears that from the initiation of mixed-mode test loading, the pre-crack propagated in a positively-deflected shear mode at the outer extrema with a discrete transition to negatively-deflected tensile cracks in the interior. Crack growth mode transition occurred in all four quadrants, as shown in Fig. 5.32(a). The sketch in Fig. 5.32(b) shows the orientation and overlap of tensile- and shear-oriented fatigue cracks, which terminate prior to tensile-only fatigue loading to failure.

Shear cracks propagated circumferentially and remained close to the specimen surface. Shear crack propagation from the pre-crack penetrated to a depth of 2.44 mm

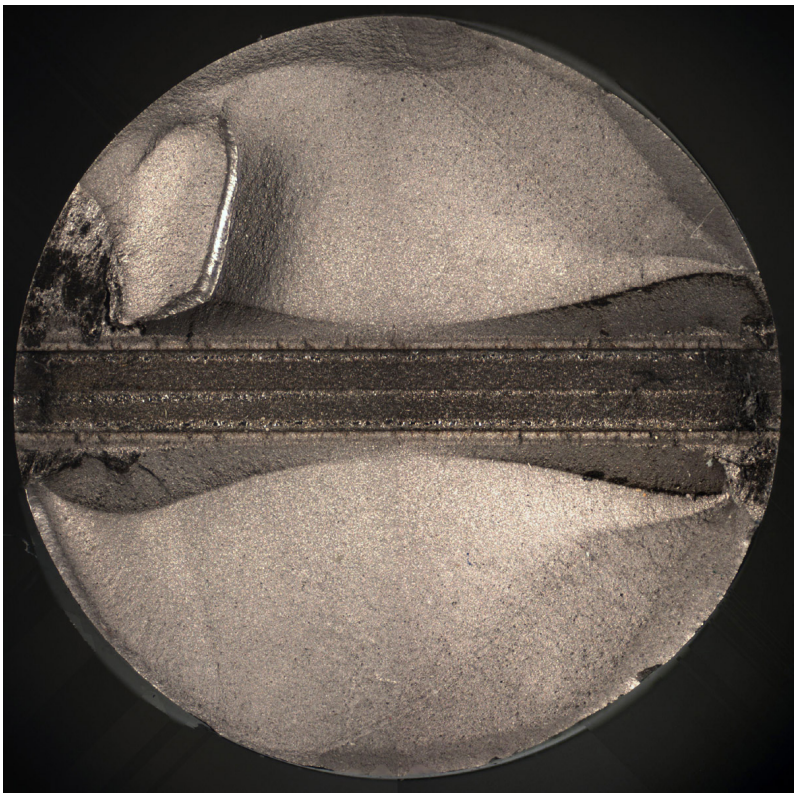

(a)

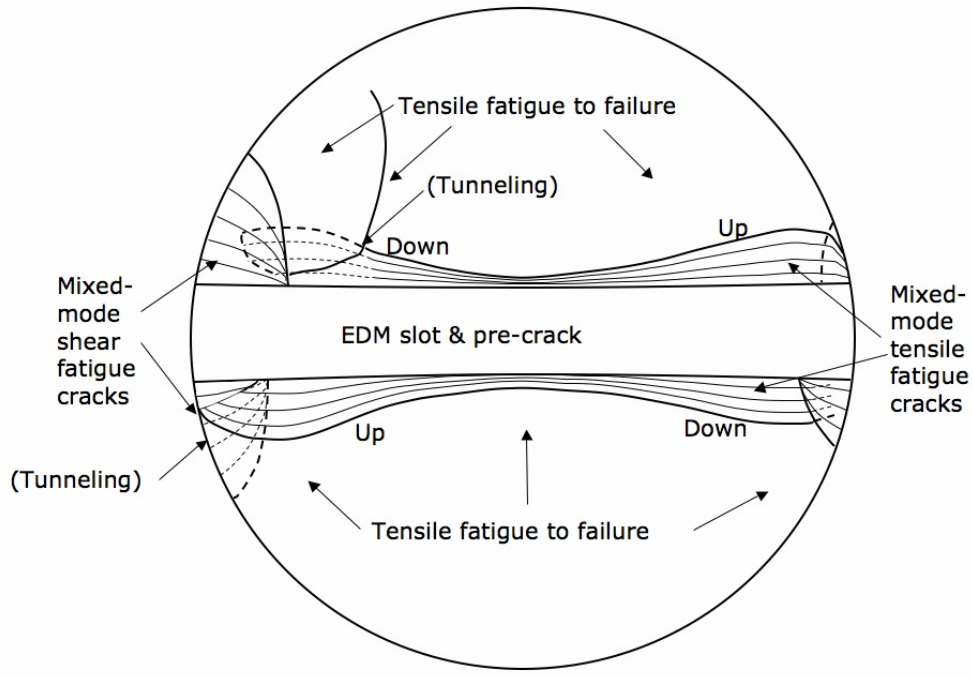

(b)

Figure 5.32: (a) Photograph and (b) sketch of bottom fracture surface of ITCR #1 (in-phase).

(left-back), 1.27 mm (left-front), 0.41 mm (right-back) and 1.12 mm (right-front) along the pre-crack front, corresponding to normalized x/b locations of 0.68, 0.83, 0.95 and 0.85 respectively. Tensile cracks spread outward and eventually intercepted the surface, resulting in the false appearance of crack branching during test observation. This tensile crack tunneling is shown from an angle in Fig. 5.33 for the right-front quadrant and Fig. 5.34 for the left-back quadrant.

5.2.1.3 Crack Deflection Angles

Crack deflection angles from the pre-crack to the mixed-mode test propagation were measured from sections of plastic castings as described in Section 3.3.3. In some of the sections, the profile of the pre-crack was not perfectly normal to the specimen axis. However, these variations were neglected in deflection angle measurement as observation of the fracture surface revealed these to be generally the result of extremely local factory-roof style grooves in the pre-crack, and the overall pre-crack profile was globally flat. There was also no observed influence of these local pre-crack grooves on the overall deflection behavior of the subsequent mixed-mode crack.

Measured crack deflection angles for this test are plotted versus normalized crack front position in Fig. 5.35, where x/b = -1 is arbitrarily the left side of the specimen as placed in the load frame from the operator's perspective. The sign of the crack deflection uses the convention that the MTS criterion predicts a -70.5° deflection for pure Mode II loading. In some locations, a small amount of crack growth after the pre-crack was observed in one direction before changing to a more stable direction; these are plotted as "putative" deflections. They are of particular interest in cases such as x/b = -0.74, where the front crack begins to grow in the MSS direction before a stable deflection occurs toward the MTS direction. Expected deflection behavior is seen as the crack deflection angles trend downward from the center of the specimen outward, approaching the MTS criterion, before a sudden transition up to the MSS

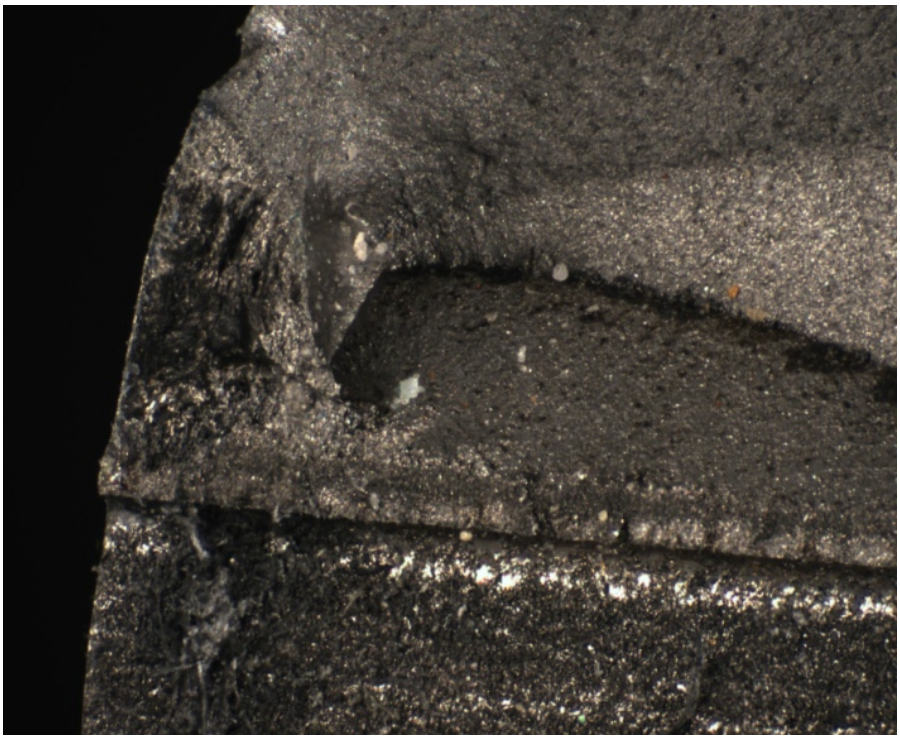

Figure 5.33: Tensile crack (center to right) tunneling below a shear crack (left) in right-front quadrant of bottom half of ITCR #1.

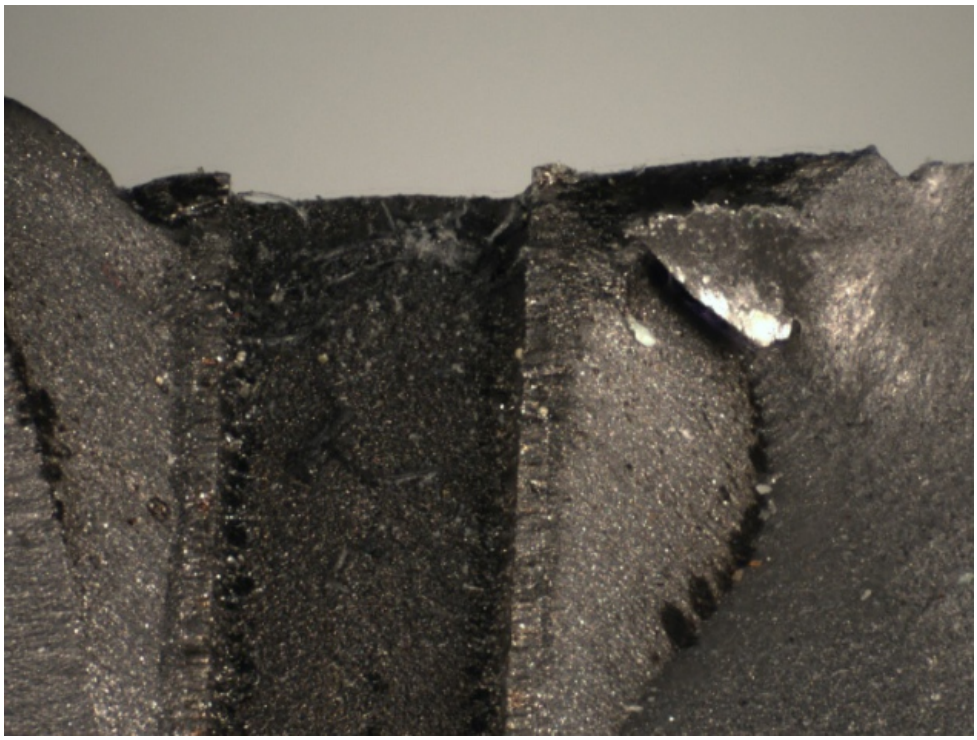

Figure 5.34: Side view of tensile crack (lower right) tunneling below a shear crack (upper right) in left-back quadrant of bottom half of ITCR #1.

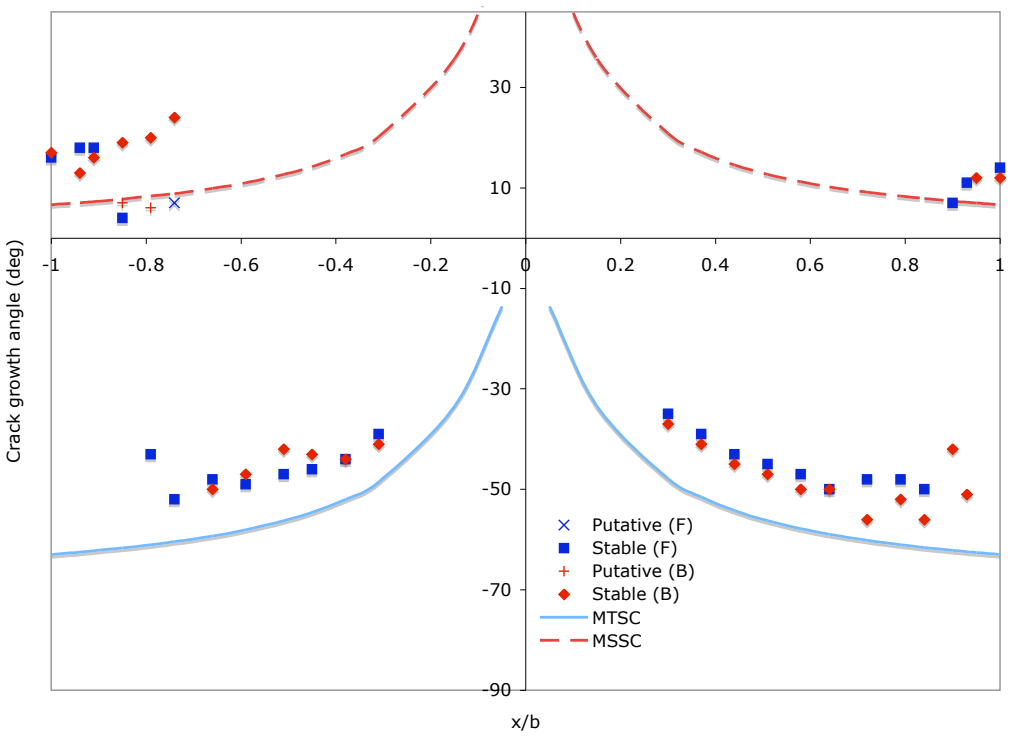

Figure 5.35: Crack deflection angle versus crack front position for ITCR #1, in-phase loading.

criterion.

The magnitude of deflection does not meet the predicted values of the MTS criterion and exceeds the predictions of the MSS criterion. This suggests a diminished influence of K_{II} loading on the crack direction for this test is the modeled SIF values are accurate. As discussed in Section 5.1.3.1, using an effective kink tip SIF range like $\overline{\Delta k}$ predicts the same angles as the standard MTS and MSS criteria regardless of exponent, so this cannot be used to enhance the prediction of crack deflection for this specimen. It is possible that the crack behavior in this type of specimen, as compared with the thin-walled tubular specimens, would require more detailed 3-D modeling of the complete interior stress field (which was not possible using the FRANC3D boundary element modeling software employed), particularly if the role of non-singular stresses must be included as also discussed in Section 5.1.3.1.

Although the angle predictions of $\overline{\Delta k}$ cannot be compared against the NASA results for accuracy, the relative values of $\overline{\Delta k}_2$ and $\overline{\Delta k}_1$ in the area of transition may be compared. However, given the questions raised about the completeness of this parameter as a predictor, any difference at this point cannot be distinguished between a result of a shortcoming of the particular parameter or the understanding of the stress field of the new specimen. For the NASA specimens, transition was identified by specimens N08 and N09 as occurring near $\overline{\Delta k}_2/\overline{\Delta k}_1$ = 0.57-0.60 for range of w_1 = 1-w_2 = 0.3-0.5. For the ITCR specimen, transition occurs in the range $\overline{\Delta k}_2/\overline{\Delta k}_1$ = 0.64-0.68. Because K_{IImax} and $\Delta k_{2\mathrm{max}}$ both increase with radius and thus are maximized near the specimen surface where plane-strain conditions likely transition to more plane-stress conditions, the effect of constraint on modal transition cannot be separated without a full 3-D finite element analysis of both specimens.

5.2.1.4 Summary of In-Phase ITCR Results

In its first use for mixed-mode crack growth testing, the ITCR specimen was validated as an effective means for studying crack path as a function of mode mixity and for identifying modal transition in crack branching. Crack deflection angles followed the general trend of the standard MTS/MSS criteria with some offset, and the values of $\overline{\Delta k}_2/\overline{\Delta k}_1$ at transition were slightly higher than those generated by the thin-walled tubular specimens. It is likely that comparison of test data between these two types of specimens combined with full 3-D FEM analysis can provide additional insight into the role of constraint on crack path selection and transition.

5.2.2 Constant Tension/Cyclic Torsion

5.2.2.1 In-Situ Crack Growth Observations

Optical measurements of crack surface intercepts on both sides of specimen ITCR #1 were taken for use in future crack growth model calibration. The projected crack

lengths are presented in Table 5.6 for the front (F) and back (B) surface intercepts on the left (L) and right (R) sides of the specimen, measured from the center of the EDM slot. Crack growth accelerated steadily with crack length as shown in Fig. 5.36, and

Table 5.6: In-situ visual measurements of projected crack surface intercept lengths (in mm from center of EDM slot; LF = left front, RB = right back, e.g.) for ITCR #2.

N	a_{LF}	a_{LB}	a_{RF}	a_{RB}
0 (pre-crack)	1.14	1.16	1.16	1.13
5,000	2.18	1.82	1.90	1.79
10,000	3.51	2.83	3.27	2.98
15,000	6.36	4.60	5.62	4.96

no crack branching was observed during testing. Crack growth rate is not presented as a function of SIF as the instantaneous interior crack shape is unknown and thus there is no prediction of SIF for each measurement.

5.2.2.2 Post-Test Characterization

Because these were the first tests using a specimen of this design, periodic crack front marking was not employed as its impact on crack growth mechanism was unknown. These tests were to serve as a baseline for future studies which could involve marker bands or crack tinting. Without a record of progressive crack front shapes on the fracture surface, description of the crack propagation behavior from fractography relies on some conjecture.

An overview of the bottom fracture surface is shown in Fig. 5.37, and an angled, obliquely-lit view is shown in Fig. 5.38 to highlight certain features. Propagation from the pre-crack occurred in a shallow positive (shear) angle at the outer extrema and proceeded circumferentially (annotated "A" in Fig. 5.38). The central third of the surface is the final fracture surface, displaying clear rupture dimpling (annotated "B"). Between the shallow outer crack propagation and the central rupture, there

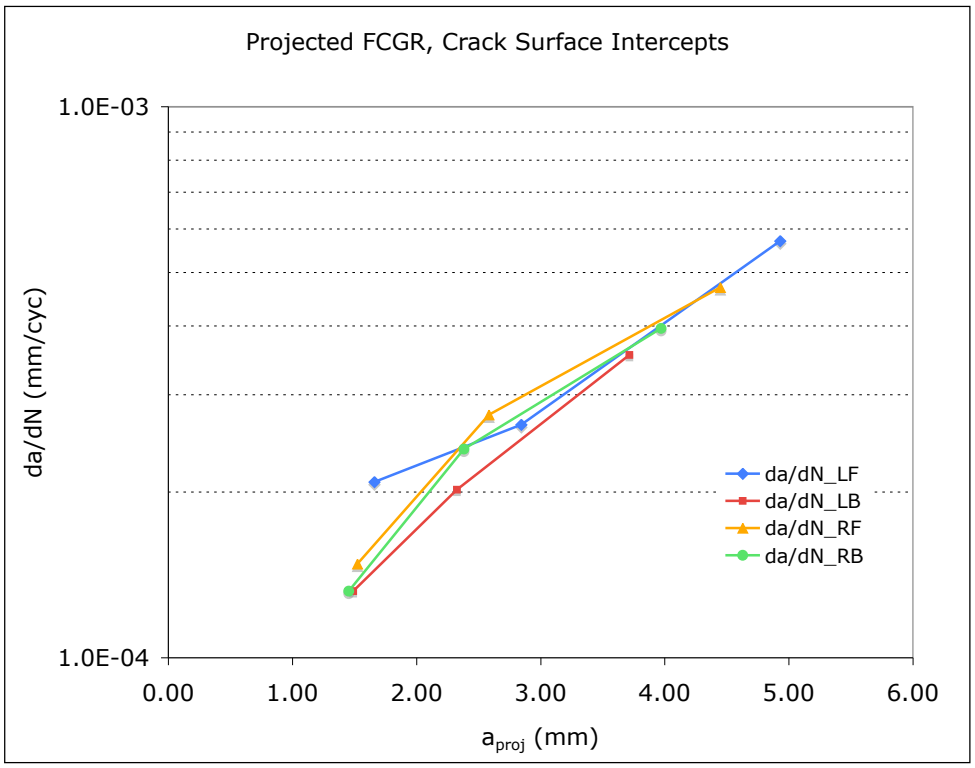

Figure 5.36: Crack growth rate (secant-slope of projected crack lengths) from in-situ observations of crack surface intercepts, ITCR #2 (LB = left back, RF = right front, e.g.).

are short, steep crack deflections in all four quadrants. Two quadrants – right-front and left-front – show deflections consistent with tensile-driven cracking such that the cyclic torque would produce crack opening displacements (annotated "C"). The other two quadrants show deflections in the opposite direction, which would have undergone negative (compressive) crack surface displacements under the action of torque if they were in fact fatigue cracks (annotated "D"). These surfaces show extensive smearing from contact, which may have occurred only during final fracture and not necessarily due to fatigue cracking.

The left-back quadrant also shows a region of crack-opening deflection between the crack-closing deflection and the final rupture (annotated "E"). A close-up of this deflection is shown in Fig. 5.39, in which it is evident that the crack has propagated

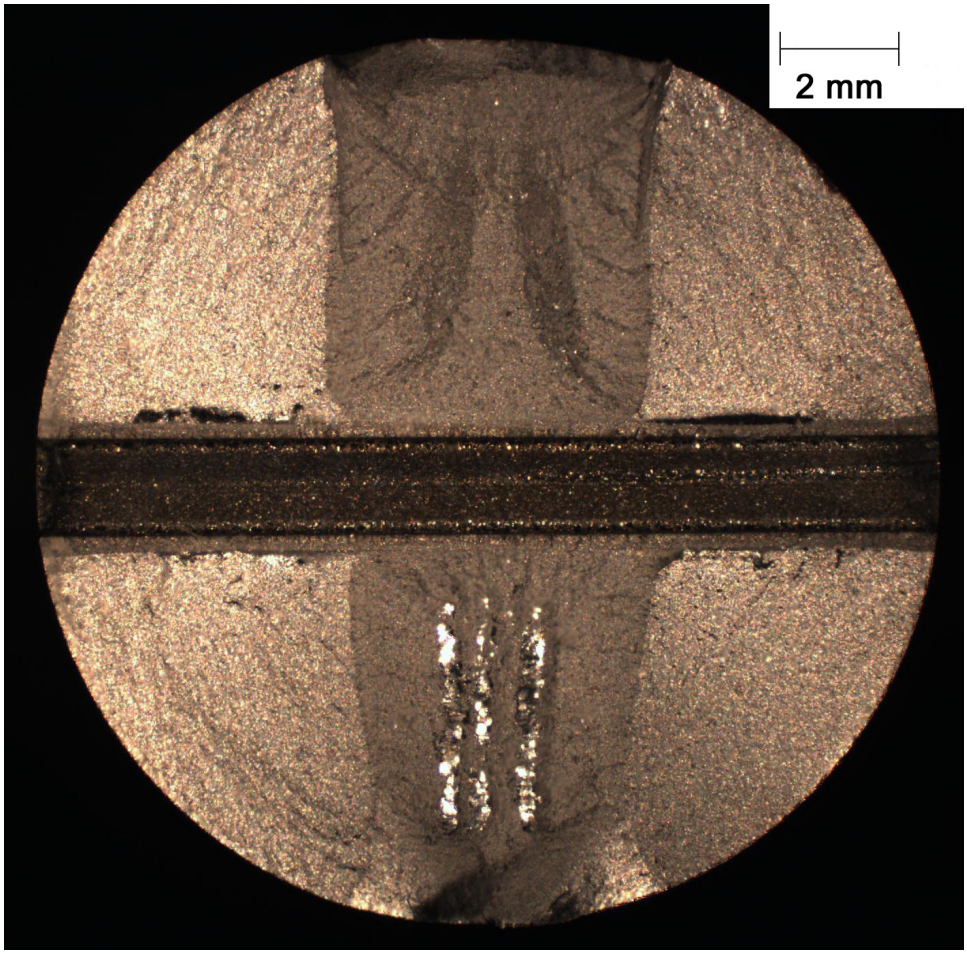

Figure 5.37: Bottom fracture surface of ITCR #2 (constant tension/cyclic torsion).

down into the specimen beneath the major shallow fatigue crack (which has propagated inward from the outer portion of the pre-crack) prior to their intersection. Similar tunneling is seen in the left-front quadrant (corresponding to the lower label "C" in Fig. 5.38) of the top fracture surface, as shown in Fig. 5.40.

The crack-opening deflection in the right-front quadrant is shown in Fig. 5.41. Examination of this region shows that the crack-opening deflection has a distinct appearance from both the dominant crack and the final fracture. This strongly suggests that the crack-opening deflection is a true fatigue crack and not an artifact of the final fracture. The crack-closing deflections (D) may however be simply smeared final fractures of the ligaments left between the pre-cracks and the dominant shallow

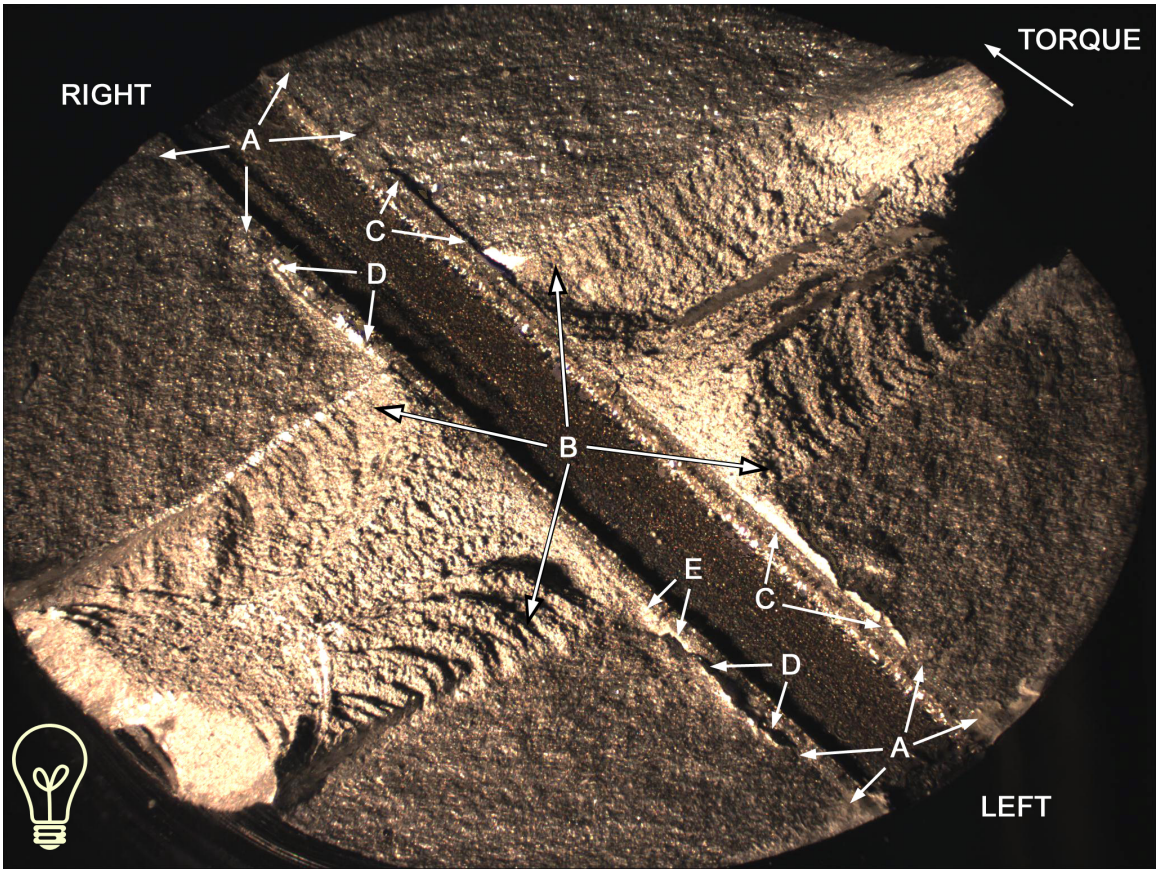

Figure 5.38: Annotated oblique view of bottom fracture surface of ITCR #2, showing (A) shallow positively-deflected crack growth, (B) final fracture, (C) and (E) steep crack-opening deflections, (D) steep crack-closing pseudo-deflections. (Rotation under torque is counter-clockwise.)

fatigue cracks which curled back inward but, due to their angle of inclination, did not re-intercept the pre-cracks. It is possible that crack-opening deflected fatigue cracks propagated from all four quadrants but that there is no exposed evidence of one in the right-back quadrant simply due to the final position of the dominant fatigue crack in that quadrant.

Based on these observations, the steep deflections from the pre-crack in the crack-closing direction (D) were not included in the crack angle measurements from the sectioned castings discussed below. Only the crack-opening deflections (C and E) were considered to be true fatigue crack deflections.

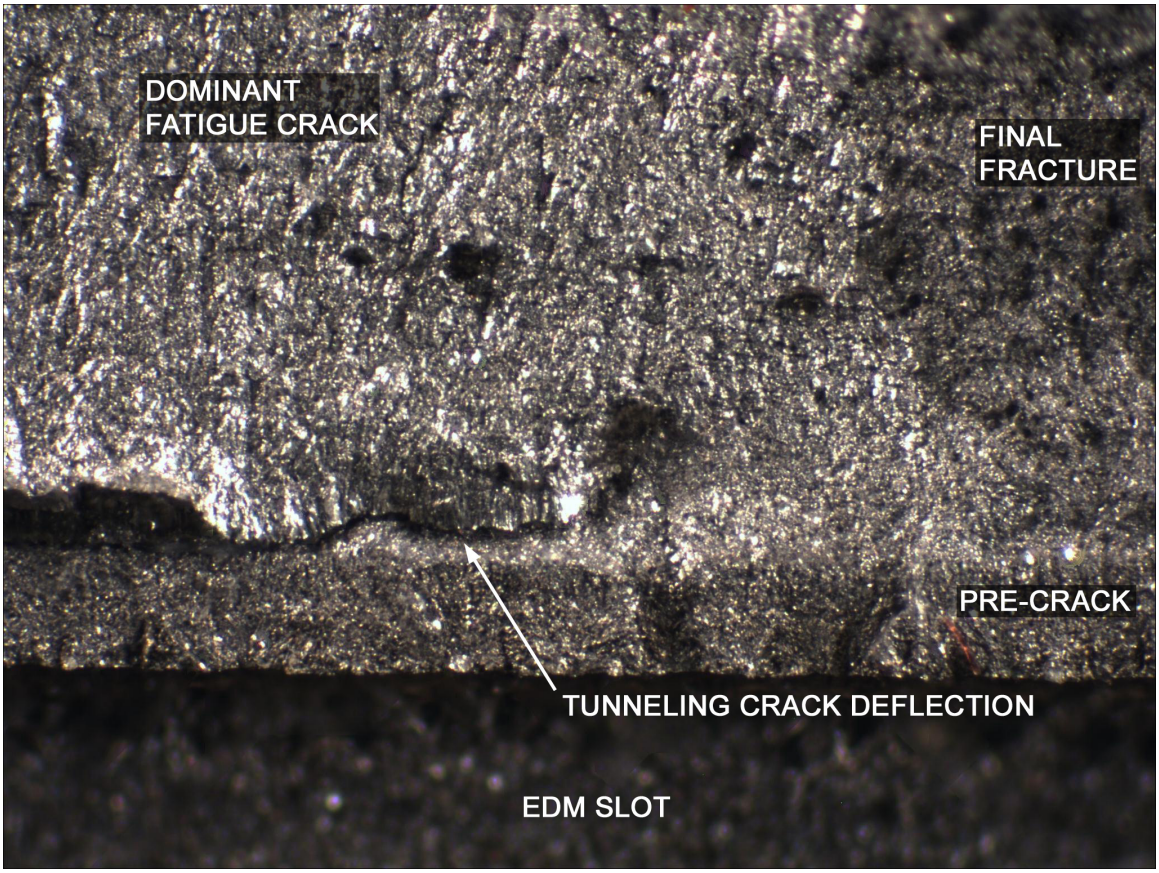

Figure 5.39: Close-up of left-back quadrant of bottom fracture surface (label "E" in Fig. 5.38) revealing a tunneling crack deflection below dominant crack.

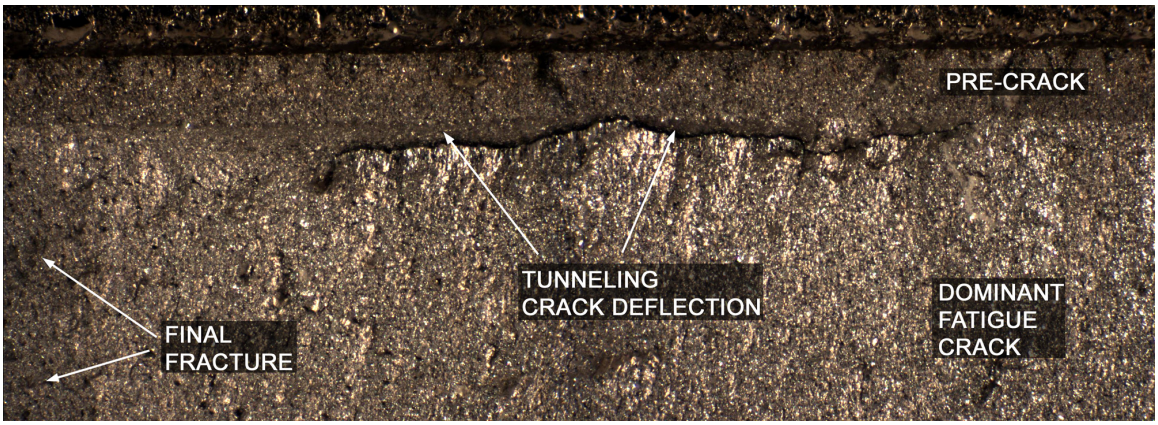

Figure 5.40: Close-up of left-front quadrant of top fracture surface (mating to lower label "C" in Fig. 5.38) revealing a tunneling crack deflection below dominant fatigue crack.

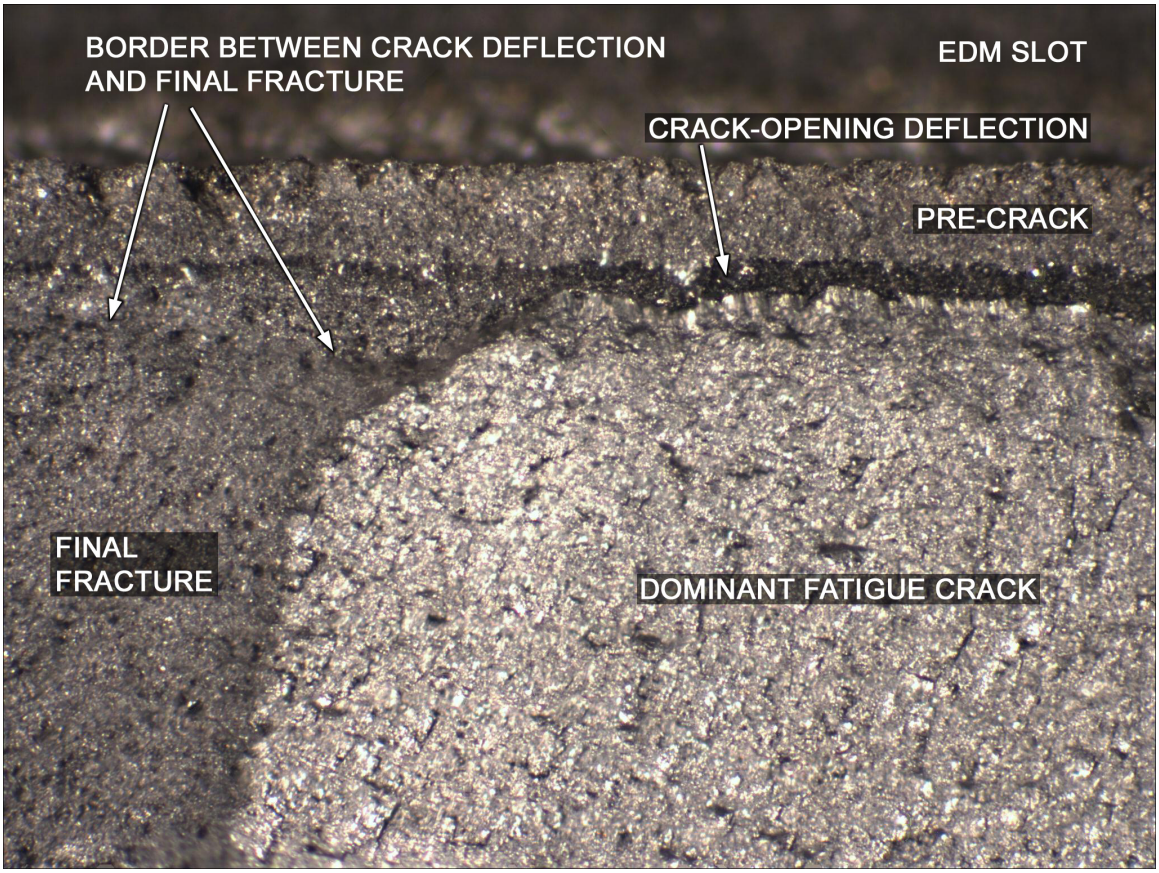

Figure 5.41: Close-up of right-front quadrant of bottom fracture surface (upper label "C" in Fig. 5.38)showing distinct surface appearance of a crack-opening deflection.

5.2.2.3 Crack Deflection Angles

Measured crack deflection angles for ITCR #2 are plotted versus normalized crack front position in Fig. 5.42, where x/b = -1 is the left side of the specimen as above. The results are qualitatively similar to the in-phase testing and the monotonic MTS and MSS criteria based on $K_{\mathrm{IImax}}/K_{\mathrm{Imax}}$ with a shift in magnitude opposite that seen for in-phase testing. As for ITCR #1, there are two distinct sets of crack deflections, with steep negative (tensile direction) deflections in the interior and a rapid shift to shallow positive (shear direction) angles nearer to the surface. At the outer extrema, crack propagation is closer to co-planar with the pre-crack, falling below the K_{max}-based MSS predictions, whereas the in-phase testing angles were above the MSS criterion. As crack deflection shifts to a tensile direction, the magnitude of the angle

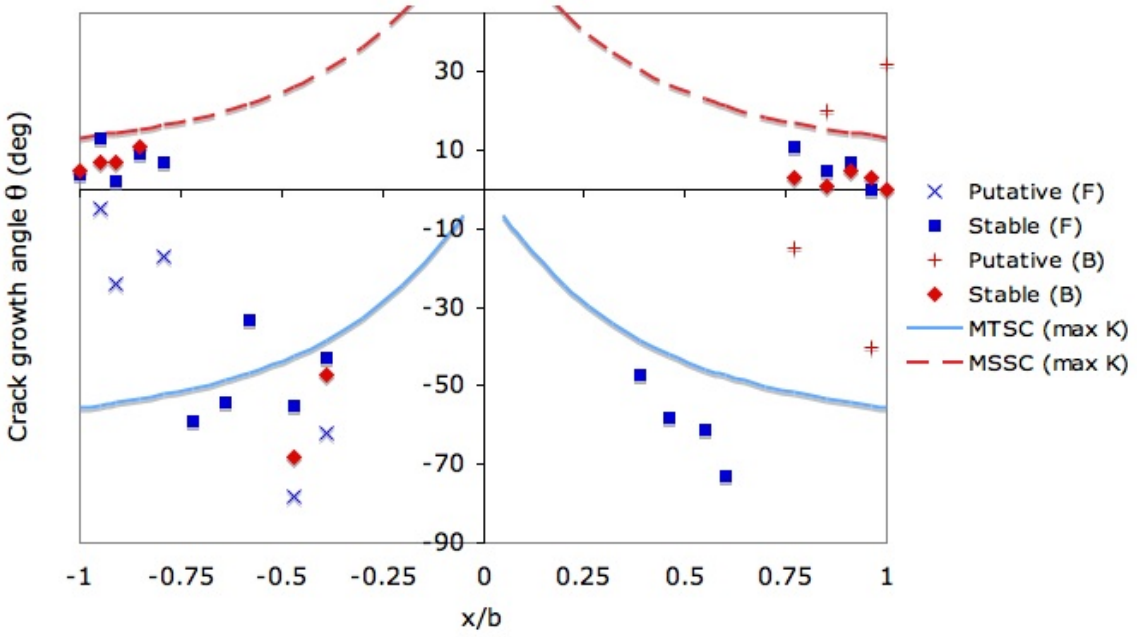

Figure 5.42: Crack deflection angle versus crack front position for ITCR #2, constant tension / cyclic torsion loading.

exceeds the $K_{\max}$-based MTS criterion, whereas the in-phase testing angles fell short of it.

These data suggest a greater influence of K_{II} as compared to ITCR #1 since ΔK_{II} is the only fatigue loading driving crack growth. Employing the same $\overline{\Delta k}$ measure as before improves the general fidelity of crack angle prediction for the exponent set $w_1 = 1$ - $w_2 = 0.3$, which was the same set chosen for the NASA data at this condition. Fig. 5.43 shows the angle predictions of $\overline{\Delta k}_{1\max}$ and $\overline{\Delta k}_{2\max}$ across the specimen front. Use of $\overline{\Delta k}_{\max}$ brings the prediction closer to the data for the shear cracks at the perimeter and passes the prediction through the data points for the interior tensile cracks. The other two sets of exponents w used previously for other conditions improve the fidelity for shear cracks somewhat but at great expense to the fidelity of tensile crack branch prediction.

The ability of $\overline{\Delta k}_{\max}$ to predict transition is ambiguous for this specimen. As Fig. 5.44 shows, the ratio of $\overline{\Delta k}_{2\max}/\overline{\Delta k}_{1\max}$ falls within a very narrow band of values,

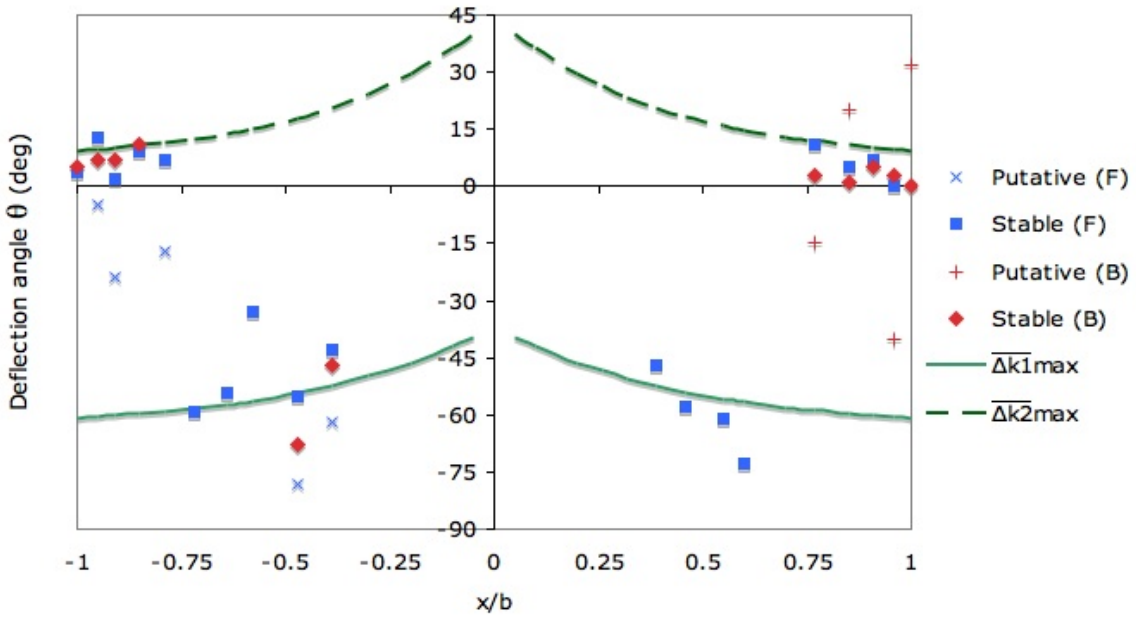

Figure 5.43: Application of $\overline{\Delta k}_{\max}$ to predict crack deflection angles in ITCR #2 constant tension/cyclic torsion loading using w_1 = 1 - w_2 = 0.3.

and within the observed data for this specimen there is considerable overlap between conditions that generated tensile and shear branches. The transition from tensile to shear crack branching takes place in a range of $\overline{\Delta k}_{2\max}/\overline{\Delta k}_{1\max}$ = 0.60-0.64.

5.2.2.4 Summary of Constant Tension/Cyclic Torsion ITCR Results

Testing of the new ITCR specimen under constant tension/cyclic torsion generated two ranges of positive (shear) and negative (tensile) crack deflections that followed general trends of LEFM parameters. Use of the same $\overline{\Delta k}$ formulation as the NASA data at the same condition produced reasonably good predictions of crack deflection angle. The ability to identify modal transition with this parameter and this specimen is not clear at this time.

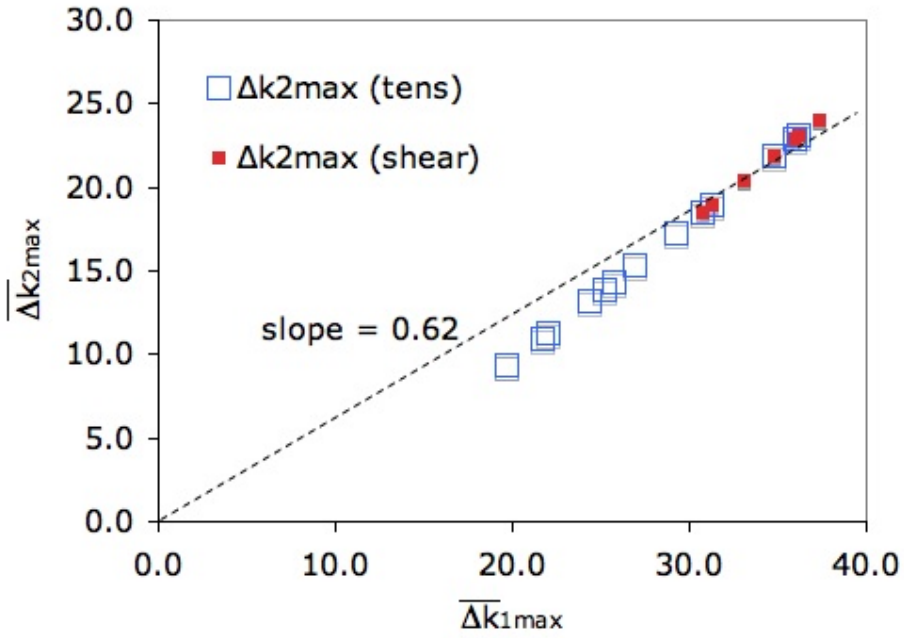

Figure 5.44: Performance of $\overline{\Delta k}_{2\max}/\overline{\Delta k}_{1\max}$ in predicting modal transition of crack branching in ITCR #2 constant tension/cyclic torsion testing.

5.2.3 180° Out-of-Phase Loading

5.2.3.1 In-Situ Crack Growth Observations

Optical measurements of crack surface intercepts on both sides of specimen ITCR #3 were taken for use in future crack growth model calibration. The projected crack lengths are presented in Table 5.6 for the front (F) and back (B) surface intercepts on the left (L) and right (R) sides of the specimen, measured from the center of the EDM slot.

Visible crack growth at the surface decelerated by over an order of magnitude over approximately the first 0.5 mm before accelerating toward failure, as shown in Fig. 5.45, in which crack growth rate is again plotted against crack intercept length in the absence of SIF models for the developing crack. The deceleration in crack growth may be attributed to crack deflections and branching that were observed during the test. It is not certain whether the observed branching on the surface was

Table 5.7: In-situ visual measurements of projected crack surface intercept lengths (in mm from center of EDM slot; LF = left front, RB = right back, e.g.) for ITCR #3.

N	a_{LF}	a_{LB}	a_{RF}	a_{RB}
0 (pre-crack)	1.20	1.20	1.16	1.16
2,700	1.41	1.48	1.47	1.44
5,600	1.45	1.63	1.48	1.59
10,350	1.54	1.69	1.54	1.66
20,000	1.60	1.76	1.55	1.71
30,000	1.66	1.83	1.61	1.74
43,000	1.81	1.91	1.61	1.79
56,100	2.03	2.10	1.70	1.79
66,000	2.63	2.96	1.84	2.01

representative of "true" crack branching caused by fracture mode transition or merely the interaction between surface crack behavior and internal crack propagation at a different deflection angle, similar to that discussed in Section 5.2.1.2. The acceleration of crack growth at the surface occurred once the crack surface intercepts coincided with the dominant interior deflection.

As will be described below, crack propagation in the specimen interior occurred at a significant angle to the normal pre-crack plane. However, the crack surface intercepts grew co-planar with the pre-crack for close to 0.5 mm. At the onset of co-planar growth from the pre-crack, there was evidence of apparent shear banding in the positive-deflection direction at all four crack tips, shown in Fig. 5.46 and Fig. 5.47 as seen through the stage microscope during testing. Based on post-fracture examination, however, this phenomenon was likely just Poisson contraction due to crack tip stresses ahead of the interior deflected portion of the crack. After 0.3-0.45 mm of nominally co-planar crack growth at the surface, all four surface cracks deflected in the positive direction (crack-closing under torque), but some minor branching in the negative (crack-opening) direction was observed at the surface. Fig. 5.47 shows a small crack-opening branch growing from the point at which the surface crack turns

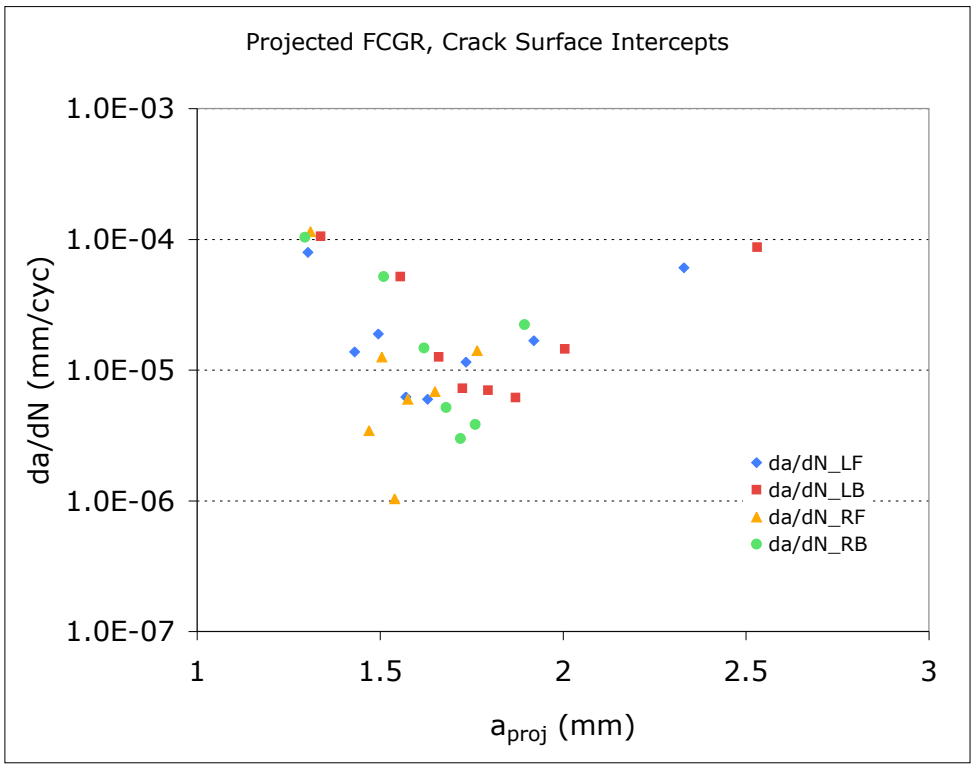

Figure 5.45: Crack growth rate (secant-slope of projected crack lengths) from in-situ observations of crack surface intercepts, ITCR #3 (LB = left back, RF = right front, e.g.).

toward the dominant internal crack-closing-oriented crack. Similar branching was observed at the left-back crack, as shown in Fig. 5.48.

A crack-opening branch was also observed on the right-front crack. Although it was not visible until the image taken at 66,000 cycles, it emanates from the prior pre-crack tip location, as shown in Fig. 5.49. The right-back crack displayed unique branching behavior, shown in Fig. 5.50, with two apparent branches in the crack-closing direction separated by a small segment of co-planar growth before merging into a single dominant crack-closing deflection. A small tensile branch crack is finally seen emerging from the turning point of the outer shear crack as well, seen in Fig. 5.50(c).

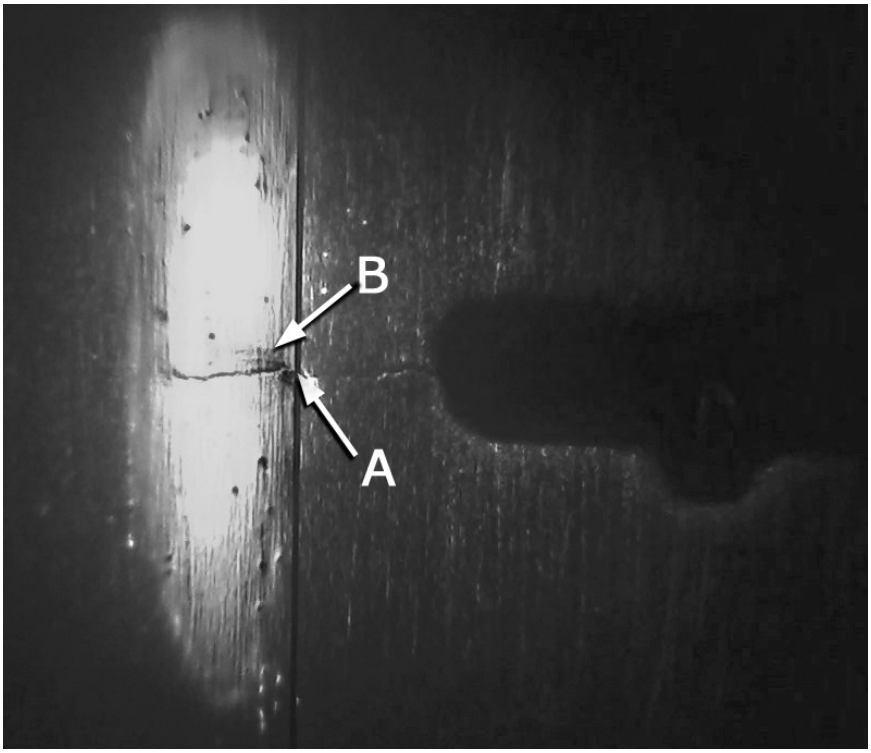

Figure 5.46: Apparent shear banding (B) above co-planar growth from end of pre-crack (A) is likely Poisson-induced surface evidence of internal crack deflection, left-back crack surface intercept. Image taken through stage microscope during test at 5,600 cycles.

5.2.3.2 Post-Test Characterization

An overview of the bottom fracture surface is shown in Fig. 5.51. Both pre-crack fronts display a smooth distribution of deflection angles from a steep crack-closing angle at either end through co-planar growth at the center of the specimen. Crack growth rate was highest at the left crack fronts, resulting in the final fracture ligaments indicated at the upper and lower right. The angle of deflection and the rotation of the specimen under torque resulted in significant smearing of the fracture surface due to contact in the front and back left quadrants; similar but smaller regions of smearing are present on the right as well. The pre-crack and EDM notch suffered some gross deformation due to torque, presumably in the final fracture stage. However, close examination of the boundaries between the smeared regions and the surrounding

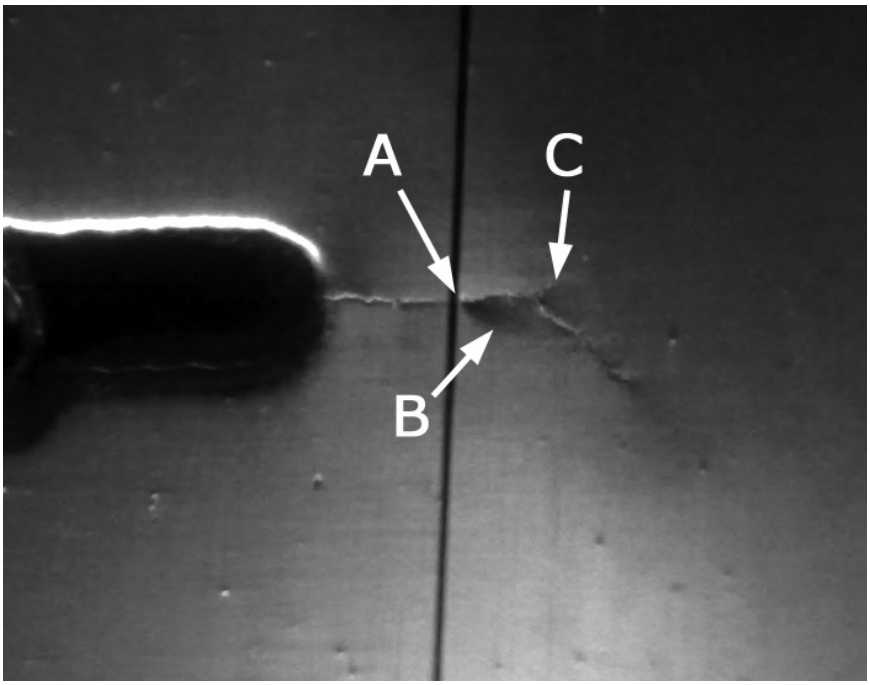

Figure 5.47: Minor crack-opening deflection (C) on left-front crack surface intercept at the point where dominant crack path turns toward the crack-closing direction after approximately 0.3 mm of co-planar growth from pre-crack tip (A). Evidence of internal crack behavior, assumed at first to be shear banding, is apparent (B). Image taken through stage microscope at 30,000 cycles.

fatigue surface indicate that gross deformation due to contact resulted in an apparent change of fracture angle of only 1°-3°. Therefore these deformations were neglected in subsequent crack angle measurement as the precise distribution of error could not be determined and the relative error was nearly negligible.

Examination of the fracture surface showed that the co-planar crack growth observed during testing at the specimen surface only extended up to 0.25 mm into the specimen, as shown in Fig. 5.52 for the left side of the pre-crack. Penetration of co-planar crack growth on the right side was similar.

5.2.3.3 Crack Deflection Angles

Measured crack deflection angles for ITCR #3 are plotted versus normalized crack front position in Fig. 5.53. All four quadrants show the same smooth distribution of

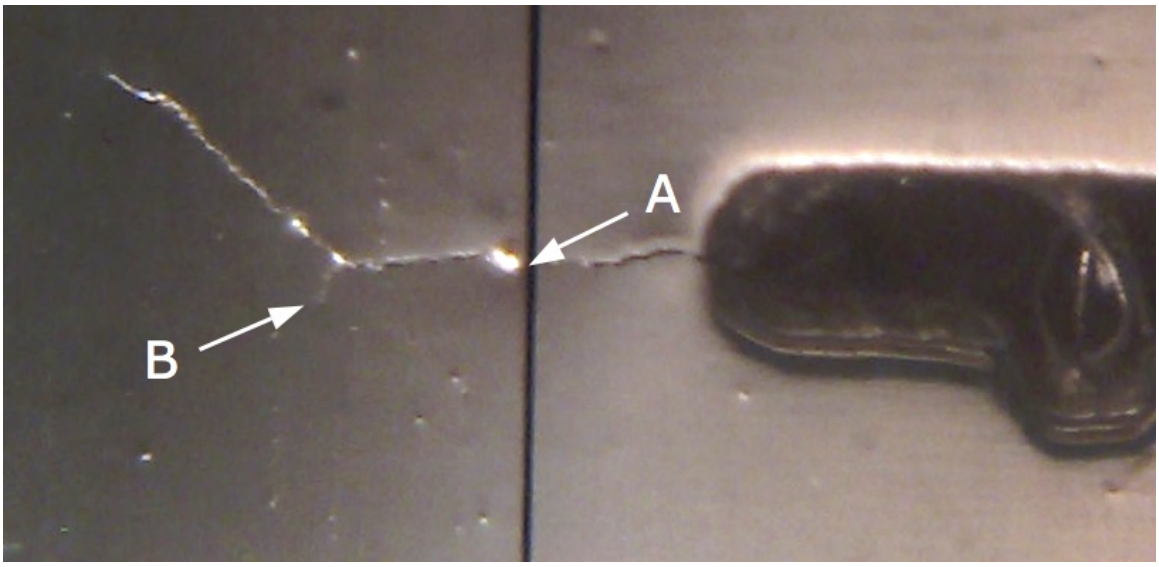

Figure 5.48: Minor crack-opening deflection (B) on left-back crack surface intercept at the point where dominant crack path turns toward the crack-closing direction after approximately 0.4 mm of co-planar growth from pre-crack tip (A). Image taken through stage microscope at 56,100 cycles.

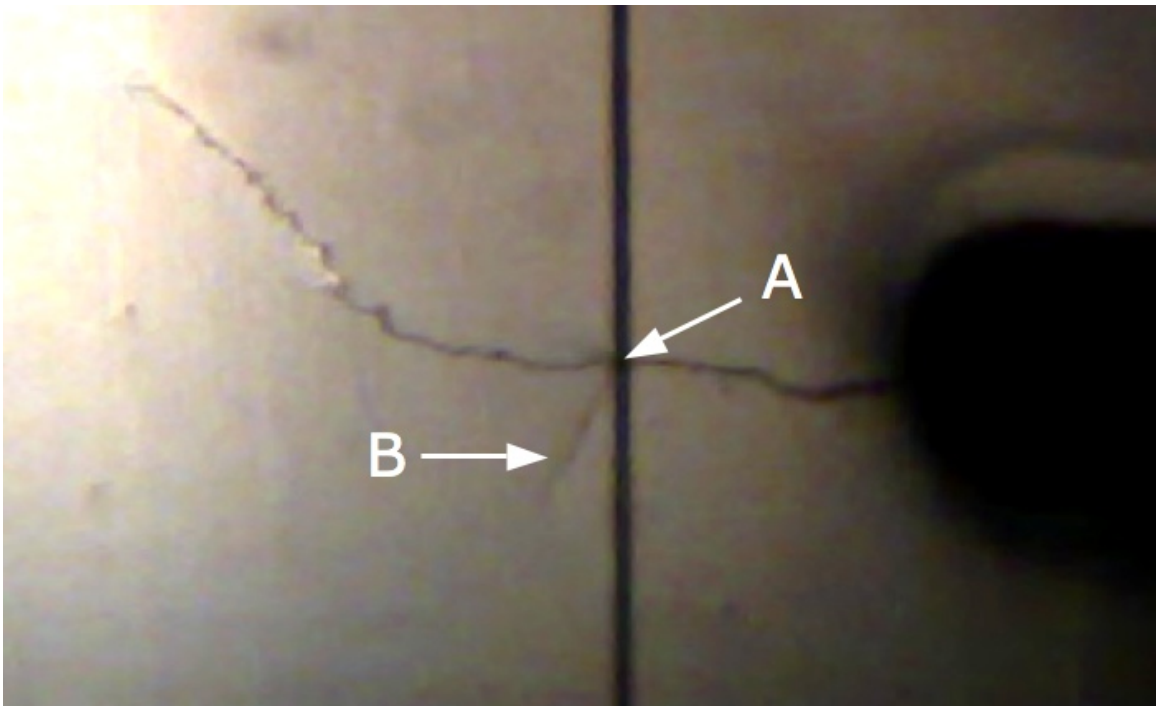

Figure 5.49: Minor crack-opening deflection (B) on right-front crack surface intercept, seen at 66,000 cycles emanating from initial pre-crack tip (A).

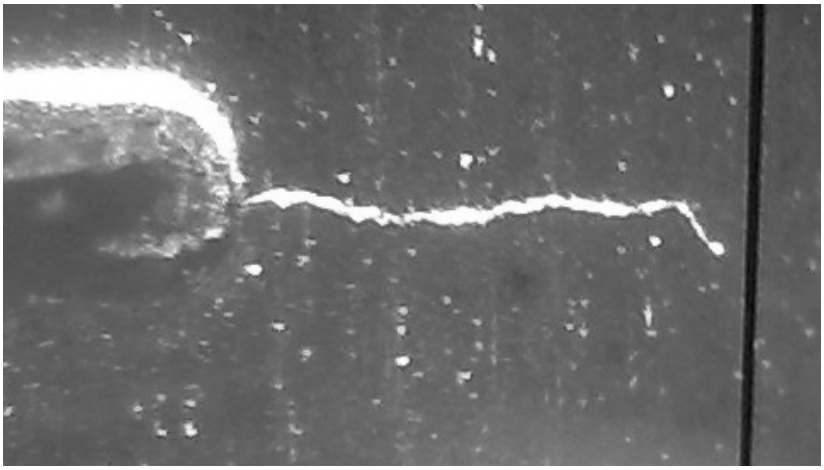

(a) N = 20,000

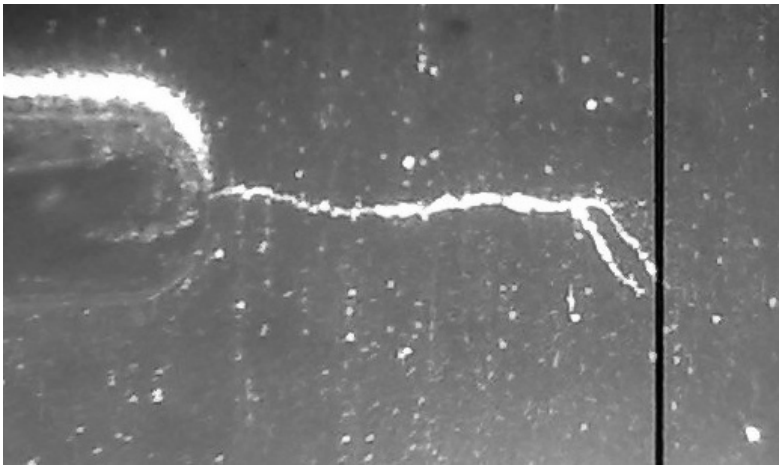

(b) N = 43,300

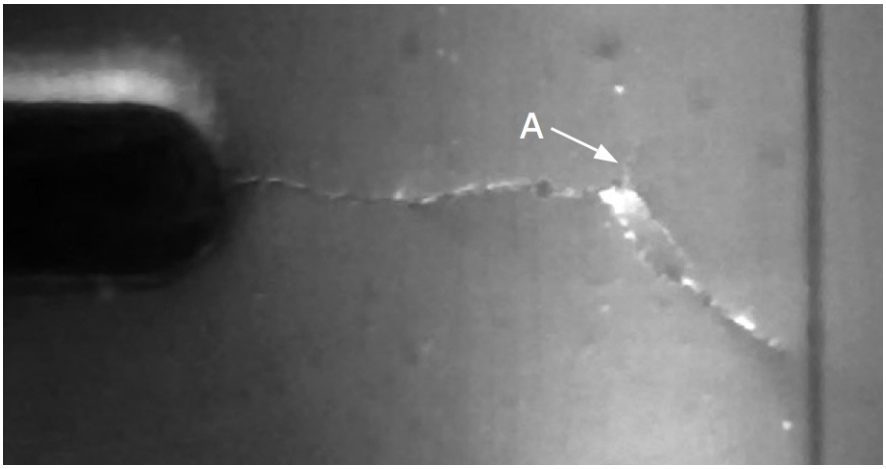

(c) N = 66,000

Figure 5.50: Formation and merging of two parallel shear-oriented crack branches at right-back crack surface intercept, shown at (a) 20,000 cycles, (b) 43,300 cycles, (c) 66,000 cycles. A small tensile crack branch is apparent at 66,000 cycles (A).

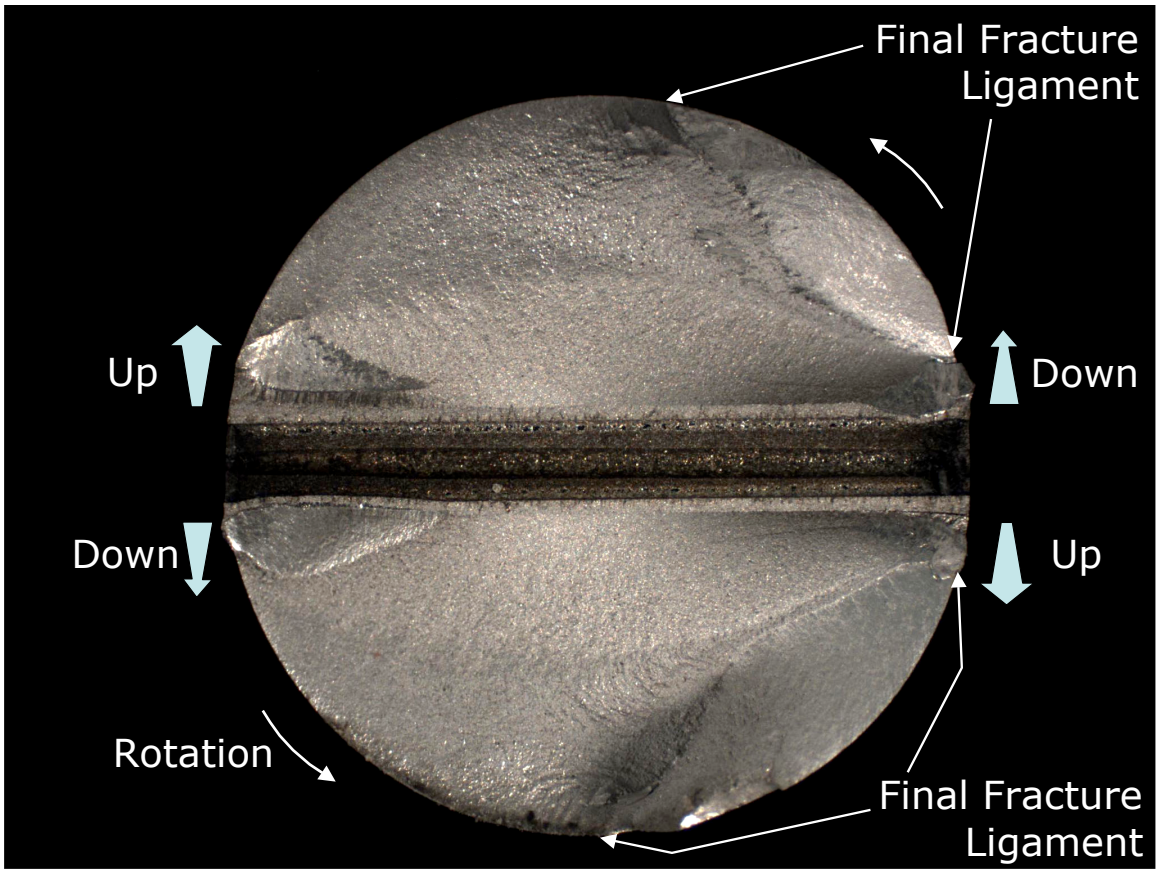

Figure 5.51: Bottom fracture surface of ITCR #3 (180° out-of-phase). Triangular regions above and below left side of pre-crack are smearing from crack surface contact; similar damage is present but less visible on right.

crack deflection from co-planar at the center of the specimen to a crack-closing angle that approaches 40°, with thin ligaments of co-planar growth at all four surface intercepts. Although unexpected results for this type of loading were already considered and explained for the NASA thin-walled tubular specimens, the magnitude of the crack-closing deflection in this specimen is even more difficult to explain.

No combination of LEFM parameters previously discussed predict the trend seen in these data. While the NASA data revealed the somewhat counter-intuitive result that the positive-angle deflections were in fact likely tensile crack branches in spite of the crack-closing orientation, the same explanation does not work in this case. None of the potential kink stress intensities or SIF ranges reach maximum values near the

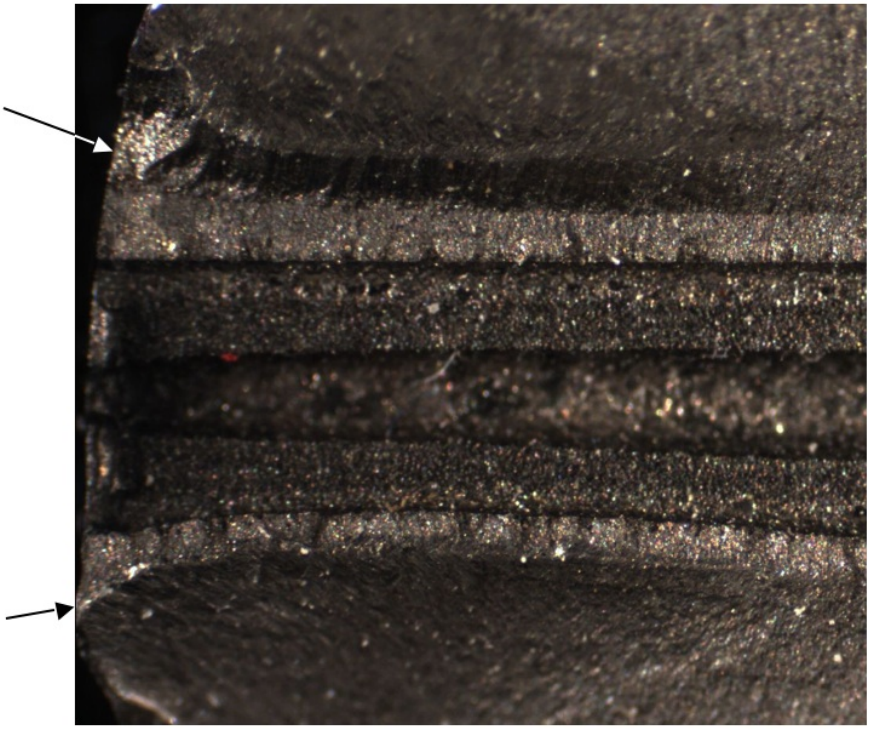

Figure 5.52: Penetration of co-planar fatigue crack growth (indicated by arrows) on left side of ITCR #3.

significant positive angles observed in specimen ITCR #3, and there is no trend in any of the values toward an increasing θ with x/b (moving out toward the maximum radius of the specimen). As an example Fig. 5.54 shows the kink SIF distributions versus deflection angle θ at the $x/b = 0.79$ location, in which it can be seen that the observed crack angle is not along an orientation that indicates any large crack driving force. The shallow positive angles observed in the NASA data for N18L and N19 are the highest location θ for any of the traditional crack driving forces as currently formulated. But there is one manipulation of LEFM terms that does produce the intended results, though it challenges some standing physical assumptions.

The SIF values for infinitesimal crack kinks have been used in these analyses in lieu of pure stress quantities such as $\sigma_{\theta\theta}$ and $\tau_{r\theta}$ because as explained before, they yield essentially the same predictions for crack path. All of the Mode I SIF calculations so far have assumed that any orientation of an infinitesimal kink that results in a negative

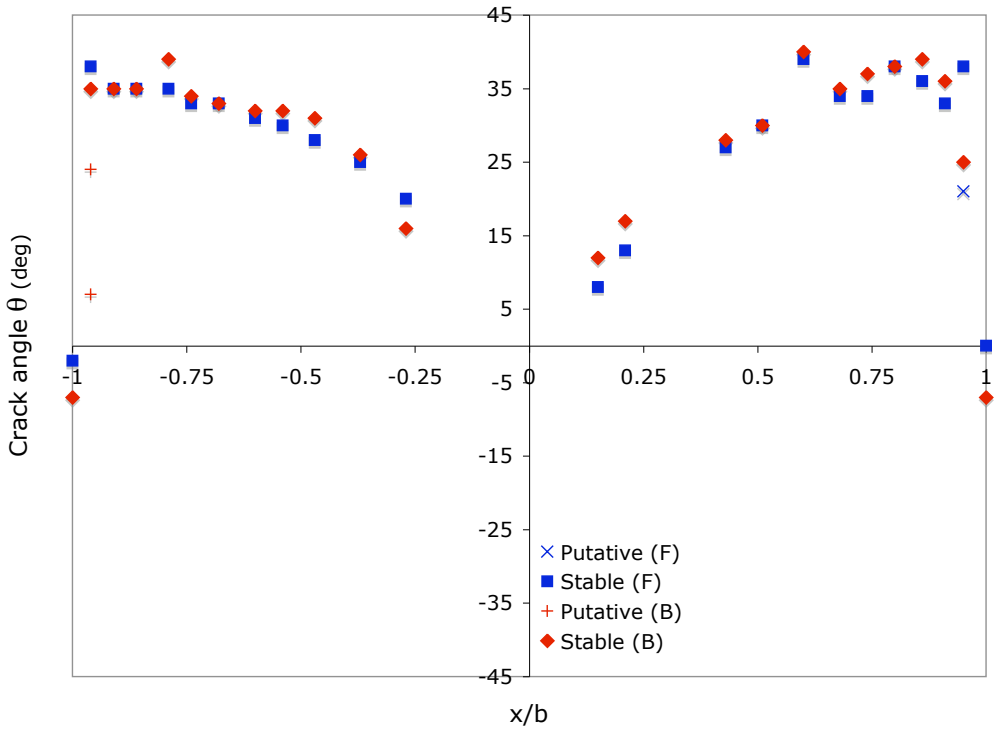

Figure 5.53: Crack deflection angle versus crack front position for ITCR #3, 180° out-of-phase loading.

value of k_1 should be replaced with $k_1 = 0$, as a closed crack would not contribute to crack propagation. The implementation of this rule can be seen in Fig. 5.54(a), for example, where k_{1b} becomes zero just above $\theta = 0°$ because a positive-deflected crack would be closed under torque, and thus $\Delta k_1 = k_{1a}$ beyond that point. Indeed this has been the approach used by the cited previous studies of mixed-mode crack growth, particularly in the rolling contact fatigue applications. This assumption was reconsidered and maintained in the implementation of the $\overline{\Delta k}$ approach in this work, as the previous work by the author showed negligible contribution to FCGR of compressive crack loadings in comparing R = -1 and R = 0.05 data.

Despite these arguments, it is found that removing the k_1 truncating assumption and allowing Δk_1 to be calculated from the full difference between k_1 endpoints, even if one is negative, finally produces peak values of crack driving force in the range of positive deflection angles observed. In order to predict the angles accurately, the

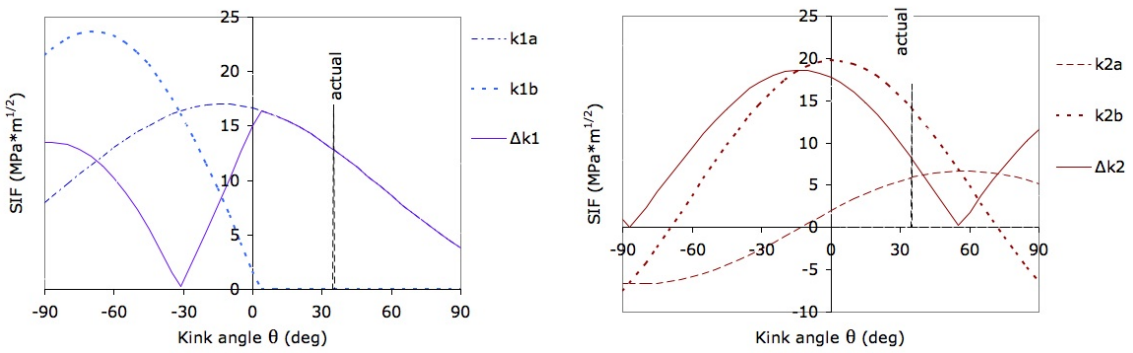

(a) (b)

Figure 5.54: Kink tip SIF and SIF range distributions in (a) Mode I and (b) Mode II at location $x/b = 0.79$ for specimen ITCR #3, 180° out-of-phase testing.

exponent $w_1 = 0.7$ has to be used, as seen in Fig. 5.55, which compares the three previously employed formulations of $\overline{\Delta k_1}$ with the observed results. The highest w_1,

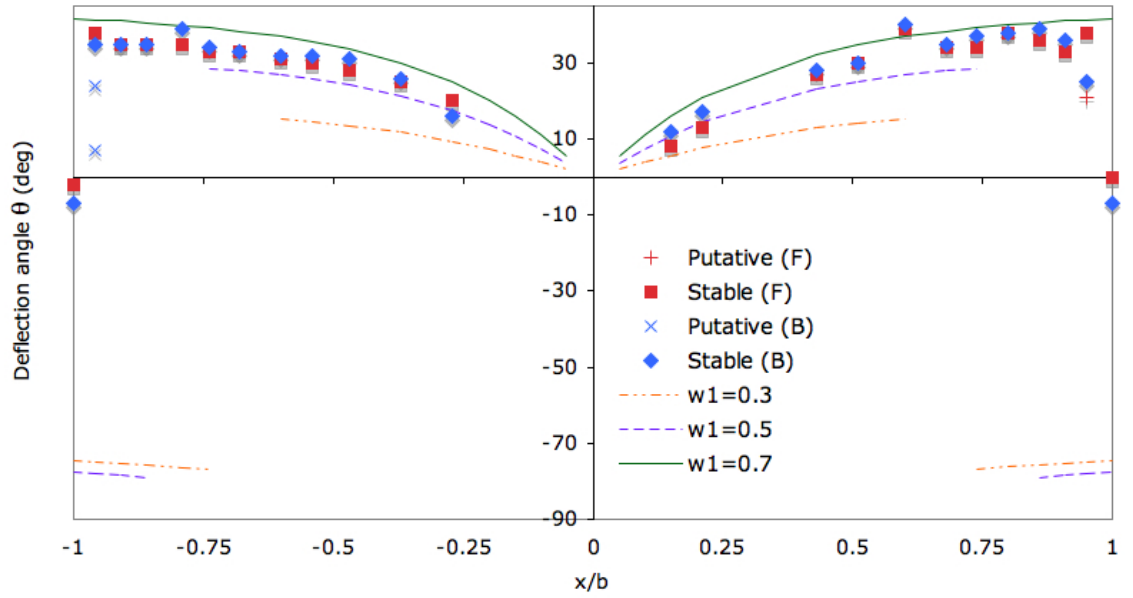

Figure 5.55: Performance of the modified $\overline{\Delta k}$ approach, which allows negative values of k_1 in predicting observed crank deflection angles for various exponents w_1.

which was the same employed in discussing the constant torsion/cyclic tension NASA data, not only improves the accuracy generally, but also avoids prediction of negative deflection angles at the outer positions, at which point the second local maximum of

$\overline{\Delta k}_1$ becomes dominant. And although the best fitting exponents are different, the inclusion of negative k_1 in this approach does not change the analysis of the previous NASA data for OP fatigue.

Finally, as there are few data to compare with any theory, it will simply be noted that $\overline{\Delta k}_{2\max}$ does predict shallow negative angles similar to those observed on the specimen surface for all three exponent selections. However, given the very limited extent of penetration of these shear crack branches from the surface, it is likely their existence is tied as closely to the plane stress state at the surface as to any particular form of $\overline{\Delta k}_2$. Further study is required to understand the role of constraint on enabling shear crack branching.

5.2.3.4 Summary of 180° Out-of-Phase ITCR Results

Crack deflection angles in the OP-tested ITCR specimen were similar to the NASA testing in that tensile branching occurred at positive instead of negative angles, but the magnitude of deflection was much larger than what was seen previously. In order to find any LEFM-based crack driving force that achieved maximum values at the large positive angles observed, the effective stress intensity factor $\overline{\Delta k}_1$ had to be modified to allow for the use of negative values of k_1 in calculating Δk_1. While this goes against common assumptions about crack propagation under Mode I closing loads, it predicts the data fairly well for the exponent $w_1 = 0.7$. If infinitesimal crack kink SIF is considered instead as a measure of crack tip stresses near the stress singularity of the pre-crack (as shown in Eq. 5.1 and Eq. 5.2), consideration of the full range of stresses is less troubling conceptually. In this case, $\overline{\Delta k}_1$ is essentially the MTSR criterion of Dahlin and Olsson [60] modified to account for mean stress effects. Exactly how these crack kinks continue to propagate under Mode I closing loads requires further study.

5.2.4 Constant Torsion/Cyclic Tension

5.2.4.1 In-Situ Crack Growth Observations

Optical measurements of crack surface intercepts on both sides of specimen ITCR #4 were taken for use in future crack growth model calibration. The projected crack lengths are presented in Table 5.8 for the front (F) and back (B) surface intercepts on the left (L) and right (R) sides of the specimen, measured from the center of the EDM slot. The crack growth rate is plotted versus crack length from the center of the EDM

Table 5.8: In-situ visual measurements of projected crack surface intercept lengths (in mm from center of EDM slot; LF = left front, RB = right back, e.g.) for ITCR #4.

N	a_{LF}	a_{LB}	a_{RF}	a_{RB}
0 (pre-crack)	1.20	1.20	1.16	1.16
2,700	1.41	1.48	1.47	1.44
5,600	1.45	1.63	1.48	1.59
10,350	1.54	1.69	1.54	1.66
20,000	1.60	1.76	1.55	1.71
30,000	1.66	1.83	1.61	1.74
43,000	1.81	1.91	1.61	1.79
56,100	2.03	2.10	1.70	1.79
66,000	2.63	2.96	1.84	2.01

slot in Fig. 5.56. Crack growth decelerated in this test as for ITCR #3, although deceleration only occurred over approximately 0.1 mm, and there was no visible crack branching or deflection to which this could be attributed as in the previous case. While it is possible that pre-cracking techniques may result in residual stresses and/or hardening ahead of the pre-crack tip, there was no measured deceleration in specimens #1 and #2, which underwent the same pre-cracking procedure, and the deceleration in specimen #3 may be attributed to crack branching and deflection.

Crack growth occurred at a shallow tensile angle in all four quadrants, with growth

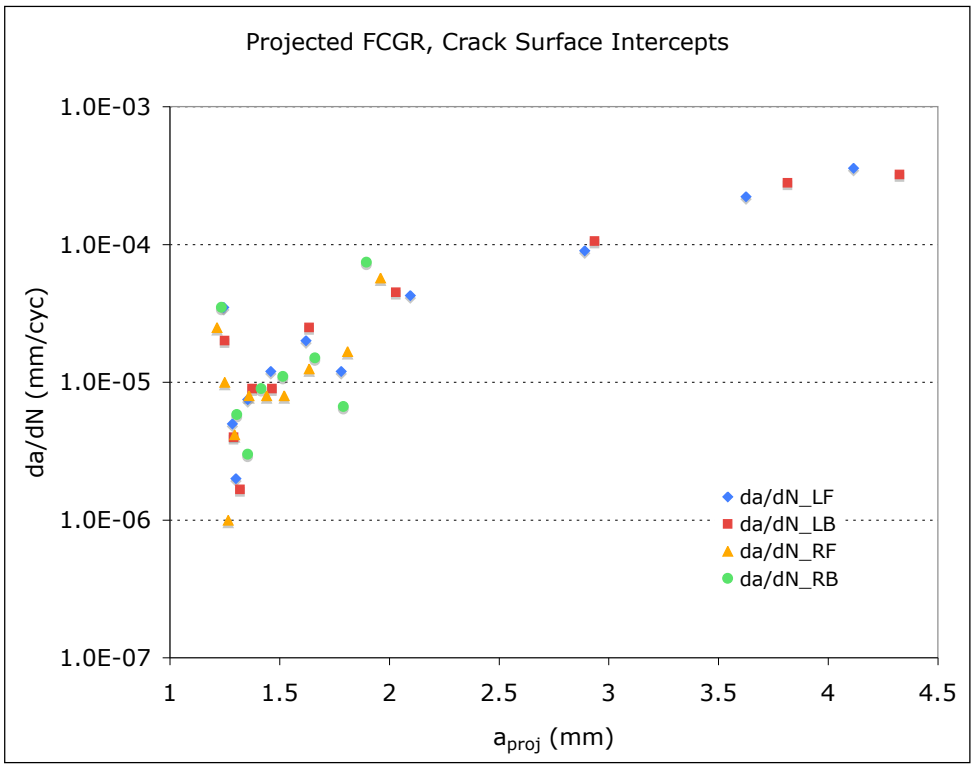

Figure 5.56: Crack growth rate (secant-slope of projected crack lengths) from in-situ observations of crack surface intercepts, ITCR #4 (LB = left back, RF = right front, e.g.).

rate on the left side outpacing the right. There was a marked increase in the magnitude of the deflection angle after approximately 0.45 mm of crack growth from the pre-crack tip on the left-front surface intercept and after approximately 1.55 mm on the left-back intercept. A composite image of the left crack surface intercept, with the increases in deflection angles marked by arrows, is shown in Fig. 5.57.

5.2.4.2 Post-Test Characterization

An overview of the bottom fracture surface is shown in Fig. 5.58. Labels on the left side of Fig. 5.58 indicate (A) the point of deflection increase on the left crack intercept and (B) the final crack front of the tested fatigue loading. There is a final increment of crack growth visible prior to final fracture, which took place under a

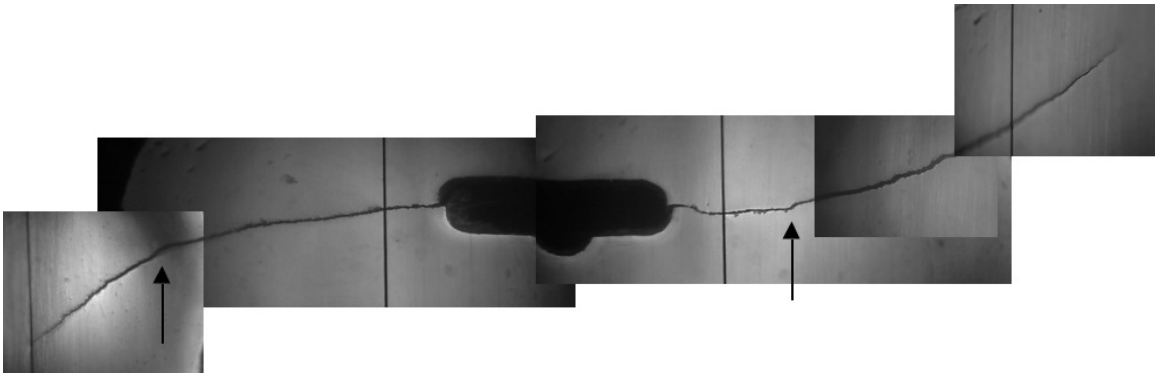

Figure 5.57: Composite image of left crack surface showing increases in deflection angle during testing. Images taken through stage microscope during testing after 83,400 cycles.

higher cyclic tensile load and constant torsion to accelerate the end of the test and reduce the required fracture load.

All four quadrants display a smooth distribution of negative (tensile) crack deflection angle from co-planar at the center to a maximum deflection at the surface. Under oblique lighting, a very small lip between the pre-crack and the mixed-mode fatigue crack was visible, with the severity of the lip increasing with radius. This feature is shown in Fig. 5.59 for the bottom right fracture surface, with the light source placed to the right side of the image as shown; the thin bright line between the pre-crack and the bulk of the fatigue crack is an increment of crack growth at a steeper angle than the rest of the crack. These features were visible in the plastic castings used for sectioning and crack angle measurement and spanned a distance of 0.4-0.5 mm of crack growth before turning to the shallower angle that dominated the rest of the test. Therefore, the angles of the initial minor deflection were included in the data below in Section 5.2.4.3 as "putative" crack deflections prior to a stable crack angle. These putative deflections may be an artifact of the pre-cracking procedure.

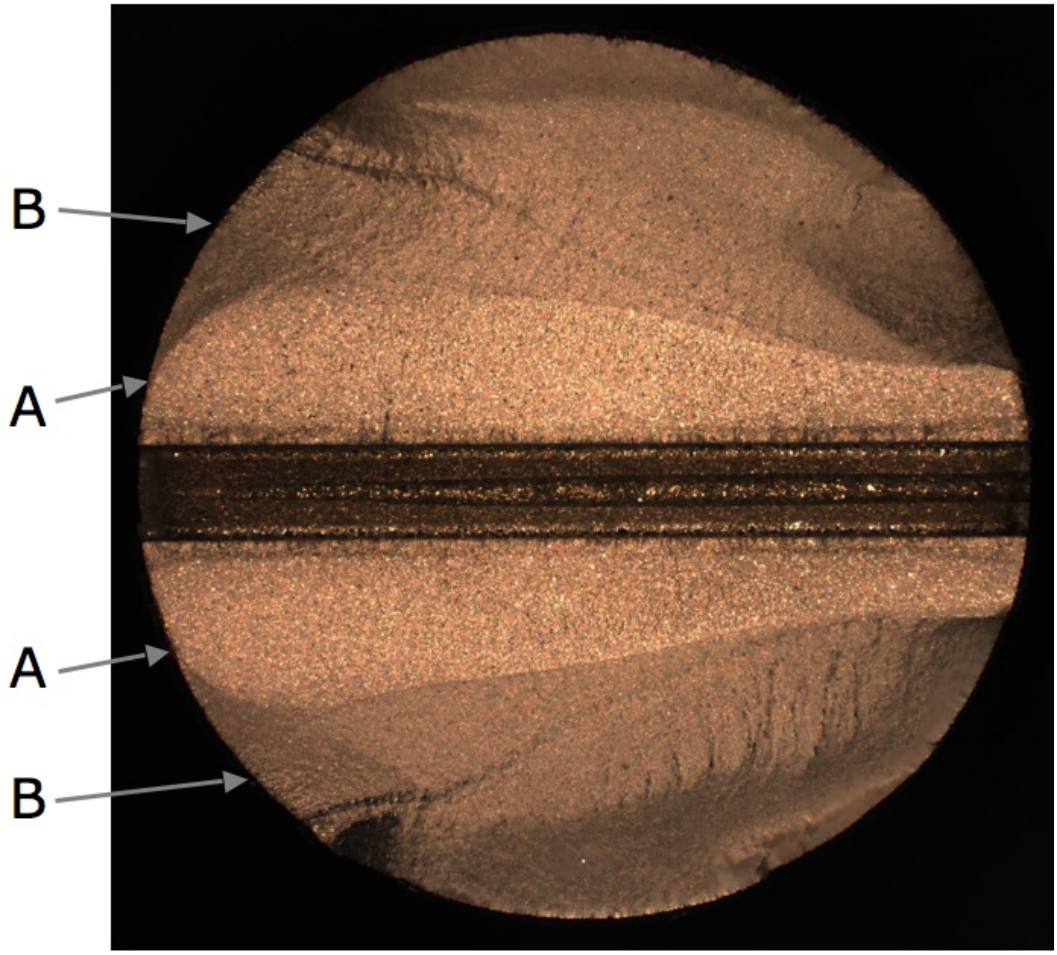

Figure 5.58: Bottom fracture surface of ITCR #4 (constant torsion/cyclic tension). Labels (A) indicate notable increase in deflection angle and (B) end of tested fatigue loading prior to increase failure load cycles.

5.2.4.3 Crack Deflection Angles

Measured crack deflection angles for ITCR #4 are plotted versus normalized crack front position in Fig. 5.60. The data for putative crack deflections at steeper angles represent the small lip ahead of the pre-crack discussed above in Section 5.2.4.2. All four crack fronts show the same general trend as the NASA data at this condition, showing that there is a moderate effect of K_{max} that, under the influence of the $k_{1\max}$ at -70.5° contributed by the constant Mode II loading, gradually "tips" the plane of crack growth downward as K_{II} increases with radius. Thus Fig. 5.60 also shows angles predicted by two formulations of $\overline{\Delta k}_{1\max}$. Although the trend is qualitatively similar

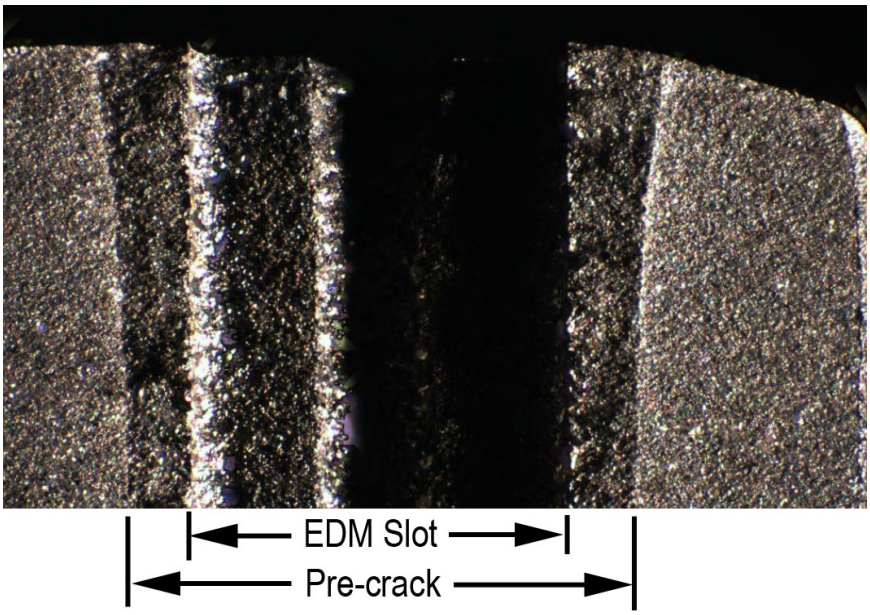

Figure 5.59: Bottom right fracture surface of ITCR #4 showing small initial crack deflections from the pre-crack (bright lines between the pre-crack and subsequent fatigue crack) highlighted by oblique lighting.

to the NASA data, the magnitude of deflection observed is much less than expected.

In the earlier discussion, it was noted that the higher exponent $w_1 = 0.7$ needed to be employed for this effective SIF range to predict the data accurately, suggesting only a modest influence of K_{max} on crack branch propagation. However, it can be seen in Fig. 5.60 that even this value of w_1 greatly over-predicts the stable crack growth direction, although it does provide a reasonable bound to the very small initial deflections (denoted "Putative" in the graph). In order to represent the stable crack directions, the exponent needs to be set to $w_1 = 0.95$. This shows there is even less influence of K_{max} on crack growth under constant torsion/cyclic tension loading for the ITCR specimen than the thin-walled tubular specimen, which again is likely due to the different levels of constraint in the stress fields of the two specimens.

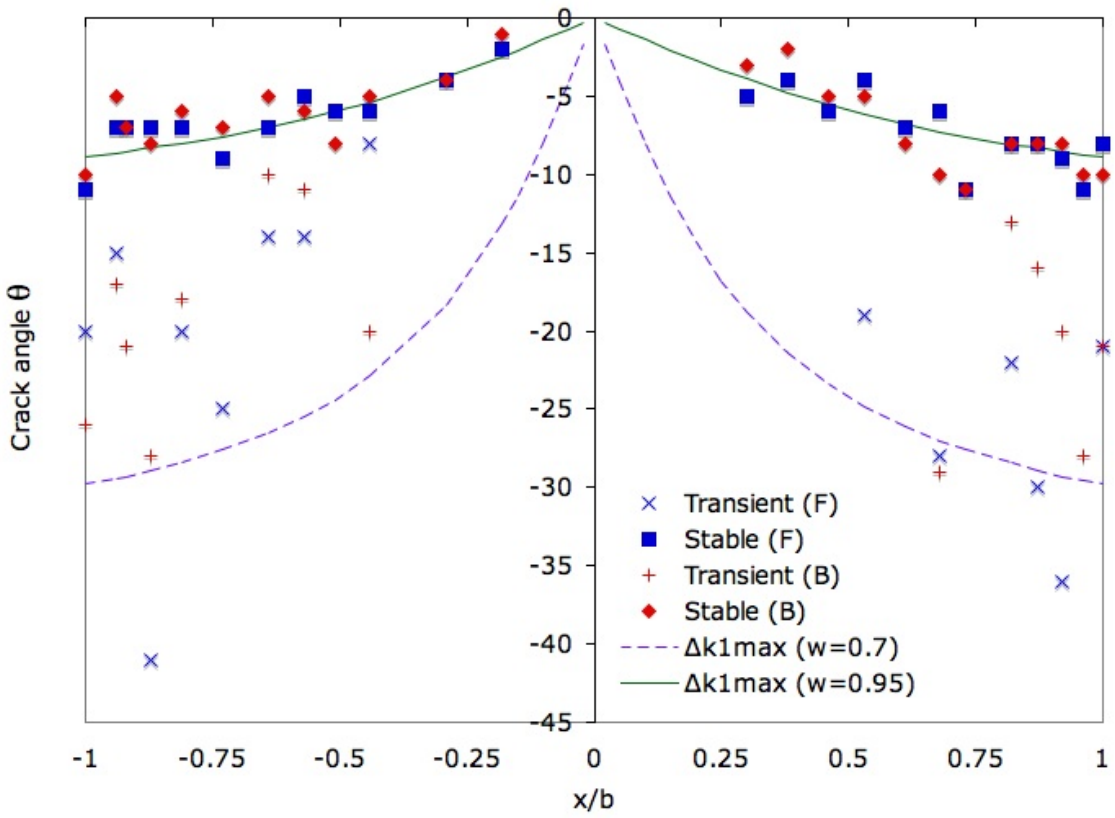

Figure 5.60: Crack deflection angle versus crack front position for ITCR #4, constant torsion/cyclic tension loading.

5.2.4.4 Summary of Constant Torsion/Cyclic Tension ITCR Results

Testing of the ITCR specimen under constant torsion/cyclic tension resulted in a single trend of tensile crack deflection that was qualitatively similar to previous observations in testing by NASA. The increasing negative crack deflection angle once again indicates the influence of K_{max} in crack growth and path selection, but the magnitude of deflection – and the relative influence of K_{max} – was much lower in the ITCR specimen than the thin-walled tubular specimen. Only a very small initial crack kink approached the previous predictions, but the crack path quickly stabilized at a much shallower angle. It is not clear whether this initial putative kink is an artifact of the purely Mode I pre-cracking or the result of a different state of stress in the ITCR specimen.

5.2.5 Discussion

The results presented above from fatigue crack growth testing of two different types of specimens under four different types of mixed-mode loading show that LEFM parameters can be used to predict the crack branch deflection angle for various non-proportional loadings. An effective stress intensity factor range $\overline{\Delta k}$ based on the Walker crack growth rate equation and using the infinitesimal kink tip SIFs k_1 and k_2 was able to account for the influence of mode mixity on branch crack orientation, although its ability to predict transition between tensile and shear crack branching is unclear. The $\overline{\Delta k}$ approach was utilized as a special case of the $(da/dN)_{\max}$ approach in the absence of sufficient material data to calculate kink crack growth rates from $\overline{\Delta k}_{1,\max}$ and $\overline{\Delta k}_{2,\max}$, particularly given the lack of available data on stable Mode II crack growth. A $(da/dN)_{\max}$ approach based on a Mode I FCGR equation provided by Soboyejo *et al.* [65] using data from Mercer *et al.* [66] (given in Eq. 3.1) was not able to predict deflection angles for Mode I crack branches. However, it is possible that a formulation of the current approach using a FCGR law based on Mode I and Mode II crack growth data may improve the ability to predict modal transition in addition to branch angle, since the fitting parameters for the FCGR law between the two modes are likely different.

Although $\overline{\Delta k}$ was able to accurately predict crack path direction for varying mode mixities within a given test condition, it was not possible to predict the data for all cases with a single set of exponents for $\overline{\Delta k}_1$ and $\overline{\Delta k}_2$. This shortcoming would not be corrected by a full $(da/dN)_{\max}$ approach and suggests that the LEFM approach employed may be inherently limited as a general predictor of crack branching behavior under non-proportional mixed-mode fatigue growth. There are a few areas in which problems with this approach may arise.

First, the difference in results between the thin-walled tube specimens and the ITCR specimens likely arises from in-plane and out-of-plane constraint, which was

not characterized. The out-of-plane constraint differed between specimens in that the thin-walled tubes create a plane-stress condition, while the bulk of the ITCR specimen creates a plane-strain condition. The shift in transition for in-phase testing between the specimen configurations suggest the added constraint of plane-strain conditions hinders shear slip and delays Mode II crack branching. Additionally, as discussed in Chapter 2, differences in the non-singular T-stress term of the crack tip stress field, which was not modeled in this work, can alter the distribution of shear stresses ahead of a crack. However, these variables would not directly explain the necessity of using different exponents for $\overline{\Delta k}$ between loading conditions for the same specimen type.

Secondly, as it was desired to find a linear elastic basis for crack path prediction, the distribution of plastic deformation, residual stresses and crack tip displacements were not analyzed. Some of the cited publications in RCF crack growth discussed interactions between sequential and overlapping Mode I and Mode II sub-cycles, which could be attributed to residual plastic opening displacements and their effect on crack surface interference or closure. Because this was the first attempt at experimental validation of the new ITCR design with a limited number of specimens, a full analysis that would enable accurate interpretation of clip-gauge data to quantify closure or interference was not attempted.

Thirdly, it was stated at the outset that this research was considering crack deflection under the general assumptions of homogenous, isotropic material behavior. The primary focus was LEFM characterization of crack path determination under non-proportional mixed-mode loading. However, crack growth behavior is of course not simply the result of the crack driving force, but also of the material properties that determine crack growth resistance. While SEM fractography was used to investigate obvious visible differences between Mode I and Mode II crack branches and suggested that different dominant crack growth mechanisms were present, the specific microstructural mechanisms of damage were not explored.

A number of previous studies cited in Chapter 2 reported that modal transition behavior varied between materials tested under identical conditions, such as aluminum alloys versus steels. One purpose of this research was to obtain data on crack path direction and modal transition in Inconel 718 in light of the fact that these phenomena already appeared to be highly material dependent. The fact that a single formulation of $\overline{\Delta k}$ could not be used even for a given specimen type could be the result of a more complex interaction of damage accumulation in the process zone with the constituents of the material microstructure. The range of SIFs tested in the current work fall within the envelope of 10 - 30 $\mathrm{MPa}\sqrt{\mathrm{m}}$ described by Mercer *et al.* [66] to be the near-threshold and lower Paris regimes, and the SEM micrographs of Mode I crystallographic transgranular cracking at $R = 0.1$ are similar, so dislocation activity is low according to Mercer's transmission electron microscopy (TEM) studies. Still, the stress states caused by the different loading conditions may predispose different failure mechanisms at the microstructural level to be operative, such as the fracture or cleavage of the Ni_3Nb δ-phases observed by Mercer *et al.*, which they suggested may involve some dislocation motion. This in turn would explain the varying influence of kink tip load ratio that required different fitting exponents between load cases. The influence of load path in non-proportional loading could be even more justified for the shear (Mode II) crack branches, the SEM micrographs of which visibly displayed signs of slip-based damage. The role of material properties on modal transition needs to be understood in terms of specific micromechanisms of damage rather than the simplistic material property ratio $\tau_{\mathrm{crit}}/\sigma_{\mathrm{crit}}$ proposed by Chao and Liu [22] to quantify transition between the MTS and MSS criteria.

The LEFM approach discussed in this work to non-proportional mixed-mode fatigue crack growth cannot in its current form provide a single formulation of criteria to predict crack direction and transition for all cases, but it does allow for quantification of the relative influences of maximum and cyclic stresses for different types

of loading. Application of this method to similar data from other materials with various microstructures and related micromechanisms of damage can help move the research question from simply predicting crack branching by LEFM to determining the relationship between specific micromechanisms and the fitting exponents required for accurate LEFM modeling of non-elastic damage phenomena.

CHAPTER 6

SUMMARY & CONCLUSIONS

6.1 Summary

A novel Inclined Through-Crack Round (ITCR) specimen design has been developed. The stress intensity factors for a variety of crack sizes and inclination angles were analyzed in FRANC3D and a closed-form SIF solution for K_{I}, K_{II}, and K_{III} was presented in Chapter 4. Although the non-zero inclination ($\beta = 30°$) version of the specimen was not tested, numerical analysis shows that it generates a significantly higher proportion of K_{III} than previously published three-mode specimen configurations generated (see [67], e.g.) in addition to a wide range of K_{II}.

Conventional notched thin-walled tubular specimens, which were tested at NASA Marshall Space Flight Center, were also analyzed in FRANC3D to determine the effect of pre-crack skew and curvature (caused by manufacturing defects) on SIF distribution across the crack front. It was shown that skew of the crack front relative to the radial axis produced moderate shifts in K_{I} and K_{II}, while faithfully modeling crack front curvature instead of using a straight line approximation resulted in more pronounced differences K_{I} and K_{II} near the free surface intercepts. The most notable effect however was the introduction of increasing amounts of K_{III} with skew, which increased rapidly from the inner to the outer surface for straight line cracks but were smoothed to a nominal constant value with the introduction of curvature. This influence of crack front shape was observed to produce modal transition between crack branch types along a single crack front on at least two cracks in NASA-tested specimens.

The two different specimen configurations were used to generate fatigue crack path direction data in polycrystalline Inconel 718 superalloy under four types of mixed-mode loading at room temperature: proportional in-phase; constant K_{I}/cyclic K_{II};

constant K_{II}/cyclic K_{I}; and 180° out-of-phase sinusoidal K_{I}- K_{II} loading. In-phase tests were well characterized as expected by the standard monotonic MTS and MSS criteria, and the results of this testing established that modal transition does occur in Inconel 718 at high levels of Mode II loading, when K_{II} equals or exceeds K_{I} under plane-stress conditions; transition is delayed to mode mixity $\phi = 55°$ - 58° for plane-strain conditions. Modal transition was also observed in the constant K_{I}/cyclic K_{II} and out-of-phase load cases, although for the ITCR specimen the out-of-phase transition only took place in a very shallow surface layer. The out-of-phase deflections for both specimen types also presented the counter-intuitive result of tensile crack branches turning toward a positive-angle, Mode I closing orientation under maximum torque while shear-driven cracks turned to negative-angle crack-opening orientations under maximum torque. Both specimen types produced only tensile crack deflections in the case of constant K_{II}/cyclic K_{I} loading, with crack surfaces tilted downward toward the K_{II}-induced tensile stress. Different dominant crack growth mechanisms for the two modes of branch crack were confirmed by SEM observation of different overall fracture surface morphologies of Mode I and Mode II crack branches.

The non-proportional load cycles established that a two-parameter model of crack growth driving force, based on ΔK as well as K_{max}, is required as a baseline for any attempt to predict crack growth direction with LEFM, as crack deflection angles were clearly influenced by both quantities. Starting from Hourlier's proposal to predict crack path based on $(da/dN)_{\max}$, an effective stress intensity factor range $\overline{\Delta k}$, based on Walker's FCGR model and kink tip SIFs k_1 and k_2, was used to predict crack deflection angle as a function of mode mixity quite accurately by maximizing $\overline{\Delta k}_1$ or $\overline{\Delta k}_2$ for a given crack branch type under a given load condition. Although the inability to characterize all of the data sets for a given specimen type with a single formulation of $\overline{\Delta k}$ rules out this approach as a final solution, it has provided an effective means for describing the trends and differences among the data. The

exponents used to manipulate $\overline{\Delta k}$ in the treatment of the data were chosen rather arbitrarily based on a nominal value from previous Mode I crack growth research, but they were used primarily as a tool to illustrate the trends in crack driving force for different conditions. The need for different exponent sets for $\overline{\Delta k}$ highlights the varying relative contributions of ΔK and K_{max} in each case and suggests that in-plane and out-of-plane constraint, plastic deformation analysis, and quantification of crack surface interference and closure may need to be included in a complete model for predicting crack path. An additional shortcoming is the lack of a consistent transition condition when defined in terms of the presumed crack driving forces. These observations may rule out a purely LEFM approach to this problem. However, investigation of the relationship between material-specific damage micromechanisms and the relative influence of cyclic and maximum stresses as captured in the $\overline{\Delta k}$ formulation may still provide a robust predictive tool for many cases.

The ITCR specimen design has provided a useful experimental tool for generating a broad array of mixed-mode loading conditions in a single test, which provides multiple data points for model generation and can quickly identify modal transition between tensile and shear cracking. However, the use of a solid bar specimen with a thin central flaw creates a different state of stress from the established thin-walled tubular specimen in two ways: in the sense of plane strain (for the interior of ITCR) versus plane stress (for tubular specimens); and in terms of in-plane constraint ahead of the crack tip as described by the non-singular T-stress in the complete elastic stress solution for a cracked body, although this is not yet quantified. Differences between the two specimen types resulted in higher values of K_{II} required for transition to Mode II branch crack growth than expected from the NASA data. A full 3-D analysis of the interior stress field is required for a complete understanding of its crack path behavior and how to use data from both specimen types to characterize fully the role of stress state on crack path selection.

6.2 Research Contributions

This research has made several contributions to the understanding of non-proportional mixed-mode fatigue crack growth in an important aerospace superalloy:

1. Previously unavailable data on crack branching direction under mixed-mode fatigue in Inconel 718 has been generated for proportional and non-proportional loading at room temperature.

2. The $\overline{\Delta k}$ approach described has provided an initial basis for accurately predicting crack branch direction in an LEFM framework for a variety of loading conditions. The loading types presented expand beyond the special cases of rolling contact fatigue in which a significant portion of mixed-mode fatigue crack growth research has been published.

3. Although a single set of fitting parameters could not be used to predict crack angle for all load cases, the current framework provides a clear measure of the varying influence of maximum and cyclic SIFs and thus has moved the research question from simply determining crack branch angles to refining the physical/micromechanical basis for the varying crack driving force formulations.

4. SEM micrographs of fracture surfaces have been obtained to (a) confirm the crystallographic transgranular Mode I cracking previously documented by Mercer *et al.* and (b) illuminate the distinct morphological appearance of Mode II crack branches which are dominated by slip-enhanced transgranular cleavage. Fractographic examination of these two crack branch types should allow for quick discernment of the dominant fracture mode in the future.

5. A novel Inclined Through-Crack Round (ITCR) specimen design has been designed, analyzed, and experimentally validated for generating a wide range of mixed-mode crack growth data in a single test, for producing three-mode load

conditions for non-zero β angles, and for generating crack growth data under different stress states than standard tubular specimens for the study of constraint in crack path determination.

6.3 Conclusions

The following conclusions can be drawn from this research:

1. Fatigue crack branching experiences a modal transition from Mode I to Mode II dominated crack growth at a mode mixity $\phi = 44°$ - $58°$ for in-phase proportional fatigue loading, depending on constraint, with plane stress favoring earlier transition than plane strain. The crack branch types are fractographically characterized by two distinct fracture surface morphologies: a sharply faceted crystallographic transgranular cracking under Mode I crack growth, and a flatter, slip-enhanced transgranular cleavage under Mode II crack growth.

2. For a given loading type and specimen configuration, crack branch deflection angle can be accurately predicted as a function of mode mixity $\phi = \tan^{-1}(K_{\mathrm{II}}/K_{\mathrm{I}})$ by maximizing the Walker effective SIF range for an infinitesimal kink $\overline{\Delta k} = \Delta k^{w} k_{\max}^{1-w}$ for the appropriate mode. In some cases a specific modal transition ratio of $\overline{\Delta k}_2/\overline{\Delta k}_1$ could be identified above which Mode II branching would occur, and below which, Mode I.

3. Transition in the thin-walled tubular specimen occurred near $\overline{\Delta k}_{2\max}/\overline{\Delta k}_{1\max} =$ 0.57-0.60 for in-phase testing and 0.48-0.49 for constant K_{I}/cyclic K_{II} testing; for the ITCR specimen those values are 0.64-0.68 and 0.60-0.64, respectively. Transition to shear cracking in the 180° out-of-phase ITCR specimen only took place in very thin ligaments at the specimen surface, which was likely dominated by the influence of plane-stress conditions. The differences between the two specimens indicates that plane-stress conditions in general promote the

formation of shear branch cracks better than plane-strain conditions.

4. Using the above formulation, it was found that the exponent w required in $\overline{\Delta k}$ for best fit varied with mode of branch crack growth, loading type, and specimen configuration. While this was instructive in terms of highlighting the relative roles played by SIF range and maximum SIF in different types of crack growth, it precludes the use of $\overline{\Delta k}$ in this form as a general predictor of crack branch direction. Variation between tests is indicative of the need to include constraint stresses in a crack path model, and the need to consider elastic-plastic modeling of crack tip deformations which can vary by load path.

5. This project was initiated with the intent of developing data for a crack path prediction model for mixed-mode loading that could be implemented in an LEFM-based fracture modeling framework like the FRANC3D software package. Despite the lack of a single formulation of predictive crack driving force for all loading types, the success within each type of experiment at predicting the direction of crack branching as a function of two-parameter mode mixity suggests that with additional data, a sufficient refinement of this approach could be implemented in crack growth software as an improvement over the standard monotonic MTS/MSS criteria.

6. Also using the above formulation, it was found that $k_{1\max}$ had a much stronger influence on crack growth direction in tensile branch cracks for constant K_{I}/cyclic K_{II} testing than for constant K_{II}/cyclic K_{I} testing. In both specimen types, a Walker exponent w of 0.3 best predicted tensile branch crack direction (indicating a greater influence of $k_{1\max}$ than of Δk_1) for the former test condition, but the latter condition required $w = 0.7$ for thin-walled tubular specimens and 0.7-0.95 for the ITCR specimen.

7. In order to generate any peak crack driving force at the observed orientation the

$\overline{\Delta k}$ for ITCR specimen data needed to include the effect of negative values of k_1. This is defensible from the perspective of kink crack SIFs being representative of original crack tip stress fields, in which case the $\overline{\Delta k}_{\max}$ criterion becomes a mean stress-modified MTSR criterion. The mechanism by which actual crack branches at this orientation continue to propagate requires explanation, but it suggests that compression of crack surface asperities under torsion enhances the Mode I crack driving force.

8. Process variations in the fabrication of specimens can result in initial flaw shapes that depart significantly from the idealized design, as observed in the thin-walled tubular specimens. Detailed BEM analyses of these pre-crack shapes showed that crack front skew (relative to the radial vector) and camber (curvature) can have a notable effect on SIF distribution across the crack front, even in a thin-walled specimen. Variation in SIF along the crack front was correlated with a mid-thickness bifurcation of crack growth in specimen N09 in particular, as the change in $K_{\mathrm{II}}/K_{\mathrm{I}}$ from the inner to the outer radius resulted in modal transition in the middle of the crack front.

CHAPTER 7

RECOMMENDATIONS

Based upon the research conducted, there are several areas in which further research would improve crack path modeling in non-proportional mixed-mode fatigue.

1. Differences between the two specimen types in terms of crack growth direction and the mode mixity required for modal transition indicate the need for a better understanding of in-plane constraint (characterized by the non-singular T-stress) and out-of-plane constraint (plane stress versus plane strain conditions) on branch crack mode and path selection. A full 3-D finite element analysis of the stress field in the ITCR specimen interior is required to include these effects in model refinement.

2. Although this project was intended to provide the basis for LEFM-based modeling of crack growth direction, and may with additional data provide a suitable empirical fit for most mixed-mode load cases encountered, the variation in $\overline{\Delta k}$ formulation between loading types suggests the need to model all of these cases in an elastic-plastic framework. The different load paths can produce different distributions of plastic deformation and residual stress – which will also be a function of the material – that may inherently predict the slight variations in tensile and shear crack branch angles for different load paths without the need for arbitrarily varying fitting parameters.

3. Just as gross quasi-static failure of a material is a function of both stress and strength, crack growth, including its rate and direction, is a function of the crack driving force (described herein by LEFM parameters) and the material resistance to crack growth. A first approximation of the nature of this material influence on crack path was given by Chao and Liu [22] as a simple ratio of

$\tau_{crit}/\sigma_{crit}$, but this is too simplistic. Beyond a continuum approach to plastic deformation in the region of a crack tip, the influence of load path should be studied in terms of dislocation movement, interaction with microstructural phases, and the fracture or shearing of such phases. These may be used to explain the relative influence of cyclic versus maximum stresses and hydrostatic versus deviatoric stresses, which in turn may explain the variation in fitting exponents in the LEFM approach described herein. Applying the Walker effective SIF range approach to crack branch behavior in different materials with different microstructures and micromechanisms of crack growth can provide a basis for studying the influence of these different stress states on the microstructural damage processes that dictate crack path selection.

4. The ITCR specimen was designed to produce 3-mode loadings for crack growth studies, including K_{III} for initial cracks inclined to the specimen normal. The detailed modeling of the crack front shapes in the NASA thin-walled tubular specimens was also performed in part to quantify the amount of K_{III} produced by the imperfect pre-crack shapes. Given the limited amount of data in the present study, attention was focused solely on the relative effects of K_I and K_{II}, and the small amounts of K_{III} present were considered negligible. As additional data is generated, particularly through the use of non-zero β-valued ITCR specimens, the influence of K_{III} must be considered, as it may interact constructively with K_{II} stress fields in order to promote shear crack branching.

APPENDIX A

DETAILED CRACK SURFACE MODELS FOR TUBULAR FCG SPECIMENS

This appendix presents post-test fractographic measurements of the pre-crack shape and the resulting BEM representation of the pre-crack for each tubular FCG specimen analyzed which were used to generate the K_{I}, K_{II}, and K_{III} values in Table 4.2.

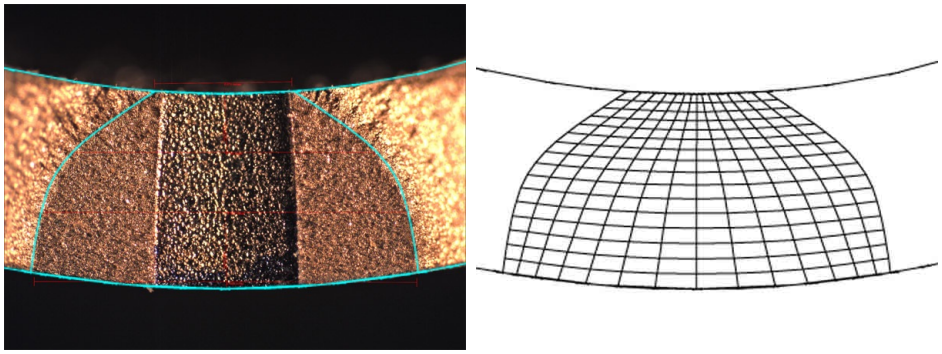

(a) (b)

Figure A.1: (a) Fractograph with BEM geometry superimposed and (b) BEM mesh of pre-crack for specimen N01.

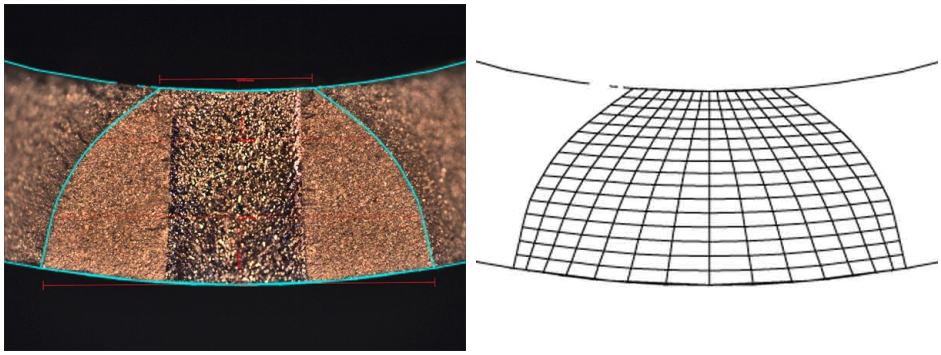

(a) (b)

Figure A.2: (a) Fractograph with BEM geometry superimposed and (b) BEM mesh of pre-crack for specimen N02.

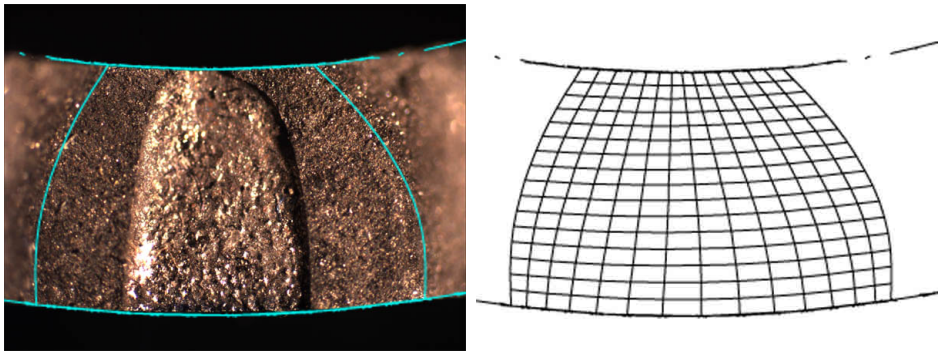

(a) (b)

Figure A.3: (a) Fractograph with BEM geometry superimposed and (b) BEM mesh of pre-crack for specimen N03.

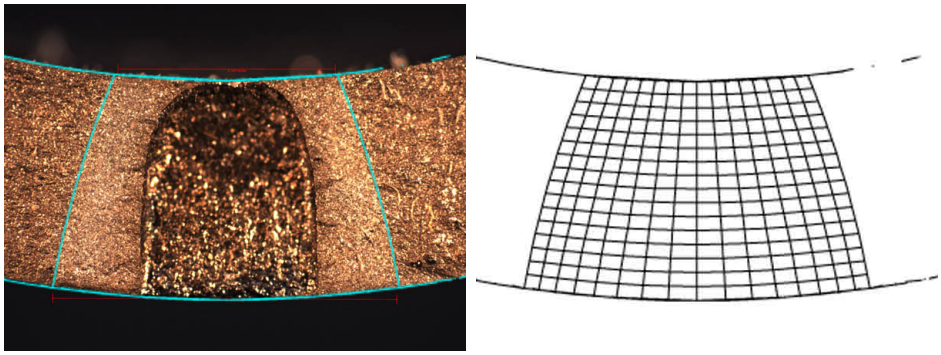

(a) (b)

Figure A.4: (a) Fractograph with BEM geometry superimposed and (b) BEM mesh of pre-crack for specimen N04.

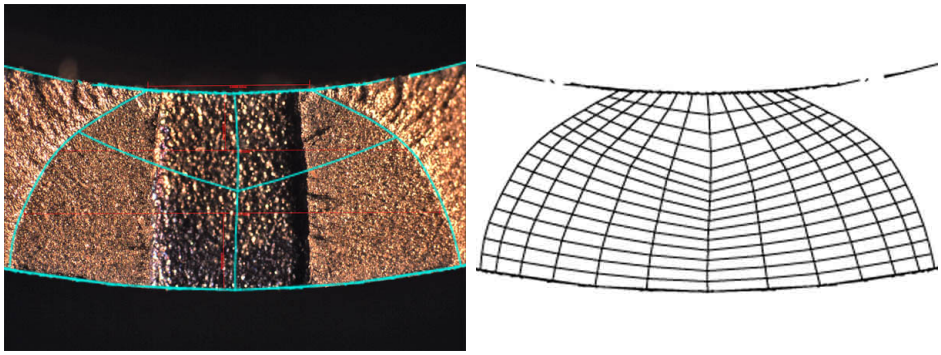

(a) (b)

Figure A.5: (a) Fractograph with BEM geometry superimposed and (b) BEM mesh of pre-crack for specimen N05.

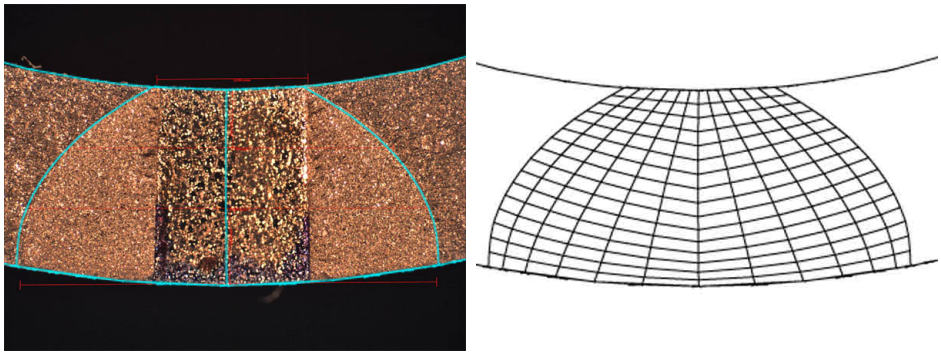

(a) (b)

Figure A.6: (a) Fractograph with BEM geometry superimposed and (b) BEM mesh of pre-crack for specimen N06.

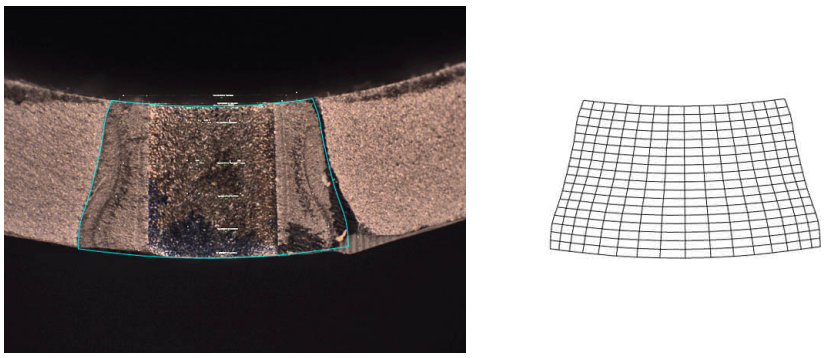

(a) (b)

Figure A.7: (a) Fractograph with BEM geometry superimposed and (b) BEM mesh of pre-crack for specimen N07. Shape of right crack front was estimated from symmetry with left front and assuming a rough bisection of contact-smeared region.

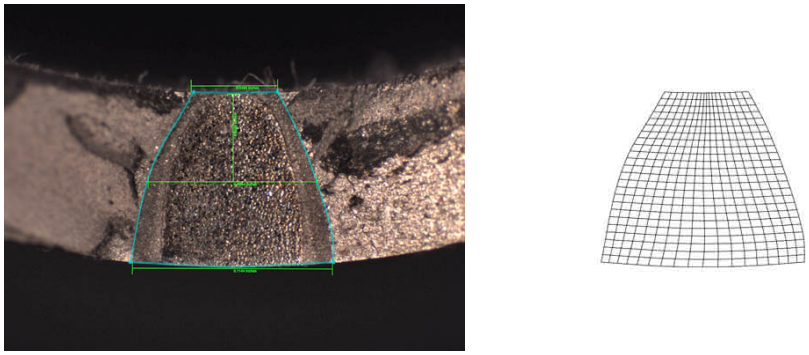

(a) (b)

Figure A.8: (a) Fractograph with BEM geometry superimposed and (b) BEM mesh of pre-crack for specimen N09.

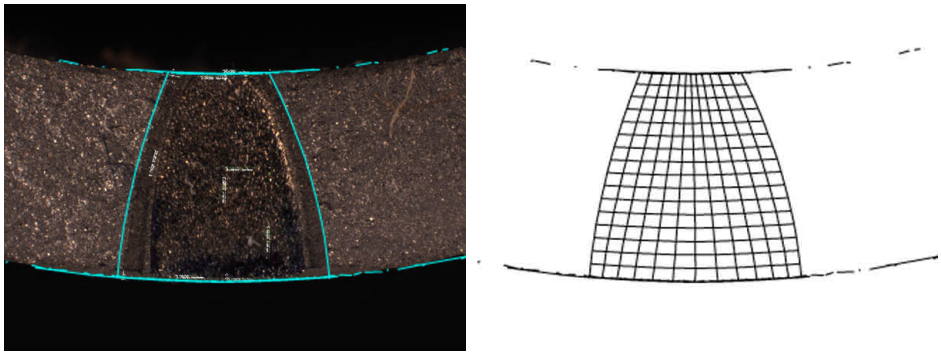

(a) (b)

Figure A.9: (a) Fractograph with BEM geometry superimposed and (b) BEM mesh of pre-crack for specimen N10.

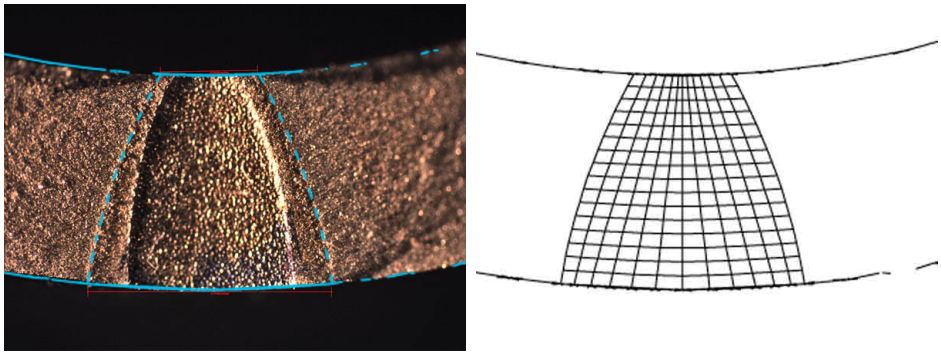

(a) (b)

Figure A.10: (a) Fractograph with BEM geometry superimposed and (b) BEM mesh of pre-crack for specimen N11.

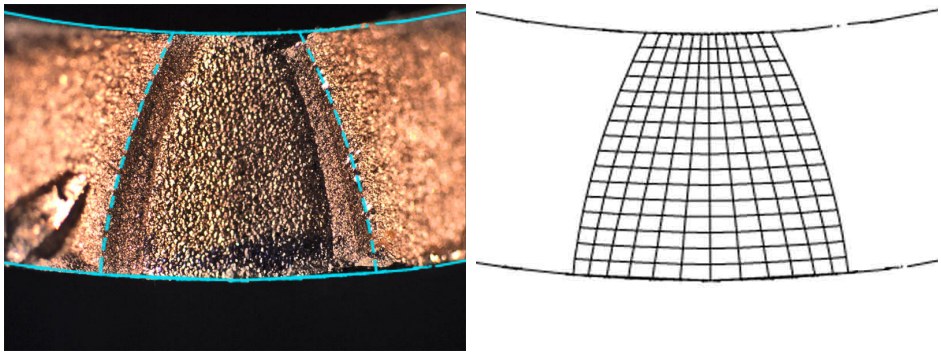

(a) (b)

Figure A.11: (a) Fractograph with BEM geometry superimposed and (b) BEM mesh of pre-crack for specimen N12.

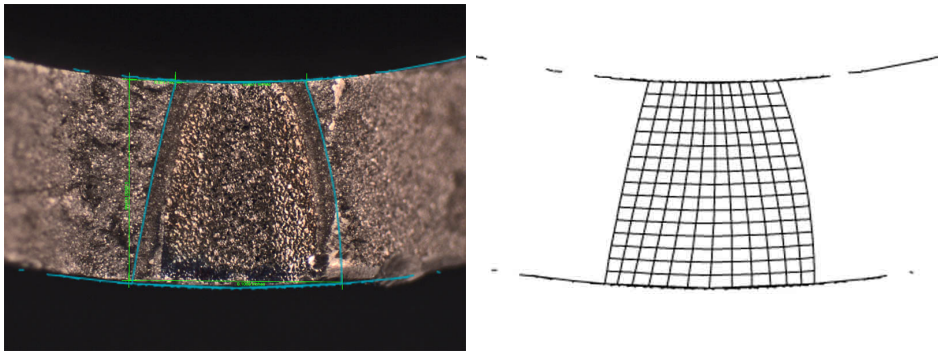

(a) (b)

Figure A.12: (a) Fractograph with BEM geometry superimposed and (b) BEM mesh of pre-crack for specimen N13. Shape of right crack front was estimated with a smooth cubic spline roughly bisecting contact-smeared region.

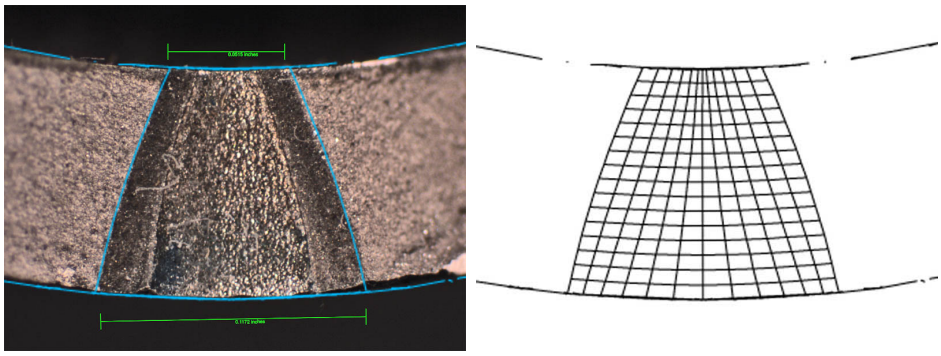

(a) (b)

Figure A.13: (a) Fractograph with BEM geometry superimposed and (b) BEM mesh of pre-crack for specimen N16.

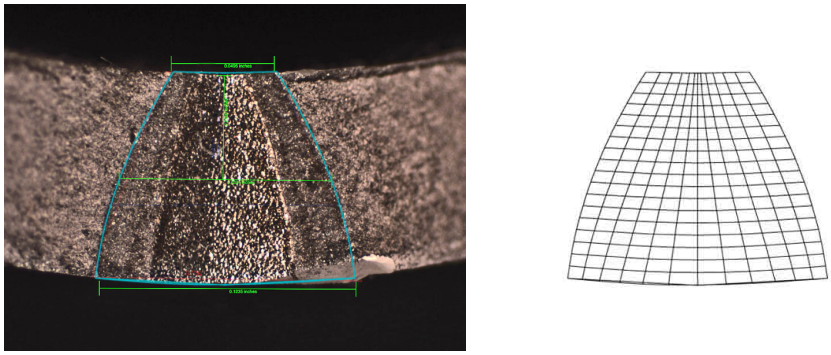

(a) (b)

Figure A.14: (a) Fractograph with BEM geometry superimposed and (b) BEM mesh of pre-crack for specimen N17.

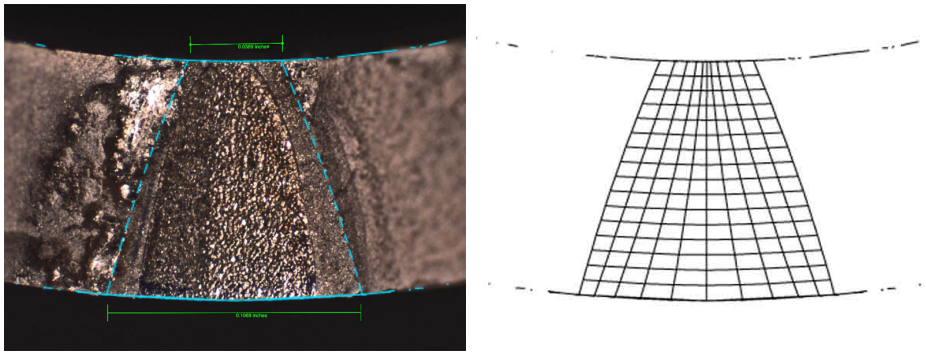

(a) (b)

Figure A.15: (a) Fractograph with BEM geometry superimposed and (b) BEM mesh of pre-crack for specimen N18.

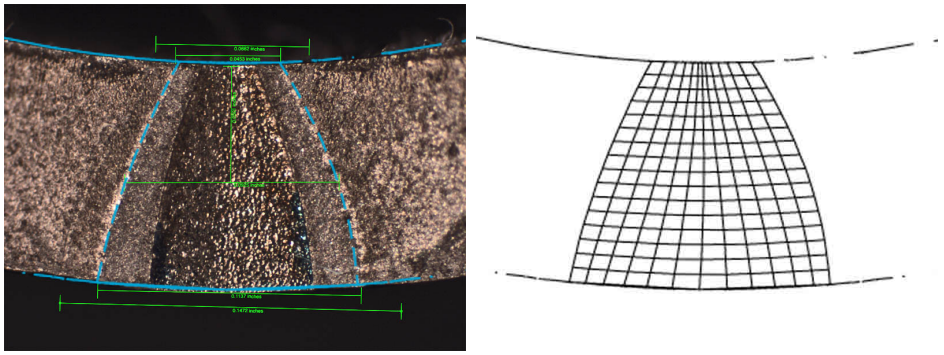

(a) (b)

Figure A.16: (a) Fractograph with BEM geometry superimposed and (b) BEM mesh of pre-crack for specimen N19.

APPENDIX B

DATA REDUCTION OF CLOSED-FORM SOLUTION FOR ITCR SPECIMEN STRESS INTENSITY FACTORS

This appendix presents the full set of FRANC3D results for the seven crack configurations used to generate and validate the closed-form SIF solution as well as the results for the two additional confirmation models of different diameters. The methodology used to generate the curve-fit for each SIF is also presented in greater detail.

B.1 ITCR Model SIF Results

Data plots from the FRANC3D analyses of SIF for the six specimen configurations used to generate influence functions $f(\beta)$ and $g(a/r)$ are presented in Figs. B.1 - B.4 below.

B.2 Data Used for Closed-Form Solution

Attempting to account for both the slight nonlinearity over most of the crack front and the more pronounced nonlinearities at the surface intercepts – which may be an artifact of the analysis more than a true stress condition – would have rendered a closed-form SIF solution prohibitively complex. Therefore, the data from the inner 75% of each crack front were assumed to be linear and used for subsequent data reduction. From the single-mode loading case of each specimen configuration, the average values of K_{I}, K'_{I}, K_{III}, and K'_{III}, and the linear slopes of K_{II} and K'_{II}, were calculated over the range $|x/b| < 0.75$. Furthermore, as there was sometimes a very small difference between the SIF magnitude on either crack front(attributable to

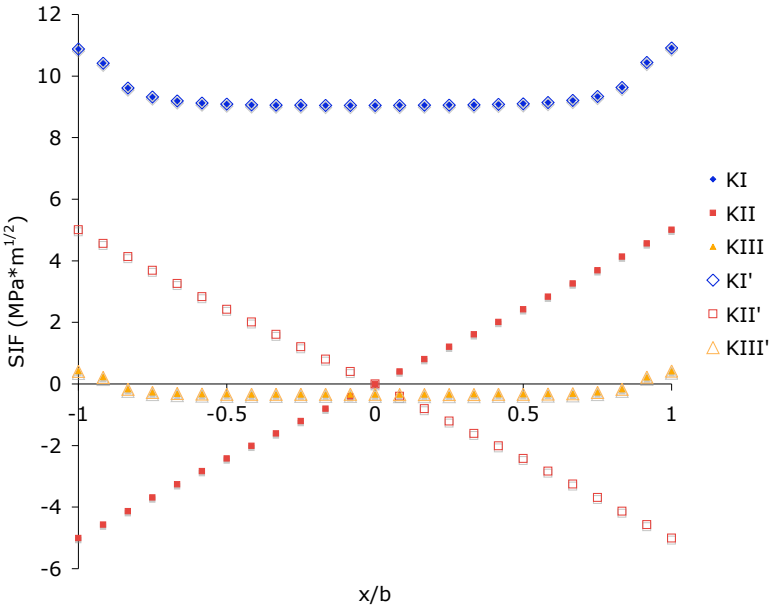

Figure B.1: SIF results from FRANC3D analysis of ITCR specimen for β=0°, a/r=0.133, r=19.05 mm, under load P=44.5 kN, T=113 N-m.

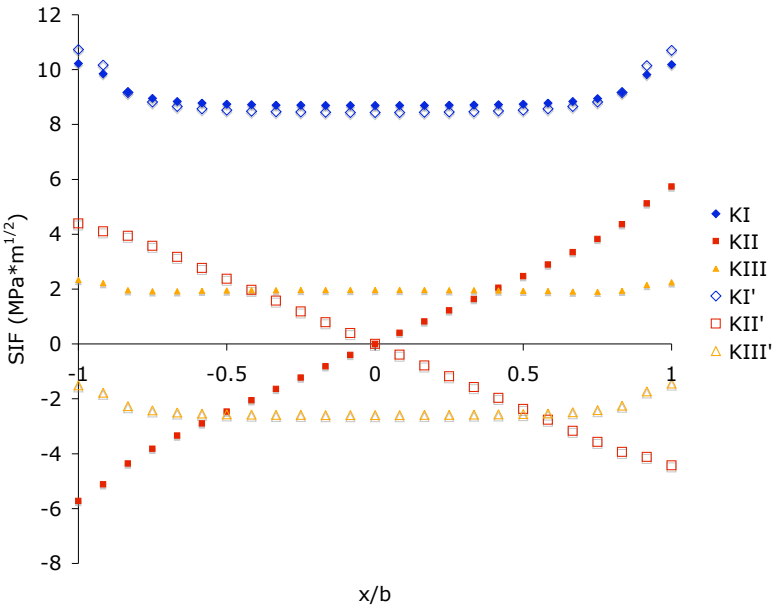

Figure B.2: SIF results from FRANC3D analysis of ITCR specimen for β=15°, a/r=0.133, r=19.05 mm, under load P=44.5 kN, T=113 N-m.

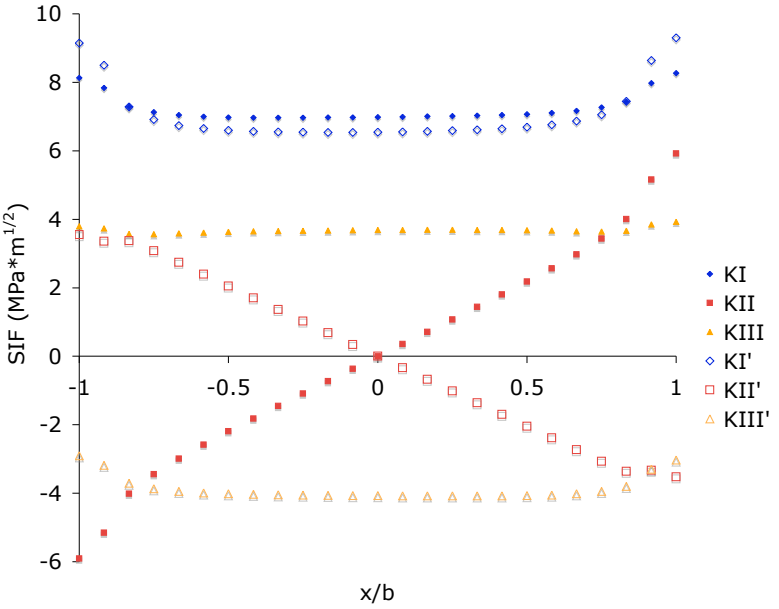

(a) β=30°, a/r=0.133

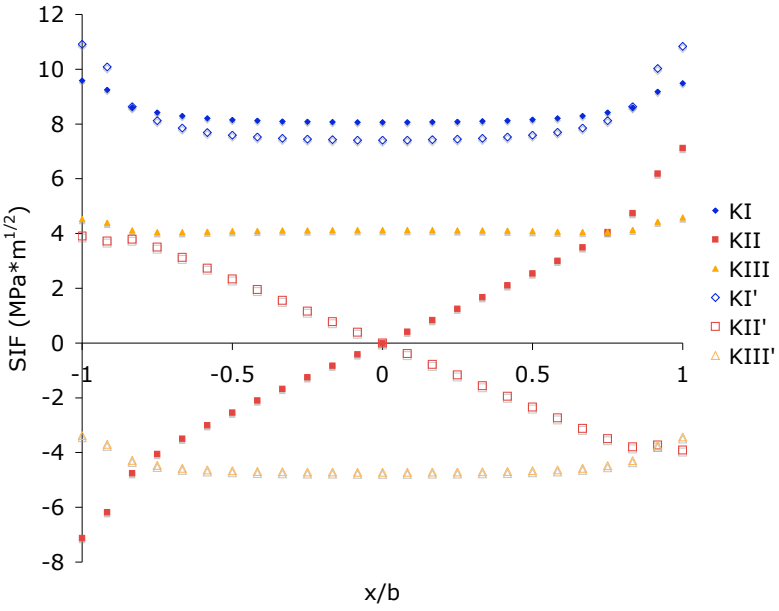

(b) β=30°, a/r=0.167

Figure B.3: SIF results from FRANC3D analysis of ITCR specimen for β=30°, r=19.05 mm and (a) a/r=0.133, (b) a/r=0.167, (c) a/r=0.233, under load P=44.5 kN, T=113 N-m.

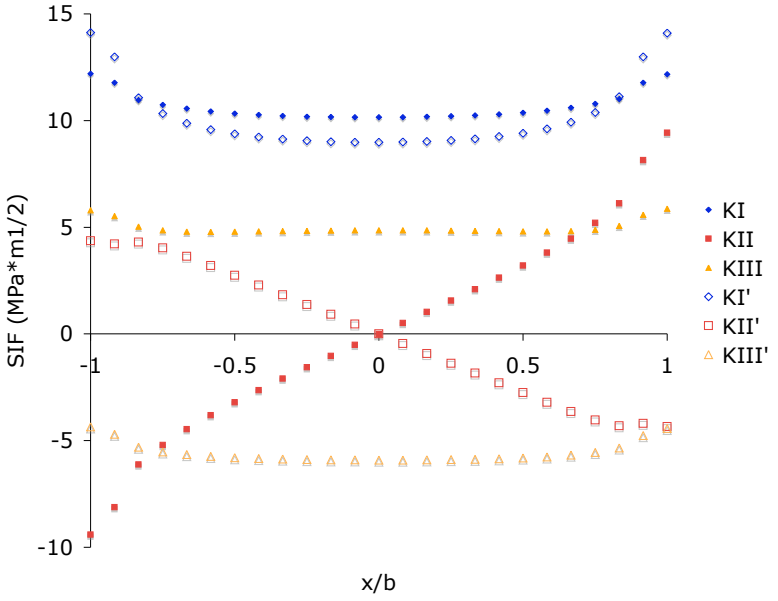

(c) β=30°, a/r=0.233

Figure B.3: Cont.

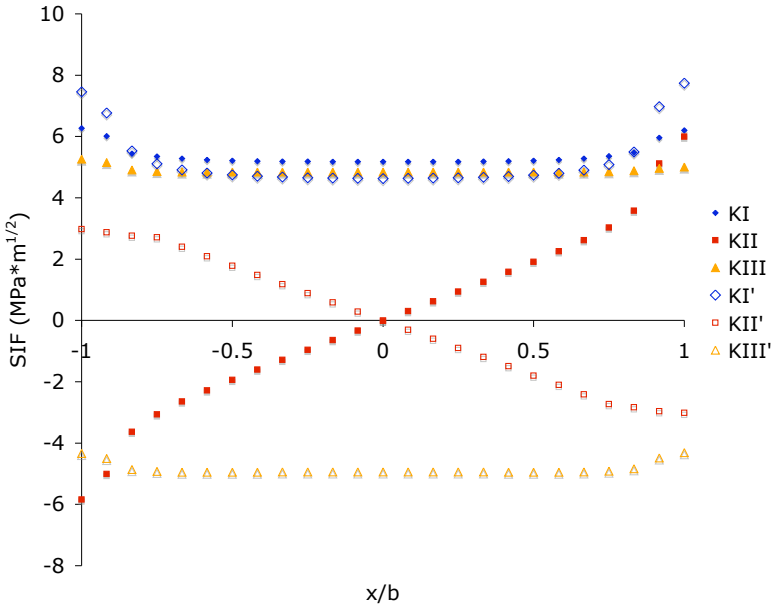

Figure B.4: SIF results from FRANC3D analysis of ITCR specimen for β=45°, a/r=0.133, r=19.05 mm, under load P=44.5 kN, T=113 N-m.

random numerical error), the average of K_i and K_i' was used for each load case.

It was initially assumed that the effects of normalized crack size a/r and crack angle β were linearly separable, according to

$$K_i = \sigma_o\sqrt{\pi a}\cdot f_{1i}(\beta)\cdot g_{1i}\left(\frac{a}{r}\right) + \tau_o\sqrt{\pi a}\cdot f_{2i}(\beta)\cdot g_{2i}\left(\frac{a}{r}\right) \tag{B.1}$$

where

$$\begin{aligned}
i &= \{\text{I, II, III}\}\\
\sigma_o &= \frac{P}{\pi r^2}\text{ , remote tensile stress}\\
\tau_o &= \frac{Tr}{J}\text{ , maximum remote (gage section) torsion}\\
f_{1i}(\beta) &= \text{influence function of } \beta \text{ for tension on } i^{th} \text{ mode SIF}\\
g_{1i}\left(\frac{a}{r}\right) &= \text{influence function of } a/r \text{ for tension on } i^{th} \text{ mode SIF}\\
f_{2i}(\beta) &= \text{influence function of } \beta \text{ for torsion on } i^{th} \text{ mode SIF}\\
g_{2i}\left(\frac{a}{r}\right) &= \text{influence function of } a/r \text{ for torsion on } i^{th} \text{ mode SIF}
\end{aligned}$$

Therefore, the SIF results for different values of β at a single crack size only ($a/r = 0.133$) were considered in order to determine the crack angle influence function $f_1(\beta)$. The smallest modeled crack size was chosen for this step in order to minimize free surface interaction effects. These average values are shown in Table B.1.

Table B.1: Average SIF values (in $\text{MPa}\sqrt{\text{m}}$) for r=19.05 mm, a/r=0.133 case used to determine $f(\beta)$ influence functions.

	P = 44.5 kN, T = 0		P = 0, T = 113 N-m		
β	$\overline{K_{\text{I}}}$	$\overline{K_{\text{III}}}$	$\overline{K_{\text{I}}}$	$\partial K_{\text{II}}/\,\partial\frac{x}{b}$	$\overline{K_{\text{III}}}$
0°	9.27	0	0.01	10.07	0.34
15°	7.88	2.25	0.11	9.76	0.30
30°	6.35	3.93	0.19	8.77	0.19
45°	4.54	4.89	0.23	7.53	0.05

For each mode and loading (tension or torque), a suitable form of $f(\beta)$ was determined by plotting variously normalized SIFs against different trigonometric functions

until a proportional relationship was established. The best relationships selected are shown in Figs. B.5 through B.7. It is assumed that $f_{1\mathrm{II}}(\beta)$ is identically zero, as the contribution to K_{II} from tension is negligible compared to that from torsion. The outlier in Fig. B.7(b) is for β=45°, where the contribution to K_{III} from torsion is negligible compared to that from tension. The final influence functions chosen for β are

$$f_{1\mathrm{I}}(\beta) = \cos^2\beta \tag{B.2}$$

$$f_{1\mathrm{III}}(\beta) = \sin\beta\cos\beta \tag{B.3}$$

$$f_{2\mathrm{I}}(\beta) = \sin\beta\cos\beta \tag{B.4}$$

$$f_{2\mathrm{II}}(\beta) = \cos\beta \tag{B.5}$$

$$f_{2\mathrm{III}}(\beta) = \sin^2\beta - \cos^2\beta \tag{B.6}$$

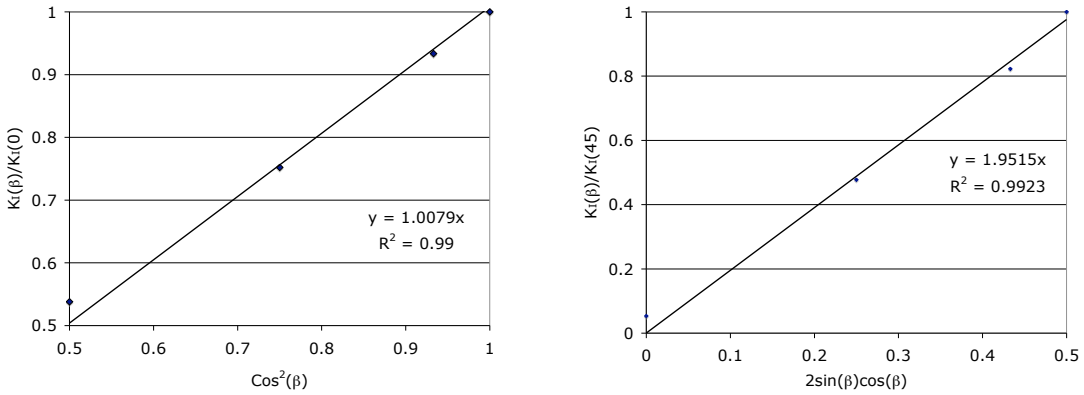

(a) (b)

Figure B.5: Best relationships observed between normalized K_{I} and functions of β: (a) $K_{\mathrm{I}}(\beta)/K_{\mathrm{I}}(0°)$ vs. $\cos^2\beta$ for tension-only loading; (b) $K_{\mathrm{I}}(\beta)/K_{\mathrm{I}}(45°)$ vs. $\sin\beta\cos\beta$ for torque-only loading.

The crack size influence functions were then determined for each mode and load source (tension and torsion) for the β=30° case. The average or slope of each SIF referenced in Table B.1 was normalized by $\sqrt{a}$, the reference stress τ_0 or σ_0, and the

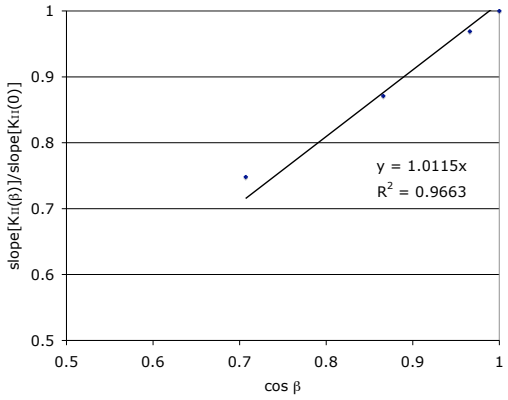

Figure B.6: Best relationship observed between normalized K_{II} and functions of β: $K_{\mathrm{II}}(\beta)/K_{\mathrm{II}}(0^\circ)$ vs. $\cos\beta$ for torque-only loading.

relevant $f_(\beta = 30^\circ)$ to solve Eq. B.7 for $g(a/r)$:

$$g_{1i}\left(\frac{a}{r}\right) = \frac{K_i(30^\circ)}{\sigma_o\sqrt{\pi a}\cdot f_{1i}(30^\circ)} \tag{B.7}$$

$$g_{2i}\left(\frac{a}{r}\right) = \frac{K_i(30^\circ)}{\tau_o\sqrt{\pi a}\cdot f_{2i}(30^\circ)} \tag{B.8}$$

These data and corresponding curve fits are plotted in Fig. B.8 for the tensile load case and Fig. B.9 for the torsion load case.

These influence functions resulted in the following set of equations for all three SIFs under combined tension and torsion loading:

$$\begin{aligned}\mathrm{K_I} = \quad & \sigma_o\sqrt{\pi a}\ \cos^2\beta\left(0.8162 + 0.8286\tfrac{a}{r}\right) \\ & \pm\ \tau_o\sqrt{\pi a}\ \sin\beta\cos\beta\left(-0.018 + 0.759\ \tfrac{a}{r}\right)\end{aligned} \tag{B.9}$$

$$\mathrm{K_{II}} = \frac{x}{b}\left[\tau_o\sqrt{\pi a}\ \cos\beta\left(0.7114 + 2.3439\frac{a}{r} - 4.6816\left(\frac{a}{r}\right)^2\right)\right] \tag{B.10}$$

$$\begin{aligned}\mathrm{K_{III}} = \quad & \sigma_o\sqrt{\pi a}\ \sin\beta\cos\beta\left(0.8513 + 0.3933\tfrac{a}{r}\right) \\ & \pm\ \tau_o\sqrt{\pi a}\ \left(\sin^2\beta - \cos^2\beta\right)\left(-0.0199 + 0.6846\tfrac{a}{r}\right)\end{aligned} \tag{B.11}$$

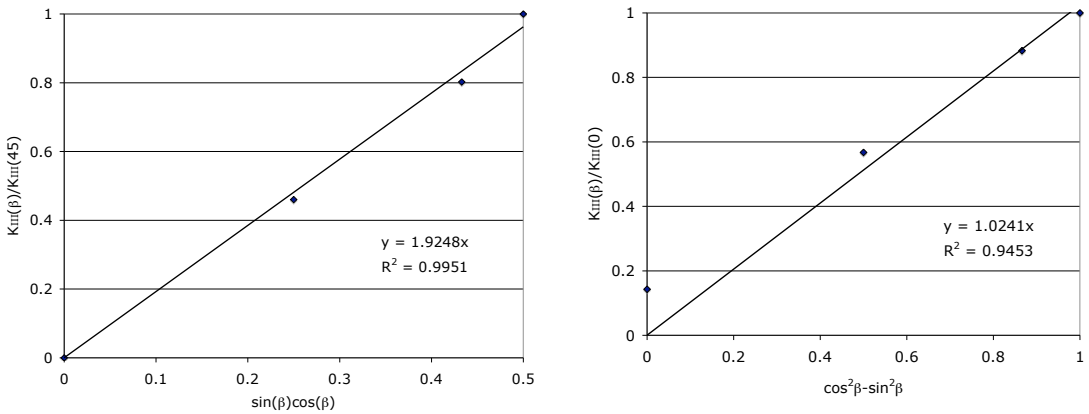

(a) (b)

Figure B.7: Best relationships observed between normalized K_{III} and functions of β: (a) $K_{\mathrm{III}}(\beta)/K_{\mathrm{I}}(45°)$ vs. $\sin\beta\cos\beta$ for tension-only loading; (b) $K_{\mathrm{III}}(\beta)/K_{\mathrm{I}}(0°)$ vs. $\cos^2\beta - \sin^2\beta$ for torque-only loading.

B.3 Closed-Form Solution Validation

Since the SIF solutions used a single crack size $a/r = 0.133$ to determine $f(\beta)$ and a single angle β=30° to determine $g(a/r)$, Fig. B.10 shows the case for $a/r = 0.233$ and β=0° as confirmation of accuracy. Error in the targeted region is less than 4%.

Additionally, in order to verify the geometric scalability of the solutions generated from a single specimen diameter, two additional models with smaller and larger diameters. The solutions were generated from a $D = 19.05$ mm specimen model; the SIF solutions were checked against $D = 12.7$ mm (Fig. B.11) and $D = 25.4$ mm (Fig. B.12). Error for both cases was less than 3% in the linear region ($|x/b| < 0.75$) for K_{I} and K_{III} and in the region $|x/b| < 0.62$ for K_{II}; the maximum error in K_{II} at $x/b = 0.75$ was 6%.

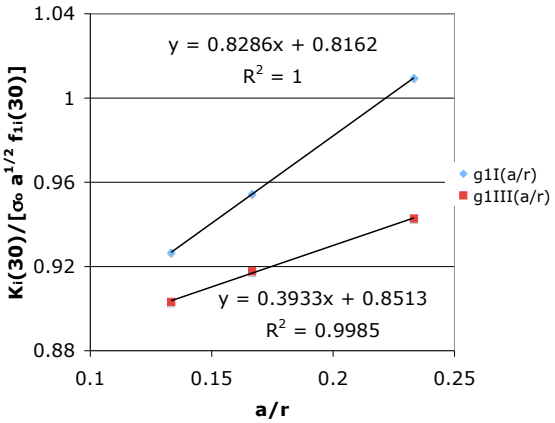

Figure B.8: Curve fits for generating $g(a/r)$ influence functions for tensile loading on K_{I} and K_{III}.

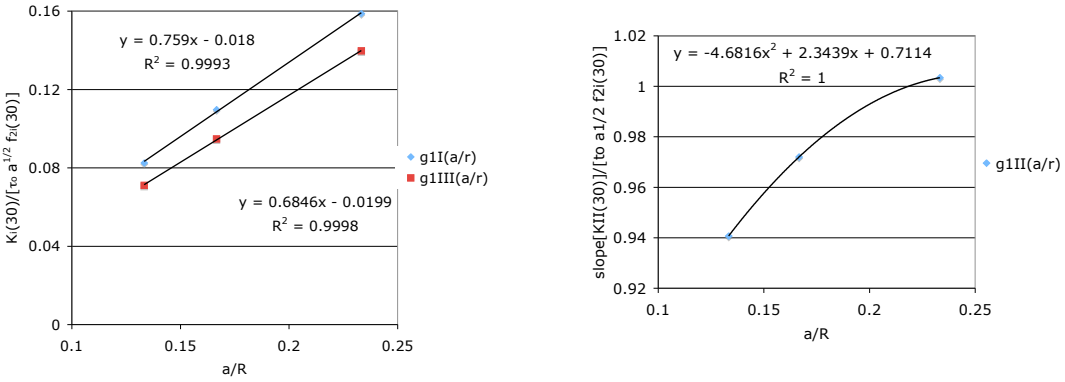

(a) (b)

Figure B.9: Curve fits for generating $g(a/r)$ influence functions for torsion loading on (a) K_{I} and K_{III}, and (b) K_{II}.

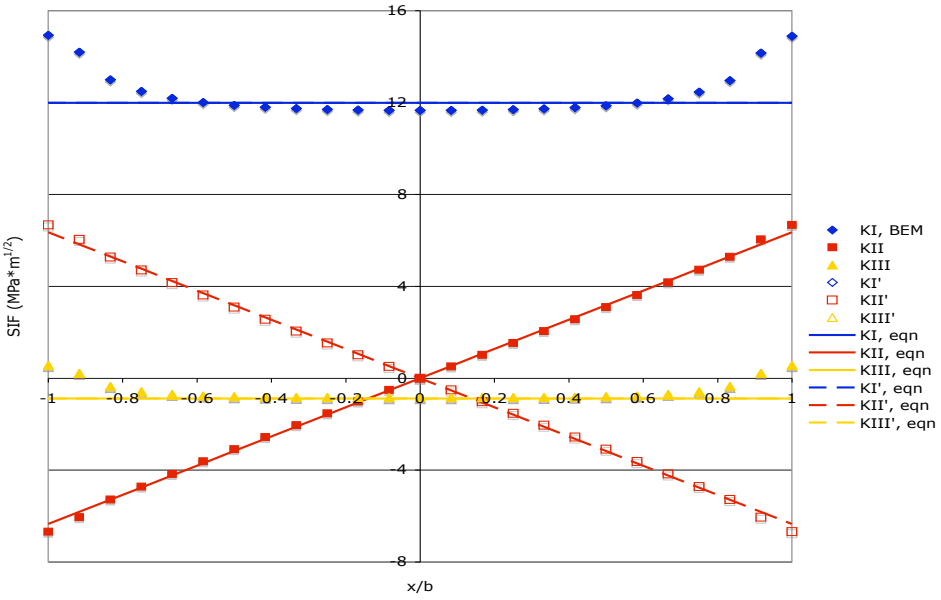

Figure B.10: Comparison of SIF closed-form solution to BEM data for $a/r = 0.233$ and β=0°.

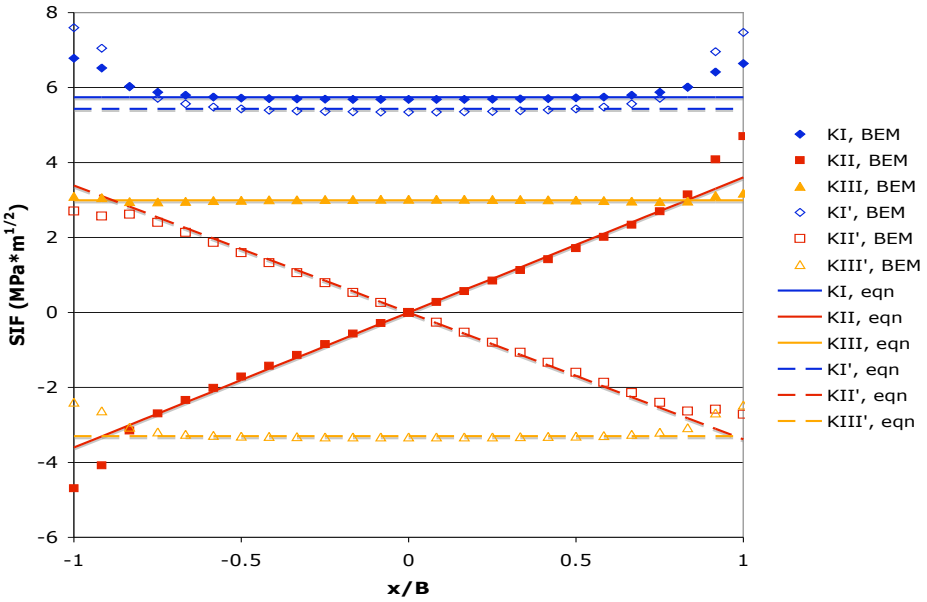

Figure B.11: Comparison of SIF closed-form solution to BEM data for $D = 12.7$ mm, $a/r = 0.133$ and β=30°.

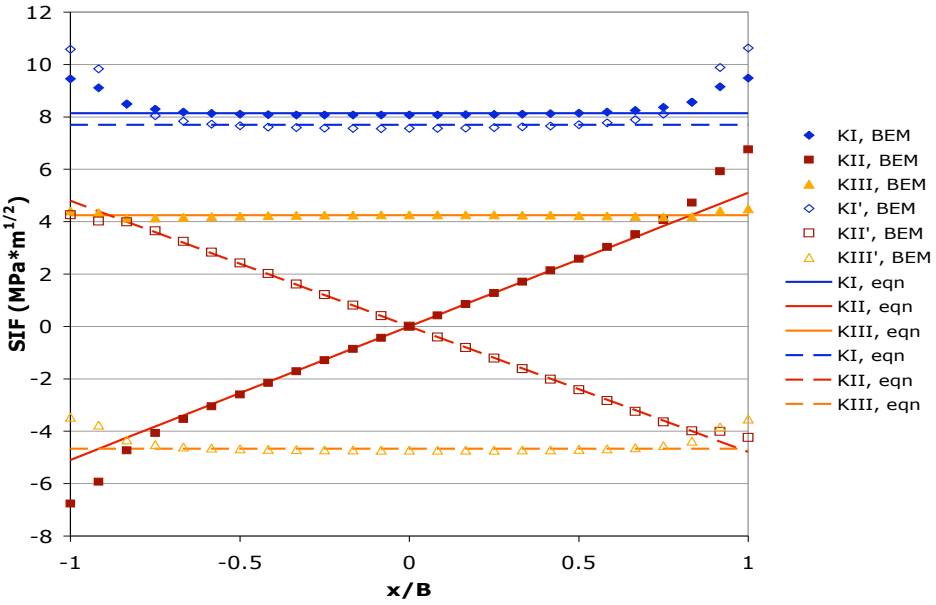

Figure B.12: Comparison of SIF closed-form solution to BEM data for D = 25.4 mm, $a/r = 0.133$ and β=30°.

APPENDIX C

SEM IMAGES OF SELECTED TUBULAR FCG SPECIMENS

C.1 Crack Front N09L

Initial test conditions at the pre-crack for crack front N09L were nominally $K_{\mathrm{Imax}} = 12.1\ \mathrm{MPa}\sqrt{\mathrm{m}}$, $K_{\mathrm{IImax}} = 11.7\ \mathrm{MPa}\sqrt{\mathrm{m}}$, in-phase $R = 0.1$ fatigue loading. Variation in SIF across the pre-crack front caused crack bifurcation into two different branch modes, $\theta = 16°$ for the Mode II crack branch and -58° for the Mode I crack branch.

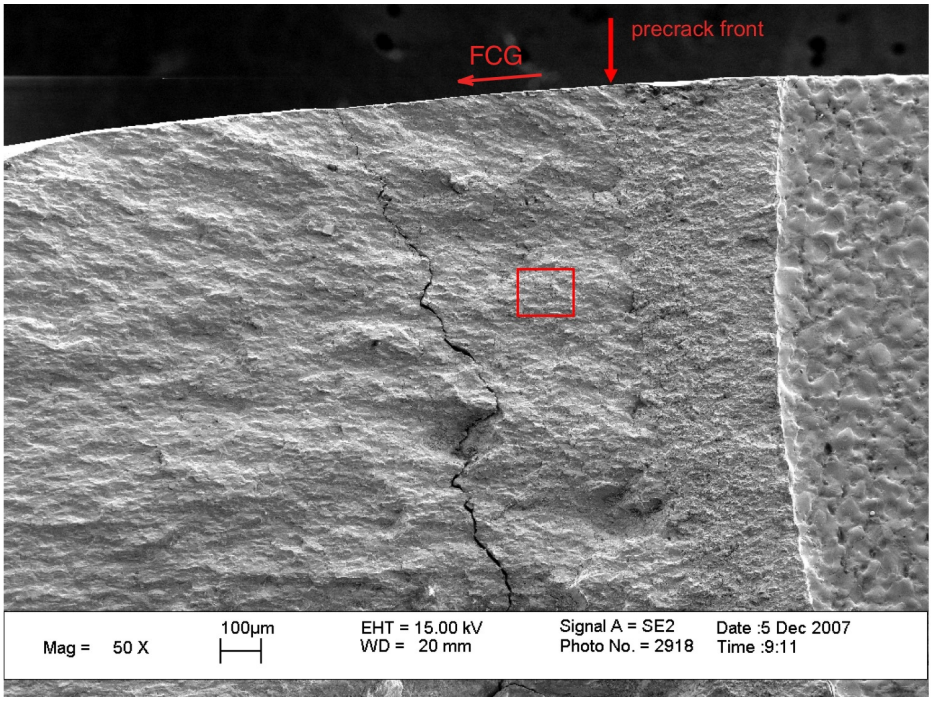

Figure C.1: Scanning electron micrograph of crack front N09L, outer branch propagating at $\theta = 16°$ in a Mode II-dominated condition of nominally $\Delta k_1 = 6.3\ \mathrm{MPa}\sqrt{\mathrm{m}}$, $\Delta k_2 = 11.3\ \mathrm{MPa}\sqrt{\mathrm{m}}$ at initial deflection, $R = 0.1$.

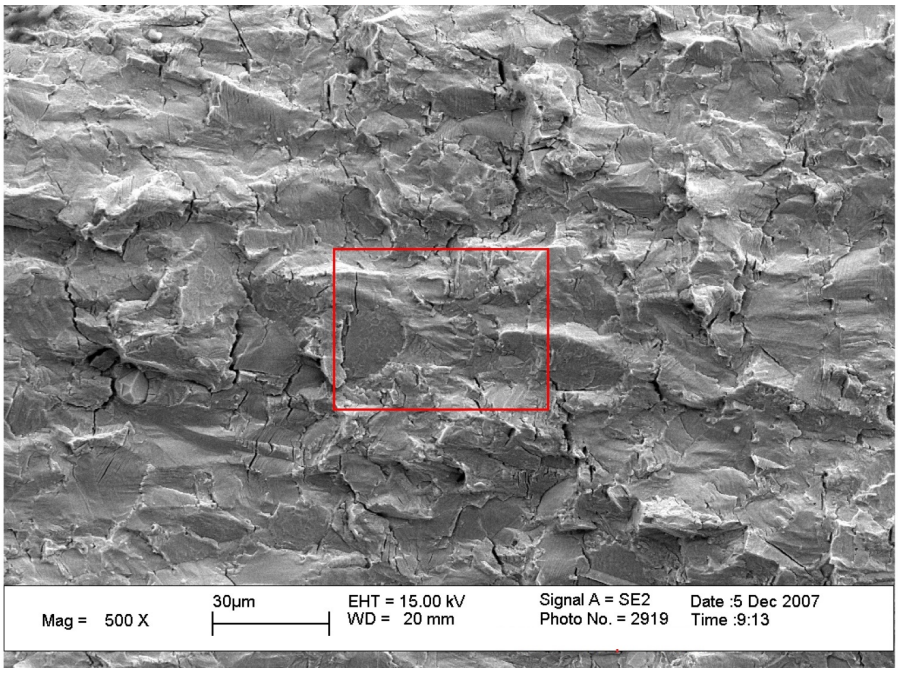

Figure C.2: Scanning electron micrograph of crack front N09L, outer branch propagating at $\theta = 16°$ in a Mode II-dominated condition of nominally $\Delta k_1 = 6.3$ MPa$\sqrt{\text{m}}$, $\Delta k_2 = 11.3$ MPa$\sqrt{\text{m}}$ at initial deflection, $R = 0.1$, region highlighted in Fig. C.1.

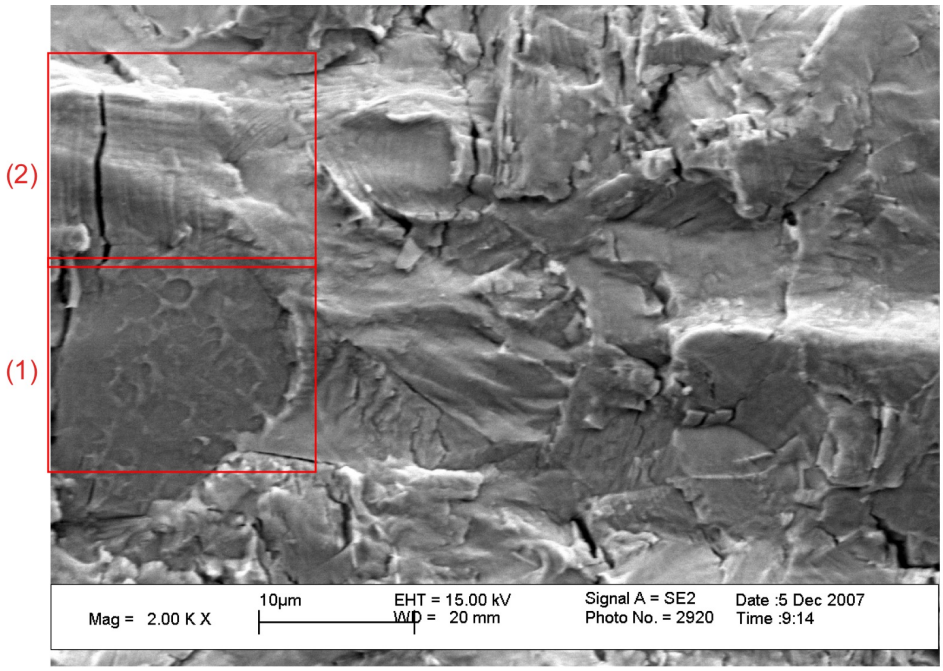

Figure C.3: Scanning electron micrograph of crack front N09L, outer branch propagating at $\theta = 16°$ in a Mode II-dominated condition of nominally $\Delta k_1 = 6.3$ MPa$\sqrt{\text{m}}$, $\Delta k_2 = 11.3$ MPa$\sqrt{\text{m}}$ at initial deflection, $R = 0.1$, region highlighted in Fig. C.2.

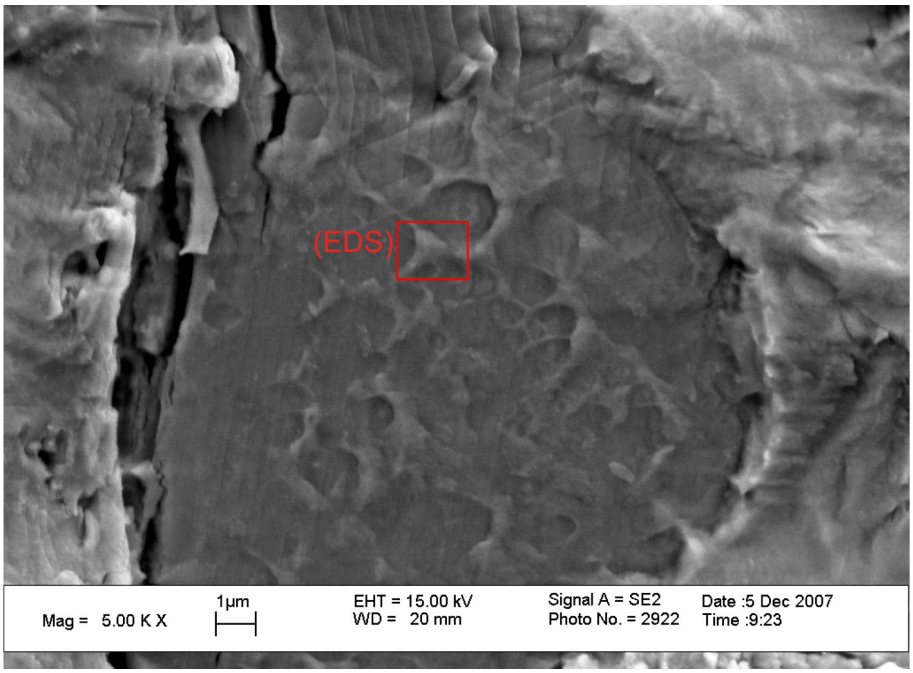

Figure C.4: Scanning electron micrograph of crack front N09L, outer branch propagating at $\theta = 16°$ in a Mode II-dominated condition of nominally $\Delta k_1 = 6.3$ MPa$\sqrt{\text{m}}$, $\Delta k_2 = 11.3$ MPa$\sqrt{\text{m}}$ at initial deflection, $R = 0.1$, region labeled (1) in Fig. C.3. Results from region labeled EDS are shown in Fig. 5.6.

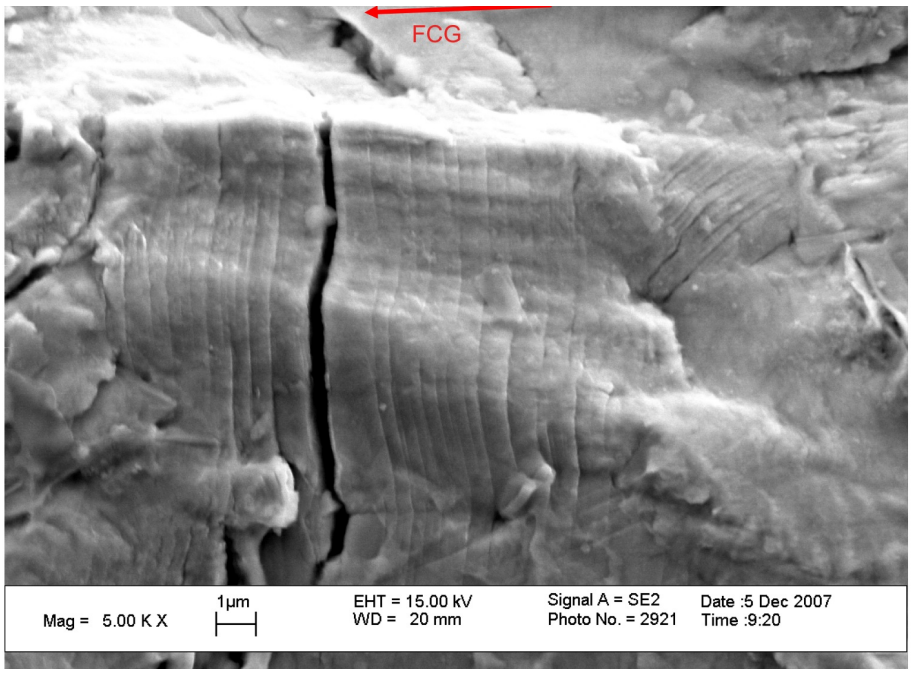

Figure C.5: Scanning electron micrograph of crack front N09L, outer branch propagating at $\theta = 16°$ in a Mode II-dominated condition of nominally $\Delta k_1 = 6.3$ MPa$\sqrt{\text{m}}$, $\Delta k_2 = 11.3$ MPa$\sqrt{\text{m}}$ at initial deflection, $R = 0.1$, region labeled (2) in Fig. C.3.

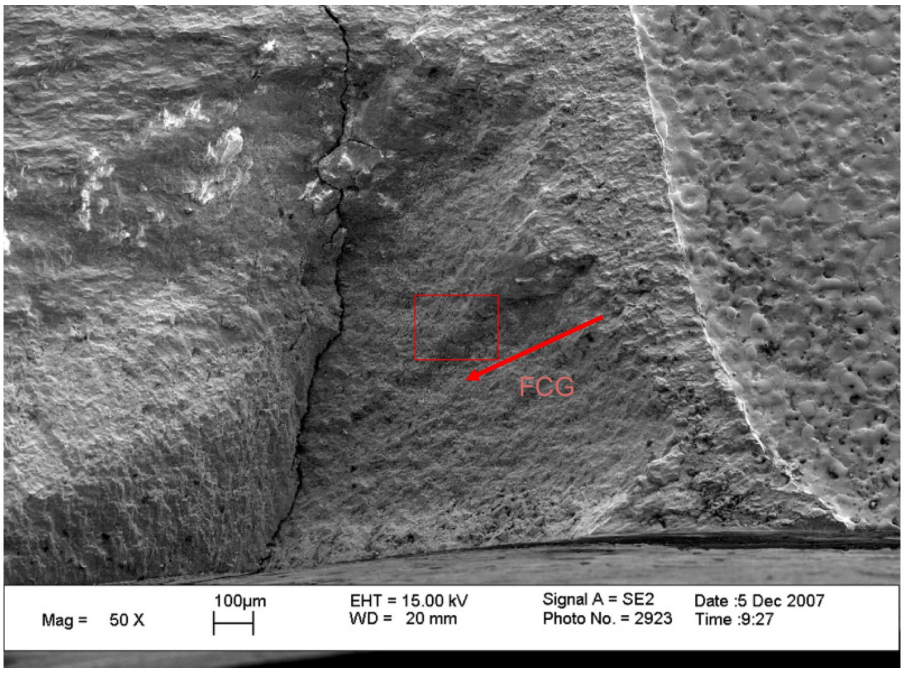

Figure C.6: Scanning electron micrograph of crack front N09L, inner branch propagating at $\theta = $ -58° in a Mode I-dominated condition of nominally $\Delta k_1 = 19.0$ MPa$\sqrt{\text{m}}$, $\Delta k_2 = 1.3$ MPa$\sqrt{\text{m}}$ at initial deflection, $R = 0.1$.

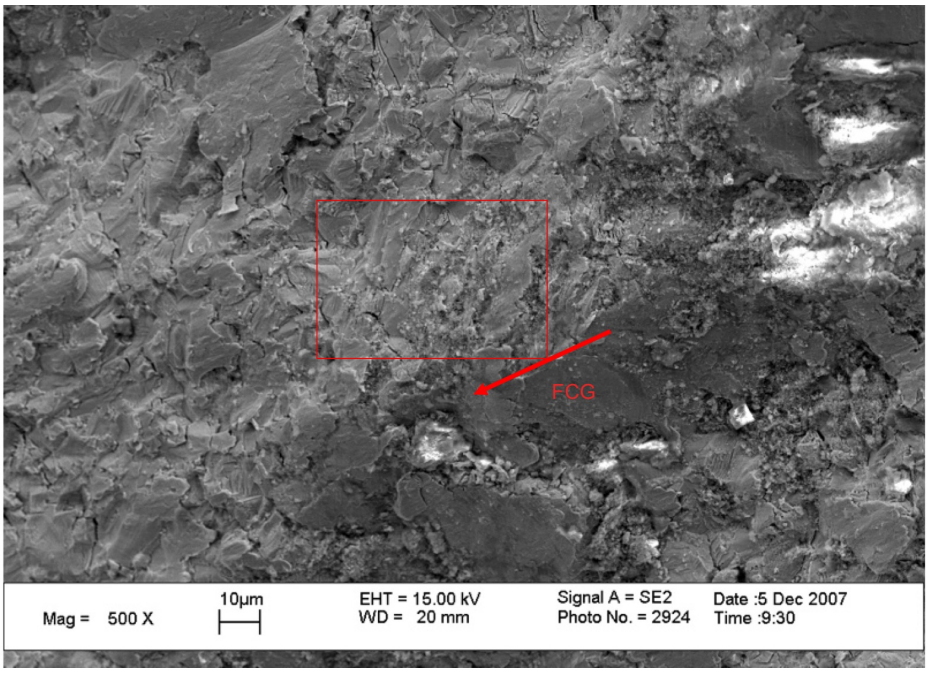

Figure C.7: Scanning electron micrograph of crack front N09L, inner branch propagating at $\theta = $ -58° in a Mode I-dominated condition of nominally $\Delta k_1 = 19.0$ MPa$\sqrt{\text{m}}$, $\Delta k_2 = 1.3$ MPa$\sqrt{\text{m}}$ at initial deflection, $R = 0.1$, region highlighted in Fig. C.6.

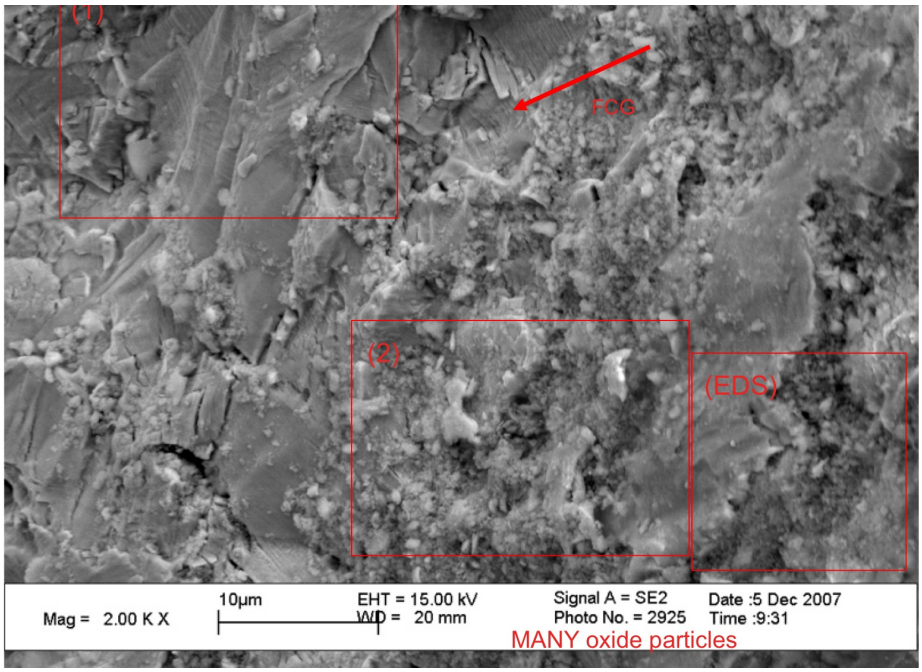

Figure C.8: Scanning electron micrograph of crack front N09L, inner branch propagating at $\theta = $ -58° in a Mode I-dominated condition of nominally $\Delta k_1 = 19.0$ MPa$\sqrt{\text{m}}$, $\Delta k_2 = 1.3$ MPa$\sqrt{\text{m}}$, $R = 0.1$, region highlighted in Fig. C.7. Results from region marked (EDS) are shown in Fig. 5.10, indicating oxide/wear particles.

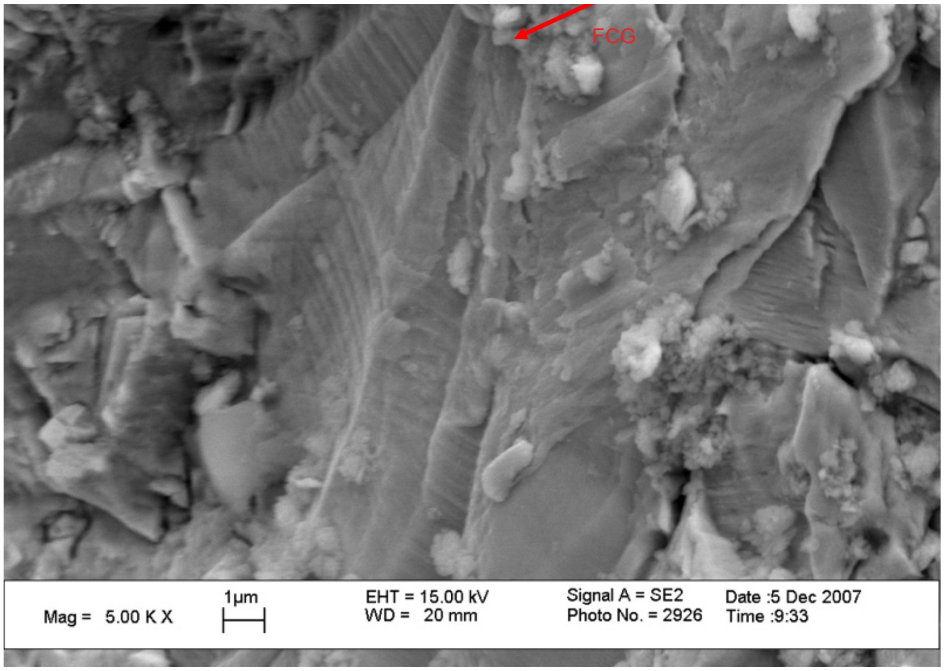

Figure C.9: Scanning electron micrograph of crack front N09L, inner branch propagating at $\theta = $ -58° in a Mode I-dominated condition of nominally $\Delta k_1 = 19.0$ MPa$\sqrt{\text{m}}$, $\Delta k_2 = 1.3$ MPa$\sqrt{\text{m}}$, $R = 0.1$, region labeled (1) in Fig. C.8.

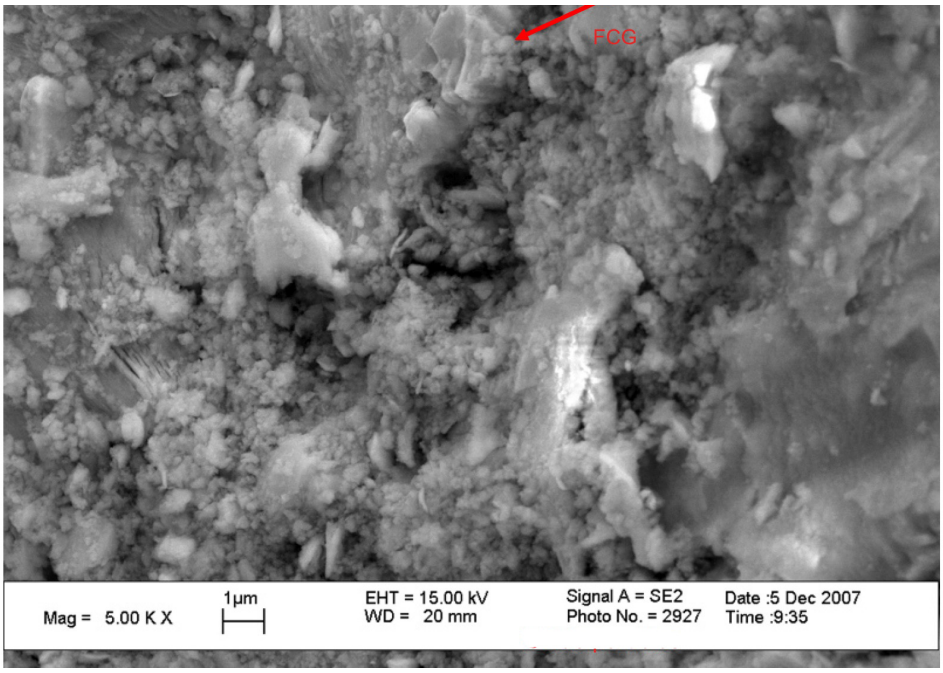

Figure C.10: Scanning electron micrograph of crack front N09L, inner branch propagating at θ = -58° in a Mode I-dominated condition of nominally $\Delta k_1 = 19.0$ MPa$\sqrt{\text{m}}$, $\Delta k_2 = 1.3$ MPa$\sqrt{\text{m}}$, $R = 0.1$, region labeled (2) in Fig. C.8.

C.2 Crack Front N09R

Initial test conditions at the pre-crack for crack front N09R were nominally K_{Imax} = 12.1 MPa$\sqrt{\text{m}}$, $K_{\text{IImax}} = 11.9$ MPa$\sqrt{\text{m}}$, in-phase $R = 0.1$ fatigue loading. Variation in SIF across the pre-crack front caused crack bifurcation into two different branch modes, θ = 18° for the Mode II crack branch and -55° for the Mode I crack branch.

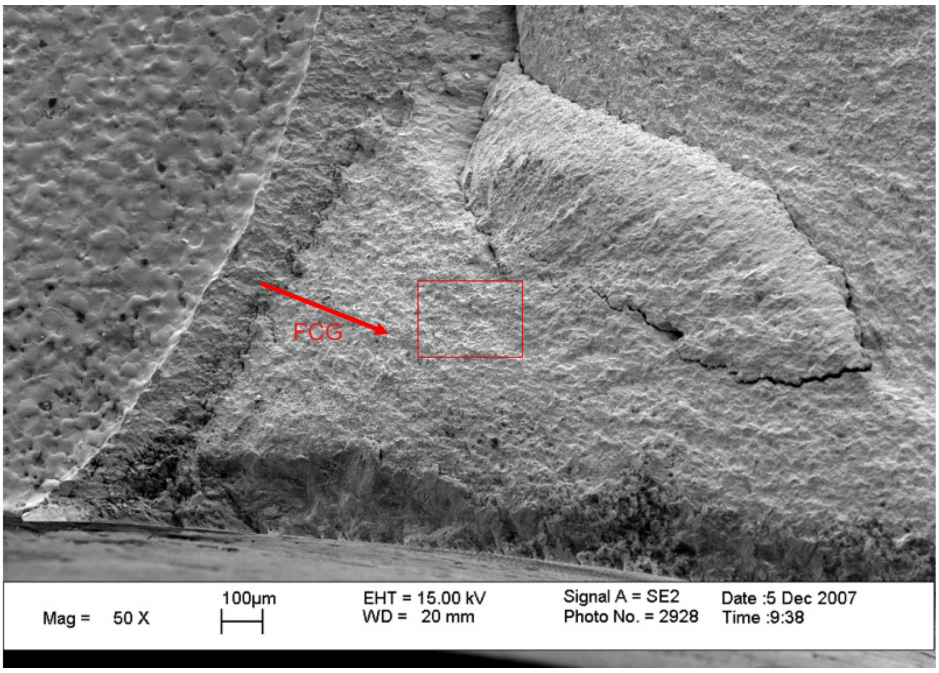

Figure C.11: Scanning electron micrograph of crack front N09R, inner branch propagating at $\theta = $ -55° in a Mode I-dominated condition of nominally $\Delta k_1 = 19.3$ MPa$\sqrt{\text{m}}$, $\Delta k_2 = 0.6$ MPa$\sqrt{\text{m}}$ at initial deflection, $R = 0.1$.

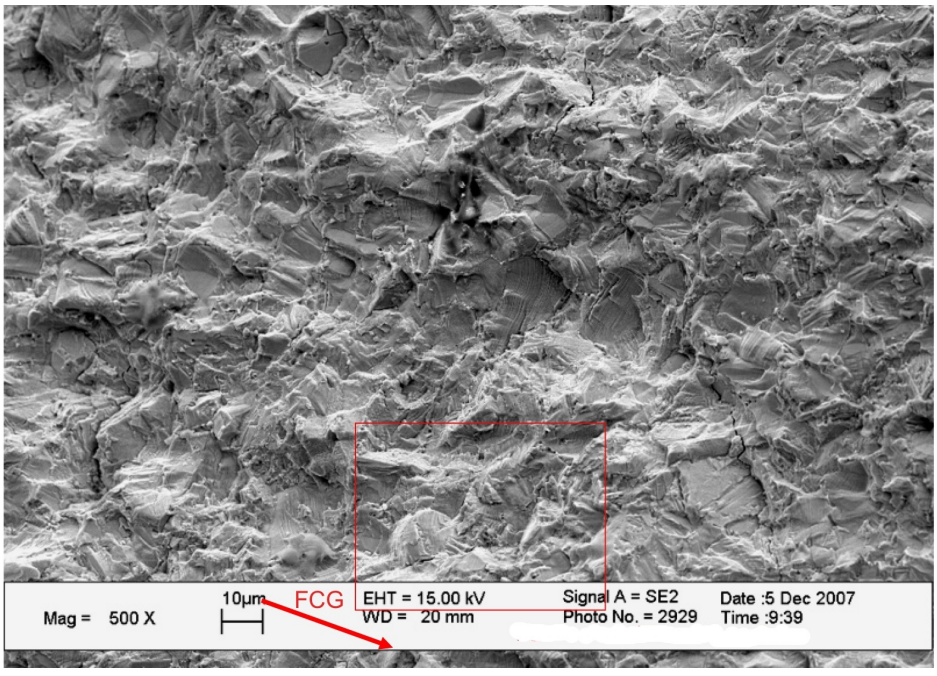

Figure C.12: Scanning electron micrograph of crack front N09R, inner branch propagating at $\theta = $ -55° in a Mode I-dominated condition of nominally $\Delta k_1 = 19.3$ MPa$\sqrt{\text{m}}$, $\Delta k_2 = 0.6$ MPa$\sqrt{\text{m}}$ at initial deflection, $R = 0.1$, region highlighted in Fig. C.11.

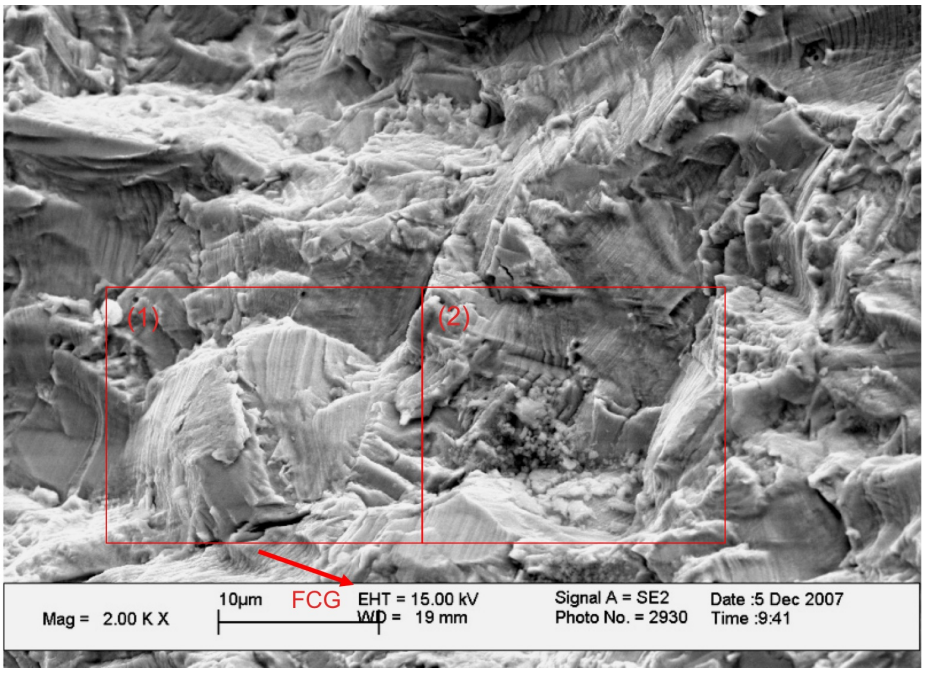

Figure C.13: Scanning electron micrograph of crack front N09R, inner branch propagating at $\theta = $ -55° in a Mode I-dominated condition of nominally $\Delta k_1 = 19.3$ MPa$\sqrt{\text{m}}$, $\Delta k_2 = 0.6$ MPa$\sqrt{\text{m}}$ at initial deflection, $R = 0.1$, region highlighted in Fig. C.12.

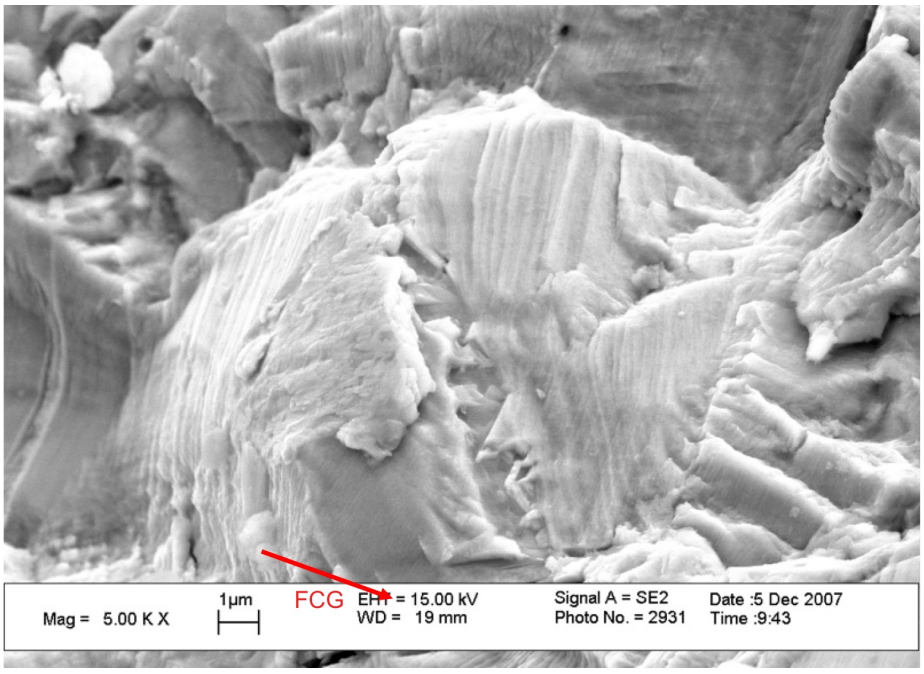

Figure C.14: Scanning electron micrograph of crack front N09R, inner branch propagating at $\theta = $ -55° in a Mode I-dominated condition of nominally $\Delta k_1 = 19.3$ MPa$\sqrt{\text{m}}$, $\Delta k_2 = 0.6$ MPa$\sqrt{\text{m}}$ at initial deflection, $R = 0.1$, region labeled (1) in Fig. C.13.

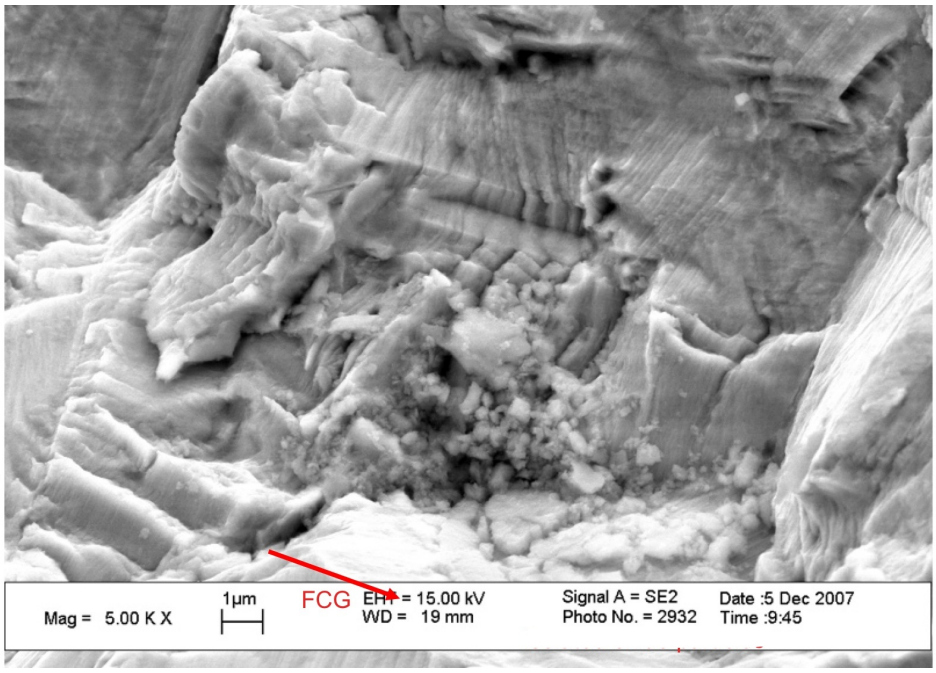

Figure C.15: Scanning electron micrograph of crack front N09R, inner branch propagating at $\theta =$ -55° in a Mode I-dominated condition of nominally $\Delta k_1 = 19.3$ MPa$\sqrt{\text{m}}$, $\Delta k_2 = 0.6$ MPa$\sqrt{\text{m}}$ at initial deflection, $R = 0.1$, region labeled (2) in Fig. C.13.

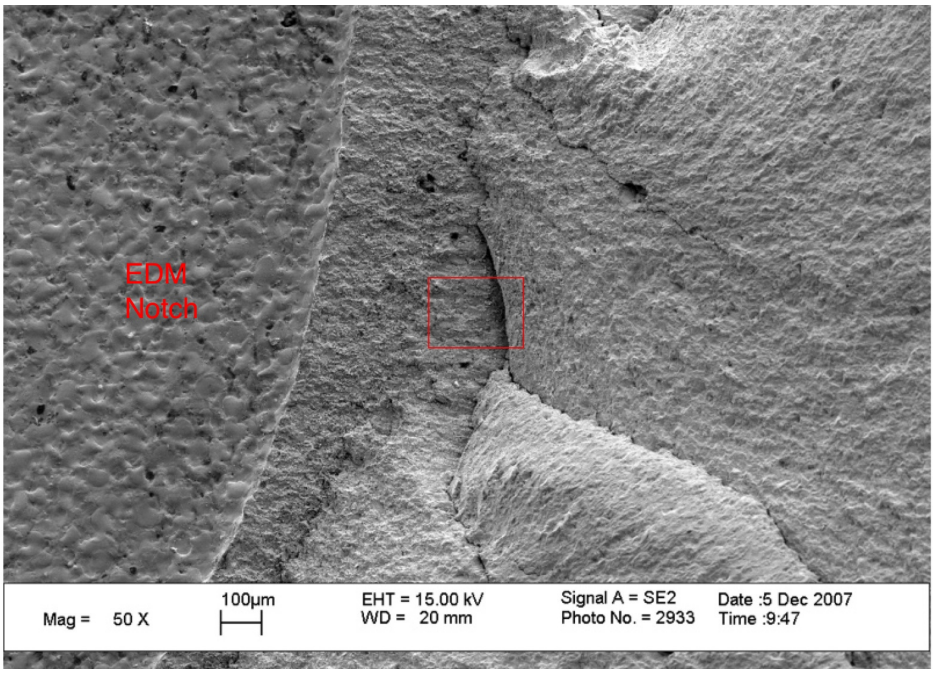

Figure C.16: Scanning electron micrograph of crack front N09R, outer branch (near mid-thickness) propagating at $\theta = 18°$ in a Mode II-dominated condition of nominally $\Delta k_1 = 5.6$ MPa$\sqrt{\text{m}}$, $\Delta k_2 = 11.4$ MPa$\sqrt{\text{m}}$ at initial deflection, $R = 0.1$.

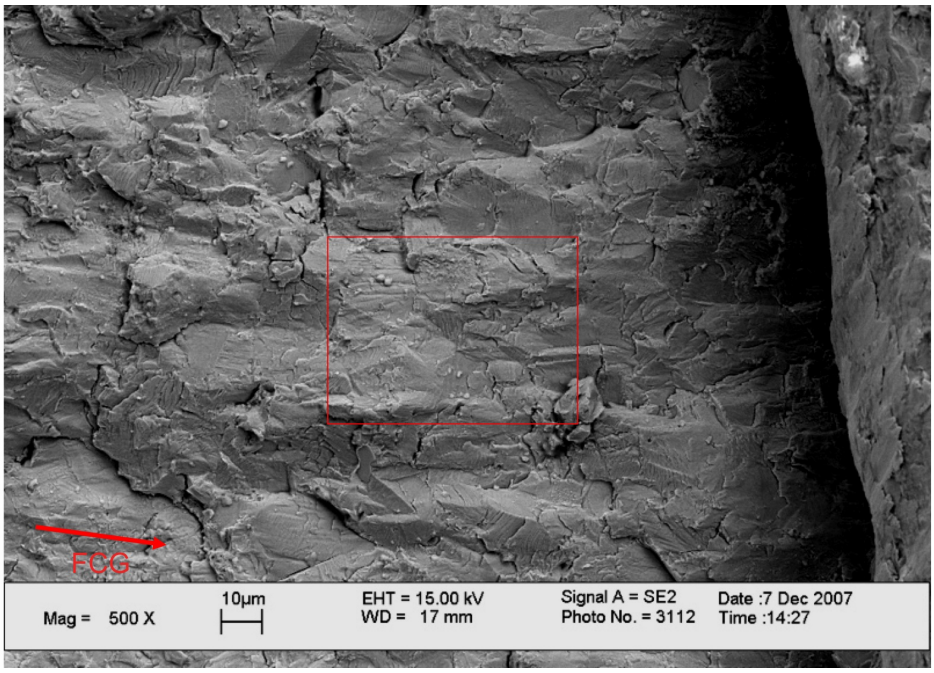

Figure C.17: Scanning electron micrograph of crack front N09R, outer branch propagating at $\theta = 18°$ in a Mode II-dominated condition of nominally $\Delta k_1 = 5.6$ MPa$\sqrt{\text{m}}$, $\Delta k_2 = 11.4$ MPa$\sqrt{\text{m}}$ at initial deflection, $R = 0.1$, region highlighted in Fig. C.16.

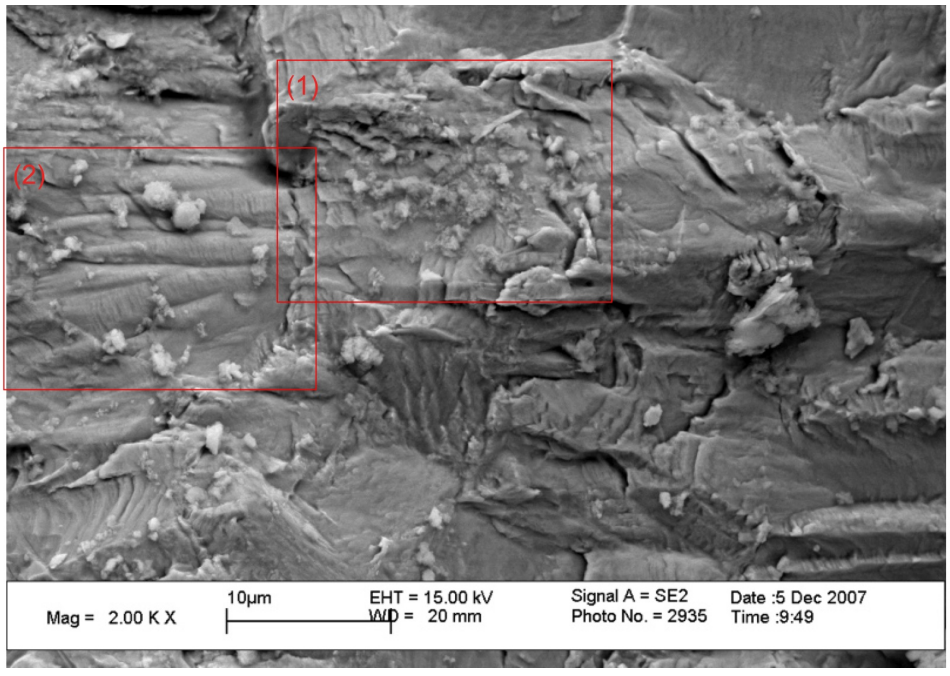

Figure C.18: Scanning electron micrograph of crack front N09R, outer branch propagating at $\theta = 18°$ in a Mode II-dominated condition of nominally $\Delta k_1 = 5.6$ MPa$\sqrt{\text{m}}$, $\Delta k_2 = 11.4$ MPa$\sqrt{\text{m}}$ at initial deflection, $R = 0.1$, region highlighted in Fig. C.17.

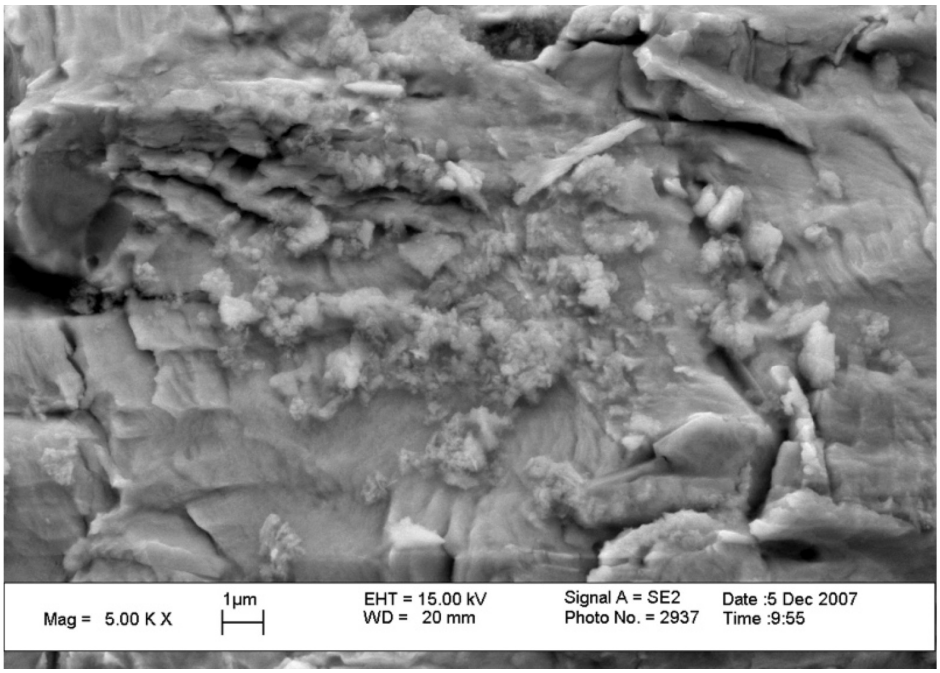

Figure C.19: Scanning electron micrograph of crack front N09R, outer branch propagating at $\theta = 18°$ in a Mode II-dominated condition of nominally $\Delta k_1 = 5.6$ MPa$\sqrt{\text{m}}$, $\Delta k_2 = 11.4$ MPa$\sqrt{\text{m}}$ at initial deflection, $R = 0.1$, region labeled (1) in Fig. C.18.

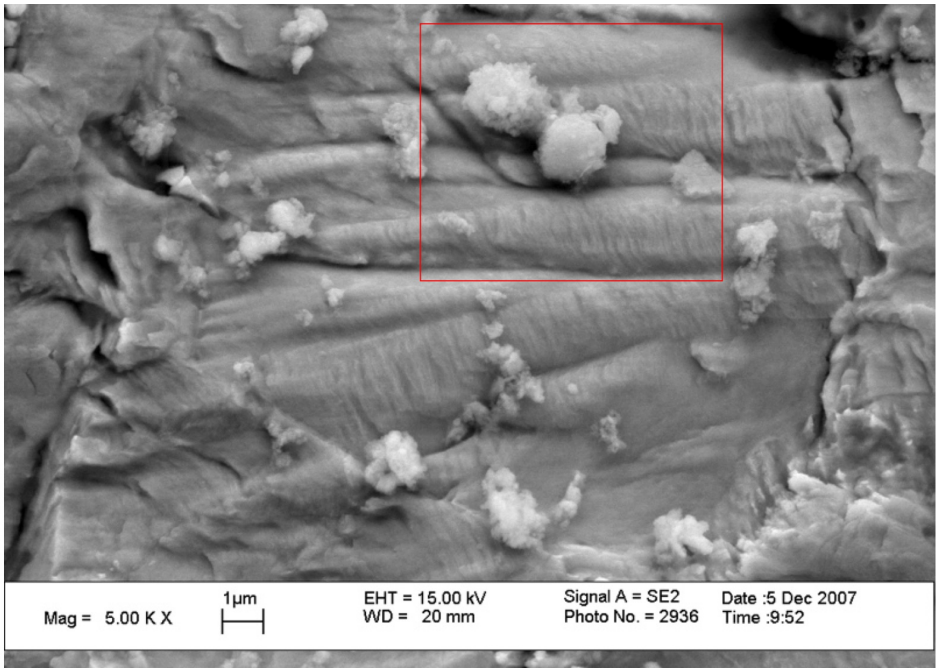

Figure C.20: Scanning electron micrograph of crack front N09R, outer branch propagating at $\theta = 18°$ in a Mode II-dominated condition of nominally $\Delta k_1 = 5.6$ MPa$\sqrt{\text{m}}$, $\Delta k_2 = 11.4$ MPa$\sqrt{\text{m}}$ at initial deflection, $R = 0.1$, region labeled (2) in Fig. C.18. Highlighted particles were subject to EDS with results shown in Fig. 5.8.

C.3 Crack Front N12R

Initial test conditions at the pre-crack for crack front N12R were nominally K_{Imax} = 18.1 MPa$\sqrt{\mathrm{m}}$, K_{IImax} = 7.9 MPa$\sqrt{\mathrm{m}}$, in-phase R = 0.1 fatigue loading. This resulted in Mode I crack deflection to θ = -26°.

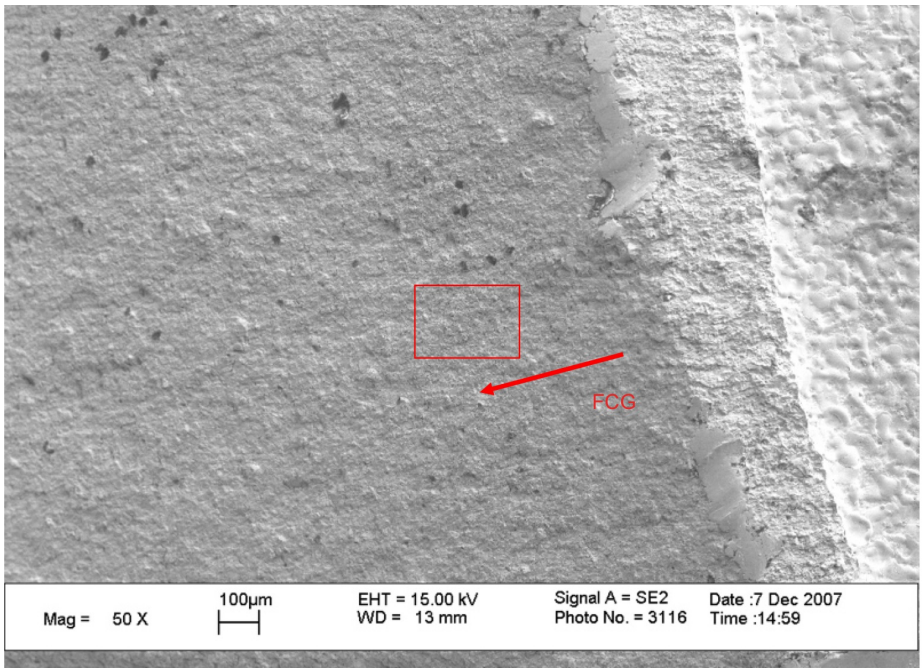

Figure C.21: Scanning electron micrograph of crack front N12R, propagating at θ = -26° in a Mode I-dominated condition of nominally Δk_1 = 19.6 MPa$\sqrt{\mathrm{m}}$, Δk_2 = 2.4 MPa$\sqrt{\mathrm{m}}$ at initial deflection, R = 0.1, near mid-thickness.

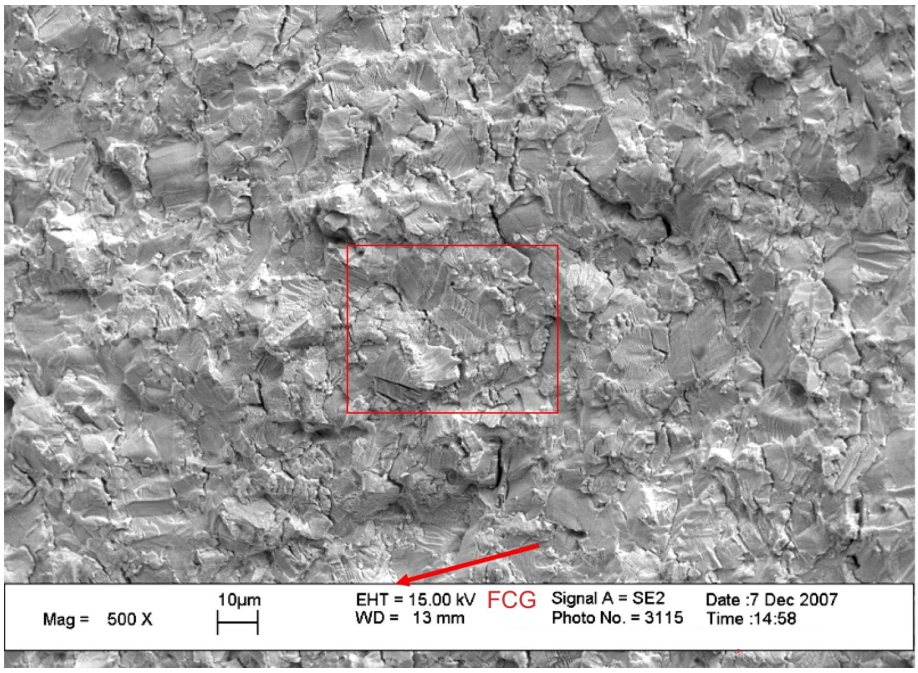

Figure C.22: Scanning electron micrograph of crack front N12R, propagating at θ = -26° in a Mode I-dominated condition of nominally $\Delta k_1 = 19.6$ MPa$\sqrt{\text{m}}$, $\Delta k_2 = 2.4$ MPa$\sqrt{\text{m}}$ at initial deflection, $R = 0.1$, region highlighted in Fig. C.21.

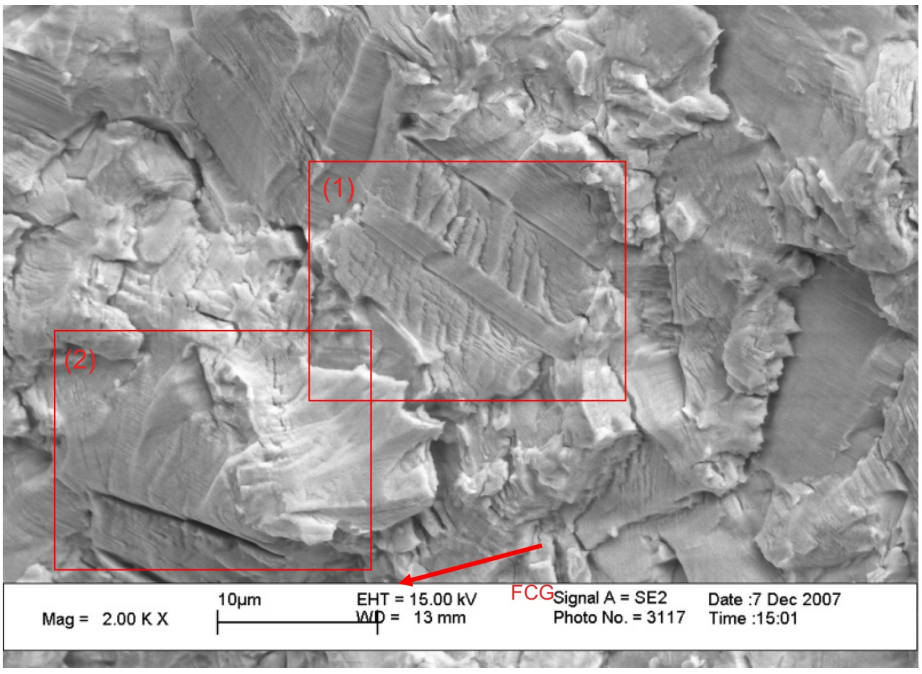

Figure C.23: Scanning electron micrograph of crack front N12R, propagating at θ = -26° in a Mode I-dominated condition of nominally $\Delta k_1 = 19.6$ MPa$\sqrt{\text{m}}$, $\Delta k_2 = 2.4$ MPa$\sqrt{\text{m}}$ at initial deflection, $R = 0.1$, region highlighted in Fig. C.22.

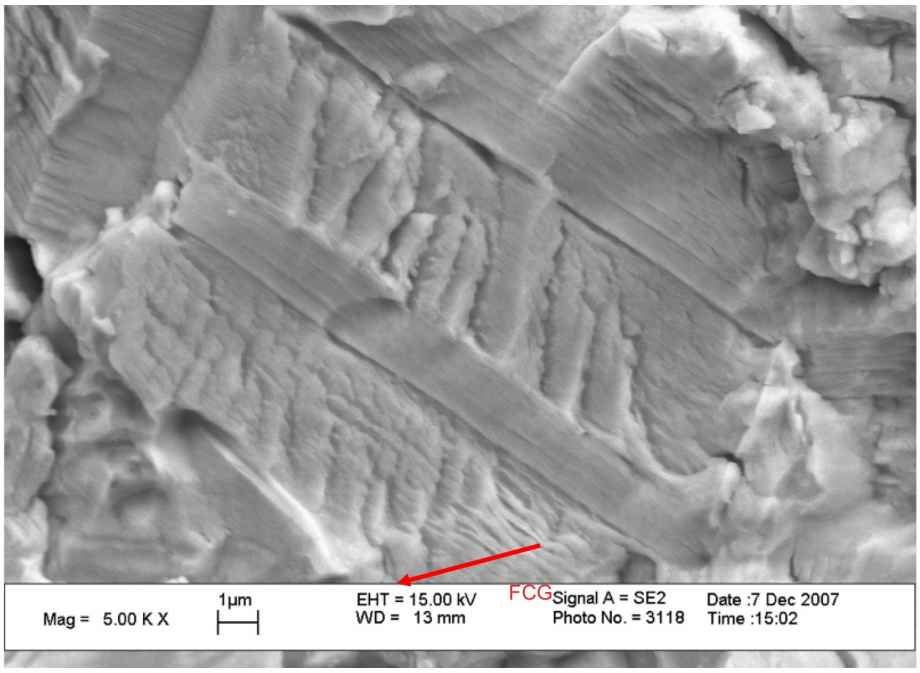

Figure C.24: Scanning electron micrograph of crack front N12R, propagating at θ = -26° in a Mode I-dominated condition of nominally $\Delta k_1 = 19.6$ MPa$\sqrt{\text{m}}$, $\Delta k_2 = 2.4$ MPa$\sqrt{\text{m}}$ at initial deflection, $R = 0.1$, region labeled (1) in Fig. C.23.

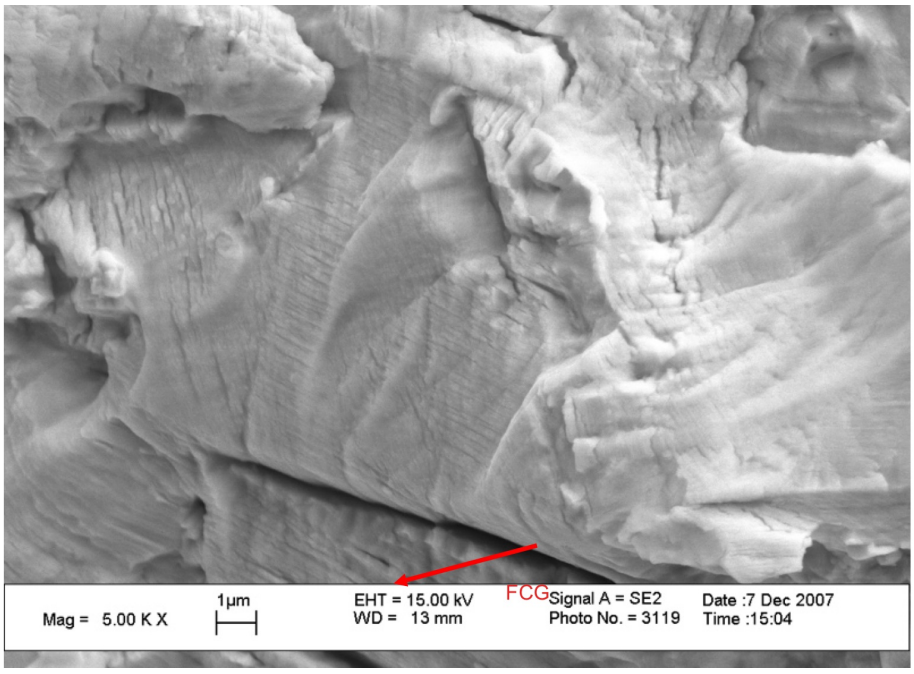

Figure C.25: Scanning electron micrograph of crack front N12R, propagating at θ = -26° in a Mode I-dominated condition of nominally $\Delta k_1 = 19.6$ MPa$\sqrt{\text{m}}$, $\Delta k_2 = 2.4$ MPa$\sqrt{\text{m}}$ at initial deflection, $R = 0.1$, region labeled (2) in Fig. C.23.

C.4 Crack Front N10R

Initial test conditions at the pre-crack for crack front N10R were nominally K_{Imax} = 11.5 MPa$\sqrt{\mathrm{m}}$, K_{IImax} = 11.3 MPa$\sqrt{\mathrm{m}}$, constant tension/cyclic torsion $R_{\mathrm{II}} = 0.1$ fatigue loading. This resulted in essentially co-planar crack growth at $\theta = 1°$.

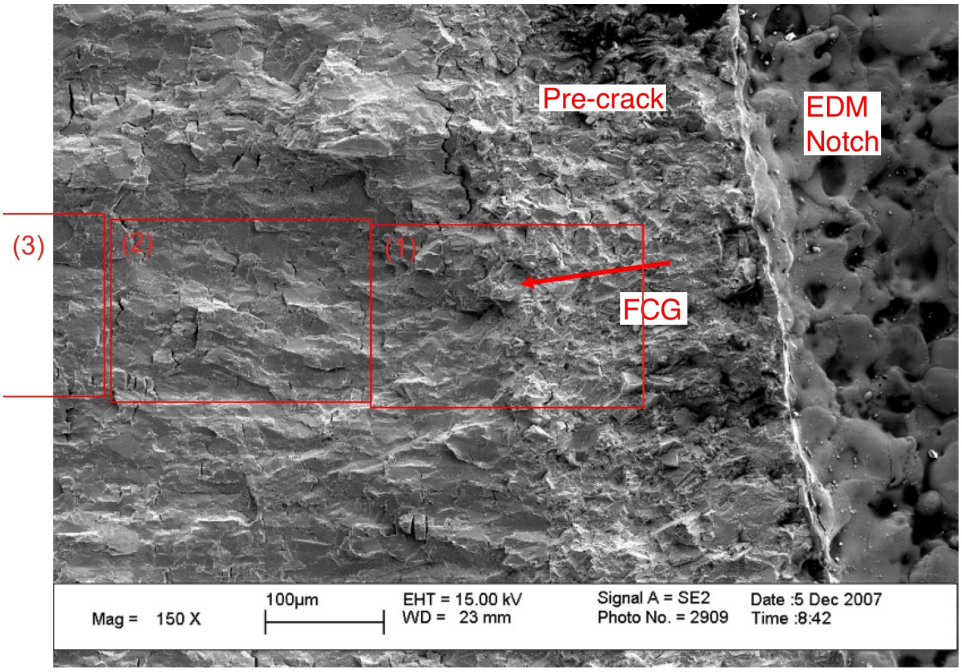

Figure C.26: Scanning electron micrograph of crack front N10R, propagating at θ = 1° in a Mode II-dominated condition of nominally $\Delta k_1 = 0.3$ MPa$\sqrt{\mathrm{m}}$, $R_1 = 0.98$, $\Delta k_2 = 10.2$ MPa$\sqrt{\mathrm{m}}$, $R_2 = 0.11$ at initial propagation, near mid-thickness.

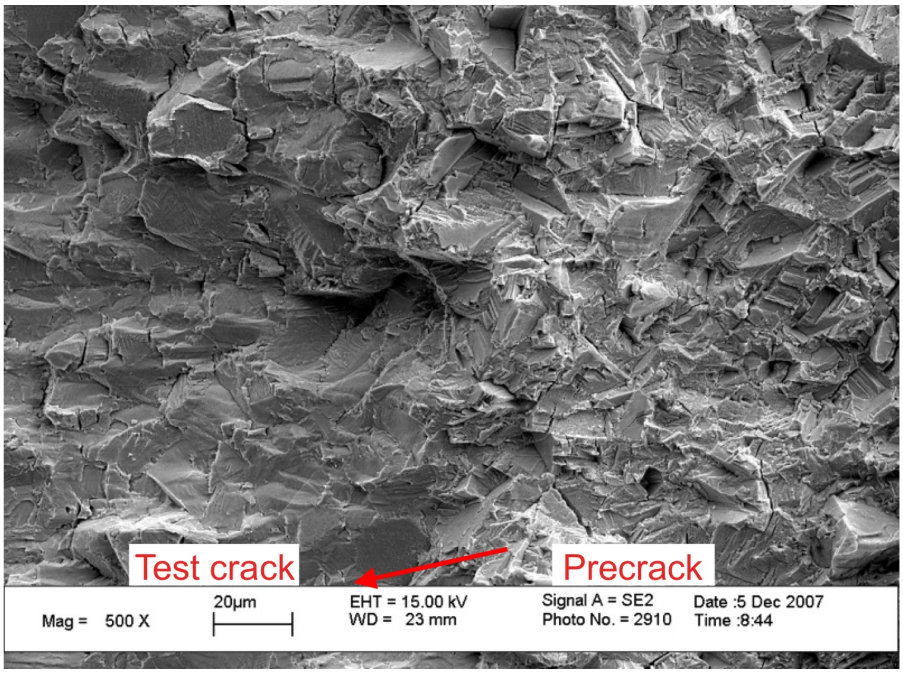

Figure C.27: Scanning electron micrograph of crack front N10R, propagating at $\theta = 1°$ in a Mode II-dominated condition of nominally $\Delta k_1 = 0.3$ MPa$\sqrt{\text{m}}$, $R_1 = 0.98$, $\Delta k_2 = 10.2$ MPa$\sqrt{\text{m}}$, $R_2 = 0.11$ at initial propagation, region highlighted (1) in Fig. C.26.

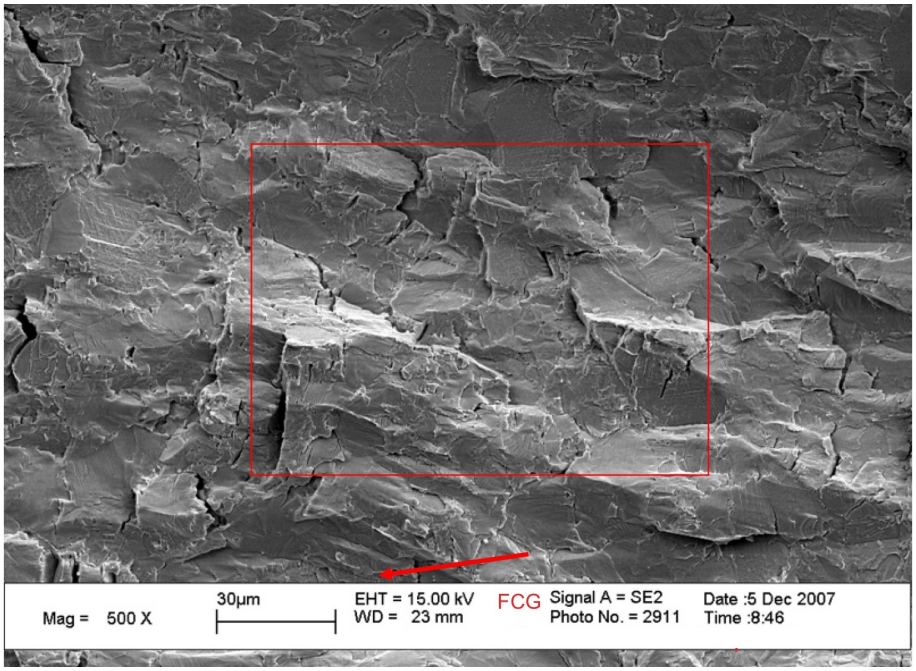

Figure C.28: Scanning electron micrograph of crack front N10R, propagating at $\theta = 1°$ in a Mode II-dominated condition of nominally $\Delta k_1 = 0.3$ MPa$\sqrt{\text{m}}$, $R_1 = 0.98$, $\Delta k_2 = 10.2$ MPa$\sqrt{\text{m}}$, $R_2 = 0.11$ at initial propagation, region highlighted (2) in Fig. C.26.

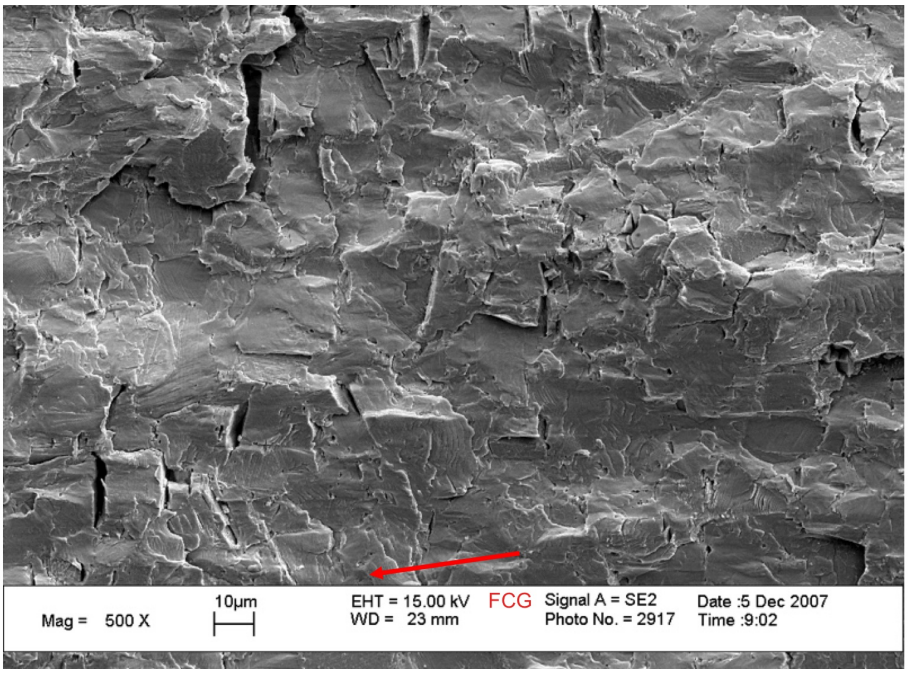

Figure C.29: Scanning electron micrograph of crack front N10R, propagating at $\theta = 1°$ in a Mode II-dominated condition of nominally $\Delta k_1 = 0.3$ MPa$\sqrt{\text{m}}$, $R_1 = 0.98$, $\Delta k_2 = 10.2$ MPa$\sqrt{\text{m}}$, $R_2 = 0.11$ at initial propagation, region highlighted (3) in Fig. C.26.

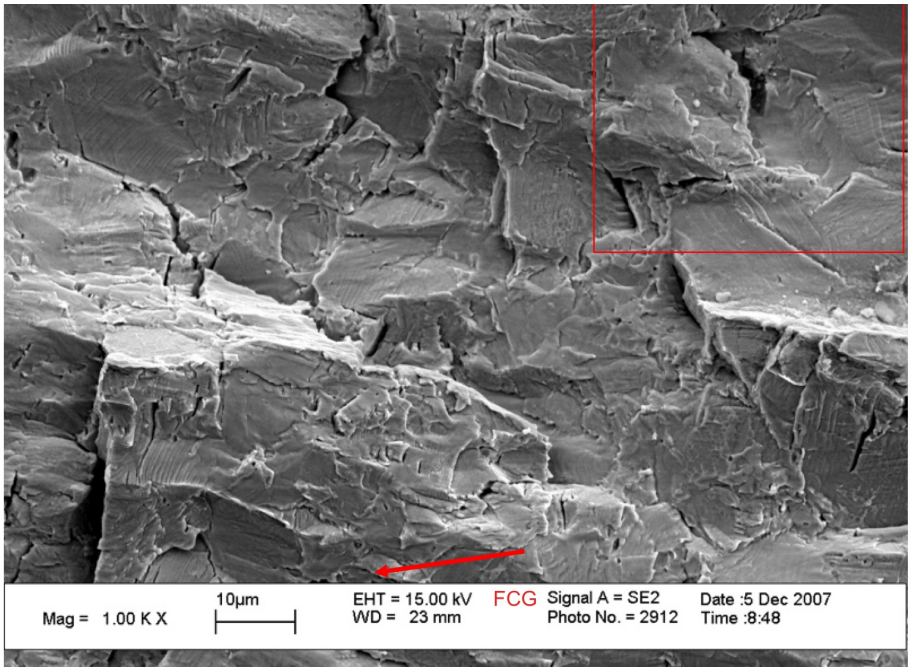

Figure C.30: Scanning electron micrograph of crack front N10R, propagating at $\theta = 1°$ in a Mode II-dominated condition of nominally $\Delta k_1 = 0.3$ MPa$\sqrt{\text{m}}$, $R_1 = 0.98$, $\Delta k_2 = 10.2$ MPa$\sqrt{\text{m}}$, $R_2 = 0.11$ at initial propagation, region highlighted in Fig. C.28.

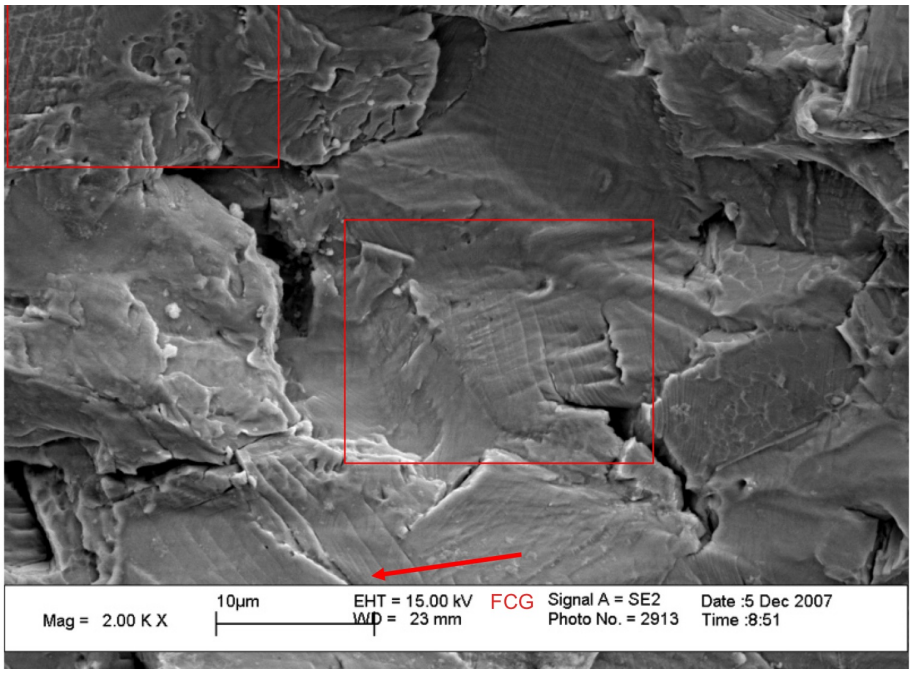

Figure C.31: Scanning electron micrograph of crack front N10R, propagating at $\theta = 1^\circ$ in a Mode II-dominated condition of nominally $\Delta k_1 = 0.3$ MPa$\sqrt{\text{m}}$, $R_1 = 0.98$, $\Delta k_2 = 10.2$ MPa$\sqrt{\text{m}}$, $R_2 = 0.11$ at initial propagation, region highlighted in Fig. C.30.

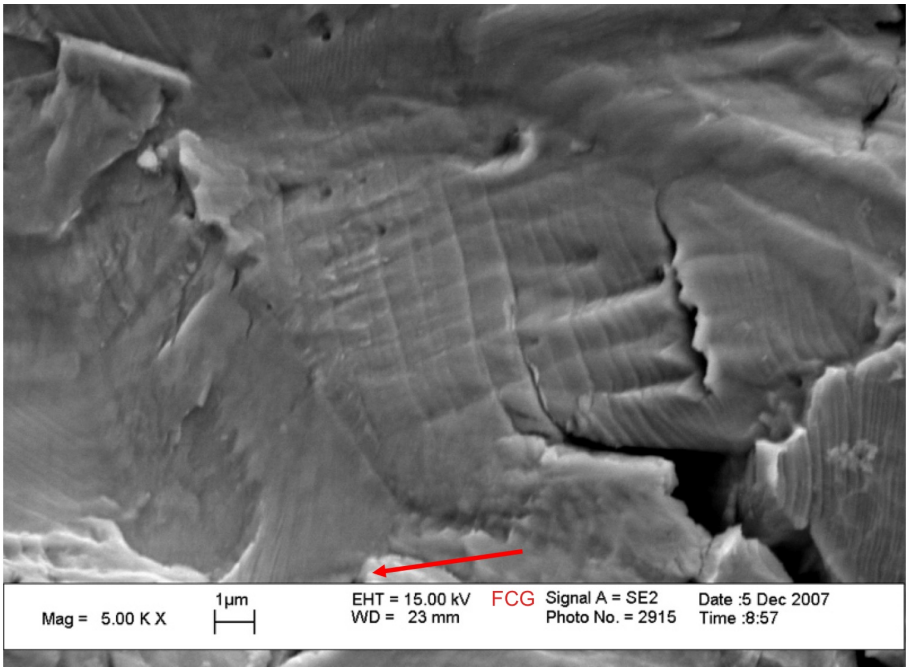

Figure C.32: Scanning electron micrograph of crack front N10R, propagating at $\theta = 1^\circ$ in a Mode II-dominated condition of nominally $\Delta k_1 = 0.3$ MPa$\sqrt{\text{m}}$, $R_1 = 0.98$, $\Delta k_2 = 10.2$ MPa$\sqrt{\text{m}}$, $R_2 = 0.11$ at initial propagation, central region highlighted in Fig. C.31.

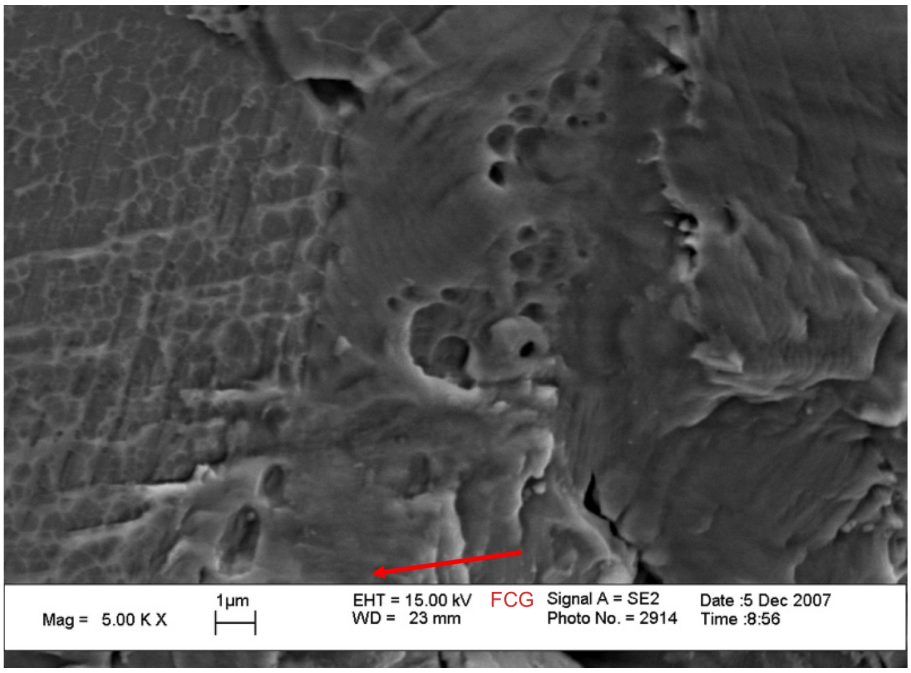

Figure C.33: Scanning electron micrograph of crack front N10R, propagating at $\theta = 1°$ in a Mode II-dominated condition of nominally $\Delta k_1 = 0.3$ MPa$\sqrt{\text{m}}$, $R_1 = 0.98$, $\Delta k_2 = 10.2$ MPa$\sqrt{\text{m}}$, $R_2 = 0.11$ at initial propagation, upper-left region highlighted in Fig. C.31.

C.5 Crack Front N13R

Initial test conditions at the pre-crack for crack front N13R were nominally $K_{\text{Imax}} = 17.7$ MPa$\sqrt{\text{m}}$, $K_{\text{IImax}} = 8.0$ MPa$\sqrt{\text{m}}$, constant tension/cyclic torsion $R_{\text{II}} = 0.1$ fatigue loading. Variation in SIF across the pre-crack front caused crack bifurcation into two different branch modes, $\theta = 1°$ for the small initial Mode II crack branch near the inner radius and -41° for the dominant Mode I crack branch.

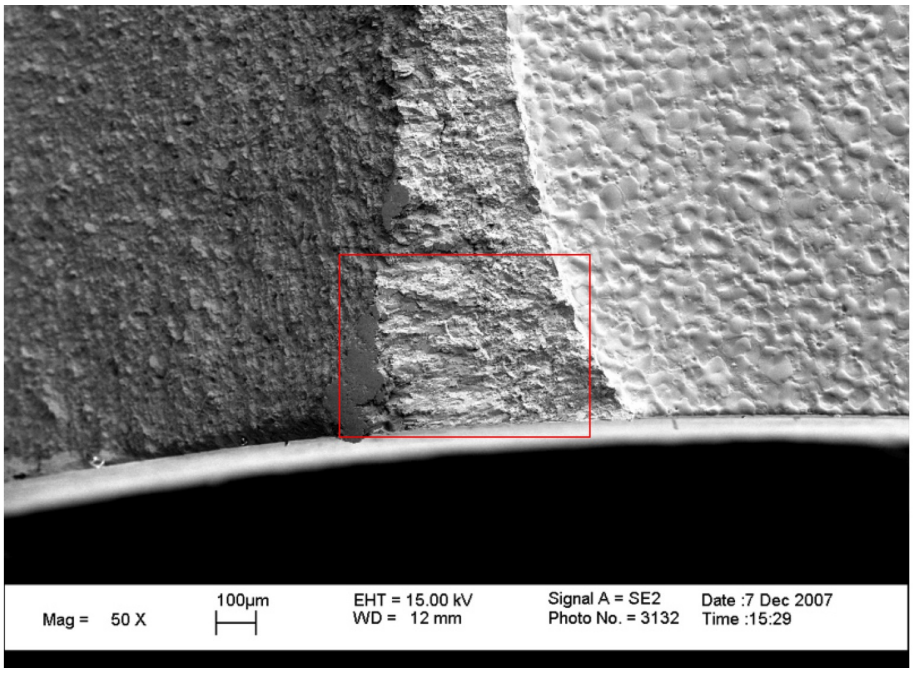

Figure C.34: Scanning electron micrograph of crack front N13R, propagating at $\theta = 1^\circ$ in a Mode II-dominated condition of nominally $\Delta k_1 = 0.2$ MPa$\sqrt{\text{m}}$, $R_1 = 0.99$, $\Delta k_2 = 7.2$ MPa$\sqrt{\text{m}}$, $R_2 = 0.12$ at initial propagation, near inner radius.

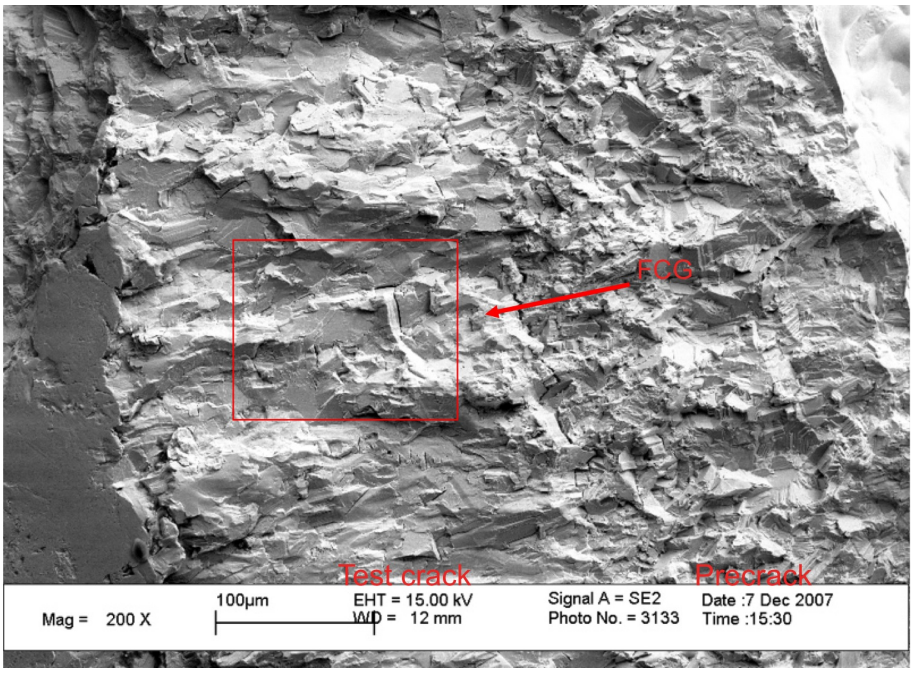

Figure C.35: Scanning electron micrograph of crack front N13R, propagating at $\theta = 1^\circ$ in a Mode II-dominated condition of nominally $\Delta k_1 = 0.2$ MPa$\sqrt{\text{m}}$, $R_1 = 0.99$, $\Delta k_2 = 7.2$ MPa$\sqrt{\text{m}}$, $R_2 = 0.12$ at initial propagation, region highlighted in Fig. C.34.

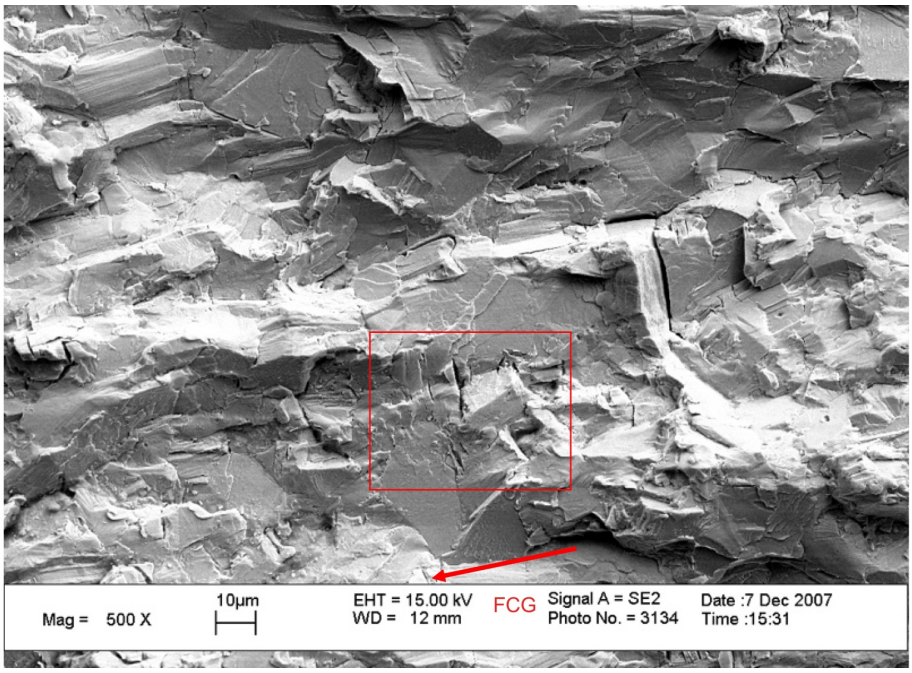

Figure C.36: Scanning electron micrograph of crack front N13R, propagating at $\theta = 1^\circ$ in a Mode II-dominated condition of nominally $\Delta k_1 = 0.2$ MPa$\sqrt{\text{m}}$, $R_1 = 0.99$, $\Delta k_2 = 7.2$ MPa$\sqrt{\text{m}}$, $R_2 = 0.12$ at initial propagation, region highlighted in Fig. C.35.

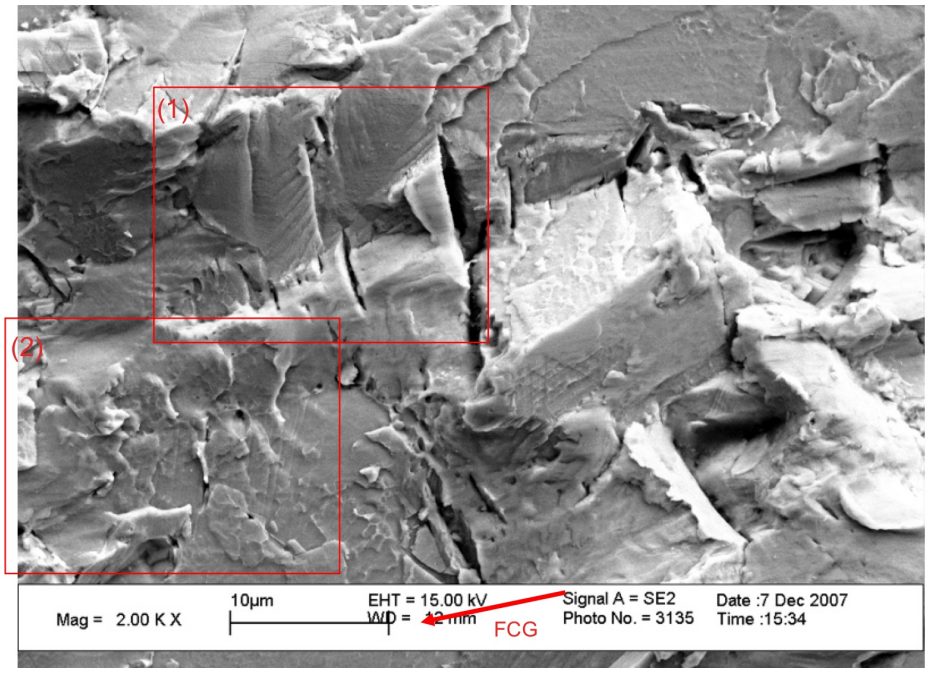

Figure C.37: Scanning electron micrograph of crack front N13R, propagating at $\theta = 1^\circ$ in a Mode II-dominated condition of nominally $\Delta k_1 = 0.2$ MPa$\sqrt{\text{m}}$, $R_1 = 0.99$, $\Delta k_2 = 7.2$ MPa$\sqrt{\text{m}}$, $R_2 = 0.12$ at initial propagation, region highlighted in Fig. C.36.

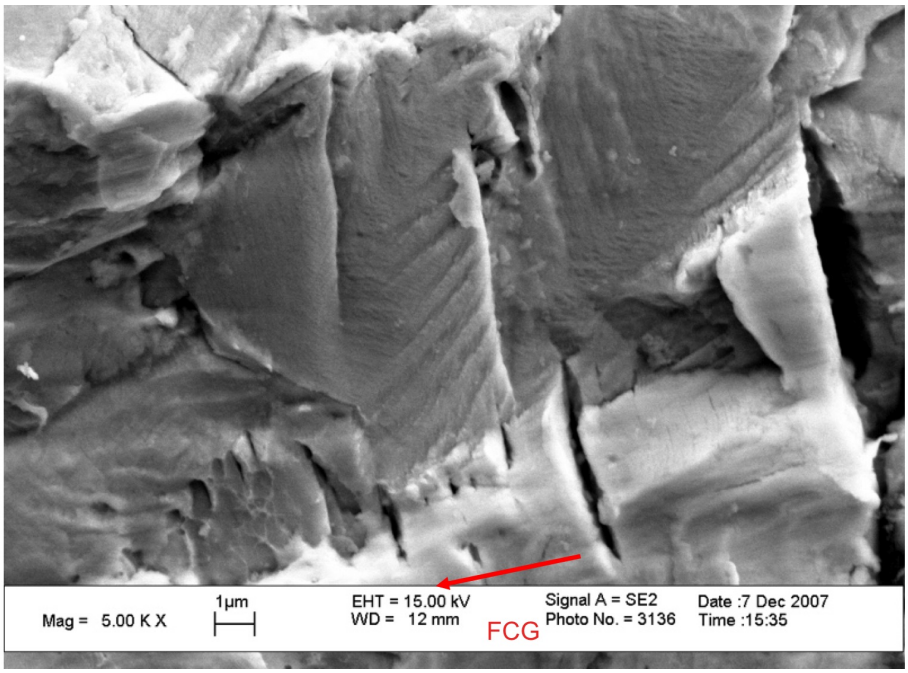

Figure C.38: Scanning electron micrograph of crack front N13R, propagating at $\theta = 1°$ in a Mode II-dominated condition of nominally $\Delta k_1 = 0.2$ MPa$\sqrt{\text{m}}$, $R_1 = 0.99$, $\Delta k_2 = 7.2$ MPa$\sqrt{\text{m}}$, $R_2 = 0.12$ at initial propagation, region highlighted (1) in Fig. C.37.

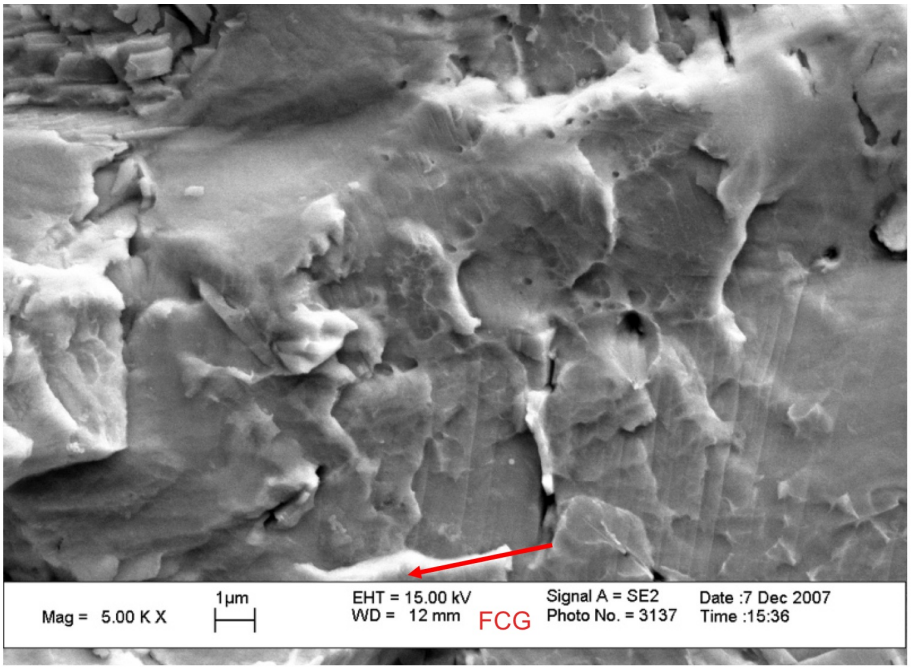

Figure C.39: Scanning electron micrograph of crack front N13R, propagating at $\theta = 1°$ in a Mode II-dominated condition of nominally $\Delta k_1 = 0.2$ MPa$\sqrt{\text{m}}$, $R_1 = 0.99$, $\Delta k_2 = 7.2$ MPa$\sqrt{\text{m}}$, $R_2 = 0.12$ at initial propagation, region highlighted (2) in Fig. C.37.

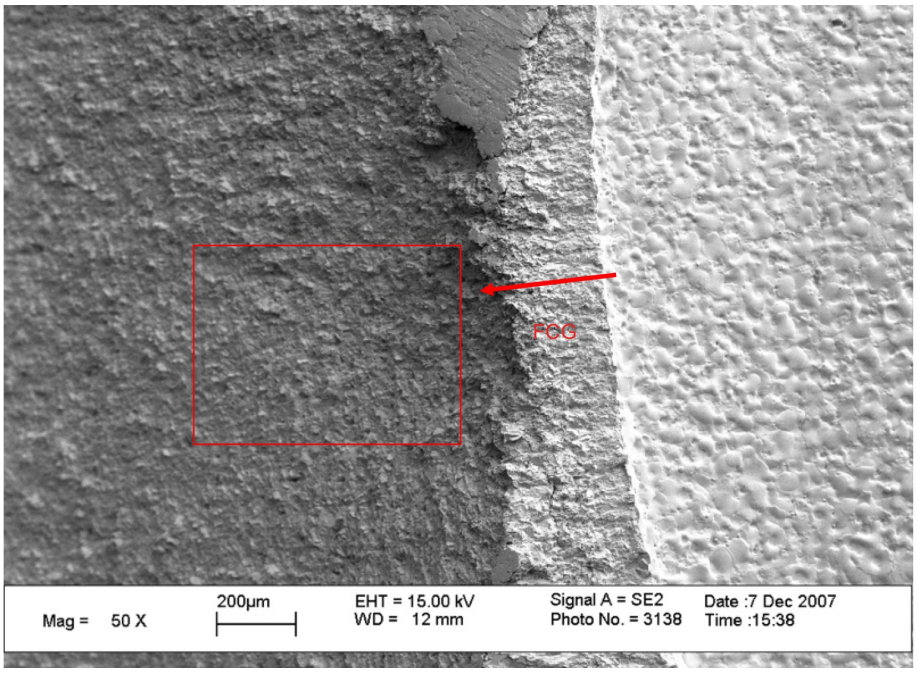

Figure C.40: Scanning electron micrograph of crack front N13R, propagating at θ = -41° in a Mode I-dominated condition of nominally $\Delta k_1 = 6.6$ MPa$\sqrt{\text{m}}$, $R_1 = 0.7$, $\Delta k_2 = 4.2$ MPa$\sqrt{\text{m}}$, $R_2 = 0.15$ at initial propagation, near mid-thickness.

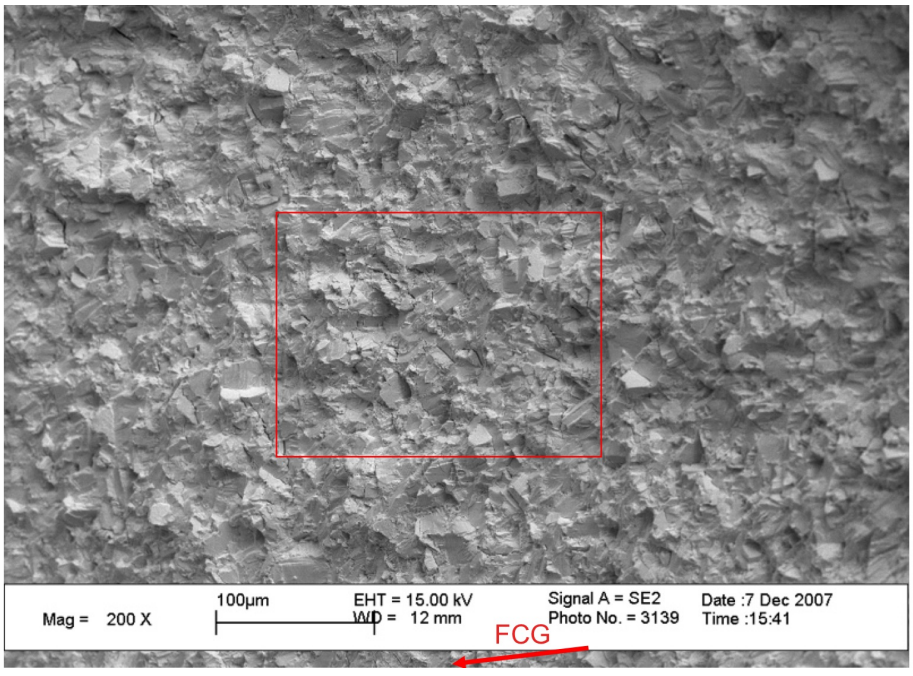

Figure C.41: Scanning electron micrograph of crack front N13R, propagating at θ = -41° in a Mode I-dominated condition of nominally $\Delta k_1 = 6.6$ MPa$\sqrt{\text{m}}$, $R_1 = 0.7$, $\Delta k_2 = 4.2$ MPa$\sqrt{\text{m}}$, $R_2 = 0.15$ at initial propagation, region highlighted in Fig. C.40.

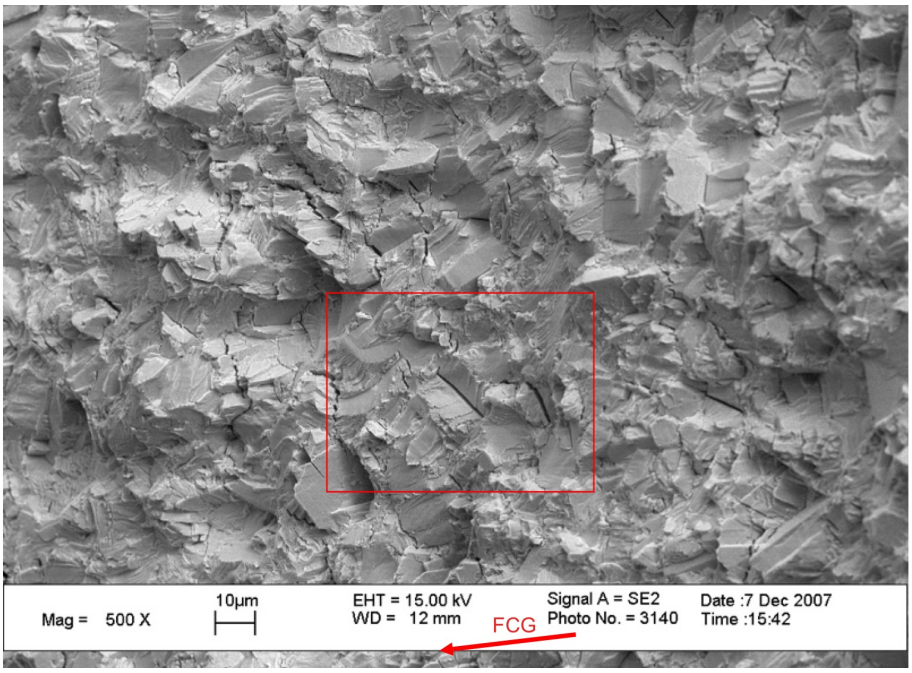

Figure C.42: Scanning electron micrograph of crack front N13R, propagating at θ = -41° in a Mode I-dominated condition of nominally $\Delta k_1 = 6.6$ MPa$\sqrt{\text{m}}$, $R_1 = 0.7$, $\Delta k_2 = 4.2$ MPa$\sqrt{\text{m}}$, $R_2 = 0.15$ at initial propagation, region highlighted in Fig. C.41.

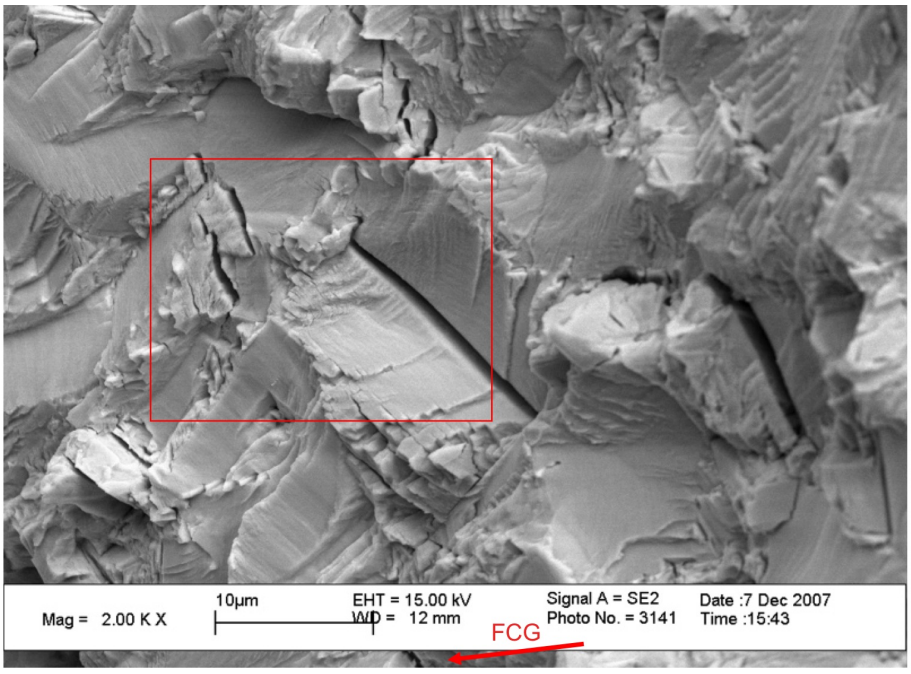

Figure C.43: Scanning electron micrograph of crack front N13R, propagating at θ = -41° in a Mode I-dominated condition of nominally $\Delta k_1 = 6.6$ MPa$\sqrt{\text{m}}$, $R_1 = 0.7$, $\Delta k_2 = 4.2$ MPa$\sqrt{\text{m}}$, $R_2 = 0.15$ at initial propagation, region highlighted in Fig. C.42.

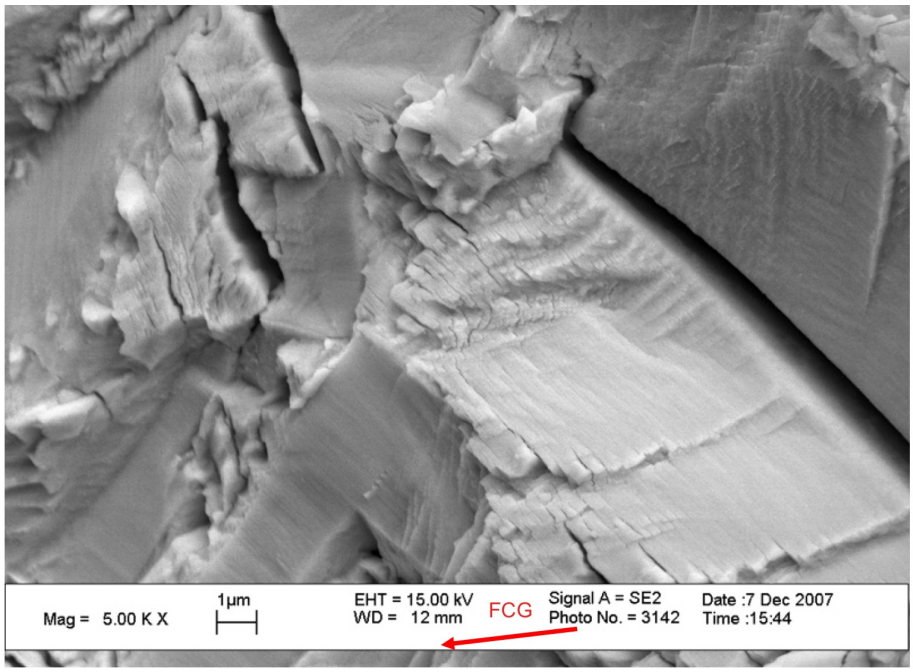

Figure C.44: Scanning electron micrograph of crack front N13R, propagating at θ = -41° in a Mode I-dominated condition of nominally $\Delta k_1 = 6.6$ MPa$\sqrt{\text{m}}$, $R_1 = 0.7$, $\Delta k_2 = 4.2$ MPa$\sqrt{\text{m}}$, $R_2 = 0.15$ at initial propagation, region highlighted in Fig. C.43.

C.6 Crack Front N13L

Initial test conditions at the pre-crack for crack front N13L were nominally K_{Imax} = 17.7 MPa$\sqrt{\mathrm{m}}$, K_{IImax} = 7.9 MPa$\sqrt{\mathrm{m}}$, constant tension/cyclic torsion R_{II} = 0.1 fatigue loading. Variation in SIF across the pre-crack front caused crack branching in two different branch modes: θ = 10° for Mode II crack branching that dominated near the inner radius; and θ = -52° for the Mode I crack branch that began at the outer radius after a transient Mode II kink and spread inward to dominate the entire crack front through the thickness.

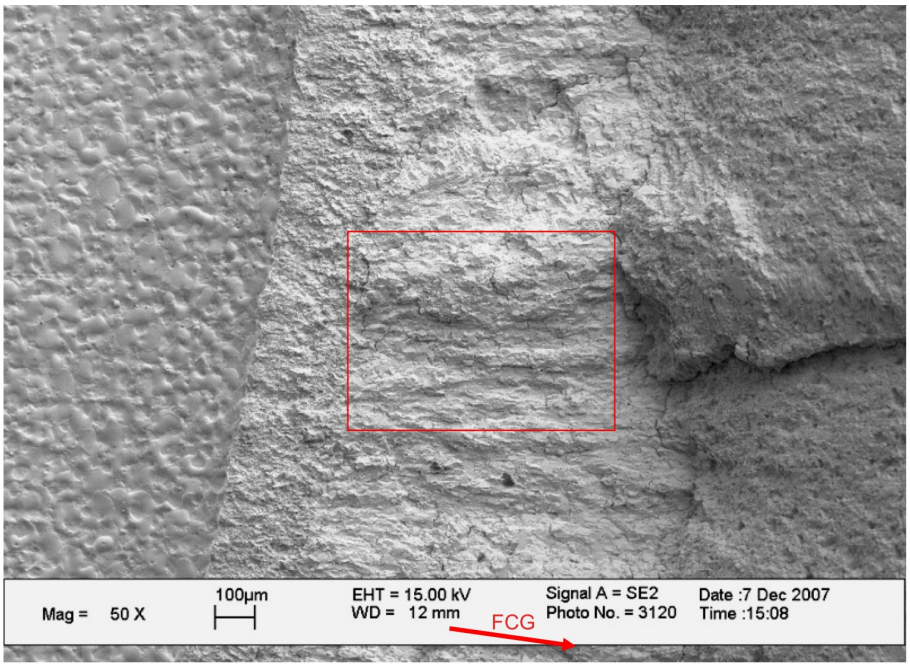

Figure C.45: Scanning electron micrograph of crack front N13L, propagating at θ = 10° in a Mode II-dominated condition of nominally Δk_1 = 1.8 MPa$\sqrt{\mathrm{m}}$, R_1 = 0.89, Δk_2 = 6.9 MPa$\sqrt{\mathrm{m}}$, R_2 = 0.25 at initial propagation, near mid-thickness.

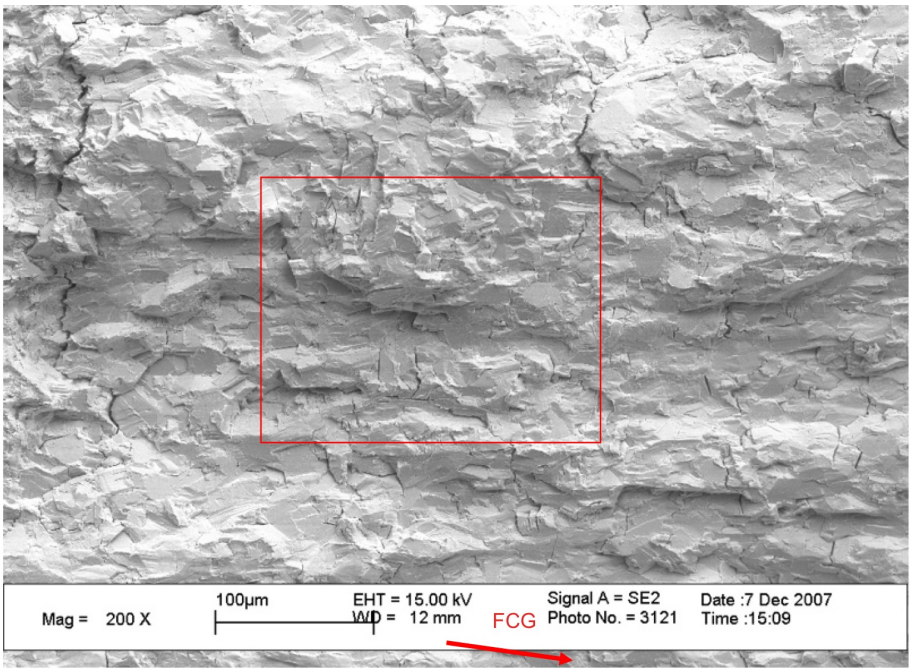

Figure C.46: Scanning electron micrograph of crack front N13L, propagating at $\theta = 10°$ in a Mode II-dominated condition of nominally $\Delta k_1 = 1.8$ MPa$\sqrt{\text{m}}$, $R_1 = 0.89$, $\Delta k_2 = 6.9$ MPa$\sqrt{\text{m}}$, $R_2 = 0.25$ at initial propagation, region highlighted in Fig. C.45.

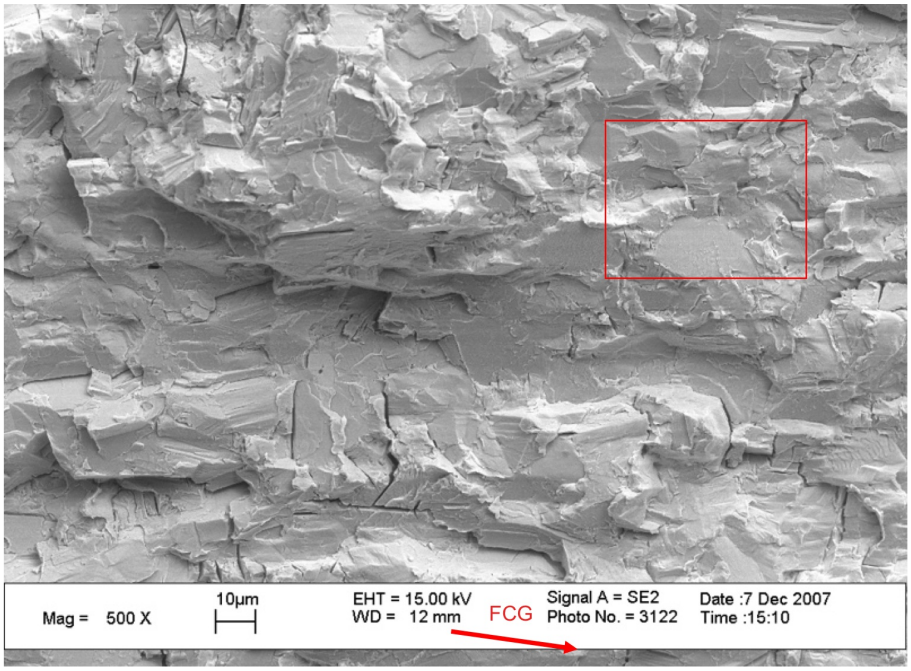

Figure C.47: Scanning electron micrograph of crack front N13L, propagating at $\theta = 10°$ in a Mode II-dominated condition of nominally $\Delta k_1 = 1.8$ MPa$\sqrt{\text{m}}$, $R_1 = 0.89$, $\Delta k_2 = 6.9$ MPa$\sqrt{\text{m}}$, $R_2 = 0.25$ at initial propagation, region highlighted in Fig. C.46.

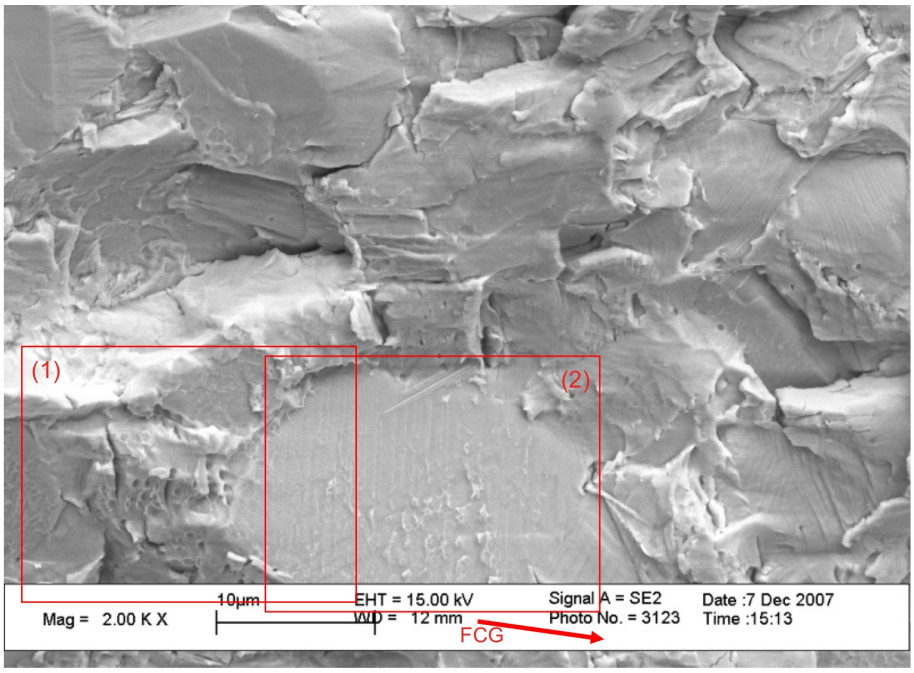

Figure C.48: Scanning electron micrograph of crack front N13L, propagating at $\theta = 10°$ in a Mode II-dominated condition of nominally $\Delta k_1 = 1.8$ MPa$\sqrt{\text{m}}$, $R_1 = 0.89$, $\Delta k_2 = 6.9$ MPa$\sqrt{\text{m}}$, $R_2 = 0.25$ at initial propagation, region highlighted in Fig. C.47.

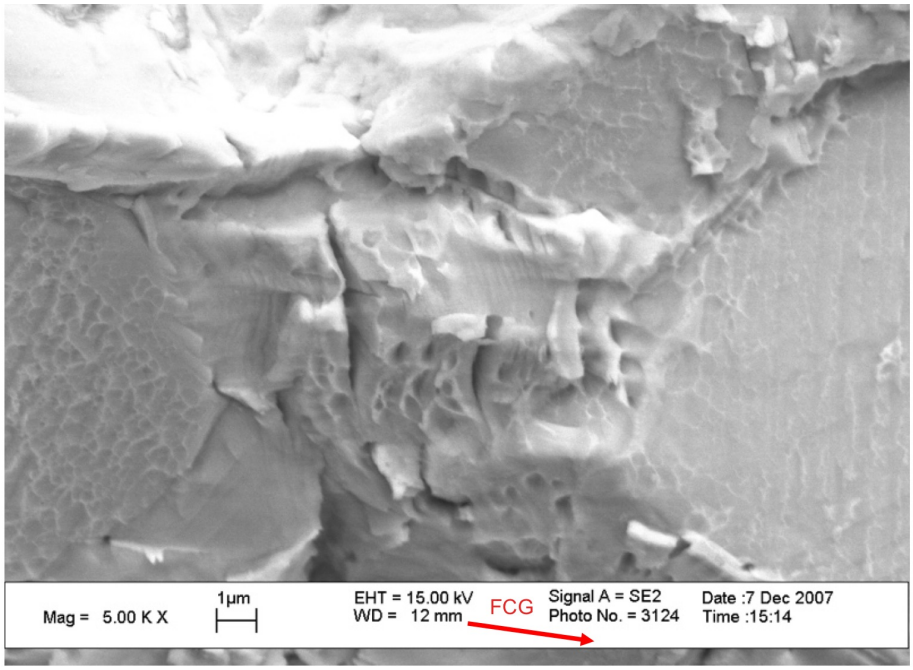

Figure C.49: Scanning electron micrograph of crack front N13L, propagating at $\theta = 10°$ in a Mode II-dominated condition of nominally $\Delta k_1 = 1.8$ MPa$\sqrt{\text{m}}$, $R_1 = 0.89$, $\Delta k_2 = 6.9$ MPa$\sqrt{\text{m}}$, $R_2 = 0.25$ at initial propagation, region highlighted (1) in Fig. C.48.

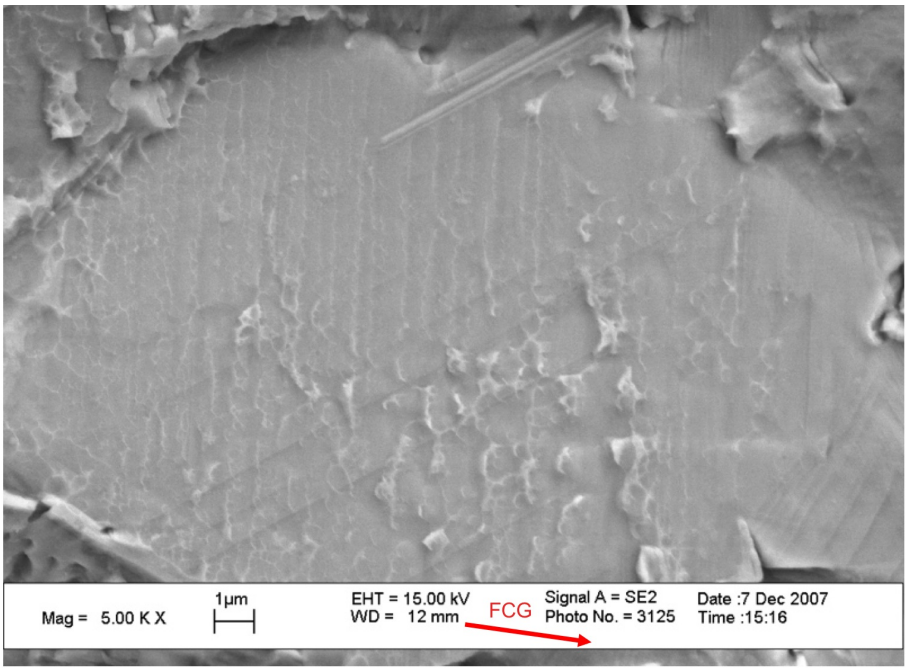

Figure C.50: Scanning electron micrograph of crack front N13L, propagating at θ = 10° in a Mode II-dominated condition of nominally $\Delta k_1 = 1.8$ MPa$\sqrt{\text{m}}$, $R_1 = 0.89$, $\Delta k_2 = 6.9$ MPa$\sqrt{\text{m}}$, $R_2 = 0.25$ at initial propagation, region highlighted (2) in Fig. C.48.

C.7 Crack Front N07L

Initial test conditions at the pre-crack for crack front N07L were nominally K_{Imax} = 17.0 MPa$\sqrt{\text{m}}$, K_{IImax} = 17.0 MPa$\sqrt{\text{m}}$, constant torsion/cyclic tension $R_{\text{I}} = 0.1$ fatigue loading. Crack deflection occurred in a Mode I-dominated direction θ = -14°.

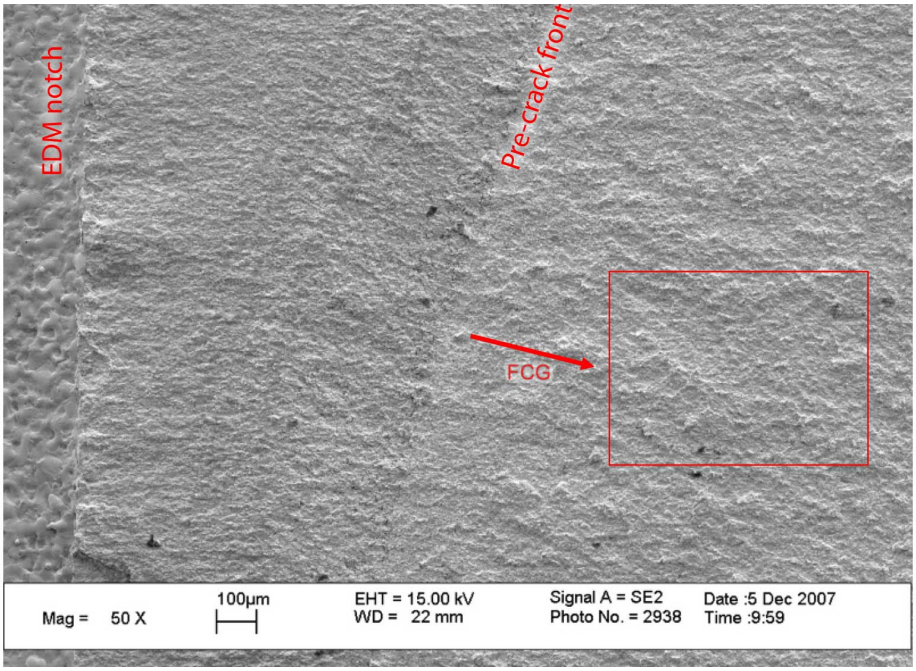

Figure C.51: Scanning electron micrograph of crack front N07L, propagating at θ = -14° in a Mode I-dominated condition of nominally $\Delta k_1 = 15.0$ MPa$\sqrt{\text{m}}$, $R_1 = 0.34$, $\Delta k_2 = 1.8$ MPa$\sqrt{\text{m}}$, $R_2 = 0.88$ at initial propagation, near mid-thickness.

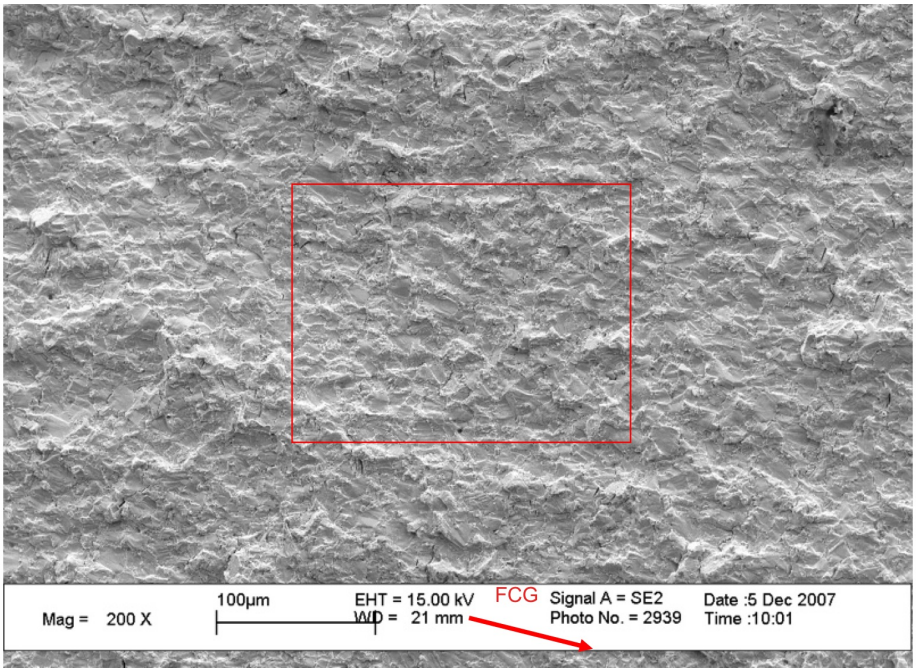

Figure C.52: Scanning electron micrograph of crack front N07L, propagating at θ = -14° in a Mode I-dominated condition of nominally $\Delta k_1 = 15.0$ MPa$\sqrt{\text{m}}$, $R_1 = 0.34$, $\Delta k_2 = 1.8$ MPa$\sqrt{\text{m}}$, $R_2 = 0.88$ at initial propagation, region highlighted in Fig. C.51.

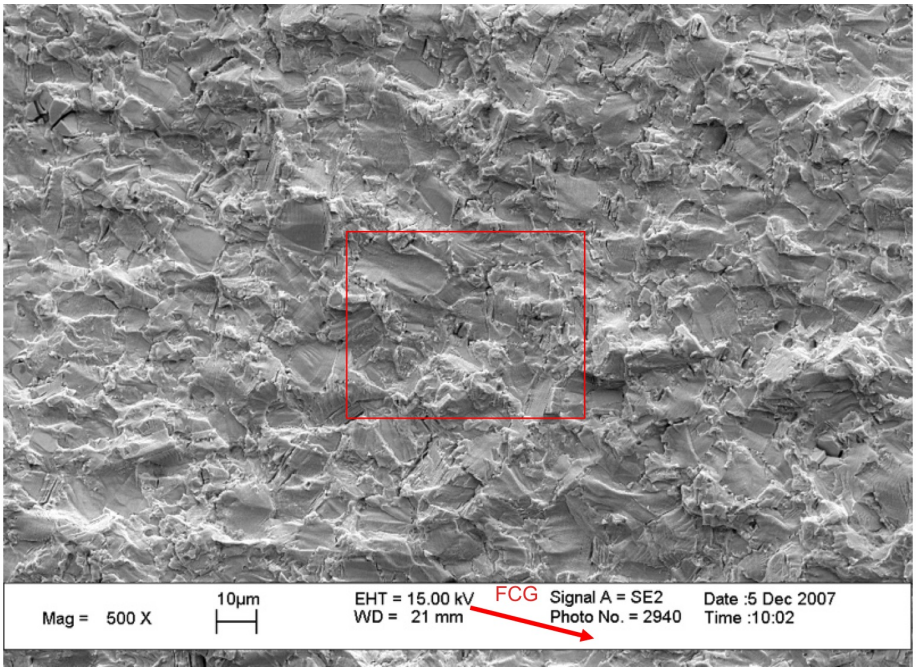

Figure C.53: Scanning electron micrograph of crack front N07L, propagating at θ = -14° in a Mode I-dominated condition of nominally $\Delta k_1 = 15.0$ MPa$\sqrt{\text{m}}$, $R_1 = 0.34$, $\Delta k_2 = 1.8$ MPa$\sqrt{\text{m}}$, $R_2 = 0.88$ at initial propagation region highlighted in Fig. C.52.

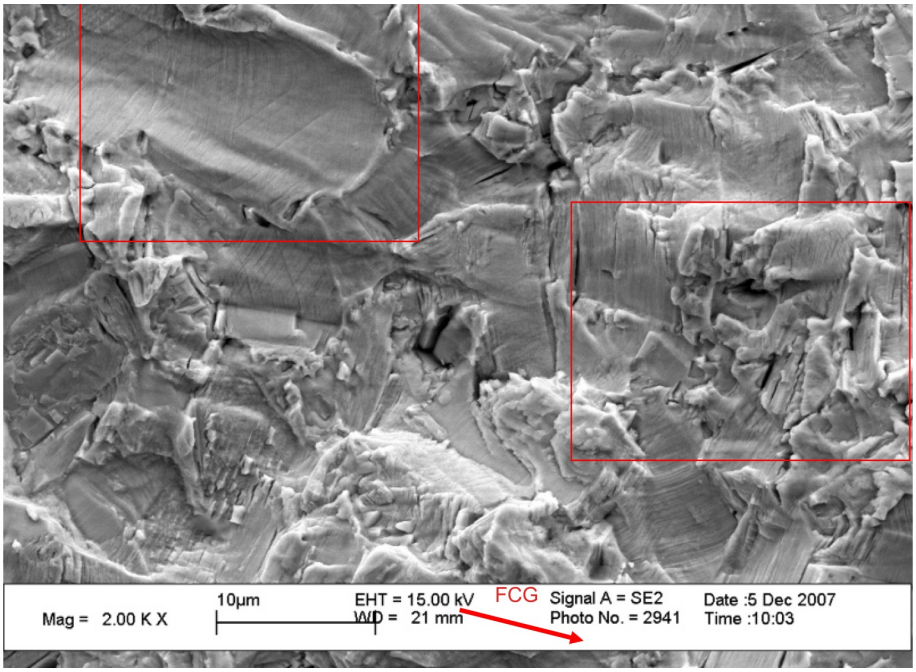

Figure C.54: Scanning electron micrograph of crack front N07L, propagating at θ = -14° in a Mode I-dominated condition of nominally $\Delta k_1 = 15.0$ MPa$\sqrt{\text{m}}$, $R_1 = 0.34$, $\Delta k_2 = 1.8$ MPa$\sqrt{\text{m}}$, $R_2 = 0.88$ at initial propagation, region highlighted in Fig. C.53.

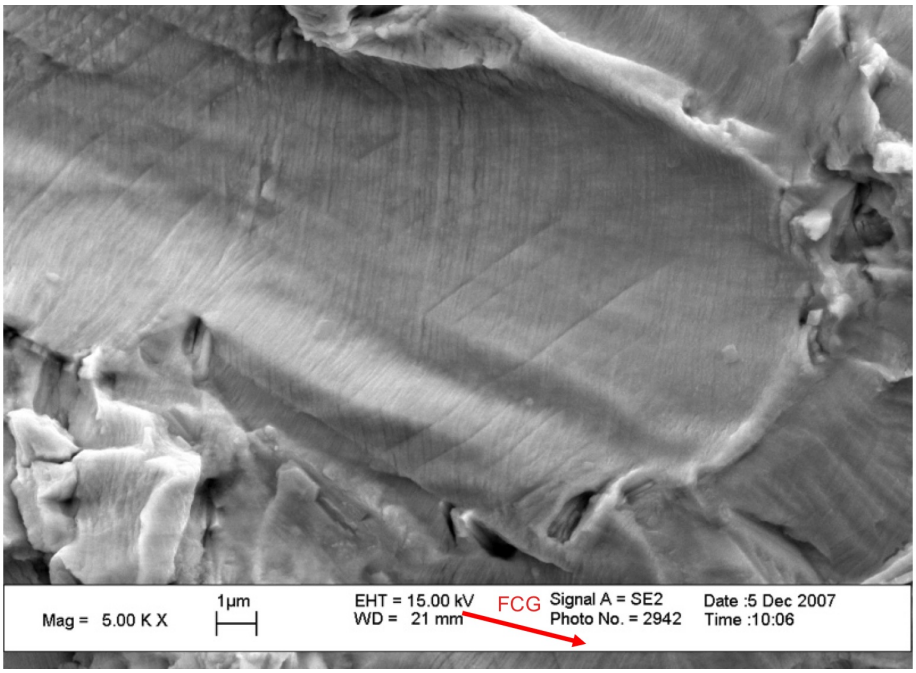

Figure C.55: Scanning electron micrograph of crack front N07L, propagating at θ = -14° in a Mode I-dominated condition of nominally $\Delta k_1 = 15.0$ MPa$\sqrt{\text{m}}$, $R_1 = 0.34$, $\Delta k_2 = 1.8$ MPa$\sqrt{\text{m}}$, $R_2 = 0.88$ at initial propagation, region highlighted (1) in Fig. C.54.

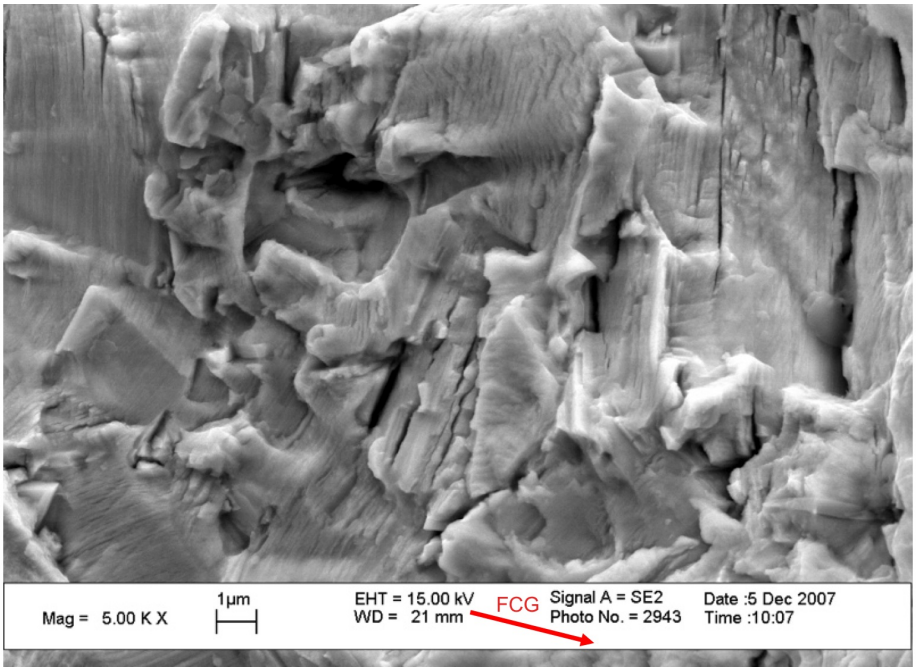

Figure C.56: Scanning electron micrograph of crack front N07L, propagating at θ = -14° in a Mode I-dominated condition of nominally $\Delta k_1 = 15.0$ MPa$\sqrt{\text{m}}$, $R_1 = 0.34$, $\Delta k_2 = 1.8$ MPa$\sqrt{\text{m}}$, $R_2 = 0.88$ at initial propagation, region highlighted (2) in Fig. C.54.

C.8 Crack Front N18R

Initial test conditions at the pre-crack for crack front N18R were nominally K_{Imax} = 10.9 MPa$\sqrt{\mathrm{m}}$, K_{IImax} = 10.6 MPa$\sqrt{\mathrm{m}}$, 180° out-of-phase sinusoidal fatigue loading, R = 0.1. Crack deflection occurred in a Mode I-dominated direction θ = -74°. There was a very small portion of nearly co-planar crack growth at the inner radius of the specimen.

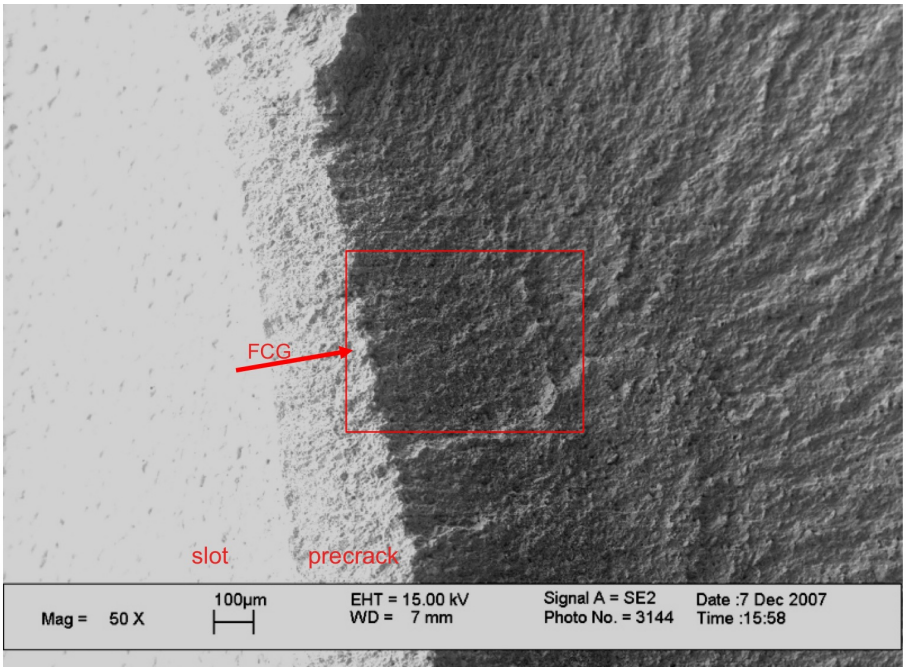

Figure C.57: Scanning electron micrograph of crack front N18R, propagating at θ = -74° in a Mode I-dominated condition of nominally Δk_1 = 6.0 MPa$\sqrt{\mathrm{m}}$, R_1 = 0.53, Δk_2 = 3.1 MPa$\sqrt{\mathrm{m}}$, R_2 = 0.27 at initial propagation, near mid-thickness.

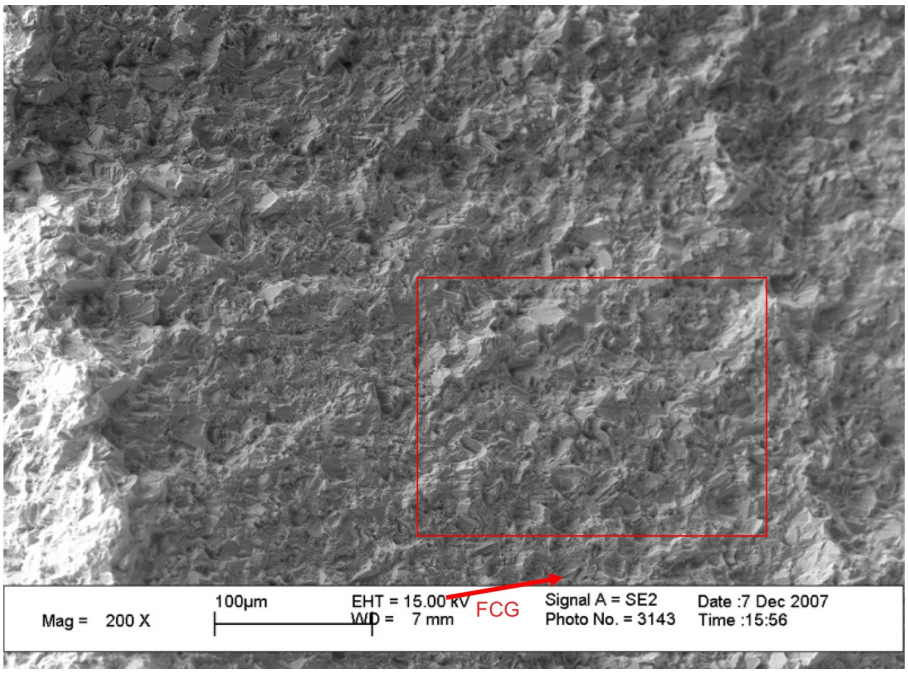

Figure C.58: Scanning electron micrograph of crack front N18R, propagating at θ = -74° in a Mode I-dominated condition of nominally Δk_1 = 6.0 MPa$\sqrt{\text{m}}$, R_1 = 0.53, Δk_2 = 3.1 MPa$\sqrt{\text{m}}$, R_2 = 0.27 at initial propagation, region highlighted in Fig. C.57.

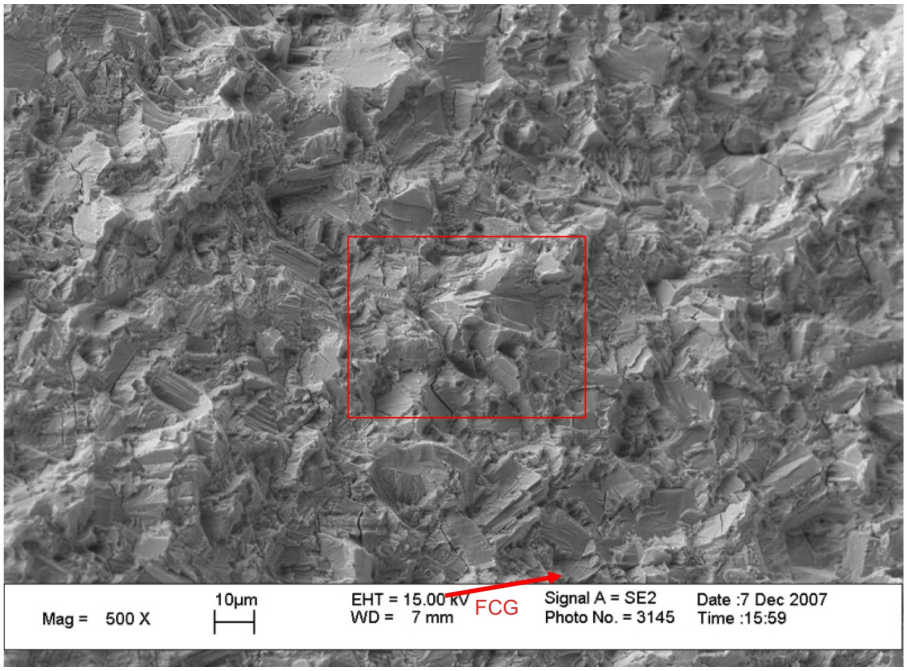

Figure C.59: Scanning electron micrograph of crack front N18R, propagating at θ = -74° in a Mode I-dominated condition of nominally Δk_1 = 6.0 MPa$\sqrt{\text{m}}$, R_1 = 0.53, Δk_2 = 3.1 MPa$\sqrt{\text{m}}$, R_2 = 0.27 at initial propagation, region highlighted in Fig. C.58.

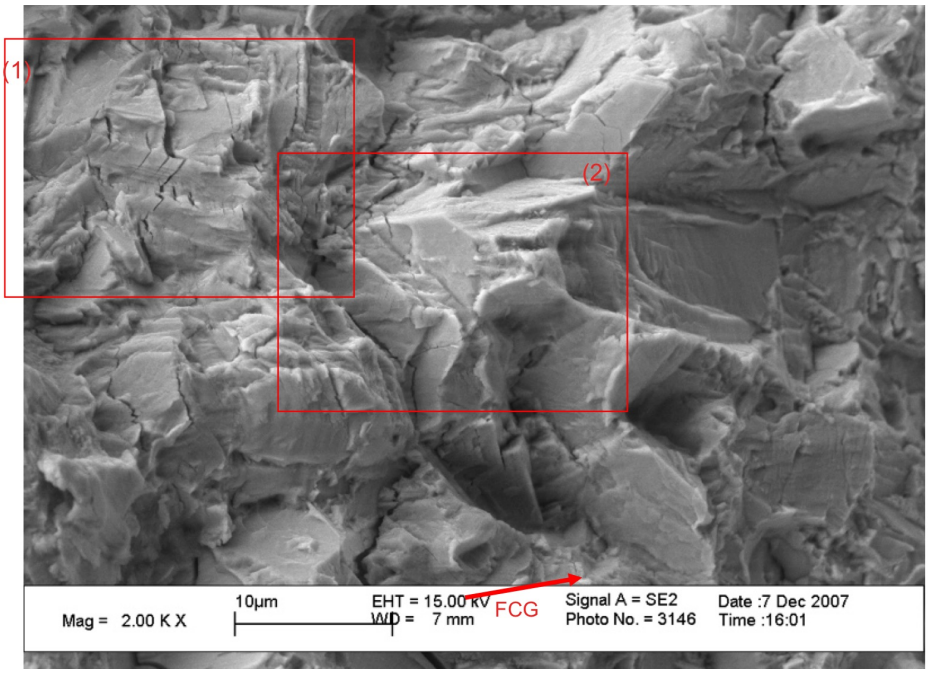

Figure C.60: Scanning electron micrograph of crack front N18R, propagating at θ = -74° in a Mode I-dominated condition of nominally $\Delta k_1 = 6.0$ MPa$\sqrt{\text{m}}$, $R_1 = 0.53$, $\Delta k_2 = 3.1$ MPa$\sqrt{\text{m}}$, $R_2 = 0.27$ at initial propagation, region highlighted in Fig. C.59.

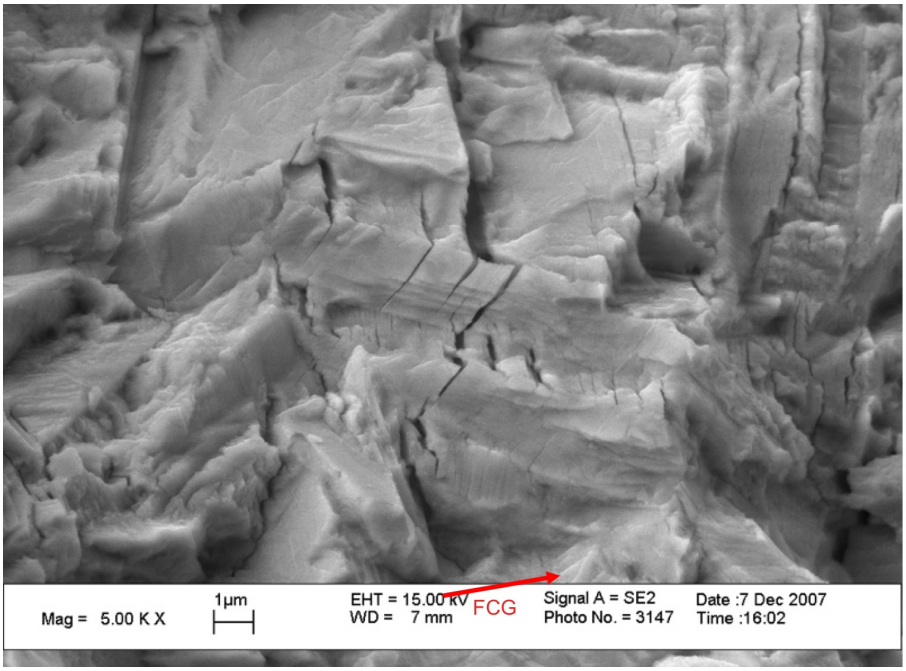

Figure C.61: Scanning electron micrograph of crack front N18R, propagating at θ = -74° in a Mode I-dominated condition of nominally $\Delta k_1 = 6.0$ MPa$\sqrt{\text{m}}$, $R_1 = 0.53$, $\Delta k_2 = 3.1$ MPa$\sqrt{\text{m}}$, $R_2 = 0.27$ at initial propagation, region highlighted (1) in Fig. C.60.

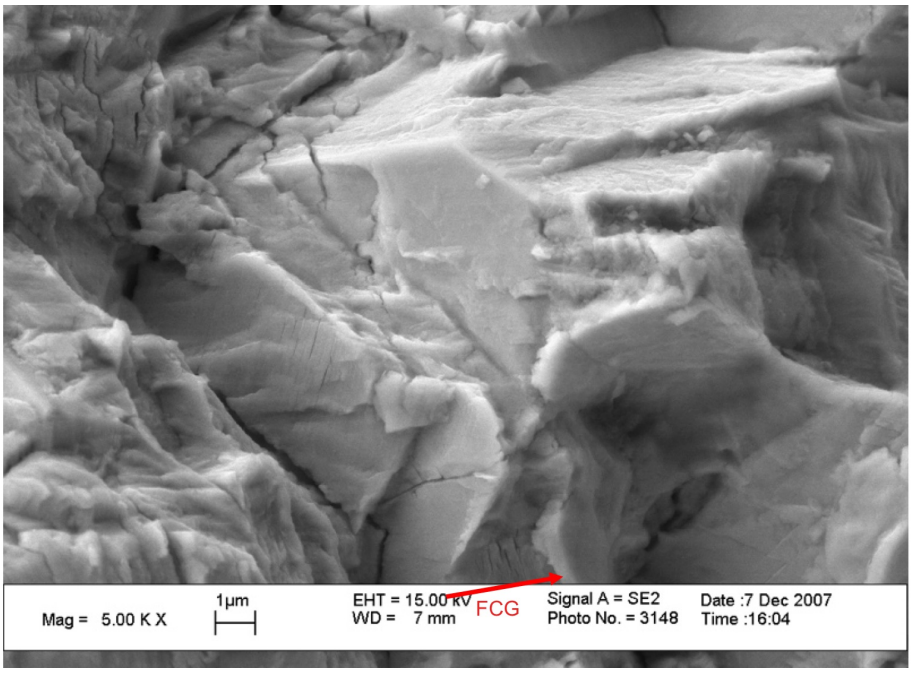

Figure C.62: Scanning electron micrograph of crack front N18R, propagating at θ = -74° in a Mode I-dominated condition of nominally $\Delta k_1 = 6.0$ MPa$\sqrt{\text{m}}$, $R_1 = 0.53$, $\Delta k_2 = 3.1$ MPa$\sqrt{\text{m}}$, $R_2 = 0.27$ at initial propagation, region highlighted (2) in Fig. C.60.

C.9 Crack Front N19R

Initial test conditions at the pre-crack for crack front N19R were nominally K_{Imax} = 17.6 MPa$\sqrt{\text{m}}$, $K_{\text{IImax}} = 7.6$ MPa$\sqrt{\text{m}}$, 180° out-of-phase sinusoidal fatigue loading, $R = 0.1$. Crack deflection occurred in a Mode I-dominated direction $\theta = 18°$.

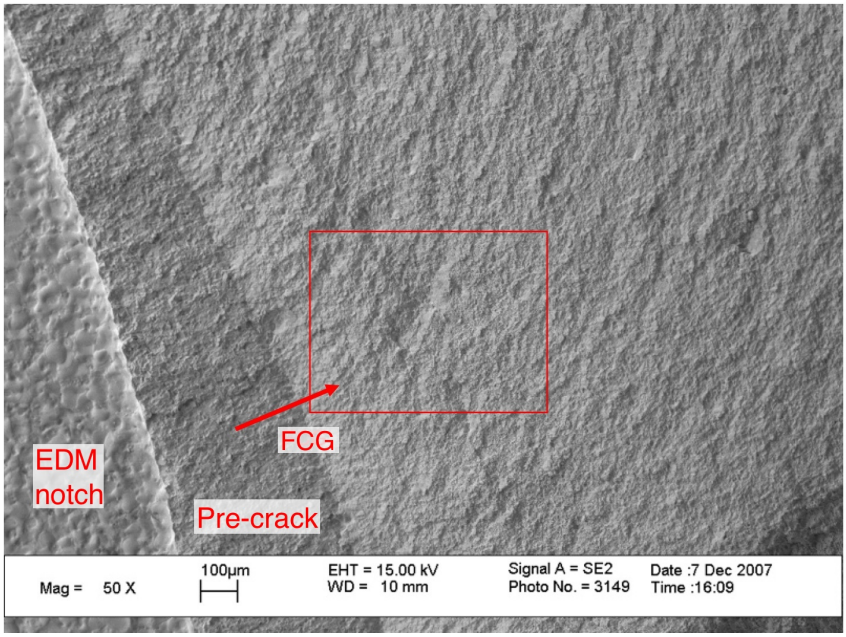

Figure C.63: Scanning electron micrograph of crack front N19R, propagating at θ = 18° in a Mode I-dominated condition of nominally Δk_1 = 18.4 MPa$\sqrt{\text{m}}$, R_1 = -0.11, Δk_2 = 3.8 MPa$\sqrt{\text{m}}$, R_2 = 0.47 at initial propagation, near mid-thickness.

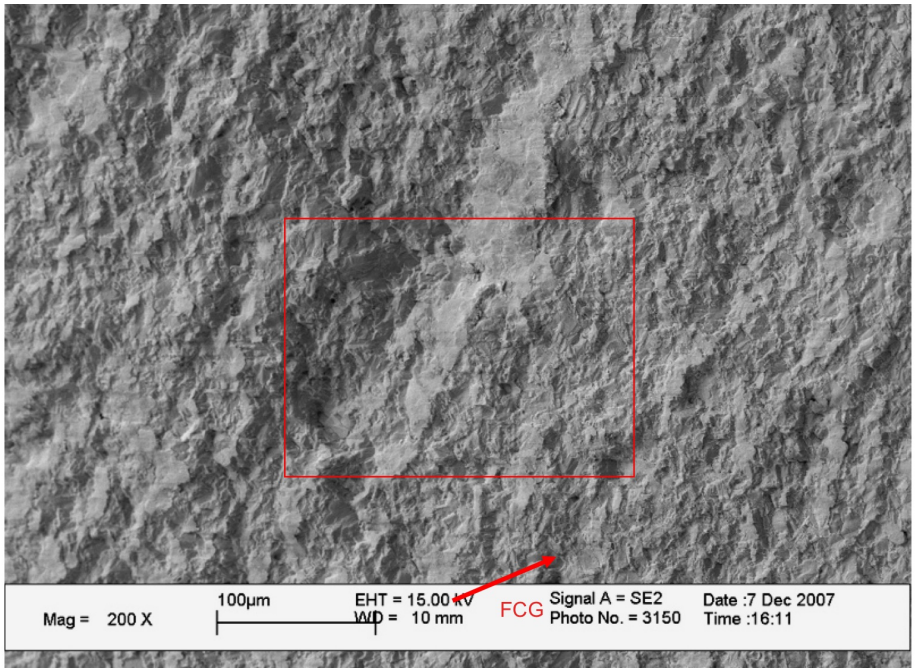

Figure C.64: Scanning electron micrograph of crack front N19R, propagating at θ = 18° in a Mode I-dominated condition of nominally Δk_1 = 18.4 MPa$\sqrt{\text{m}}$, R_1 = -0.11, Δk_2 = 3.8 MPa$\sqrt{\text{m}}$, R_2 = 0.47 at initial propagation, region highlighted in Fig. C.63.

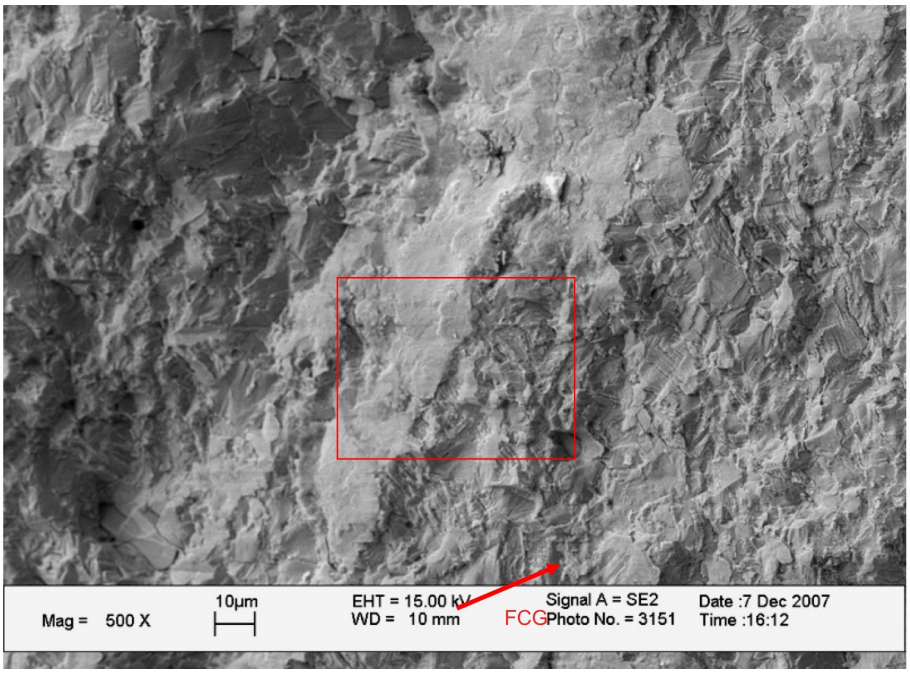

Figure C.65: Scanning electron micrograph of crack front N19R, propagating at θ = 18° in a Mode I-dominated condition of nominally Δk_1 = 18.4 MPa$\sqrt{\text{m}}$, R_1 = -0.11, Δk_2 = 3.8 MPa$\sqrt{\text{m}}$, R_2 = 0.47 at initial propagation region highlighted in Fig. C.64.

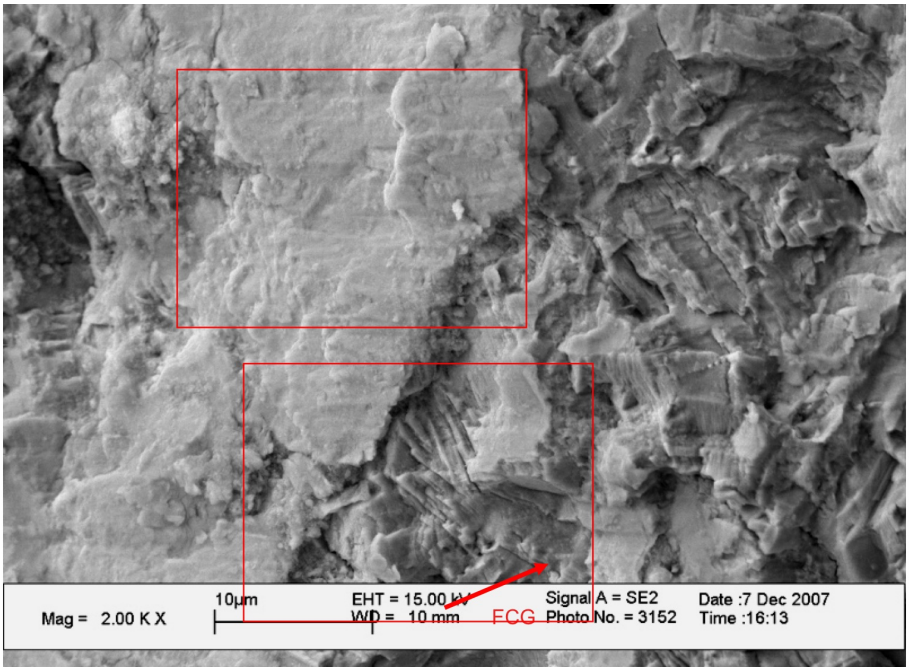

Figure C.66: Scanning electron micrograph of crack front N19R, propagating at θ = 18° in a Mode I-dominated condition of nominally Δk_1 = 18.4 MPa$\sqrt{\text{m}}$, R_1 = -0.11, Δk_2 = 3.8 MPa$\sqrt{\text{m}}$, R_2 = 0.47 at initial propagation, region highlighted in Fig. C.65.

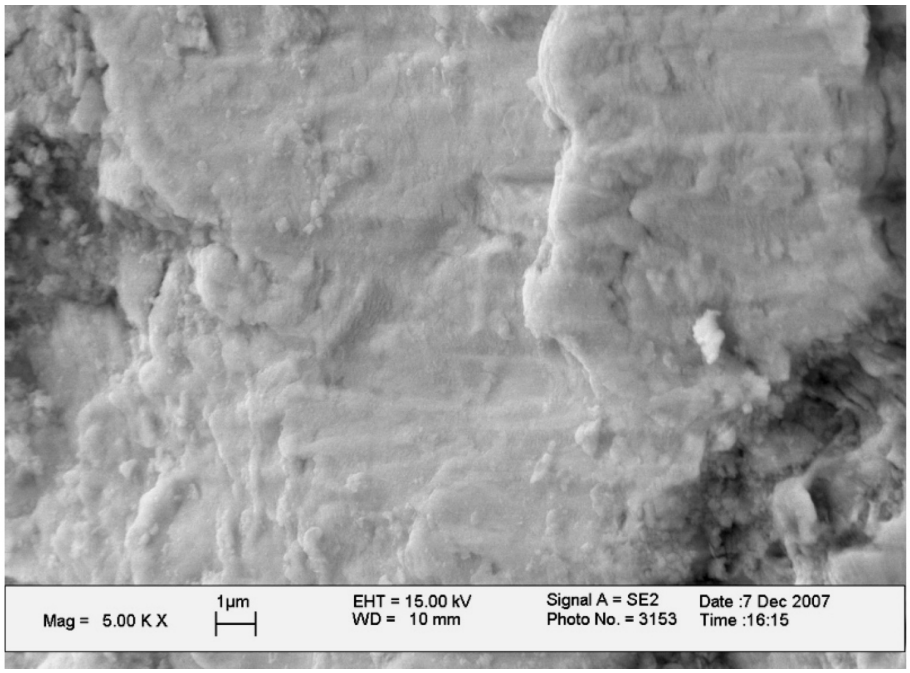

Figure C.67: Scanning electron micrograph of crack front N19R, propagating at θ = 18° in a Mode I-dominated condition of nominally Δk_1 = 18.4 MPa$\sqrt{\text{m}}$, R_1 = -0.11, Δk_2 = 3.8 MPa$\sqrt{\text{m}}$, R_2 = 0.47 at initial propagation, region highlighted (1) in Fig. C.66.

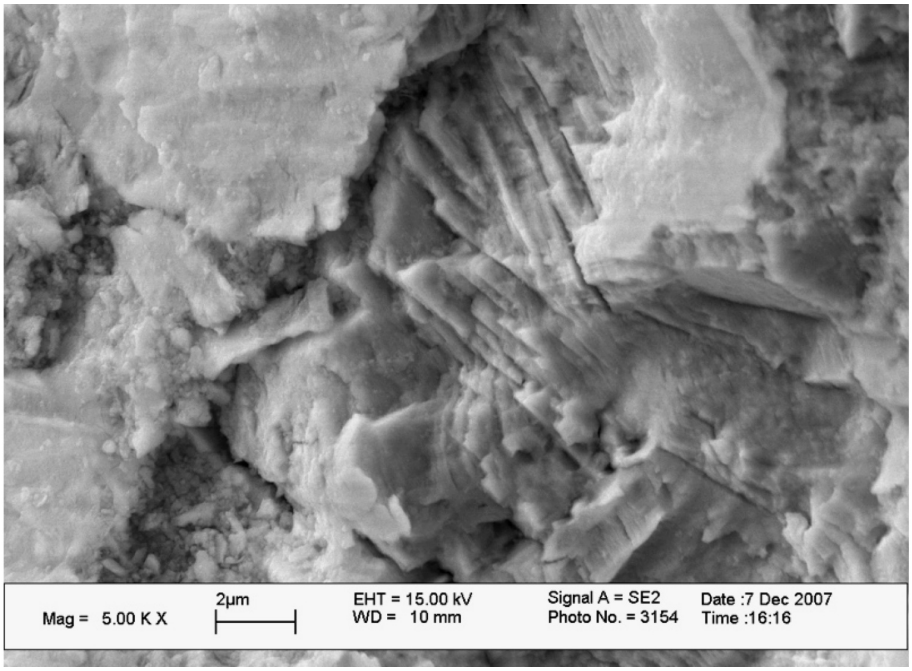

Figure C.68: Scanning electron micrograph of crack front N19R, propagating at θ = 18° in a Mode I-dominated condition of nominally Δk_1 = 18.4 MPa$\sqrt{\text{m}}$, R_1 = -0.11, Δk_2 = 3.8 MPa$\sqrt{\text{m}}$, R_2 = 0.47 at initial propagation, region highlighted (2) in Fig. C.66.

REFERENCES

[1] Erdogan, F. and Sih, G. C., "On the Crack Extension in Plates Under Plane Loading and Transverse Shear," *Journal of Basic Engineering*, vol. 85D, no. 4, pp. 519–527, 1963.

[2] Maccagno, T. M. and Knott, J. F., "The Mixed Mode I/II Fracture Behaviour of Lightly Tempered HY130 Steel at Room Temperature," *Engineering Fracture Mechanics*, vol. 41, no. 6, pp. 805–820, 1992.

[3] Hallback, N. and Nilsson, F., "Mixed-mode I/II fracture behavior of an aluminum alloy," *Journal of Mechanics and Physics of Solids*, vol. 42, no. 9, pp. 1345–1374, 1994.

[4] Qian, J. and Fatemi, A., "Mixed mode fatigue crack growth: a literature survey," *Engineering Fracture Mechanics*, vol. 55, no. 6, pp. 969–990, 1996.

[5] Chao, Y. J. and Zhu, X., "A simple theory for describing the transition between tensile and shear mechanisms in Mode I, II, III, and mixed-mode fracture," in *Mixed-Mode Crack Behavior, ASTM STP 1359* (Miller, K. J. and McDowell, D. L., eds.), pp. 41–57, West Conshohocken, PA: American Society for Testing and Materials, 1999.

[6] Sih, G. C., "Strain energy density factor applied to mixed mode crack problems," *International Journal of Fracture*, vol. 10, pp. 305–321, 1974.

[7] Sih, G. C. and Barthelemy, B. M., "Mixed mode fatigue crack growth predictions," *Engineering Fracture Mechanics*, vol. 13, no. 3, pp. 439–451, 1980.

[8] Badaliance, R., "Application of strain energy density factor to fatigue crack growth analysis," *Engineering Fracture Mechanics*, vol. 13, no. 3, pp. 657–666, 1980.

[9] Hussain, M. A., Pu, S. L., and Underwood, J. H., "Strain energy release rate for a crack under combined mode i and mode ii," in *Fracture Analysis, ASTM STP 560*, pp. 2–28, Philadelphia: ASTM, 1974.

[10] Chang, J., Xu, J.-q., and Mutoh, Y., "A general mixed-mode brittle fracture criterion for cracked materials," *Engineering Fracture Mechanics*, vol. 73, pp. 1249–1263, 2006.

[11] Shih, C. F., "Small-scale yielding analysis of mixed mode plane-strain crack problems," in *Fracture Analysis* (Paris, P. C. and Irwin, G. R., eds.), pp. 187–210, Philadelphia, PA: American Society for Testing and Materials, 1974.

[12] Hutchinson, J. W., "Plastic stress and strain fields at crack tip," *Journal of the Mechanics and Physics of Solids*, vol. 16, no. 5, pp. 337–347, 1968.

[13] Rice, J. R. and Rosengren, G. F., "Plane strain deformation near crack tip in power-law hardening material," *Journal of Mechanics and Physics of Solids*, vol. 16, no. 1, pp. 1–12, 1968.

[14] Pettit, R. G., *Crack turning in integrally stiffened aircraft structures*. PhD Thesis, Cornell University, 2000.

[15] Liebowitz, H., Lee, J. D., and Eftis, J., "Biaxial load effects in fracture mechanics," *Engineering Fracture Mechanics*, vol. 10, no. 2, pp. 315–335, 1978.

[16] Cotterell, B. and Rice, J. R., "Slightly Curved or Kinked Cracks," *International Journal of Fracture*, vol. 16, pp. 155–169, 1980.

[17] Maccagno, T. M. and Knott, J. F., "The fracture behaviour of PMMA in mixed modes I and II," *Engineering Fracture Mechanics*, vol. 34, no. 1, pp. 65–86, 1989.

[18] Maccagno, T. M. and Knott, J. F., "The low temperature brittle fracture behaviour of steel in mixed modes I and II," *Engineering Fracture Mechanics*, vol. 38, no. 2-3, pp. 111–128, 1991.

[19] Amstutz, B. E., Sutton, M. A., Dawicke, D. S., and Boone, M. L., "Effects of mixed mode i/ii loading and grain orientation on crack initiation and stable tearing in 2024-t3 aluminum," in *Fracture Mechanics: 27th Volume, ASTM STP 1296* (Piascik, R. S., Newman, J. C., and Dowling, N. E., eds.), vol. 27, pp. 105–125, American Society for Testing and Materials, 1997.

[20] Dalle Donne, C. and Doeker, H., "Plane stress crack resistance curves of an inclined crack under biaxial loading," *SAE Special Publications*, no. 1280, pp. 243–263, 1997.

[21] Ghosal, A. K. and Narasimhan, R., "A Finite Element Analysis of Mixed-Mode Fracture Initiation by Ductile Failure Mechanisms," *Journal of the Mechanics and Physics of Solids*, vol. 42, no. 6, pp. 953–978, 1994.

[22] Chao, Y. J. and Liu, S., "On the failure of cracks under mixed-mode loads," *International Journal of Fracture*, vol. 87, pp. 201–223, 1997.

[23] Liu, S., Chao, Y. J., and Zhu, X., "Tensile-shear transition in mised mode I/III fracture," *International Journal of Solids and Structures*, vol. 41, pp. 6147–6172, 2004.

[24] Kfouri, A. P. and Brown, M. W., "A fracture criterion for cracks under mixed-mode loading," *Fatigue and Fracture of Engineering Materials and Structures*, vol. 18, no. 9, pp. 959–969, 1995.

[25] Shah, R. C., "Effects of combined mode loadings on fracture and flaw growth," *AIAA Journal*, vol. 13, no. 9, pp. 1158–1164, 1975.

[26] Otsuka, A., Mori, K., and Miyata, T., "The condition of fatigue crack growth in mixed mode condition," *Engineering Fracture Mechanics*, vol. 7, no. 3, pp. 429–432, IN15–IN18, 433–439, 1975.

[27] Tanaka, K., "Fatigue crack propagation from a crack inclined to the cyclic tensile axis," *Engineering Fracture Mechanics*, vol. 6, no. 3, pp. 493–498, IN13–IN14, 499–507, 1974.

[28] Iida, S. and Kobayashi, A. S., "Crack-propagation rate in 7075-T6 plates under cyclic tensile and transverse shear loadings," *Transactions of the ASME. Series D, Journal of Basic Engineering*, vol. 91, no. 4, pp. 764–9, 1969.

[29] Roberts, R. and Kibler, J. J., "Mode II fatigue crack propagation," *Journal of Basic Engineering*, vol. 93 Ser D, no. 4, pp. 671–80, 1971.

[30] Lam, Y. C., "Mixed mode fatigue crack growth and the strain energy density factor," *Theoretical and Applied Fracture Mechanics*, vol. 12, no. 1, pp. 67–72, 1989.

[31] Liu, H. W., "Shear fatigue crack growth: a literature survey," *Fatigue and Fracture of Engineering Materials and Structures*, vol. 8, no. 4, pp. 295–313, 1985.

[32] Gao, H., Brown, M. W., and Miller, K. J., "Mixed-Mode Fatigue Thresholds," *Fatigue of Engineering Materials and Structures*, vol. 5, no. 1, pp. 1–17, 1982.

[33] Gao, H., Alagok, N., Brown, M. W., and Miller, K. J., "Growth of fatigue cracks under combined mode i and mode ii loads," in *Multiaxial Fatigue, ASTM STP 853* (Miller, K. J. and Brown, M. W., eds.), pp. 184–202, Philadelphia, PA: American Society for Testing and Materials, 1985.

[34] Yokobori, A. T., J., Yokobori, T., Sato, K., and Syoji, K., "Fatigue crack growth under mixed modes I and II," *Fatigue and Fracture of Engineering Materials and Structures*, vol. 8, no. 4, pp. 315–325, 1985.

[35] Magill, M. A. and Zwerneman, F. J., "Sustained mode I and mode II fatigue crack growth in flat plates," *Engineering Fracture Mechanics*, vol. 55, no. 6, pp. 883–899, 1996.

[36] Tong, J., Yates, J. R., and Brown, M. W., "The formation and propagation of mode I branch cracks in mixed mode fatigue failure," *Engineering Fracture Mechanics*, vol. 56, no. 2, pp. 213–31, 1997.

[37] Campbell, J. P. and Ritchie, R. O., "Mixed-mode, high-cycle fatigue-crack growth thresholds in Ti-6Al-4V I. A comparison of large- and short-crack behavior," *Engineering Fracture Mechanics*, vol. 67, pp. 209–227, 2000.

[38] Campbell, J. P. and Ritchie, R. O., "Mixed-mode, high-cycle fatigue-crack growth thresholds in Ti-6Al-4V II. Quantification of crack-tip shielding," *Engineering Fracture Mechanics*, vol. 67, pp. 229–249, 2000.

[39] Otsuka, A., Tohgo, K., and Matsuyama, H., "Fatigue crack initiation and growth under mixed mode loading in aluminum alloys 2017-T3 and 7075-T6," *Engineering Fracture Mechanics*, vol. 28, no. 5/6, pp. 721–732, 1987.

[40] Bold, P. E., Brown, M. W., and Allen, R. J., "A review of fatigue crack growth in steels under mixed mode I and II loading," *Fatigue And Fracture of Engineering Materials And Structures*, vol. 15, no. 10, pp. 965–77, 1992.

[41] Melin, S., "Fracture from a straight crack subject to mixed mode loading," *International Journal of Fracture*, vol. 32, pp. 257–263, 1987.

[42] Chan, K. S., Hack, J. E., and Leverant, G. R., "Fatigue Crack Growth in MAR-M200 Single Crystals," *Metallurgical Transactions A*, vol. 18A, pp. 581–591, 1987.

[43] Reed, P. A. S. and King, J. E., "Mixed mode fatigue effects in Ni-base single crystals - preliminary results," *Scripta Metallurgica et Materialia*, vol. 26, no. 12, pp. 1829–1834, 1992.

[44] Wu, X. D. and Reed, P. A. S., "Mode i and mixed mode i/ii fatigue of ni-base single crystal udimet 720 in air and vacuum," in *Fatigue 96: Sixth International Fatigue Congress*, vol. 2, (Berlin, Germany), pp. 855–860, 1996.

[45] Zhang, G. P. and Wang, Z. G., "Mode I and mixed mode I/II fatigue cracking in Ni3Al(CrB) single crystals," *Fatigue and Fracture of Engineering Materials and Structures*, vol. 20, no. 6, pp. 883–894, 1997.

[46] John, R., DeLuca, D., Nicholas, T., and Porter, J., "Near-threshold crack growth behavior of a single crystal Ni-base superalloy subjected to mixed-mode loading," *ASTM Special Technical Publication Proceedings of the 1998 Symposium on Mixed-Mode Crack Behavior, May 6-May 7 1998*, no. 1359, pp. 312–328, 1999.

[47] Hourlier, F., d'Hondt, H., Truchon, M., and Pineau, A., "Fatigue crack path behavior under polymodal fatigue," in *Multiaxial Fatigue, ASTM STP 853*, pp. 228–248, Philadelphia, PA, USA: American Society for Testing and Materials, 1985.

[48] Hourlier, F. and Pineau, A., "Fatigue crack propagation behavior under complex mode loading," in *5th International Conference on Fracture* (Francois,

D., Bathias, C., and Bilby, B. A., eds.), vol. 4, (Cannes, France), pp. 1833–1840, Oxford: Pergamon Press, 1981.

[49] Smith, M. C. and Smith, R. A., "Toward an understanding of mode ii fatigue crack growth," in *Basic Questions in Fatigue: Volume I, ASTM STP 924* (Fong, J. T. and Fields, R. J., eds.), pp. 260–280, Philadelphia, PA: American Society for Testing and Materials, 1988.

[50] Bold, P. E., Brown, M. W., and Allen, R. J., "Shear mode crack growth and rolling contact fatigue," *Wear*, vol. 144, pp. 307–317, 1991.

[51] Bogdanski, S., Stupnicki, J., Brown, M. W., and Cannon, D. F., "A two dimensional analysis of mixed-mode rolling contact fatigue crack growth in rails," in *Multiaxial Fatigue and Fracture* (Macha, E., Bedkowski, W., and Lagoda, T., eds.), pp. 235–248, Oxford: Elsevier Science Ltd., 1997.

[52] Miller, K. J., Brown, M. W., and Yates, J. R., "Some observations on mixed-mode fatigue behavior of polycrystalline metals," *ASTM Special Technical Publication Proceedings of the 1998 Symposium on Mixed-Mode Crack Behavior, May 6-May 7 1998*, no. 1359, pp. 229–257, 1999.

[53] Doquet, V. and Pommier, S., "Fatigue crack growth under non-proportional mixed-mode loading in ferritic-pearlitic steel," *Fatigue and Fracture of Engineering Materials and Structures*, vol. 27, pp. 1051–1060, 2004.

[54] Wong, S. L., Bold, P. E., Brown, M. W., and Allen, R. J., "A branch criterion for shallow angled rolling contact fatigue cracks in rails," *Wear*, vol. 191, no. 1-2, pp. 45–53, 1996.

[55] Desimone, H. and Beretta, S., "Mechanisms of mixed mode fatigue crack propagation at rail butt-welds," *International Journal of Fatigue*, vol. 28, no. 5-6, pp. 635–42, 2006.

[56] Wong, S. L., Bold, P. E., Brown, M. W., and Allen, R. J., "Fatigue crack growth rates under sequential mixed-mode I and II loading cycles," *Fatigue and Fracture of Engineering Materials and Structures*, vol. 23, pp. 667–674, 2000.

[57] Otsuka, A., Mori, K., Ohshima, T., and Tsuyama, S., "Mode II fatigue crack propagation in aluminium alloys and mild steel," in *5th International Conference on Fracture* (Francois, D., Bathias, C., and Bilby, B. A., eds.), vol. 4, (Cannes, France), pp. 1851–1859, Oxford: Pergamon Press, 1981.

[58] Plank, R. and Kuhn, G., "Fatigue crack propagation under non-proportional mixed mode loading," *Engineering Fracture Mechanics*, vol. 62, no. 2, pp. 203–229, 1999.

[59] Prasad, N. N. V., Aliabadi, M. H., and Rooke, D. P., "Thermomechanical fatigue crack growth," *International Journal of Fatigue*, vol. 18, no. 6, pp. 349–361, 1996.

[60] Dahlin, P. and Olsson, M., "The effect of plasticity on incipient mixed-mode fatigue crack growth," *Fatigue and Fracture of Engineering Materials and Structures*, vol. 26, no. 7, pp. 577–588, 2003.

[61] Tanaka, K., Akiniwa, Y., Kato, T., and Mikuriya, T., "Fatigue crack propagation from a precrack under combined torsional and axial loading," *Fatigue and Fracture of Engineering Materials and Structures*, vol. 28, pp. 73–82, 2005.

[62] Spievak, L. E., Wawrzynek, P. A., Ingraffea, A. R., and Lewicki, D. G., "Simulating fatigue crack growth in spiral bevel gears," *Engineering Fracture Mechanics*, vol. 68, no. 1, pp. 53–76, 2001.

[63] Yu, X. and Abel, A., "Fatigue crack growth in notched thin-walled tubes under non-proportional mixed mode loads," vol. 4 of *Proceedings of the International Offshore and Polar Engineering Conference*, (Golden, CO, USA), pp. 23–28, International Society of Offshore and Polar Engineers, 2000.

[64] Yu, X. and Abel, A., "Crack surface interference under cyclic mode I and steady mode II loading. I. Experimental study," *Engineering Fracture Mechanics*, vol. 66, no. 6, pp. 503–18, 2000.

[65] Soboyejo, A. B. O., Shademan, S., Foster, M., Katsube, N., and Soboyejo, W. O., "A multiparameter approach to the prediction of fatigue crack growth in metallic materials," *Fatigue and Fracture of Engineering Materials and Structures*, vol. 24, pp. 225–241, 2001.

[66] Mercer, C., Soboyejo, A. B. O., and Soboyejo, W. O., "Micromechanisms of fatigue crack growth in a forged Inconel 718 nickel-based superalloy," *Materials Science and Engineering A*, vol. 270, no. 2, pp. 308–322, 1999.

[67] Buchholz, F. G., Just, V., and Richard, H. A., "Computational simulation and experimental results on 3d crack growth in a 3pb-specimen with an inclined crack plane," in *Advances in Fracture Mechanics* (Buchholz, F. G., Richard, H. A., and Aliabadi, M. H., eds.), pp. 85–90, Zurich: Trans Tech Publications, 2003.

[68] FRANC3D and OSM software and documentation, Cornell Fracture Group, downloaded July 15, 2006 from `http://www.cfg.cornell.edu/software/franc3d_osm.htm`.

[69] BES software and documentation, Cornell Fracture Group, downloaded July 15, 2006 from `http://www.cfg.cornell.edu/software/bes.htm`.

[70] Walker, K., "The Effect of Stress Ratio During Crack Propagation and Fatigue for 2024-T3 and 7075-T6 Aluminum," in *Effects of Environment and Complex Load History for Fatigue Life - ASTM STP 462*, pp. 1–14, Philadelphia: American Society for Testing and Materials, 1970.

[71] Highsmith, J. and Johnson, W. S., "Elevated temperature fatigue crack growth in directionally solidified GTD-111 superalloy," *Fatigue and Fracture of Engineering Materials and Structures*, vol. 29, no. 1, pp. 11–22, 2006.

[72] Tada, H., Paris, P. C., and Irwin, G. R., *Stress Analysis of Cracks Handbook*. Hellertown, PA: Del Research Corporation, 2000.

VITA

Shelby Highsmith, Jr. was born in Miami, FL to Shelby and Mary Jane Highsmith, and graduated from the Ransom-Everglades School, Coconut Grove, FL in 1992. He attended the University of Notre Dame in Notre Dame, IN, receiving bachelor's degrees in Aerospace Engineering and Philosophy in May 1997. He worked in Propulsion Technology Development for AlliedSignal Engines (later Honeywell Engines & Systems) in Phoenix, AZ prior to attending Georgia Tech for graduate school. He received a master's degree in Materials Science & Engineering in December 2003. During the 2008 presidential election, he was an independent contributing producer/reporter to *Choose or Lose '08* for MTV News as well as the *Huffington Post*. He is the recipient of the National Science Foundation Graduate Research Fellowship, the Georgia Tech President's Fellowship, and the ARCS Atlanta Fellowship. He also received a Sam Nunn Security Studies Pre-Doctoral Fellowship in 2005-2006 to study science and technology policy and national security, the field in which he intends to pursue a career.